The Application of Bis-terpyridine Zinc(II) Complexes in LECs, OLEDs and DSCs

Inauguraldissertation

zur
Erlangung der Würde eines Doktors der Philosophie
vorgelegt der
Philosophisch-Naturwissenschaftlichen Fakultät
der Universität Basel

von
Niklaus Hostettler

aus Guggisberg (BE)

Basel, 2015

Genehmigt von der Philosophisch-Naturwissenschaftlichen Fakultät

auf Antrag von

Prof. Dr. Edwin C. Constable und Prof. Dr. Oliver S. Wenger

Basel, den 09. Dezember 2014

Prof. Dr. Jörg Schibler

Dekan

Namensnennung-Keine kommerzielle Nutzung-Keine Bearbeitung 3.0 Schweiz
(CC BY-NC-ND 3.0 CH)

Sie dürfen: **Teilen** — den Inhalt kopieren, verbreiten und zugänglich machen

Unter den folgenden Bedingungen:

Namensnennung — Sie müssen den Namen des Autors/Rechteinhabers in der von ihm festgelegten Weise nennen.

Keine kommerzielle Nutzung — Sie dürfen diesen Inhalt nicht für kommerzielle Zwecke nutzen.

Keine Bearbeitung erlaubt — Sie dürfen diesen Inhalt nicht bearbeiten, abwandeln oder in anderer Weise verändern.

Wobei gilt:

- **Verzichtserklärung** — Jede der vorgenannten Bedingungen kann **aufgehoben** werden, sofern Sie die ausdrückliche Einwilligung des Rechteinhabers dazu erhalten.
- **Public Domain (gemeinfreie oder nicht-schützbare Inhalte)** — Soweit das Werk, der Inhalt oder irgendein Teil davon zur Public Domain der jeweiligen Rechtsordnung gehört, wird dieser Status von der Lizenz in keiner Weise berührt.
- **Sonstige Rechte** — Die Lizenz hat keinerlei Einfluss auf die folgenden Rechte:
    - Die Rechte, die jedermann wegen der Schranken des Urheberrechts oder aufgrund gesetzlicher Erlaubnisse zustehen (in einigen Ländern als grundsätzliche Doktrin des **fair use** bekannt);
    - Die **Persönlichkeitsrechte** des Urhebers;
    - Rechte anderer Personen, entweder am Lizenzgegenstand selber oder bezüglich seiner Verwendung, zum Beispiel für **Werbung** oder Privatsphärenschutz.
- **Hinweis** — Bei jeder Nutzung oder Verbreitung müssen Sie anderen alle Lizenzbedingungen mitteilen, die für diesen Inhalt gelten. Am einfachsten ist es, an entsprechender Stelle einen Link auf diese Seite einzubinden.

Quelle: http://creativecommons.org/licenses/by-nc-nd/3.0/ch/ Datum: 12.11.2013

Acknowledgements

First of all, I would like to thank Prof. Dr. Edwin C. Constable and Prof. Dr. Catherine E. Housecroft for giving me the opportunity to work on this project. It was certainly not always easy, but whenever a problem occurred, they took their time to help me solving it. I am also very thankful for the freedom they gave me during my research.
I thank Prof. Dr. Oliver S. Wenger for being my co-examiner and co-referee.
Many thanks go to the people of the NMR group, namely PD Dr. Daniel Häussinger, Dr. Heiko Gsellinger and Kaspar Zimmermann. Not only did they teach me a lot about NMR and how to properly change a probe-head, they also do a great job maintaining the NMR machines in the department.
I thank all the supporting staff of the department, namely Dr. Heinz Nadig for recording EI- and FAB-MS spectra, Werner Kirsch and Sylvie Mittelheisser for performing elemental analysis, Markus Hauri and Roy Lips for material supply. Markus Hauri in particular for preventing the building from falling into pieces and his constantly raising my hopes that they will finally build in new windows in lab 215. Dr. Gabriel Schneider, Dr. Sven Brauchli, Dr. Collin Morris and Dr. Niamh Murray are acknowledged for recording ESI-MS spectra and Steffen Müller for measuring MALDI-TOF spectra. Marcel Düggelin from the ZMB I would like to thank for the numerous SEM – FIB images he recorded for me. Many thanks also go to the group of Dr. Henk Bolink in Valencia, Spain for the assembly and measurement of LEC and OLED devices, in particular to Dr. David Vonlanthen who did all the work.
Big thanks go to current and former members of the Constable/Housecroft group, in particular for the informal atmosphere:
I would like to thank Dr. Markus Neuburger for solving crystal structures and for at least trying to. I also thank Liselotte Siegfried and Dr. Biljana Bozic-Weber for electrode manufacturing and solar cell measurements at the beginning of my PhD. Beatrice Erismann I would like to thank for all her administrative work and the many entertaining coffee breaks. I thank Dr. Iain Wright and Dr. Colin Martin for their advice concerning synthetic problems and electrochemistry. Cedric Wobill I thank for his valuable contributions to chapter 7 during his Wahlpraktikum.
I deeply thank Dr. Sven Brauchli and Dr. Ewald Schönhofer for the brilliant time we had during the last four years, sharing a lab together. It was an honour and great pleasure to work with you guys! I thank Prof. Dr. Catherine Housecroft, Dr. Collin Morris, Dr. Biljana Bozic-Weber for proof reading this manuscript.

Special thanks go to Dr. Samuel Bader, Andreas Bünzli, Dr. Sven Brauchli, Annika Büttner, Beatrice Erismann, Cathrin Ertl ,Sebastian Fürer, Markus Hauri, Dr. Simon Kessler, Dr. Peter Kopecky, Dr. Colin Martin, Dr. Collin Morris, Dr. Gabriel Schneider, Dr. Jonas Schönle, Dr. Ewald Schönhofer, Florian Weiss and Dr. Iain Wright for the great time we had inside and also outside the lab. I enjoyed it a lot and I hope that friendships will be conserved.

Special thanks go to my parents and family who constantly motivated and supported me during all stages of my life.

Finally, I thank Danielle for her love and friendship and for enduring my grumpiness during the last few months.

Abstract

This thesis concerns the applications of easy to synthesize zinc(II) bis-terpyridine complexes in light emitting electrochemical cells (LECs), organic light emitting diodes (OLEDs) and dye sensitized solar cells (DSCs). Furthermore, the design and synthesis of new ligands and dyes for DSCs is presented.

Chapter 1 gives an introduction about the current energy situation and the necessity of a change in energy usage.

Chapter 2 describes general experimental methods and the instruments used during the project.

Chapter 3 shows the application of zinc(II) complexes in LECs and OLEDs and the optimizations done in the manufacturing process.

Chapter 4 is about the application of zinc(II) bis-terpyridine complexes in DSCs. Furthermore, a new stepwise method for the dye assembly on the semiconductor is introduced.

Chapter 5 discusses the problem of electron recombination in DSCs and presents potential solutions for zinc(II) bis-terpyridine dyes.

Chapter 6 describes the design and synthesis of a versatile donor – acceptor building block based on the benzothiadiazole (BTZ) unit and its use in a terpyridine based and an organic dye for DSCs.

Chapter 7 reports a design and possible synthetic pathway for two new anchoring ligands, based on the BTZ unit, for DSCs.

Chapter 8 shows the development and preparation of ZnO electrodes for the use in DSCs. Their performance is evaluated in combination with various dyes.

Chapter 9 concludes the thesis and gives a short outlook for further work in the field of zinc(II) based DSC.

Parts of this work have been published

Bozic-Weber, B.; Constable, E. C.; Hostettler, N.; Housecroft, C. E.; Schmitt, R.; Schönhofer, E. *Chem. Commun.* **2012**, *48*, 5727.

Hostettler, N.; Fürer, S. O.; Bozic-Weber, B.; Constable, E. C.; Housecroft, C. E. *Dye. Pigment.* **2015**, *116*, 124.

List of abbreviations

A	ampere
Å	Ångström
AcO	acetyl
Ar	aryl
Black dye	[Ru(4,4',4''-tricarboxylic acid-2,2’:6’,2’’-terpyridine)$(NCS)_3$]
bpy	2,2’-bipyridine
BTZ	benzothiadiazole
2D	two dimensional
C101	[Ru(2,2’-bipyridyl-4,4’-dicarboxylic acid)(4,4'-bis(5-hexylthiophen-2-yl)-2,2'-bipyridine)$(NCS)_2$]
°C	degree celsius
calc.	calculated
cd	candela
CH_2Cl_2	dichloromethane
cm	centimetre
COSY	correlation spectroscopy
δ	chemical shift [ppm]
D	deuterium
dba	dibenzylideneacetone
dm	decimetre
DMAP	4-(dimethylamino)-pyridine
DMSO	dimethyl sulfoxide
DSC	dye sensitized solar cell
ε	molar absorption coefficient

E	half-cell potential
EL	electroluminescence
ESI	electrospray ionisation
Et	ethyl
Et_2O	diethyl ether
eq.	equivalent
EQE	external quantum efficiency
eV	electron volt
Fc/Fc^+	Ferrocene/Ferrocenium
FF	fill factor
FTIR	Fourier-transform infrared spectroscopy
FTO	fluorine doped tin oxide
g	gram
h	hour
HMBC	heteronuclear multiple bond correlation
HMQC	heteronuclear multiple quantum coherence
HOMO	highest occupied molecular orbital
Hz	hertz
ILCT	intra-ligand charge transfer
IR	infrared; for the IR spectra with w for weak, s for strong, m for medium
ITO	indium tin oxide
J	coupling constant
J_{SC}	current density measured at short-circuit
K	Kelvin
λ_{abs}	absorption wavelength

λ_{em}	emission wavelength
λ_{ex}	excitation wavelength
LCD	liquid crystal display
LEC	light emitting electrochemical cell
LED	light emitting diode
LMCT	ligand to metal charge transfer
LT-N865	1,3-bis[3,5-di(pyridin-3-yl)phenyl]benzene
LUMO	lowest unoccupied molecular orbital
µmol	micromole
m	metre
M	mol L^{-1} or parent ion
mA	milliampere
MALDI-TOF	matrix assisted laser desorption ionisation-time of flight
Me	methyl
MeCN	acetonitrile
MeOH	methanol
mg	milligram
MHz	megahertz
min	minute
mL	millilitre
MLCT	metal to ligand charge transfer
mm	millimetre
mmol	millimole
MPP	maximum power point
MS	mass spectrometry

mV	millivolt
mW	milliwatt
m/z	mass to charge ratio
η	overall conversion efficiency from solar to electrical energy for a photovoltaic device
[^{n}Bu$_4$N][PF$_6$]	tetra-*n*-butyl ammonium hexafluoridophosphate
ν	frequency in Hz
$\tilde{\nu}$	wavenumbers in cm^{-1}
N3	[Ru(4,4'-(dicaboxylicacid)-2,2'-bipyridine)$_2$(NCS)$_2$]
N719	[Ru(4,4'-(dicaboxylicacid)-2,2'-bipyridine)$_2$(NCS)$_2$][TBA]$_2$
NIR	near infrared
nm	nanometre
NMR	nuclear magnetic resonance, with the signals being identified as singlet (s), doublet (d), triplet (t), quartet (q), septet (h)
NOESY	nuclear overhauser enhancement spectroscopy
ns	nanosecond
OLED	organic light emitting diode
PEDOT	poly(3,4-ethylenedioxythiophene)
PET	polyethylenterephthalat
Ph	phenyl
P_{in}	intensity of the incident light
PJ	petajoule (PJ = 10^{15} J)
PL	photo luminescence
PLQE	photo luminescence quantum yield
PMMA	1-(4-methoxyphenyl)-*N*-methyl-propan-2-amine/polymethylmethacrylate

ppm	parts per million
PPO27	2,7-bis(diphenylphosphoryl)-9-phenyl-9H-carbazole
PSS	poly(styrene sulfonic acid)
PVK	polyvinylcarbazole
rpm	rounds per minute
RT	room temperature
sh	shoulder
SPPO13	2,7-Bis(diphenylphosphoryl)-9,9'-spirobifluorene
TBA	*tert*-butylammonium
^{t}Bu	*tert*-butyl
TCTA	tris(4-carbazoyl-9-ylphenyl)amine
TEOS	tetraethylorthosilicate
TFA	trifluoroacetic acid
THF	tetrahydrofuran
TMS	tetramethylsilane
tpy	2,2’:6’,2’’-terpyridine
UV	ultraviolet
Vis	visible
VL367	2,7-bis(pentylsulfonyl)-9,9'-spirobi[fluorene]
V_{OC}	open-circuit photovoltage
Vol.	volume
vs.	versus
W	watt
wt	weight

Table of Contents

Chapter 1

Chapter 1: Introduction

1.1. The energy problem

Today's modern society is facing an energy problem. The technical achievements of the last 30 years and the growth of population lead to an explosion in energy consumption, namely in the form of electrical energy. Not only the very basic needs have to be satisfied such as heating, lighting or cooking, but also charging mobile phones, watching TV or playing computer games. Figure 1-1 shows how the electricity was consumed in Switzerland in the year 2013. A large part was used by industry, but almost 1/10 of the energy was consumed for heating and another 1/8 for lighting. Another interesting category is information and communication (I & C), which grew by 16.5% from 2000 to 2013. However, this section did not grow at the expense of another one. Since 2000, all of these categories increased by at least 3.3%. The total energy consumption increased by 12.0% from 187.1 PJ in the year 2000 to 209.6 PJ (PJ = petajoule = 10^{15} J) in 2013.[1]

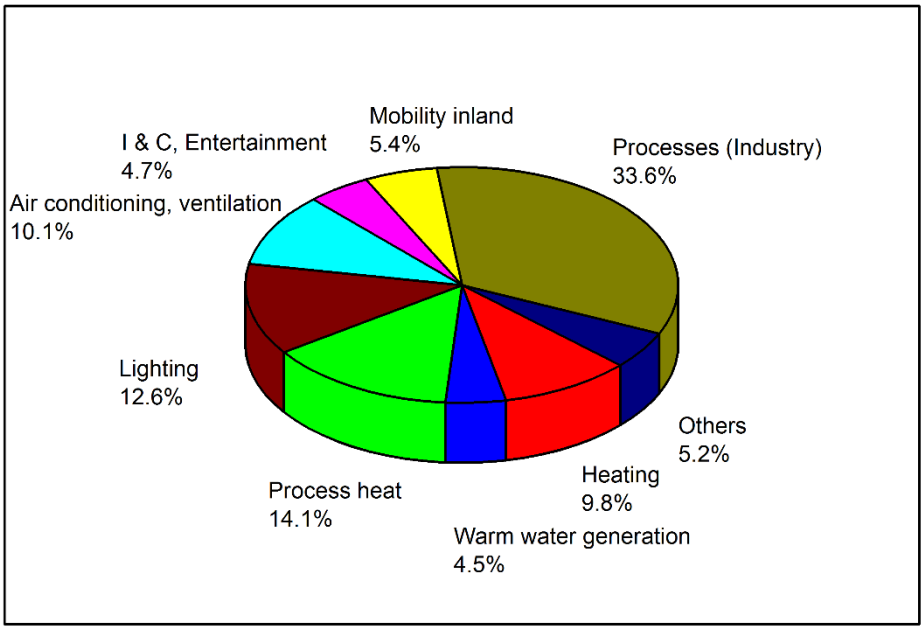

Figure 1-1: Usage of energy in Switzerland in the year 2013.[1]

However, where does the produced electricity come from? In the year 2013 nuclear power plants generated 39.3% of Switzerland's electricity, which corresponds to an absolute value of 24.8 x 10^9 kWh. 58% is produced by hydroelectric power stations

and 5.7% by conventional thermal power plants and others (Figure 1-2). To this category also belong renewable energy sources like wind, or photovoltaics.[2] Although this shows that renewable energy in the form of photovoltaics is not very popular yet, statistics show that the amount of electricity produced by photovoltaics in Switzerland increased by 85.3% from 2011 to 2012.[2]

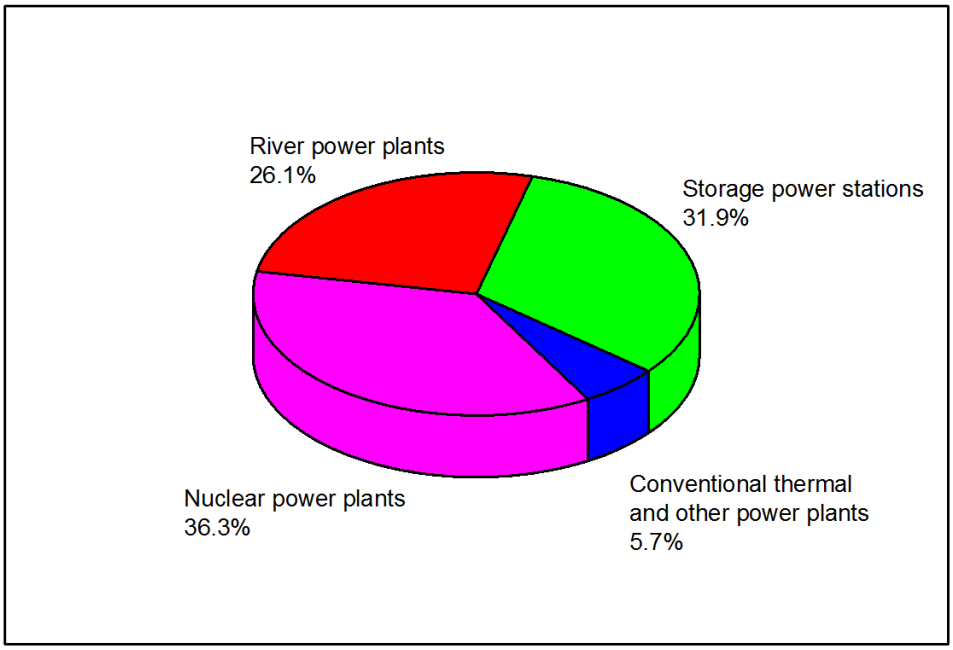

Figure 1-2: Energy production in Switzerland.[2]

The ratio of renewable electricity that was produced in Switzerland in 2013 lies at 3.39% of the total energy production. Figure 1-3 shows how the different sustainable energy sources makes up these 3.39%. One can see that half of the renewable energy stems from waste regeneration. Approximately 1/4 is produced by photovoltaics and only 4.1% by wind power stations.[3] Reasons for the very low contribution of renewable energy sources in Switzerland can be found in the small size of the country and the mountained and therefore impracticable areas, which make the construction of wind power stations rather challenging. In addition, the meteorological conditions are not convenient for large area photovoltaic power plants, which makes the technology more suitable for rooftop installation for private households.

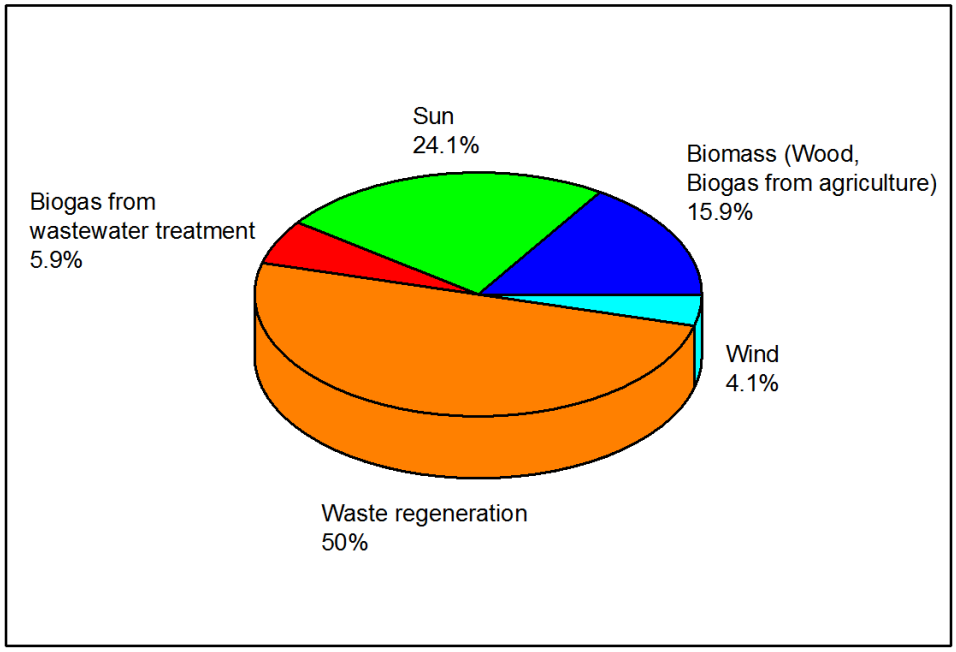

Figure 1-3: Ratios of contributions of the renewable energy sources to the 3.39% of total renewable energy production in Switzerland.

However, one has to keep in mind that the presented numbers only represent the consumption of electrical power in Switzerland, which is a small country with only 8.1 million residents.[4] If this is extrapolated to a global scale it is an enormous amount. The Statistical Review of World Energy 2014 from BP calculates the worldwide use of primary energy (energy that has not yet been converted in any form[5]) in 2013 to 2730.4 mio. tonnes oil equivalent. This corresponds to about 115 x 10^{18} J.[6]

For a long time, nuclear power was said to be the future energy source, because it delivers cheap energy without releasing greenhouse gases. Therefore, it was considered as being clean. Nevertheless, in the last decade people started to realize that the problems with radioactive waste disposal are still not definitely solved and the unstable political situation in certain countries leads to a rethinking. Additionally accidents like the one in Lucens (VD) in 1969, where an underground research reactor had a core meltdown or the one in 1989 in Chernobyl, where after an explosion in the reactor building vast amounts of radioactive material were blown into the environment, clarified that this form of energy generation can lead to disastrous environmental catastrophes.[7],[8] The latest accident dates from 2011 where a tsunami, caused by an earthquake, severely damaged a nuclear power plant in Fukushima (JPN). Among the

consequences are polluted subterranean water and radioactive water flowing into the sea.[9] As a direct consequence of the accident in Fukushima (JPN), the Swiss federal council decided to put in place a nuclear phase-out by the year 2034 and to focus on the development of sustainable energy instead.[10]

Considering the increasing world population and the associated rising energy demand in the future it is certainly important to think about powerful substitutes to fill the emerging energy gap. Taking into account the fact that every hour 4.3 x 10^{20} J of energy from the sun strike our planet, makes photovoltaics a very promising alternative to fossil fuels and nuclear energy.

Although it is a major issue to find alternative energy sources, it is as important to reduce the usage of energy. One very prominent example is lighting. It was a milestone in the history of lighting when Thomas A. Edison patented his “Electric-Lamp” on the 27th of January 1880 and at the same time it was the start of the electrification of the cities and the build-up of an area-wide grid. The light bulb has survived in almost the same form until now, but the traditional design of tungsten filament bulbs wastes a large amount of energy in the form of heat. A few years ago, the European Union decided to ban classical light bulbs from the market. This law was adopted by the Swiss government, which means that in Switzerland and the European Union, conventional light bulbs, with more than 7 W power, have been prohibited from sale since September 1st 2012.[11],[12] This should smooth the way for more efficient lighting technologies such as light emitting diodes (LEDs). In principle, LEDs have been known since the 1960s but enjoy greater popularity nowadays because of improved production techniques. To award the very important investigations about LEDs, this year’s (2014) Nobel Prize in Physics was awarded to Isamu Akasaki, Hiroshi Amano and Shuji Nakamura "for the invention of efficient blue light-emitting diodes which has enabled bright and energy-saving white light sources".[13]

However, it is not only important to develop new and energy efficient technologies, but also to base them on abundant materials, e.g. it does not make sense to develop new lighting sources based on materials that will never be available in big enough amounts to satisfy the needs of industry. This is the reason why our research group, wherever possible, tries to use earth abundant materials. This is not only beneficial for the environment, but has also positive effects on the final price of the product.

This thesis focuses mainly on applications of the metal zinc, or more precisely on bis-terpyridine complexes of the zinc(II) ion. Figure 1-4 shows the abundance of the

elements in the earth's upper continental crust, normalized to an abundance of 10^6 for silicon. It reveals that the elements ruthenium and iridium, which are very often used in dye sensitized solar cells (DSCs) or light emitting electrochemical cells (LECs), are among the rarest on earth. On the other hand zinc is much more abundant and therefore much cheaper and more economically reliable.

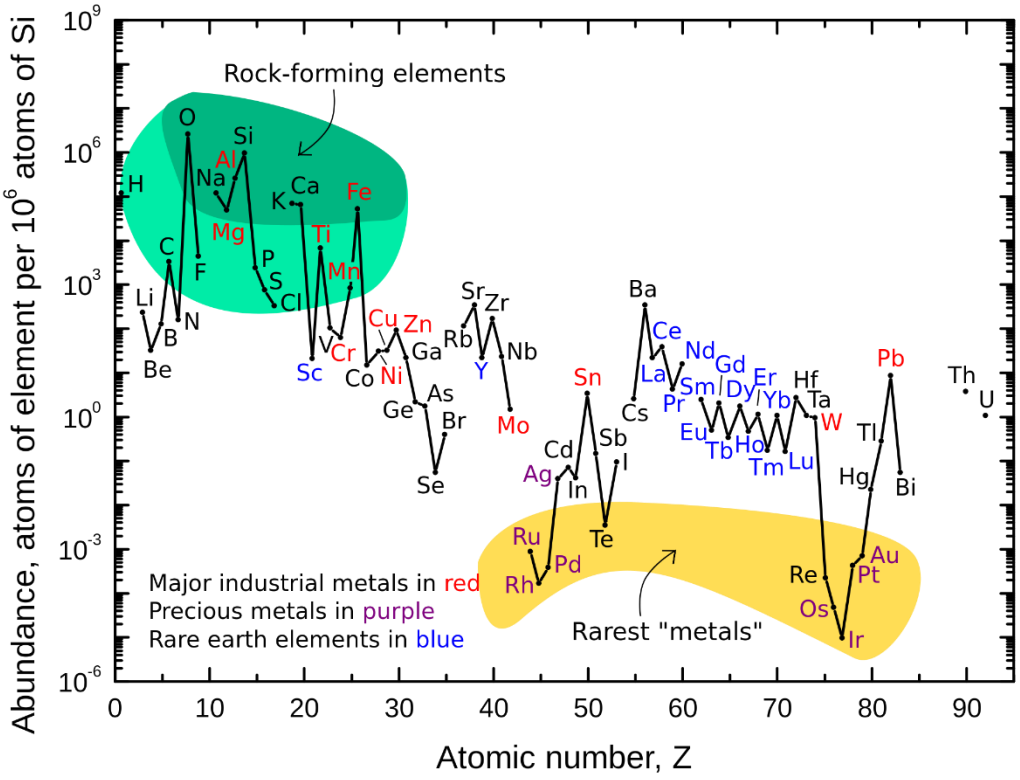

Figure 1-4: Abundance of the elements found in the upper continental earth crust (graphic courtesy of the Wikimedia Commons).[14]

1.2. Zinc

The bluish-white chemical element zinc (Zn) with the atomic number 30 is the first element of group 12 and the last of the first row of transition metals in the periodic table (Picture 1-1). The name is derived from the German word "Zink", which originates from the Persian word "sing" for stone. Its electron configuration is [Ar] $3d^{10}$ $4s^2$ and the most common oxidation state is 2+ in the electron configuration [Ar] $3d^{10}$. It reacts with acids and bases and forms coordination compounds of various geometries (e.g. octahedral, tetrahedral and square planar). Since the d^{10} configuration has no crystal field stabilization energy, there are no electronically favoured geometries, steric factors are therefore important. Complexes are in most cases colourless because of the d^{10}

configuration of the Zn^{2+} ion. As will be discussed in the later chapters there are exceptions depending on the ligands used.[15][16]

Picture 1-1: Image of zinc metal in different forms. Image by Heinrich Pniok (www.pse-mendelejew.de), Licence: Free Art Licence (FAL).

Zinc is, after iron, aluminium and copper, the most commonly used metal in commercial applications. It finds applications in steel coatings, paints and it is a component of brass. Furthermore, it is an important element in most living organisms. One of the most prominent examples is the zinc finger protein, which can bind to DNA. Other functions are in enzymes regulating e.g. fertility and growth or in carbonic anhydrases, which help living organisms to convert carbon dioxide and water to bicarbonate and protons or vice versa.[15],[17]

It probably was already known to the Romans, and was first refined on a large scale in Rajasthan, India between 1100 and 1500. There is also proof that the Chinese refined zinc at the end of this period, but the awareness of zinc being a new element was credited to a German chemist named Andreas Marggraf in 1746. Today the element is mined in over 50 countries and Australia has the largest natural sources. Its natural abundance in the earth's crust is 72 ppm, which makes it the 23rd most abundant element on earth. [17],[18],[19]

The main commercial source of zinc metal is the mineral sphalerite (ZnS), which normally also contains other metals such as iron (≤ 10%), cadmium, indium, gallium and germanium. Other natural sources of zinc are $ZnCO_3$, $ZnSO_4$ and ZnO.[20]

1.3. Light emitting devices

Current research focusses on novel lighting techniques like organic light emitting diodes (OLEDs) and light emitting electrochemical cells (LECs), although the latter are not yet commercially available on a large scale. These two lighting technologies are embraced by the term “solid-state lighting”. OLEDs normally incorporate organic emitters, whereas LECs require charged species, which are often transition-metal complexes. Lighting devices based on these two techniques work on the basis of electroluminescence (EL), which is luminescence produced by electrode reactions.[21] When a voltage is applied to such a device, on the cathode side electrons are injected into the LUMO and on the anode side electrons are extracted (which corresponds to the injection of a hole) from the HOMO. These charges can migrate through the film and eventually get close enough to each other to pair. Upon pairing, an exciton is formed, which then decays (Figure 1-5). Due to this decay, the electronic ground state is restored and photon is emitted.[22]

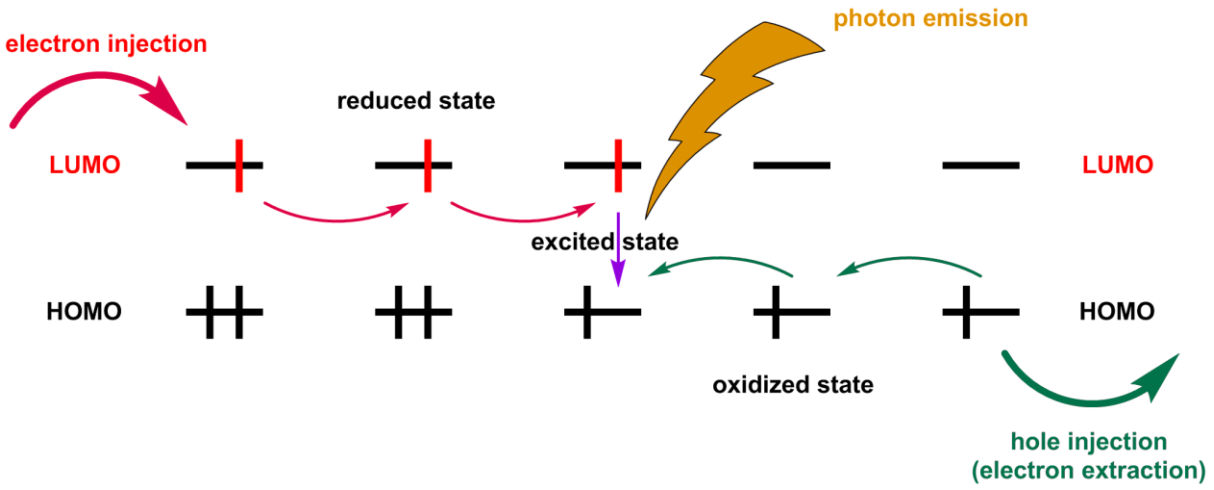

Figure 1-5: Schematic representation of the EL principle.[23]

Electroluminescence was discovered and first reported by Hercules[24] in 1964. He investigated hydrocarbons such as anthracene or perylene and was able to observe electroluminescence from these compounds upon application of a current. This discovery was probably the starting point for more investigations about electroluminescence. Electroluminescent behaviour of one of the most well studied compounds until now, $[Ru(bpy)_3]^{2+}$, was reported by Tokel and Bard in 1972.[25] They

also discussed possible mechanisms that are at the basis of electroluminescence. These findings only involved electroluminescence in solution. Pope et al.[26] and Helfrich and Schneider[27] were the first to report electroluminescence in solids, namely anthracene crystals.

1.3.1. OLEDs

Almost two decades elapsed until Tang and van Slyke developed what is considered as the first OLED device, using low-weight organic molecules.[28] From their development until now, there has been enormous progress in the performance and durability of OLED devices. There are several properties that make them interesting for commercial use and for the replacement of classical light sources. OLED devices can be manufactured by screen printing methods or using inkjet printing.[29] This offers the possibility of large-scale industrial production and the realisation of flexible lightweight devices on plastic substrates like PET, which makes OLEDs suitable for applications in clothing or bent displays.[30],[31] Furthermore, OLEDs offer wider viewing angles, better contrasts and true black compared to conventional liquid crystal displays (LCDs). This is due to the needlessness of a backlight. This also makes OLEDs more power efficient than LCDs.

Nevertheless, OLEDs do not only have advantages, there are several problems that have to be taken into account. Since the emissive species is in most cases an uncharged organic material, additional components are necessary to support electron and hole transport throughout the film, which means that several layers have to be processed. Furthermore, it was found that electrodes with low work functions can have a positive impact on the efficiency of a device, therefore materials have to be used that are often not air-stable. The multi-layer build-up and the necessary encapsulation to prevent degradation caused by moisture and oxygen, makes the manufacturing process a challenging task.[32]

1.3.2. LECs

In 1995 a LEC device consisting of a single layer of conjugated polymer with ion-conducting polymer and an inorganic salt, was reported by Pei et al. [33],[34] They showed that due to the high concentration of mobile ions in the emitting layer, no additional layers are needed to support the transport of charges within the film. This build-up has the advantage that it is not dependent on the work function of the electrode, which permits one to use less reactive electrode materials that do not require complete encapsulation and protection from moisture and oxygen. Later, ionic transition metal complexes with small, non-coordinating counter ions (e.g. BF_4^-, PF_6^-) were introduced as emitters. Due to the charged nature of these compounds the addition of inorganic salts had become unnecessary and all components needed (ionic conduction, electronic transport and luminescence) were combined in one compound.[35]

The working principle of a LEC is the same as shown in Figure 1-5. On the cathode electrons are injected into the layer containing the emitting species. On the anode electrons are extracted (or holes injected). These charges move through the film by hopping. On their way to the opposite electrode, the oppositely charged species can eventually meet and combine, which can be followed by the emission of a photon.

Figure 1-6 shows the striking difference between OLEDs and LECs in the number of different layers that are needed for a working device. This is probably by far the most important advantage of the LEC over the OLED.

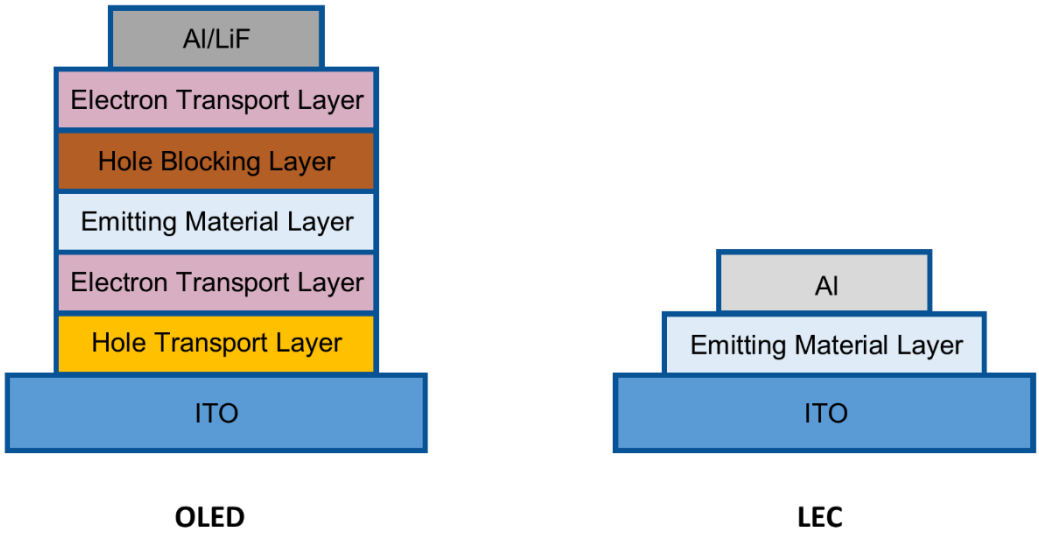

Figure 1-6: Comparison of the layered structure of OLEDs and LECs.[36]

However, LECs still suffer from a variety of disadvantages. They offer still very slow turn-on times and poor efficiencies. Another problem is the short life time and the tunability of the emitted wavelength.[37] These disadvantages have to be overcome before an industrial-scale production can be realized.

1.4. Dye sensitized solar cells (DSCs)

1.4.1. History and working principle

It is possible to trace back the history of photosensitization of semiconductors to 1873, when Vogel discovered the photographic process,[38] or to Moser who, in 1887[39] in Vienna, discovered that he could increase the photoelectric current between two halogenated silver plates by first immersing the plates in a dye solution. Making a step in the 20th century, Goodenough and coworkers[40] in 1979 described the sensitization of TiO_2 with a ruthenium dye. However, it took more than another decade and a publication by Grätzel and O'Regan[41] to definitely launch the extensive research on DSCs. Figure 1-7 shows the exponential increase of publications related to the research topic "dye sensitized solar cells", after the publication by Grätzel and O'Regan in 1991.[41]

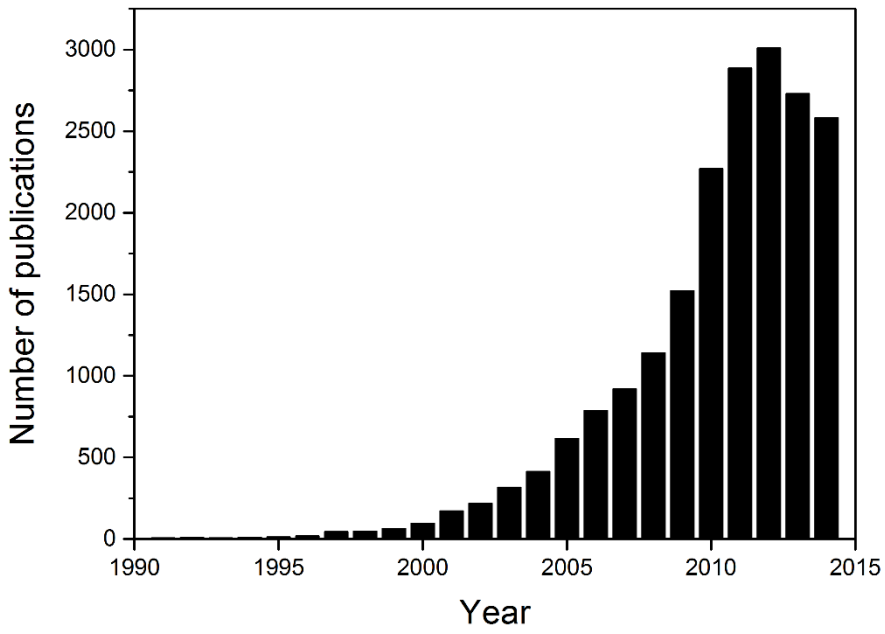

Figure 1-7: Number of DSC publications found in Scifinder® (as at 17.11.2014).

The DSCs that Grätzel introduced are based on a transparent TiO_2 semiconductor. This material only absorbs UV light, therefore an inorganic dye was attached to the semiconductor surface to widen the absorption range.[42],[43]

Figure 1-8 shows a schematic representation of the processes happening in an n-type DSC. The cycle is started by the absorption of an incident photon by the dye, which excites it from its ground state (S) to its excited state (S*). The excited dye injects then an electron into the conducting band of the semiconductor. In most cases, this is microcrystalline TiO_2. The injected electron subsequently travels through the semiconductor layer to the back electrode, which consists of a glass slide covered with ITO or FTO to make it conductive. The electron travels then through an external circuit, where it can do electrical work. After this, it enters the cell through the counter electrode, which consists of an ITO cover glass slide incorporating a platinum catalyst to reduce resistance. The electron is now able to reduce oxidized redox mediator, which thereupon reduces the oxidized dye molecule to restore the initial state.[44] All these processes take place in a millisecond to hundred-nanosecond time domain.[45]

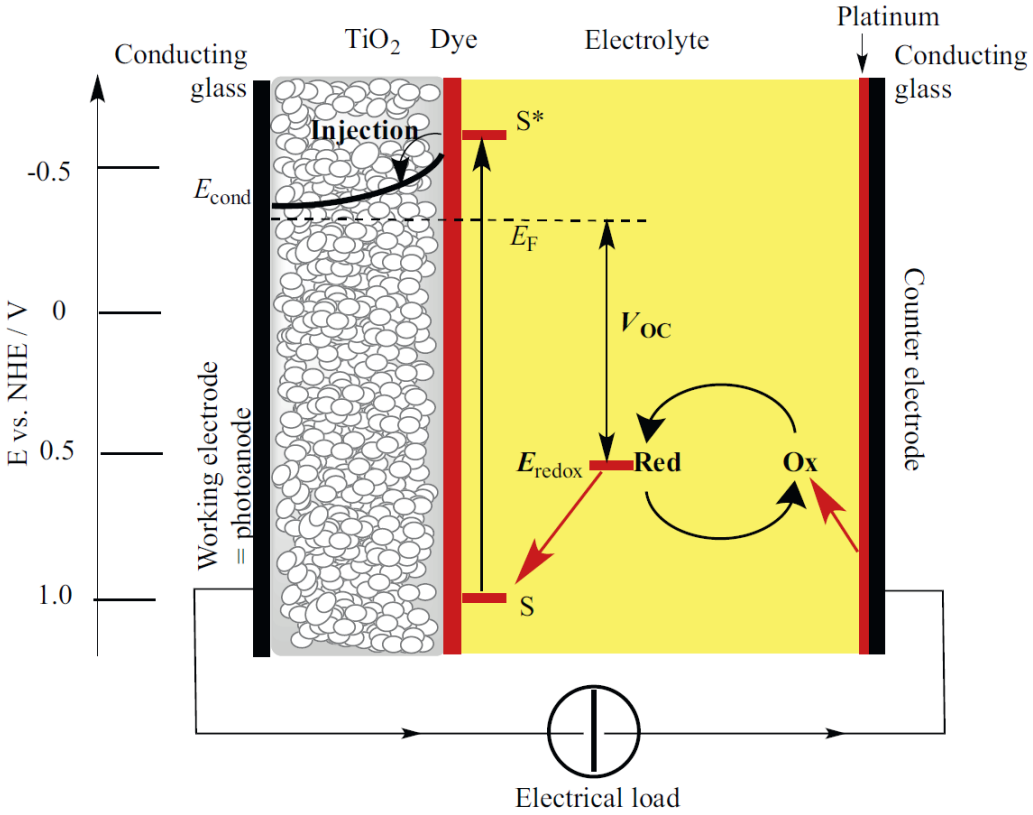

Figure 1-8: Schematic representation of the processes happening in a DSC.[46]

1.4.2. Important parts of a DSC

A DSC consists of a number of components, as Figure 1-8 illustrates. These parts have to work together in a way that the whole system works as efficiently as possible. It is therefore not trivial to optimize single components, because every change can have an influence on the other parts of the system, e.g. changing the dye or even the anchoring group in the dye influences the properties of the semiconductor or the electrolyte. It is important that one understands the interrelationships between the separate parts.

1.4.2.1. Semiconductor

Semiconductors are solid materials that have small enough band-gaps, which can be overcome by the expenditure of thermal energy or absorption of photons and can therefore be conducting under certain circumstances. In contrast to this, insulators show large band-gaps.[16] Most DSCs contain n-type semiconductors and numerous n-type semiconductor materials have been well studied, e.g. TiO_2, ZnO, WO_3, V_2O_5, ZnS and many more.[47] Nevertheless, the most often used is still TiO_2. It is nontoxic, inert, readily available and can form transparent layers. It is widely used as white pigment in paints or in toothpastes. TiO_2 exists mainly as three different polymorphs, namely rutile, anatase (Figure 1-9) and brookite, but not all of them are suitable for the use in DSCs. For this purpose anatase is used because it shows the higher photo catalytic activity than rutile or brookite.[48]

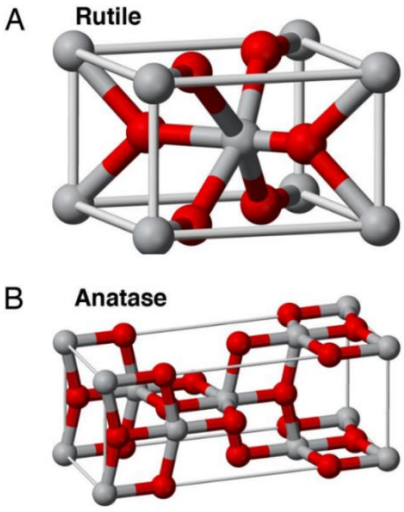

Figure 1-9: Crystal structures of (A) rutile and (B) anatase.[49]

There are different ways to apply TiO_2 on the ITO or FTO covered glass slide, but the mainly used ones are doctor blading or screen printing (Chapter 8). For this, pastes containing TiO_2 nanoparticles are used. This is very important, since a layer of nanoparticles shows a much higher surface area than just a layer of bulk TiO_2 material and is therefore able to adsorb many more dye molecules.

1.4.2.2. Dyes

Dyes used in DSCs can be classified into metal containing and purely organic dyes and since there are so many different dye molecules known by now, this is probably the most variable part within a DSC. Nevertheless, there are certain properties that a good dye should fulfil: (a) A good dye should absorb as much light as possible over the whole visible spectrum as well as into the near-infrared region. (b) The dye should exhibit suitable functional groups to anchor it permanently on the semiconductor surface, e.g. $–PO(OH)_2$, -COOH or –OH. (c) It is important that the energy levels of the dye fit to the band energies of the used semiconductor material, namely the excited state of the dye should lie above the conduction band edge of the semiconductor, to provide unhindered injection of electrons into the semiconductor. (d) The potential of the oxidized state of the dye should be more positive than the redox potential of the used electrolyte to guarantee efficient dye recovery. (e) Dye molecules should be designed in a way that aggregation can be avoided, since this can have a negative influence on the performance of the dye and thus also on the efficiency of the DSC. This can be achieved by the application of coadsorbers e.g. chenodeoxycholic acid [50] or the introduction of aliphatic substituents (Chapter 5). (f) The dye molecule should exhibit photostability as well as thermal and electrochemical stability.[45]

Concerning the anchoring of a dye on the semiconductor, there is still debate as to how the dyes are attached to the semiconductor surface. In general, six different modes can be thought of: (1) the dye can be anchored covalently, (2) by electrostatic interactions, such as ion-pairing, ion exchange or donor-acceptor interactions, (3) by hydrogen bonding interactions, (4) by hydrophobic interactions that arise from the interaction of hydrophobic groups, such as long alkyl chains. (5) by weak attachment of the dye through van der Waals interactions, (6) or by trapping of the dye molecule in cavities on the surface.[51] One of the most commonly used anchoring groups is, as already mentioned above, the carboxylate unit. In Figure 1-10 the different possible

anchoring modes of the carboxylate anchoring group are shown. It is not possible to definitely say which one occurs and of course, the protonation state depends on the pH. It is also possible that it is an interplay of different binding modes.

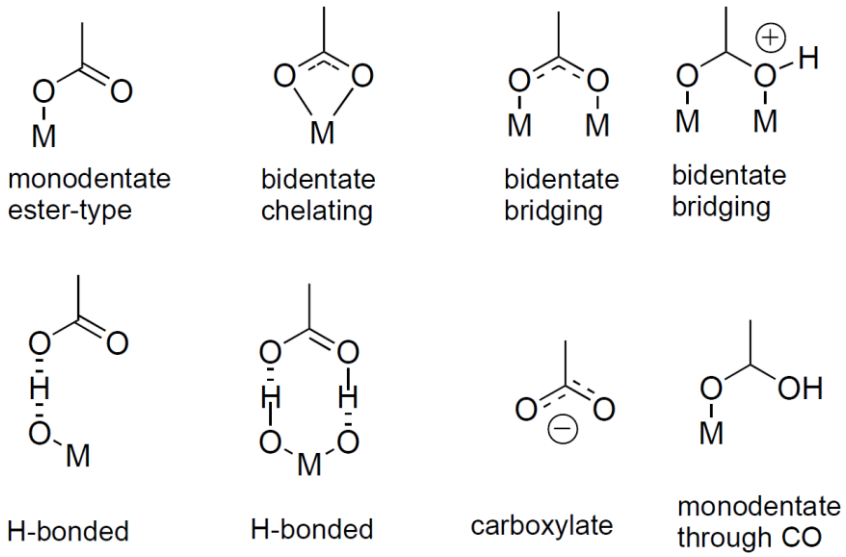

Figure 1-10: Different anchoring modes of the carboxylate ancoring group to a metal oxide, such as TiO_2.[52]

As mentioned at the beginning of this section, there is a huge variety of dyes available in literature. The most common and well-studied examples are ruthenium(II) dyes. A very prominent representative of this group is N719 (Scheme 1-1), which serves as a reference dye in most of the published papers about DSCs. There are also other ruthenium-based dyes that show remarkable efficiencies (Scheme 1-1). Dye C101[53] can reach an efficiency of about 11.1%, black dye[54] of about 10.9% and N719 and N3 both more than 10%.[46]

Taking into account the important argument of sustainability, copper(I) complexes are also a very interesting class of dyes for DSCs. Although they are not yet able to compete with ruthenium based dyes, there has been remarkable progress in the last years on this field. The most efficient copper-based dyes exhibit efficiencies between 2% and 3%.[55],[56] Recently, Odobel[57] reported a copper(I) based DSC with an efficiency of 4.7% using chenodeoxycholic acid as co-adsorbent.

Purely organic dyes that are often designed in a donor - π-bridge - acceptor manner (Chapter 6) are also promising. Organic dyes have the advantage of not incorporating precious metals, which makes them cheaper and therefore more attractive to large-

scale production than e.g. ruthenium based dyes. DSCs using organic dyes can reach efficiencies up to 9.5%, using the example of an indoline dye.[58]

Another very interesting class of sensitizers are porphyrins. Grätzel recently reported a DSC based on a zinc porphyrin with an efficiency of 13%.[59] However, asymmetric porphyrins normally are very time consuming to synthesize and require extensive cleaning protocols, since a variety of different porphyrins can form during the synthesis.

The last class of dyes to mention are zinc(II) bis-terpyridine based. The work presented in this thesis demonstrates the first results in the literature in this field.[60]

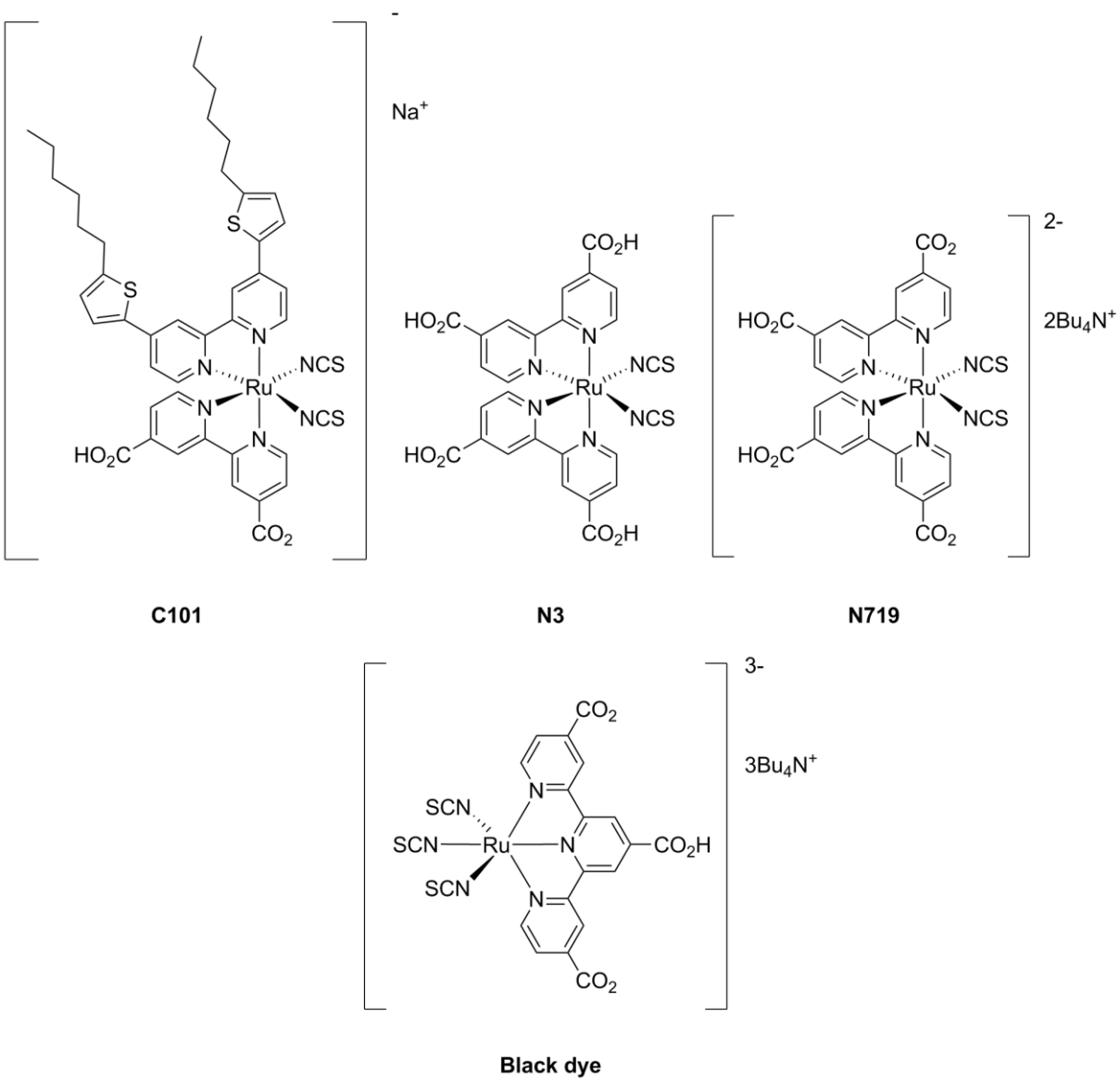

Scheme 1-1: Chemical structures of four of the most efficient ruthenium dyes.

1.4.2.3. Electrolytes

Electrolytes play a very important role within a DSC, since they ensure the efficient electron transport between the oxidized dye molecules and the counter electrode. Furthermore, the electrolyte should not undergo unwanted electron/hole recombination reactions with the semiconductor, which would lower the DSC efficiency. However, there are a few criteria that an ideal electrolyte should match. It should be (a) chemically stable, (b) show low viscosities to reduce mass transport problems, (c) readily dissolve the redox active species and all additives, but not dissolve the electrode material or the adsorbed dye and (d) should not attack the sealing material of the DSC to avoid damaging of the cell.[45]

The standard electrolyte that is used the most is the I^-/I_3^- redox couple. This was optimized mainly for ruthenium based DSCs. Nevertheless, there are also other electrolytes that are widely used, e.g. Co^{2+}/Co^{3+} based ones that have proved to be suitable for organic[61] and copper(I)[62] based dyes.

1.4.3. Measurement of the DSCs

When an IV measurement (I = current, V = potential) of a DSC is carried out, one obtains characteristic parameters for the device (Figure 1-11). In such a measurement, the current is recorded against the voltage. The first thing to take into account is that current is a one dimensional measure, but since the solar cell consists of an area of semiconductor material, the obtained current has to be divided by the area of said semiconductor. This coverts the measured current values (I) into current density (J), usually measured in mA/cm^2. Two very important measures are the short circuit current density (J_{SC}), which is the highest possible current density the cell can deliver, and the open circuit voltage (V_{OC}), which is the maximum potential the cell is able to produce. The rectangle (R) (Figure 1-11) that J_{SC} and V_{OC} span, gives the theoretically maximum power (P) that the cell could deliver if no losses occur (Equation 1-1).

$$P = V \times J$$

Equation 1-1

This is important for the later calculation of the fill factor. The inner rectangle (R´) (Figure 1-11) is spanned by J_{MMP} and V_{MPP}. These two measures are the two maximum current and potential values that can be reached in dependence from each other. The product of these two values gives the maximum power that the cell is able to deliver. When R´ is divided by R, the fill factor is obtained (Equation 1-2), which is a measure of the cell quality, since it reflects the difference between the real and an ideal system.

$$ff = \frac{V_{MPP} \times J_{MPP}}{V_{OC} \times J_{SC}} = \frac{R´}{R}$$

Equation 1-2

The most cited parameter, the cell efficiency (η), is obtained by multiplication of the three factors V_{OC}, J_{SC} and fill factor, divided by P_{in} (Equation 1-3).

$$\eta = \frac{V_{OC} \times J_{SC} \times ff}{P_{in}}$$

Equation 1-3

P_{in} is the intensity of the light that was given into the system, namely 1000 W/m^2.

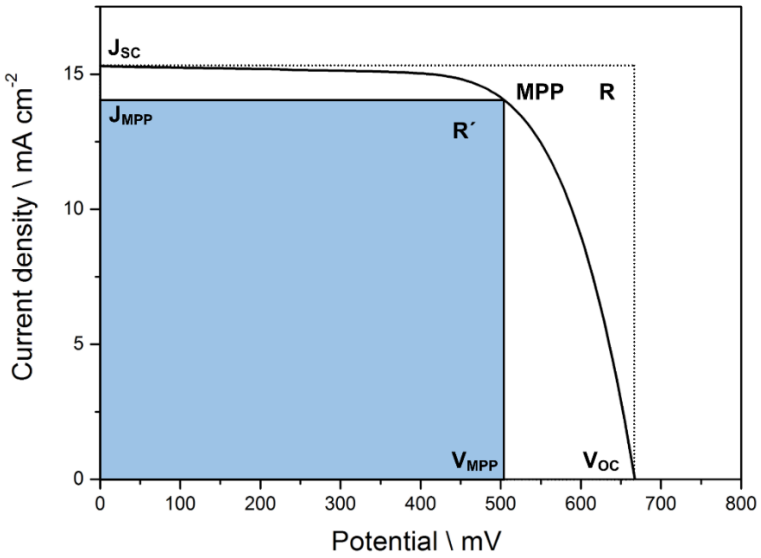

Figure 1-11: Result of JV-measurement with all necessary key parameters highlighted.

Chapter 2

Chapter 2: General experimental

2.1. Used equipment

^{1}H, ^{11}B, ^{13}C NMR spectra were recorded on Bruker DRX-400, DRX- 500, Bruker Avance III-400, Avance III-500 NMR spectrometers. The chemical shifts were referenced as follows: for ^{1}H and ^{13}C NMR spectra, chemical shifts were referenced to residual solvent peaks with respect to δ(TMS) = 0 ppm, for ^{11}B with respect to $Et_2O.BF_3$ = δ_B 0 ppm. Spectra were assigned using COSY, NOESY, DEPT, HMQC and HMBC techniques. Solution absorption spectra were recorded on an Agilent 8453 or Agilent Cary 5000 UV-Vis-NIR spectrophotometer. Solution emission spectra were recorded on a Shimadzu RF-5301 PC spectrofluorometer. FT-IR spectra were recorded using a Shimadzu 8400S instrument with Golden Gate accessory for solid samples or PerkinElmer UATR Two spectrometer. Electrospray ionization (ESI) mass spectra were measured using a Bruker esquire 3000plus mass spectrometer. Elemental analyses were measured on a Leco CHN-900 microanalyser. Electrochemical measurements were carried out using cyclic voltammetry and were recorded using a CH Instruments 900B potentiostat with glassy carbon working and platinum auxiliary electrodes; a silver wire was used as a pseudo-reference electrode. Solvent was dry, purified MeCN or CH_2Cl_2 and 0.1 M [nBu$_4$N][PF_6] was used as supporting electrolyte. Cp_2Fe was used as internal reference. All solutions were degassed with argon. A Biotage Initiator 8 reactor was used for the syntheses under microwave conditions. Crystallographic data were collected on a Bruker-Nonius Kappa APEX diffractometer with data reduction, solution and refinement using the programs APEX2,[63] SIR92,[64] and CRYSTALS,[65] Structures were analysed using Mercury v. 3.5.[66],[67] The manufactured electrodes for DSCs were sintered in a Nabertherm N 15/65HA oven. For screen printing a 90-48Y PET mesh from Serilith AG was used. Electrodes were cut with a CAMAG smartCUT glass cutter. Height profiles were measured with a KLA Tencor AlphaStep® D-100 profilometer. SEM pictures were recorded either on a SEM - FEI Nova Nano SEM 230 or on a SEM - FEI Helios Nano Lab 650 dual beam microscope. It features focussed ion beam (FIB) cutting and SEM imaging as well as energy dispersive X-ray spectroscopy (EDX). Pastes for screen printing were milled using a Exakt 50 I three roll mill with aluminium oxide rolls, 20 µm spacing. Current-voltage (IV) measurements were made by irradiating from the back side of the electrode using a light source SolarSim 150 (100 mW/cm^2 = 1 sun). The power of the

simulated light was calibrated by using a reference Si photodiode. The standard dye N719 was purchased from Solaronix. The quantum efficiency measurements of the DSCs were performed on a Spe-Quest quantum efficiency setup from Rera Systems (Netherlands) equipped with a 100 W halogen lamp (QTH) and a lambda 300 grating monochromator from Lot Oriel. The monochromatic light was modulated to 3 Hz using a chopper wheel from ThorLabs. The cell response was amplified with a large dynamic range IV converter from CVI Melles Griot and then measured with a SR830 DSP Lock-In amplifier from Stanford Research.

2.2. Genaral solar cell preparation method

The following method was used to prepare solar cells containing ancillary ligands **5a** and **6a** in Chapter 4:[60]

TiO_2 paste was prepared by a procedure based on that descibed by Grätzel and coworkers.[68] The adaptations to the published procedure were use of a porcelain mortar, a sonicator bath, and terpineol (CAS: 8000-41-7) in place of α-terpineol, and the omission of the three roll mill treatment. The FTO glass (Solaronix TCO22-7, 2.2 mm thickness, sheet resistance ≈7 Ω/square) was cleaned by sonicating in acetone, EtOH, Hellmanex® surfactant (2% in water), water and EtOH bath sequentially for 10 min. After treatment in a UV-O_3 system (Model 256-220, Jelight Company Inc), the FTO plates were immersed into 40 mM aqueous $TiCl_4$ solution at 70 °C for 30 min, and washed with water and EtOH. Nanocrystalline TiO_2 electrodes were made by doctor blading the TiO_2 paste onto a conducting glass slide and kept at room temperature for 10 min so that the paste could mature to reduce the surface irregularity. The electrode coated with the TiO_2 paste was gradually heated under an air flow at 70 °C for 30 min, 135 °C for 5 min, 325 °C for 5 min, 375 °C for 5 min, 450 °C for 15 min, and 500 °C for 15 min. After annealing, the TiO_2 film was treated with 40 mM $TiCl_4$ solution as described above, rinsed with water and EtOH and sintered at 500 °C for 30 min. After cooling to about 80 °C, each slide was immersed in a DMSO solution of ligand **8**, **9** or **10** (1 mmol/L) for 24 h. The colourless slide was moved from the solution, washed with DMSO and EtOH, and dried. The electrode was next immersed in an EtOH solution of $Zn(OAc)_2$ dihydrate or $ZnCl_2$ (0.5 mmol/L) for 24 h. The electrode was removed from the solution and was washed with EtOH. Finally, the electrode was immersed in a

CH_2Cl_2 solution of ligand **5a** or **6a** (0.5 mmol/L) for 64 h during which time the slide turned from colourless to orange.

To prepare the counter electrode, a hole was drilled in the FTO glass, and the perforated sheet was heated in air for 15 min at 450 °C to remove organic residues and was then washed as described for the working electrode. The Pt catalyst was deposited on the FTO glass by coating with a drop of H_2PtCl_6, 5 mmol/L in propan-2-ol and heated to 400 °C for 15 min.

The dye-covered TiO_2 electrode and Pt counter-electrode were assembled using thermoplast hot-melt sealing foil (Solaronix, Meltonix 1170-25 Series, 25 microns thick) by heating while pressing them together. The electrolyte was a mixture of LiI (0.1 mol/L), I_2 (0.05 mol/L), 1-methylbenzimidazole (0.5 mol/L) and 1-butyl-3-methylimidazolinium iodide (0.6 mol/L) in valeronitrile, and was introduced into the cell via vacuum backfilling. The hole on the counter electrode was finally sealed using the hot-melt sealing foil and a cover glass.

The following method was used to prepare solar cells containing ancillary ligand **7**, **13**, **14**, **15** and **22** in Chapters 4, 5 and 6:[60]

Solaronix test cell titania electrodes made from TCO22-7 FTO coated glass, prepared by screen-printing for a homogenous surface using Ti-Nanoxide pastes, active layer from Ti-Nanoxide T/SP covered by a reflective layer of Ti-Nanoxide R/SP, active area: 6 × 6 mm, thickness: titania layer 9 µm plus scattering layer 3 µm were used. The electrodes were sintered at 450 °C for 30 min, then cooled to ca. 80 °C and immersed in a 1 mM DMSO solution of the anchoring ligands **8** and **10** for 24 h. The colourless slide was removed from the solution, washed with DMSO and EtOH, and dried. The electrode was next immersed in an EtOH solution of $ZnCl_2$ (0.5 mmol/L) for 24 h. The electrode was removed from the solution and was washed with EtOH. Finally, the electrode was immersed in a CH_2Cl_2 (**7**) or THF (**13**, **14**, **15**, **22**) solution of the corresponding ancillary ligand (0.5 mmol/L) for 64 h, during which time the slide turned from colourless to orange. Solaronix test cell platinum electrodes were used for the counter electrodes, and residual organic impurities were removed by heating at 450 °C for 30 min. The dye-covered TiO_2 electrode and Pt counter-electrode were assembled using thermoplast hot-melt sealing foil (Solaronix Test Cell Gaskets) by heating while pressing them together. The electrolyte (LiI (0.1 mol/L), I_2 (0.05 mol/L),

1-methylbenzimidazole (0.5 mol/L) and 1-butyl-3-methylimidazolinium iodide (0.6 mol/L) in 3-methoxy-propionitrile) was introduced into the DSC by vacuum backfilling. The hole in the counter electrode was sealed using hotmelt sealing foil (Solaronix Test Cell Sealings) and a coverglass (Solaronix Test Cell Caps).
Electrodes for solid electronic absorption measurements were dyed using the same protocol with Solaronix transparent test cell titania electrodes made from TCO22-7 FTO coated glass, prepared by screen-printing for a homogenous surface using Ti-Nanoxide pastes, active layer from Ti-Nanoxide T/SP active area: 6 × 6 mm, thickness: titania layer 9 µm, no scattering layer.

For the organic dye **24** in chapter 6 the following dyeing and assembling protocol was used with the electrodes described in the above paragraph:

Electrodes were immersed in a solution of organic dye **24** (0.5 mmol/L in DMSO) for 24 h, after which the electrodes were washed with DMSO and EtOH and then assembled according to the above mentioned protocol. Solaronix test cell platinum electrodes were used for the counter electrodes, and residual organic impurities were removed by heating at 450 °C for 30 min. The dye-covered TiO_2 electrode and Pt counter-electrode were assembled using thermoplast hot-melt sealing foil (Solaronix Test Cell Gaskets) by heating while pressing them together. The electrolyte (LiI (0.1 mol/L), I_2 (0.05 mol/L), 1-methylbenzimidazole (0.5 mol/L) and 1-butyl-3-methylimidazolinium iodide (0.6 mol/L) in 3-methoxy-propionitrile) was introduced into the DSC by vacuum backfilling. The hole in the counter electrode was sealed using hotmelt sealing foil (Solaronix Test Cell Sealings) and a coverglass (Solaronix Test Cell Caps).
Electrodes for solid electronic absorption measurements were prepared after the same protocol, using Solaronix transparent Test Cell Titania Electrodes made from TCO22-7 FTO coated glass, prepared by screen-printing for a homogenous surface using Ti-Nanoxide pastes, active layer from Ti-Nanoxide T/SP active area: 6 × 6 mm, thickness: titania layer 9 µm, no scattering layer.

Part 1

Chapter 3

Part 1: Emitting zinc(II) complexes

Chapter 3: Emitting zinc(II) complexes and their performance in devices

3.1. Motivation

Zinc complexes are not commonly used as emitters in OLEDs or LECs. Except for a few examples in the literature where mainly zinc based coordination polymers[69] were investigated towards their possible use in lighting devices, the most used in the LEC business are still Ir(III) complexes. They offer nicely tuneable emission properties which makes many emission colours accessible and they show acceptable device life-times. Furthermore, Ir(III) complexes have been under investigation for quite a few years now, which makes them well studied and thus optimized systems are present.[70] The company Osram GmbH recently designed a 210 cm^2 device.[71] Although zinc complexes are not the first choice for this kind of application, it does not mean that they are not of interest for this purpose. It will be shown in this chapter that Zn(II) bis-2,2':6',2''-terpyridine complexes have some potential for use in light emitting devices. Also it will be made clear that the emission properties of the complexes can be nicely altered by simply changing the substituent at the 4'-position of the ligand. This is beneficial because compared to the commonly used Ir(III) complexes, zinc(II) complexes require much shorter synthetic pathways and also allow one to use cheaper materials, since zinc (≈ 2150 CHF/t)[72] is fairly cheap compared to iridium (≈ 13500 CHF/kg)[73]. Additionally, zinc is by eight factors of magnitude more abundant in the Earth's crust than iridium. All these factors make zinc complexes promising candidates for future lighting.

3.2. Compounds under investigation

The focus was deliberately laid on very simple compounds, namely homoleptic Zn(II) bis-2,2':6',2''-terpyridine complexes. The 4'-phenyl substituted terpyridines can be synthesized in a very straightforward one-pot synthesis.[74] It refers to the method of synthesis by Hanan and Wang in 2005 and allows to synthesize 2,2':6',2''-terpyridines with an aryl substituent in the 4' position starting from 2-acetylpyridine and the

corresponding aromatic aldehyde under basic conditions.[75] It is often referred to as the “feel-good reaction” in our group (Scheme 3-1).

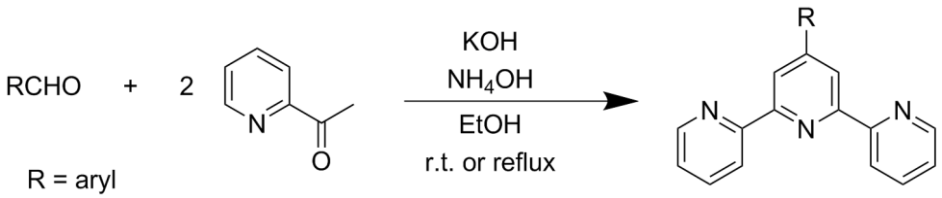

Scheme 3-1: General reaction scheme of a “feel-good reaction”.[75]

The selected pathway allows one to obtain the homoleptic zinc complexes in only two or three steps in the case of the triphenylamine substituted compounds, respectively. This is a huge advantage over the very often used Ir(III) complexes, which have to be synthesized over several steps and are sometimes very difficult to obtain in the desired purity, which can be an imminent problem. This was recently shown by Dr. Gabriel Schneider in our group, who proved that even very small quantities of Cl^- impurities, left-over from the synthesis, present in the LEC device can result in a dramatic reduction of the device performance[76].

According to the before mentioned protocol, the following three ligands were synthesized. Their corresponding homoleptic Zn(II) complexes were obtained by the reaction of two equivalents of ligand with 1.2 equivalents of zinc acetate dihydrate in EtOH in a microwave reactor and the subsequent precipitation with NH_4PF_6 (Scheme 3-2).

The obtained complexes have been characterized by NMR, mass spectrometry and electronic absorption spectroscopy.

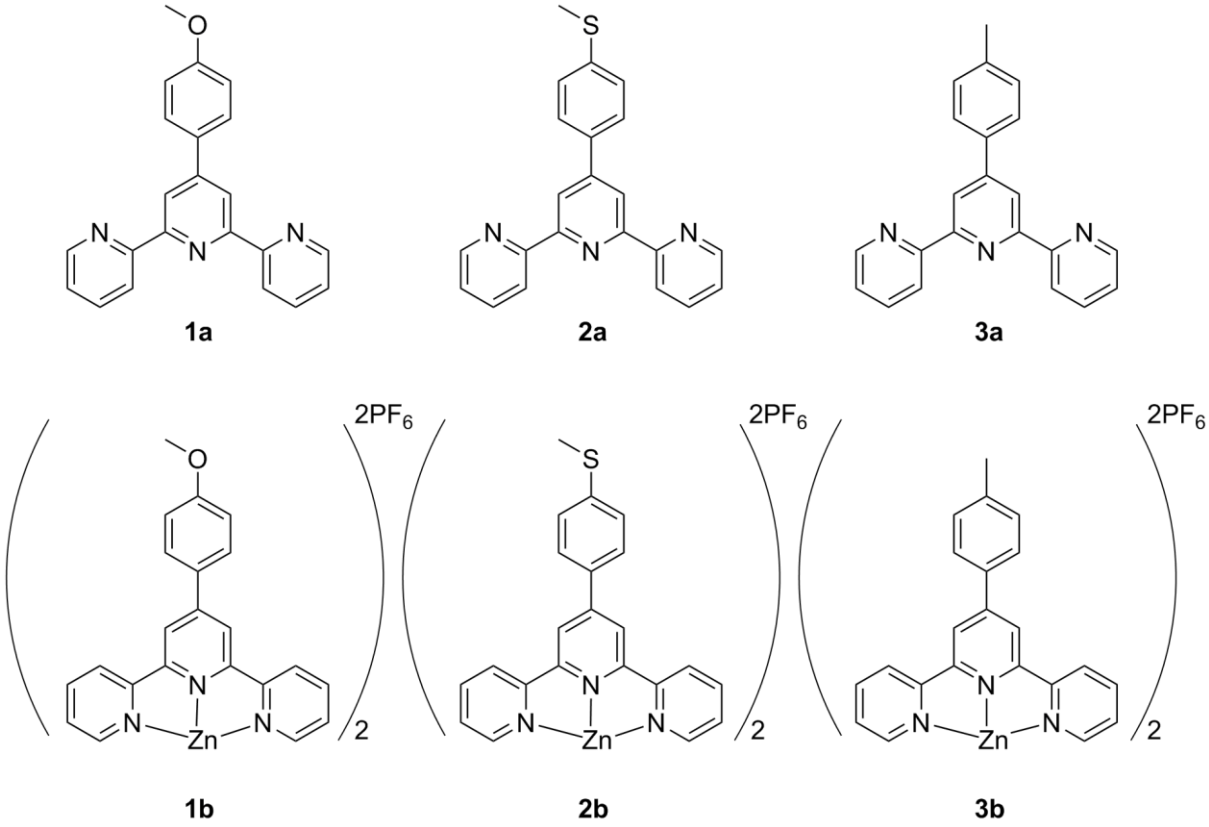

Scheme 3-2: Ligands synthesized according to the Wang and Hanan one pot method[75] *and their corresponding Zn(II) complexes.*

The compound **4a** exhibiting an OH-group in the 4-position of the pendant phenyl ring was synthesized via deprotection of compound **1a**, using pyridinium chloride in a microwave reactor. The triphenylamine containing ligands were synthesized via a Hartwig-Buchwald reaction[77] between 4'-(4-bromophenyl)-2,2':6',2''-terpyridine and the corresponding diphenylamine under standard conditions.

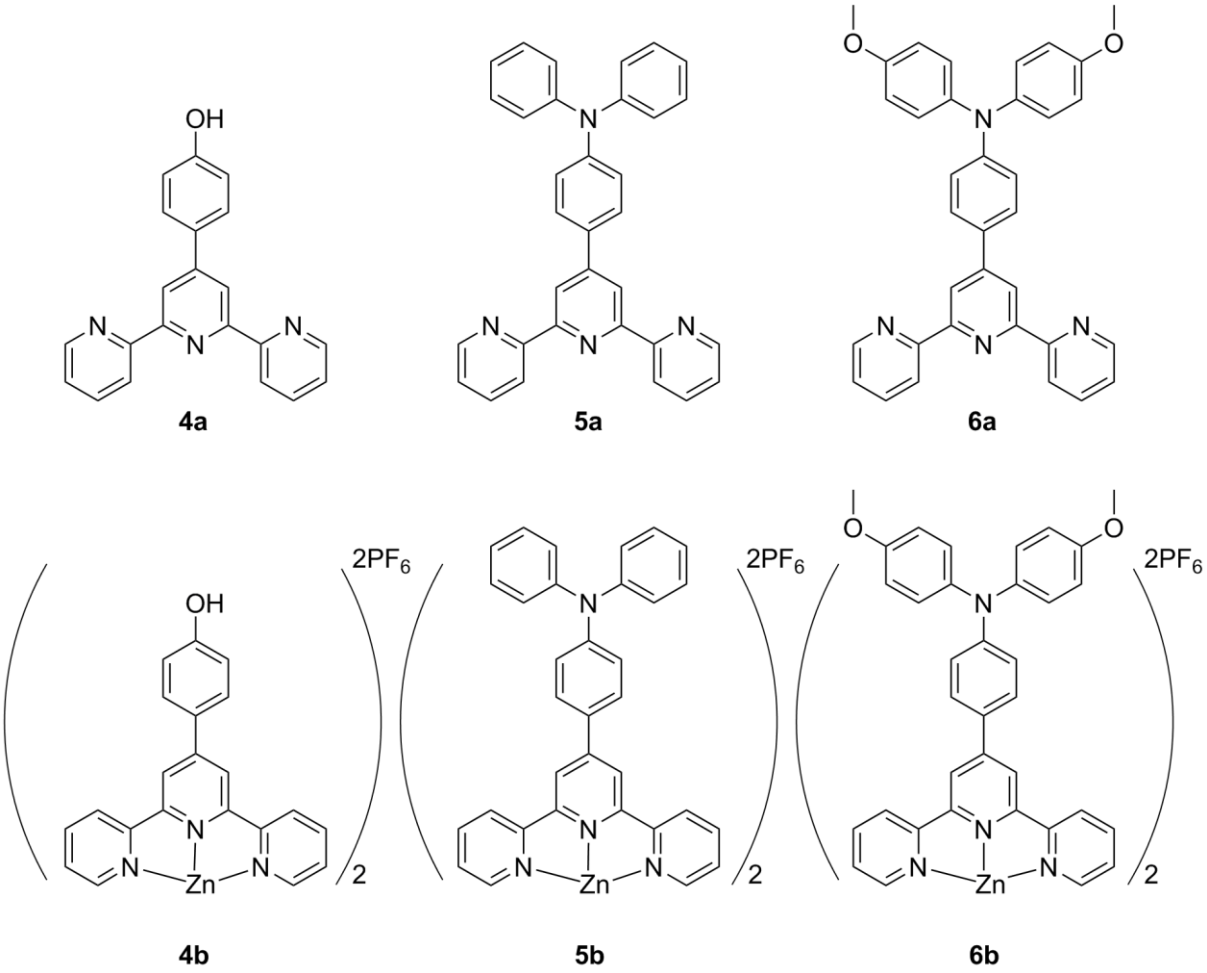

Scheme 3-3: The other three ligands and their corresponding Zn(II) complexes.

These 12 ligands and complexes were investigated in terms of electronic absorption and emission properties and some of the complexes were selected to be used as emitters in LECs or OLEDs.

3.3. Results and Discussion

3.3.1. Electronic absorption properties of compounds 1b – 6b

The absorption spectroscopic properties of the Zn(II) complexes were investigated, because this can give a hint about the optical HOMO – LUMO gap of the compounds. All absorption spectra were recorded in acetonitrile solution and should therefore be comparable.

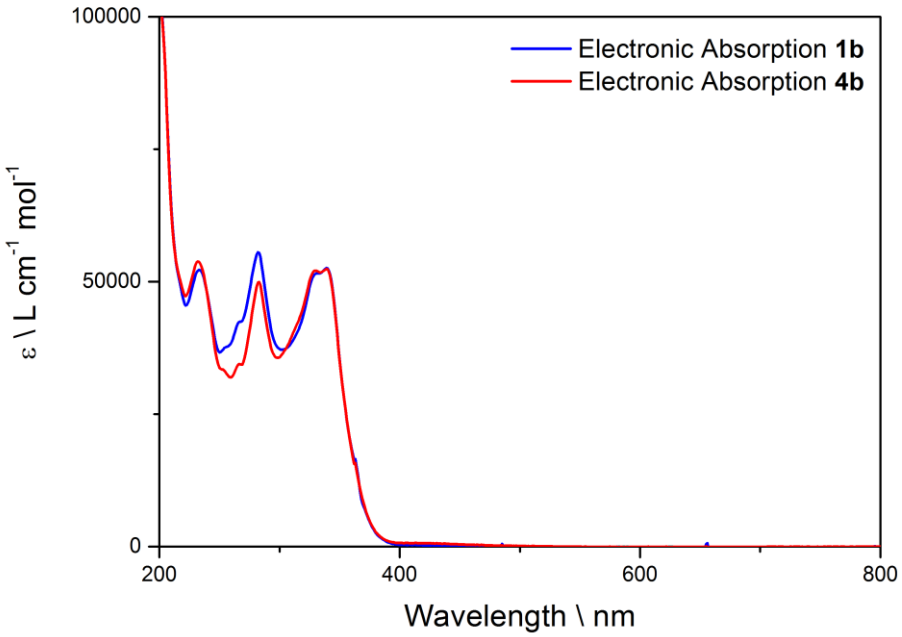

*Figure 3-1: Electronic absorption spectra of **1b** (blue) and **4b** (red).*

Figure 3-1 shows the UV-VIS spectra of compounds **1b** and **4b**. These two compounds are structurally and electronically very similar and the absorption spectra are consistent with this. Both spectra show similar high energy transitions between 200 nm and 400 nm. There are no absorptions in the visible region, consistent with the fact that both compounds are colourless.

In Figure 3-2 one can see the electronic absorption spectra of compounds **2b** and **3b**. Both spectra show again π* ← π transitions in the UV region and no absorptions in the visible range. The absorption of **2b** tails slightly into the visible part of the spectrum. Thus the compound shows an off-white to pale yellow colour.

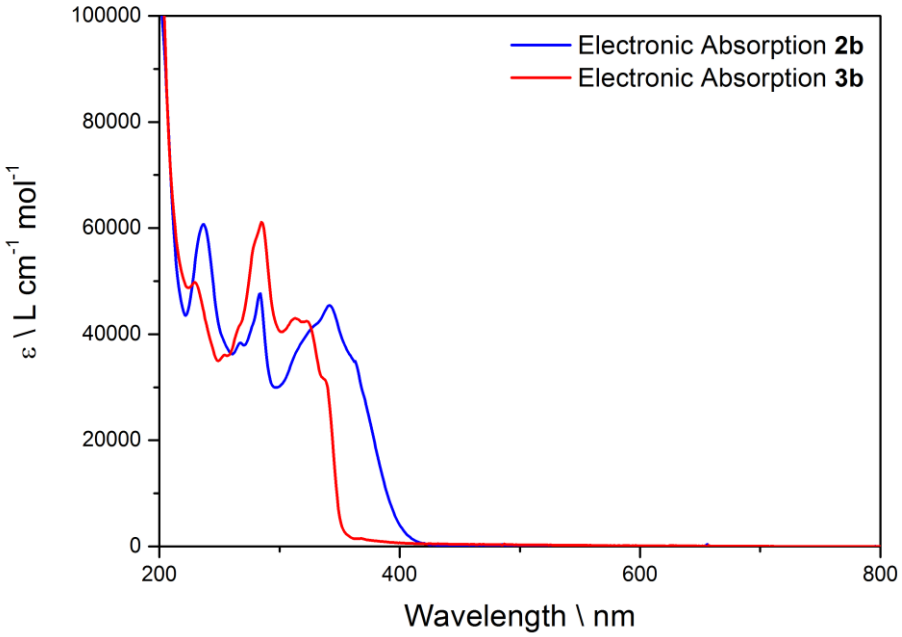

*Figure 3-2: Electronic absorption spectra of **2b** (blue) and **3b** (red).*

In contrast to compound **1b**, **2b** and **4b**, complex **3b** shows absorptions only up to about 360 nm, this can be attributed to the less electron donating nature of the tolyl substituent compared to the anisyl substituent, and its inability to further extend the π-system of the ligand by the formation of resonance structures.

Compounds **5b** and **6b** are the most interesting in this series. One can clearly see in Figure 3-3 that they not only show the π* ← π transitions in the UV region observed for compounds **1b** – **4b**, but also broad absorptions at the high energy end of the visible range with a maximum at 407 nm for **5b** and 420 nm for **6b**, respectively.

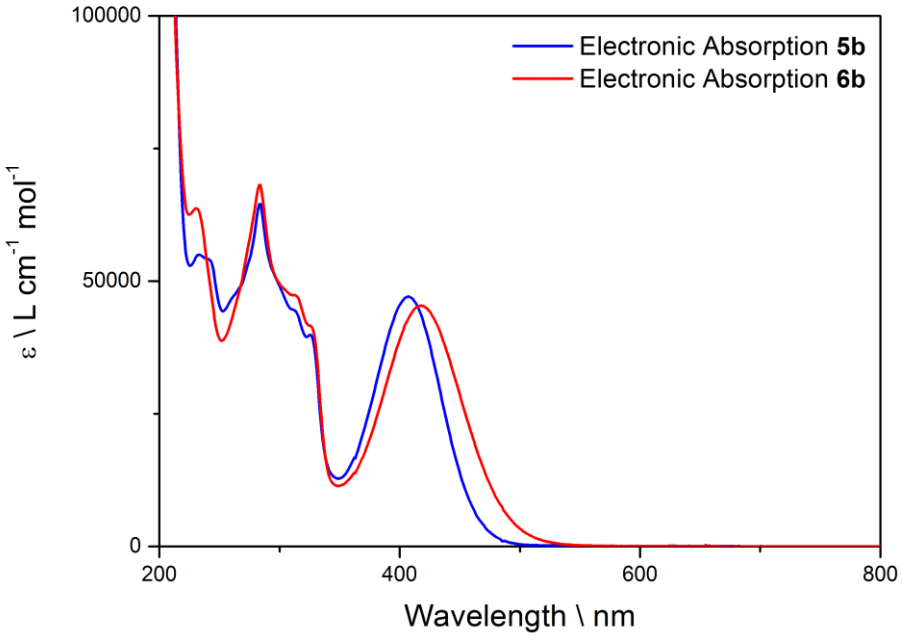

*Figure 3-3: Electronic absorption spectra of **5b** (blue) and **6b** (red).*

Since there are no charge transfers expected that involve the d^{10} metal centre, this behaviour can be attributed to the electron donating diphenylamine substituent on the ligand, which is able to donate an electron through the π-system to the central pyridine ring when absorbing photons.[78] Scheme 3-4 shows the underlying principle of this intra-ligand charge transfer (ILCT) on the basis of **5a**.

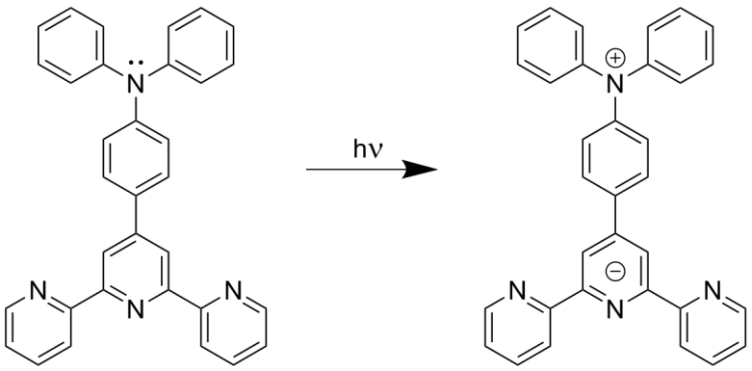

*Scheme 3-4: Principle of charge transfer in compounds **5b** and **6b**.*[78]

These absorptions in the visible range explain why both compounds (**5b** and **6b**) exhibit an orange colour. This is rather exciting, since most Zn(II) bis-terpyridine complexes are known to be colourless.

Table 3-1 shows a summary of the most intense absorptions of compounds **1b** – **6b**.

Compound	Absorption wavelength \ nm [ε \ L cm^{-1} mol^{-1}]							
1b	233 [52212]		282 [55562]		331 [51606]	339 [52551]		
2b	236 [60658]		284 [47817]		328sh [41574]	341 [45326]	362sh [34831]	
3b	231 [49744]		282 [60844]	313 [43185]	324 [42394]	337 [31295]		
4b	231 [53816]		282 [49891]		329 [52088]	339 [52410]		
5b	232 [55046]	242 [54109]	283 [64447]	311 [44591]	326 [39905]			407 [47080]
6b	231 [63766]		283 [68163]	313 [47350]	326 [41399]			420 [45372]

*Table 3-1: Most intense electronic absorptions of compounds **1b** - **6b**.*

3.3.2. Emission and electrochemical properties of compounds 1a - 6a

The presented excitation and emission spectra were normalized to unity, since the intensity of a peak cannot be interpreted quantitatively. Furthermore, all the measurements were done in HPLC grade acetonitrile.

Figure 3-4 shows the emission and excitation curves of compound **1b**.

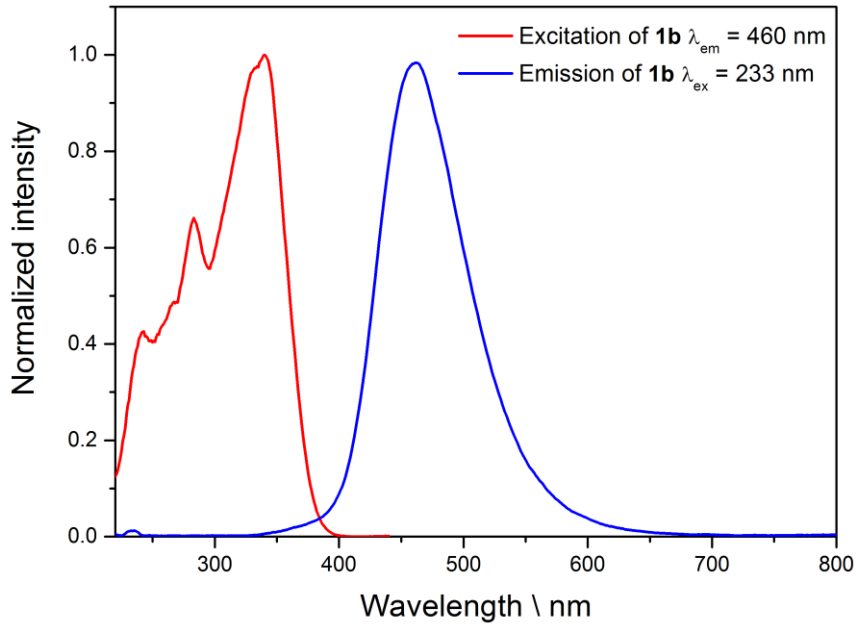

*Figure 3-4: Excitation (red) and emission (blue) curves of compound **1b**.*

Complex **1b** shows a broad emission with a maximum at 460 nm when excited at 233 nm. The corresponding excitation spectrum is shown in red and shows different local maxima that are all in agreement with the UV-Vis spectrum of compound **1b**. Furthermore, excitation and emission spectra appear as mirror images (Figure 3-4, Table 3-1).

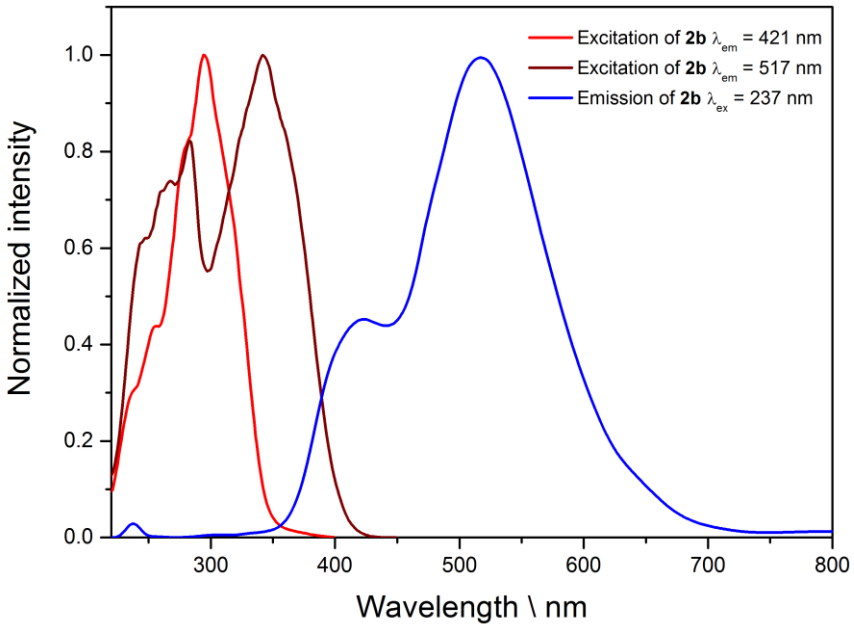

*Figure 3-5: Excitation (red & brown) and emission (blue) curves of compound **2b**.*

In Figure 3-5 one can see that **2b** shows two different emissions at 421 nm and 517 nm upon excitation at 237 nm. The excitation spectra for each emission maximum were recorded and show which absorptions cause the emission at 421 nm and 517 nm, respectively. A possible reason why this compound shows two emission maxima, is that the complex dissociates upon irradiation. It is also possible that the methyl sulfide is partially oxidized. These spectra correspond to the absorption maxima in the UV-Vis spectrum of **2b**. The excitation of the other absorption maxima leads to the same emission maxima (Figure 3-5, Table 3-1).

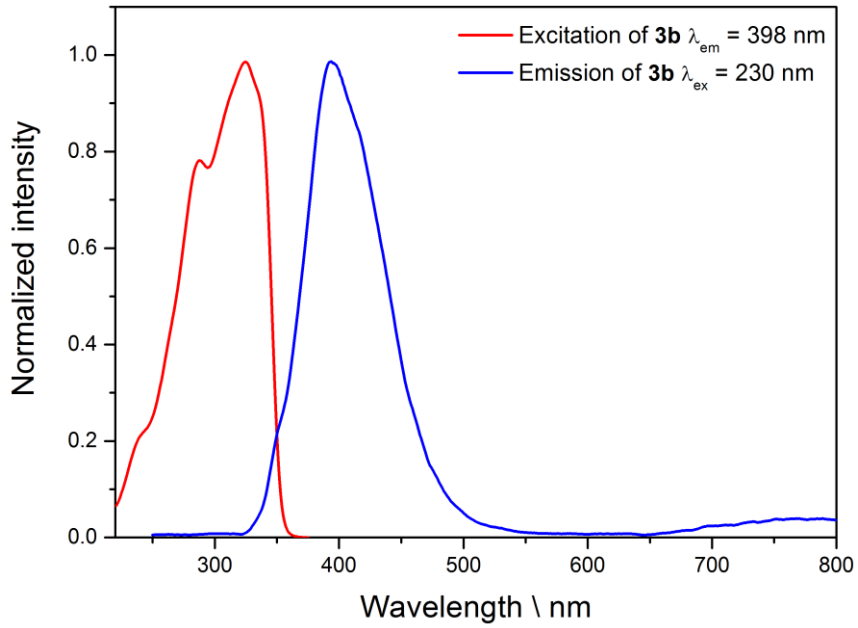

*Figure 3-6: Excitation (red) and emission (blue) curves of compound **3b**.*

Compound **3b** shows an emission maximum at 398 nm; it is therefore the only complex of the series that does not emit in the visible region of the spectrum (Figure 3-6). The corresponding excitation spectrum corresponds to the UV-Vis spectrum of the compound (Figure 3-2, Table 3-1). The two spectra also appear as mirror images in this example.

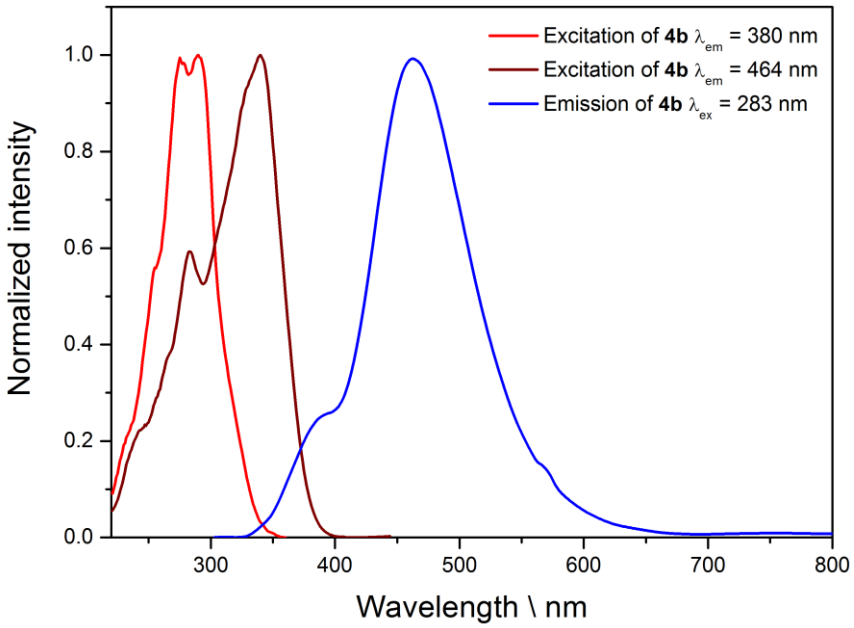

*Figure 3-7: Excitation (red & brown) and emission (blue) curves of compound **4b**.*

In Figure 3-7 one can see the excitation spectra that correspond to the emission of **4b** at 380 nm (red) and 464 nm (brown), respectively. These spectra are in agreement with the UV-Vis spectrum of **4b**. The excitation of the other absorption maxima (Figure 3-1, Table 3-1) lead to the same emission maxima. As already mentioned, complex **4b** shows two emission maxima (blue curve) at 380 nm and 464 nm. This could be the case because of different protonation states of the hydroxyl group. It is also possible that the complex dissociates upon irradiation.

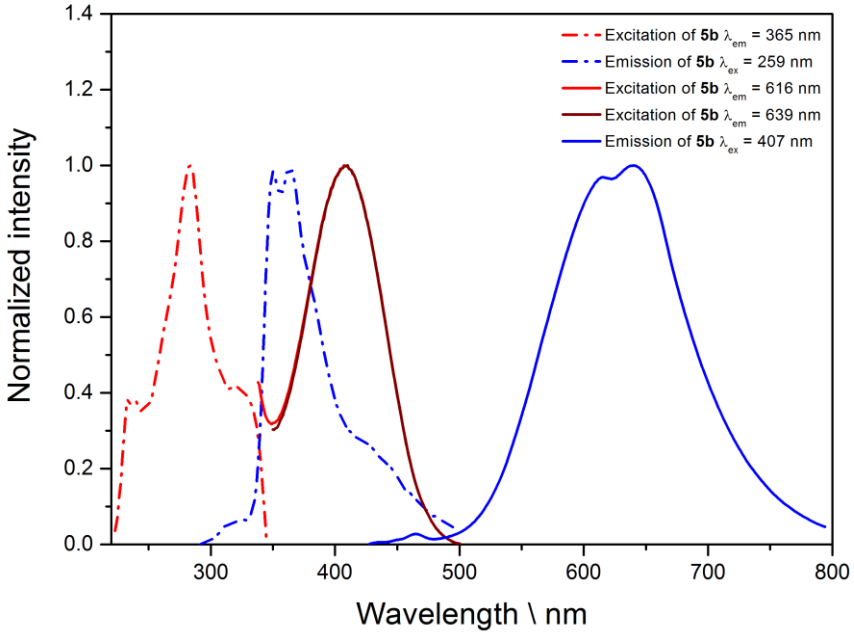

*Figure 3-8: Excitation (brown, red & red dashed) and emission spectra (blue & blue dashed) of **5b**.*

As already mentioned in section 3.3.1 compounds **5b** and **6b** are distinct from the others in the series. Figure 3-8 shows two sets of excitation and emission spectra. On the one hand there is the emission at around 365 nm (blue dashed) and the corresponding excitation (red dashed), which behave like mirror images.

When the complex is excited at 407 nm, which corresponds to the charge transfer absorption, two emission maxima at 616 nm and 639 nm are observed. Furthermore the excitation spectra correspond to the UV-Vis data of compound **5b** (Figure 3-3, Table 3-1).

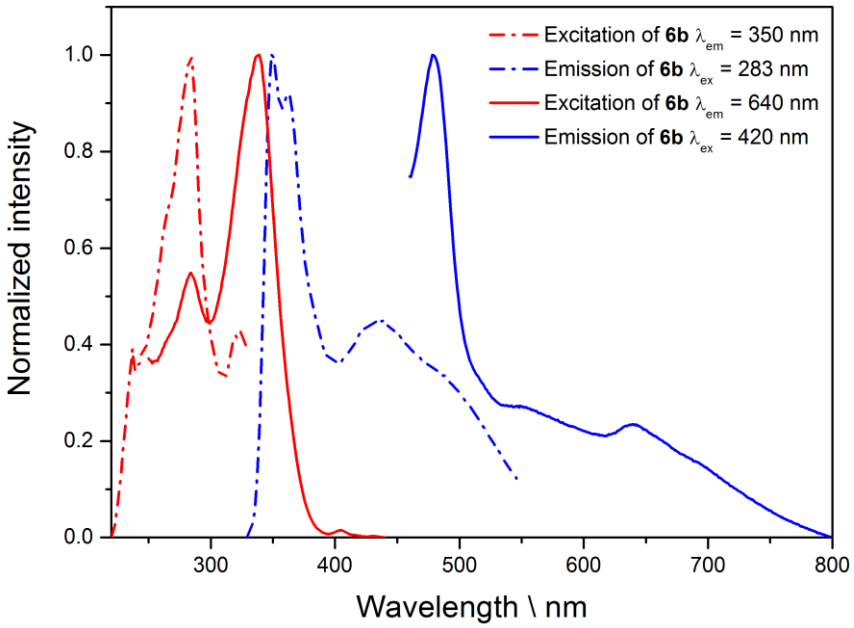

*Figure 3-9: Excitation (red & red dashed) and emission spectra (blue & blue dashed) of **6b**.*

In Figure 3-9 the solid blue spectrum shows the emission of **6b** when excited in the charge transfer absorption band at 420 nm. It consists of a sharp emission at 479 nm and a broad, but, relatively to the sharp line, not very intense tail, with a local maximum at 640 nm. The corresponding excitation spectrum (solid red line) shows that the complex does not necessarily have to be excited at 420 nm to emit at 640 nm.

The blue and red dashed lines show excitation and emission spectra of **6b** at higher energy. The excitation spectra correspond well to the UV-Vis spectrum of **6b** (Figure 3-3, Table 3-1).

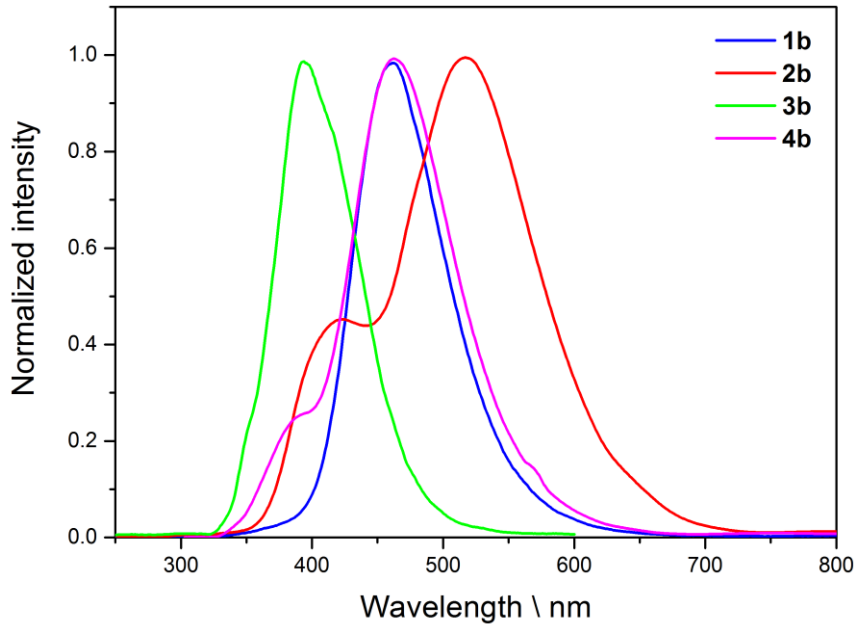

*Figure 3-10: Emission spectra of **1b** - **4b**.*

Figure 3-10 shows that for complexes **1b** – **4b** there is a connection between the electron donating nature of the substituent in 4-position of the phenyl substituent and the emission of the corresponding homoleptic Zn(II) complex. Compounds **1b** and **4b** are very similar, hence it is not a surprise that the emissions are also very similar. It can be stated that the more electron donating the ligands are, the more red shifted the emission of the compound will be. From electrochemical measurements, the electrochemical HOMO–LUMO gaps can be calculated (Table 3-2). One can reason that the different substituents have an effect mainly on the LUMO levels of the corresponding complexes, since the HOMO energies lie around -5.7 eV for compounds **1b** – **4b**. So the more electron donating the substituents in 4-position, the more the LUMO is stabilized and moves to lower energy, decreasing the HOMO-LUMO gap, leading to a red-shift in emission.

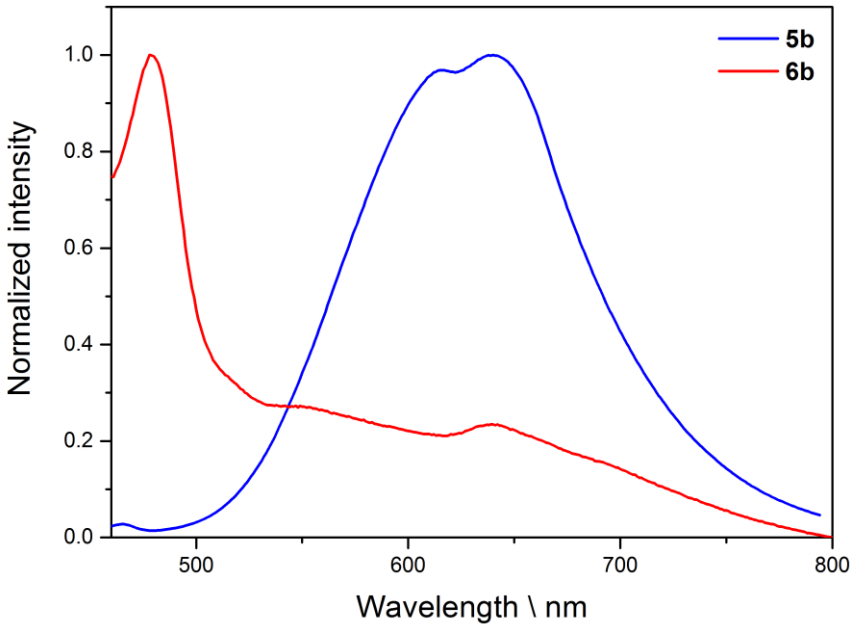

*Figure 3-11: Emission spectra of **5b** and **6b**.*

The emission spectra of compounds **5b** and **6b** are shown in Figure 3-11. One can see that both complexes show emissions above 600 nm, which arise from the ILCT. Looking at the HOMO and LUMO energies suggests that the introduction of the diphenylamine unit changes the orbital energies in the complex. Still there is no contribution from the metal centre, but the HOMO seems to lie on the very easily oxidised amine-nitrogen atoms, since the HOMO energies of **5b** and **6b** are different due to the electron donating effect of the methoxy substituents in **6b**. The LUMO energies of **5b** and **6b** are almost the same and most probably the LUMO is located over the terpyridine units (Scheme 3-4), which are the same in both compounds.

Table 3-2 shows a summary of the HOMO and LUMO levels calculated from electrochemical measurements (cyclic voltammetry)[79], as well as the corresponding HOMO-LUMO gaps derived from these values. Table 3-2 also lists the optical HOMO-LUMO gap, calculated from the electronic absorption spectra.

Compound	HOMO energy \ eV	LUMO energy \ eV	HOMO-LUMO gap \ eV	Optical HOMO-LUMO gap \ eV
1b	-5.99	-3.25	2.74	3.11
2b	-5.90	-3.84	2.06	2.96
3b	-	-3.25	-	3.41
4b	-	-	-	3.15
5b	-5.34	-2.77	2.57	2.40
6b	-5.08	-2.69	2.39	2.25

Table 3-2: Summary of HOMO and LUMO energies, HOMO-LUMO gaps from cyclic voltammetry and optical HOMO-LUMO gaps from electronic absorption spectra.

HOMO and LUMO levels from cyclic voltammetry were calculated using the following equations,

$$\mathrm{E_{HOMO}} = \text{-}4.8\ \mathrm{eV} - \mathrm{E_{Ox}}$$

Equation 3-1

$$\mathrm{E_{LUMO}} = \text{-}4.8\ \mathrm{eV} - \mathrm{E_{Red}}$$

Equation 3-2

where -4.8 is the reference energy level of ferrocene (-4.8 eV below the vacuum level)[80] and E_{Ox} is the onset oxidation potential relative to the Fc/Fc^{+} reference couple, set as being at 0 V. This also applies for E_{red} which is the onset reduction potential.

Optical HOMO-LUMO gaps were calculated using the following physical correlations:

The energy gap between HOMO and LUMO can be derived from Equation 3-3, which can also be used to calculate the energy of a photon. The energy of the photon, or in this case the energy difference between the HOMO and the LUMO, equals the Planck constant times the frequency of the light emitted be the photon.

$$\mathrm{E} = \mathrm{h}\,\nu$$

Equation 3-3

The frequency variable can then be substituted using Equation 3-4, which leads to the term shown in Equation 3-5.

$$\mathrm{c} = \lambda\,\nu$$

Equation 3-4

$$E = \frac{h\,c}{\lambda}$$

Equation 3-5

Two factors have to be taken into account, firstly the result should be in units of eV and not in J (1 eV = 1.602×10^{-19} J), and secondly this term has to be corrected by 9 orders of magnitude because c is given in ms^{-1}, whereas λ is given in nm, leading to Equation 3-6:

$$E = \frac{h\,c}{\lambda \times 1.602 \times 10^{-19} \times 10^{-9}}$$

Equation 3-6

Solving this equation, inserting all the constants, leads to the term seen in Equation 3-7.

$$E = \frac{1239.84}{\lambda}$$

Equation 3-7

To know λ for a specific compound, one has to evaluate the wavelength at the onset of the lowest energy transition in the electronic absorption spectrum.

3.4. Computational calculations of HOMO-LUMO gaps

For some of the compounds, computational calculations of the ground state energy levels were made by David Vonlanthen with the software tool Turbomol V6.01, using DFT methods with B3LYP functional and def-SV(P) basis set. Calculations were done in acetonitrile environment (dielectric constant: 36.64). Figure 3-12 shows the calculated HOMO and LUMO levels and the HOMO-LUMO gaps.

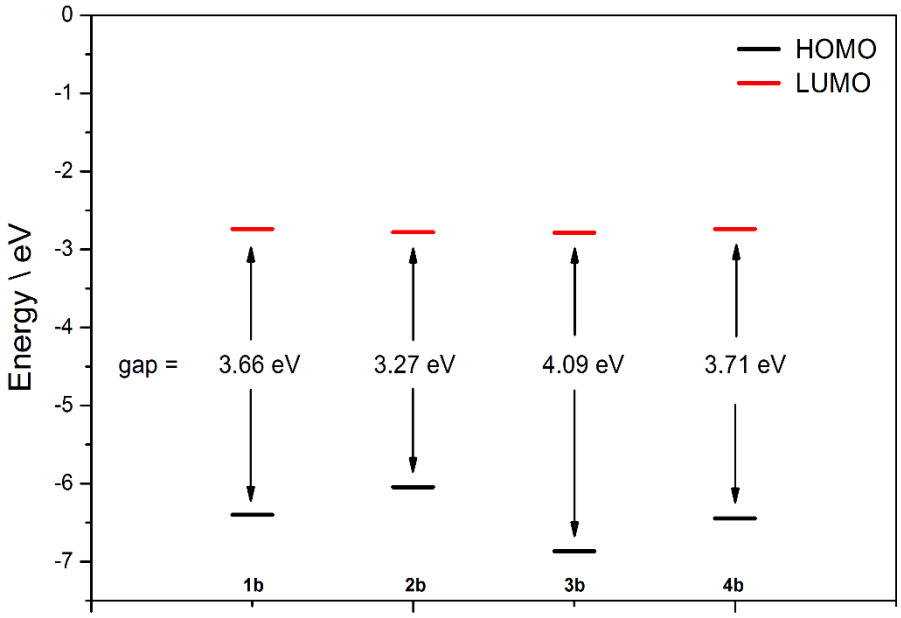

*Figure 3-12: Calculated energies for HOMOs, LUMOs and HOMO-LUMO gaps of **1b**-**4b**.*

Table 3-3 summarizes the information about the HOMO-LUMO gaps. For compounds **1b**-**4b** the computationally obtained values support the hypothesis that more electron donating substituents in the 4-position of the 4'-phenyl group cause a decrease of the HOMO-LUMO gap. It also shows the similarity of **1b** and **4b**, since spectroscopic values are very close together (3.11 eV and 3.15 eV), as well as the calculated HOMO-LUMO gaps (3.66 eV and 3.71 eV). The gap values obtained from cyclic voltammetry do not completely support this theory. But it has to be taken into account that there is always a difference between HOMO-LUMO gaps calculated from electrochemistry and such calculated from electronic absorption spectra, since the optical method actually measures the amount of energy a certain electron transition needs, whereas electrochemical methods do change the electronic properties of the studied compound by adding or removing an electron.

Compound	HOMO-LUMO gap \ eV	Optical HOMO-LUMO gap \ eV	Computed HOMO-LUMO gap \ eV
1b	2.30	3.11	3.66
2b	1.88	2.96	3.27
3b	-	3.41	4.09
4b	-	3.15	3.71
5b	2.57	2.40	-
6b	2.39	2.25	-

Table 3-3: Summary of the gathered information about the HOMO-LUMO gaps.

3.5. Optimization of LEC devices

All device preparation and measurements were carried out by Dr. David Vonlanthen in the laboratory of Dr. Henk Bolink in Valencia, Spain. The presented results are based on the report of Dr. David Vonlanthen.

Compound **1b** was selected as a model compound to establish a working system for the other compounds, since it was available in larger quantities and it also exhibits a deep to sky blue emission in solution, which makes the compound attractive for use in LECs. Furthermore, it exhibits the highest photoluminescence quantum yield (PLQY) in PMMA films (Table 3-4) at an emission wavelength of 428 nm.

Compound	Content in PMMA film	QY (PL) \ %
1b	5%	57.9
2b	5%	57.4
3b	5%	36.0
4b	5%	14.4
5b	5%	59.0
6b	5%	10.2

*Table 3-4: Photo luminescence QY of compounds **1b** – **6b** 5% in PMMA.*

A first device was prepared using a solution of **1b** in MeCN (without any ionic liquid), which was spin-coated on the electrode. The measurements at constant current (100 mA/cm^2) (Figure 3-13) show that the device has a very short turn-on time, which might have to do with its very high intrinsic ionic concentration. The EL emission spectra show maxima at 484 nm and 552 nm, which corresponds to a red shift compared to the PL emission in films.[81] It is not clear, why two emissions are observed, but it is possible that the complex decomposes under the given measuring conditions. A look at the CIE coordinates (x = 0.2925, y = 0.4009) shows how close to white the EL emission of this device is. Unfortunately, the device lifetime is very short ($t_{1/2} \approx 21$ s).

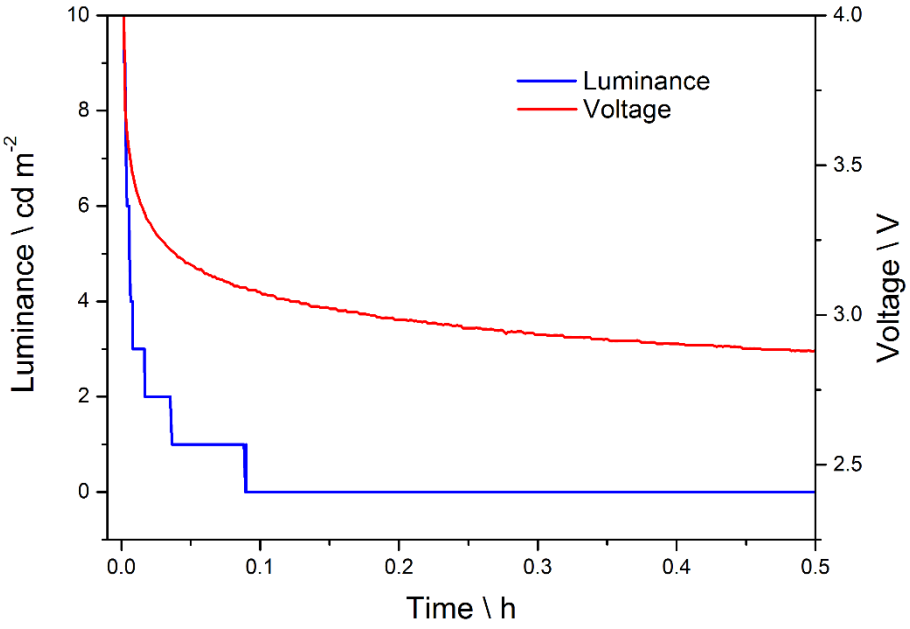

*Figure 3-13: Luminance (blue) and voltage (red) curves of the device incorporating **1b** at constant current density (100 mA cm^{-2}).*

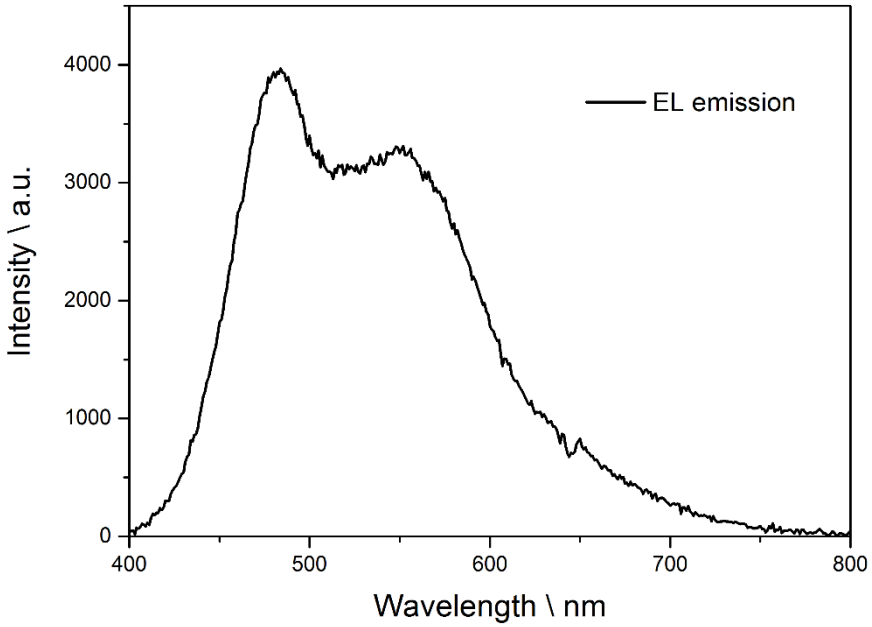

*Figure 3-14: EL emission of compound **1b**.*

In a second device configuration it was tried to slow down the turn-on time by using a mixture of PMMA (2.5 mg/mL) and **1b** (20 mg/mL) in MeCN, which was spin-coated, resulting in a 122 nm thick active layer. The use of PMMA and a driving voltage of

8.5 V showed a longer turn-on time of 35 s and a luminance maximum of 10 cd/m^2 (Figure 3-15). Although the turn-on time was reduced and therefore more gentle conditions were used, the lifetime of the device could not be enhanced compared to the previous setting ($t_{1/2} \approx 20$ s).

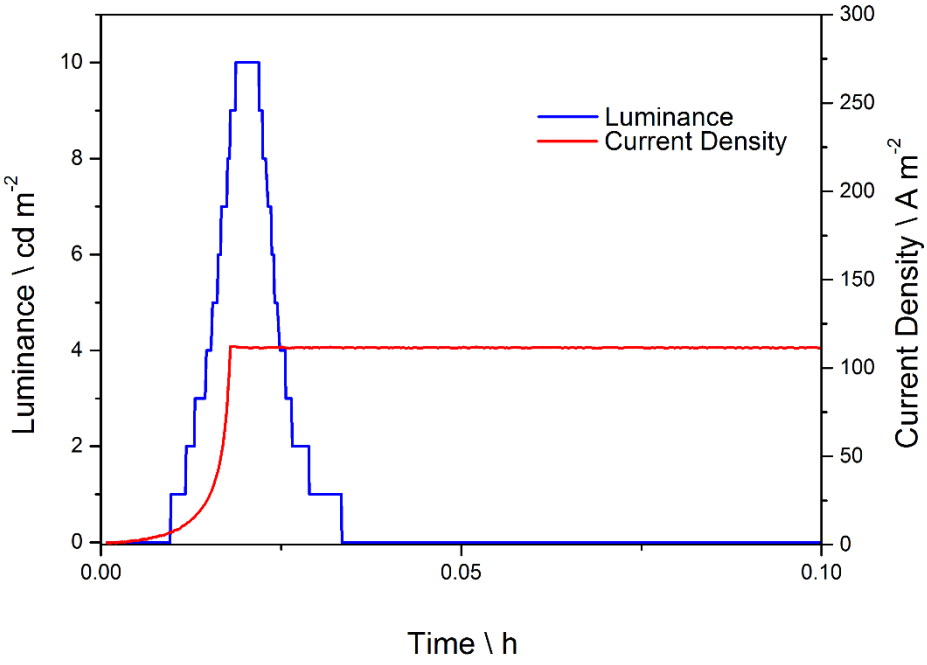

*Figure 3-15: Luminance (blue) and current density (red) curves of the device incorporating **1b** at constant voltage (8.5 V).*

To further enhance the stability of this kind of device, lower driving voltages of 6 V and 7 V were used, unfortunately this did not show any improvement.

3.5.1. Photoluminescence studies in different host blends

In further experiments, it was tried to improve the luminance of the devices by using matrix materials to get better hole and electron transport.

Initially, a mixture of SPPO13:TCTA (2:1) (Scheme 3-5) with 10% of a solution of **1b** in anisole (30 mg/mL) was prepared and spin-coated on PEDOT.

The measurement of the device at constant current density (100 mA/cm^2) showed a maximum luminance of 22 cd/m^2 and a fast turn-on time. The device lifetime was still very short ($t_{1/2}$ ≈ 6.5 min) (Figure 3-16).

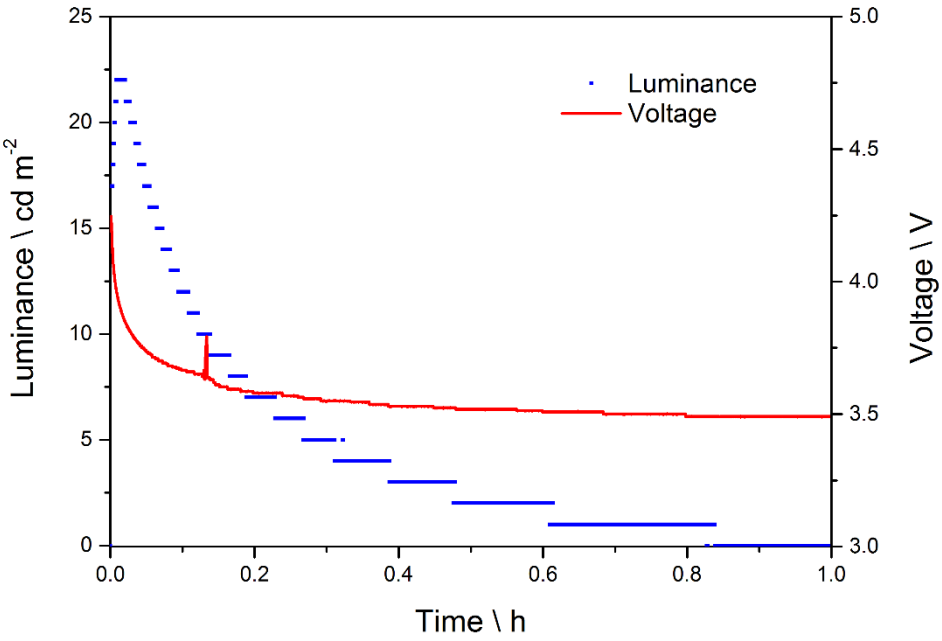

*Figure 3-16: Luminance (blue, dotted) and voltage (red, solid line) curves of the device incorporating **1b** at constant current density (100 mA cm^{-2}).*

For further investigations of the performance of **1b** in different blends of TCTA, SPPO13 and VL367 (Scheme 3-5), a stock solution of **1b** (1.0 mg/mL) in anisole was prepared. Each different host material was added to 0.2 mL of stock solution to result in a mass ratio (**1b** /host blends) of 1:10. Scheme 3-5 shows the chemical structure of the host materials and additives.

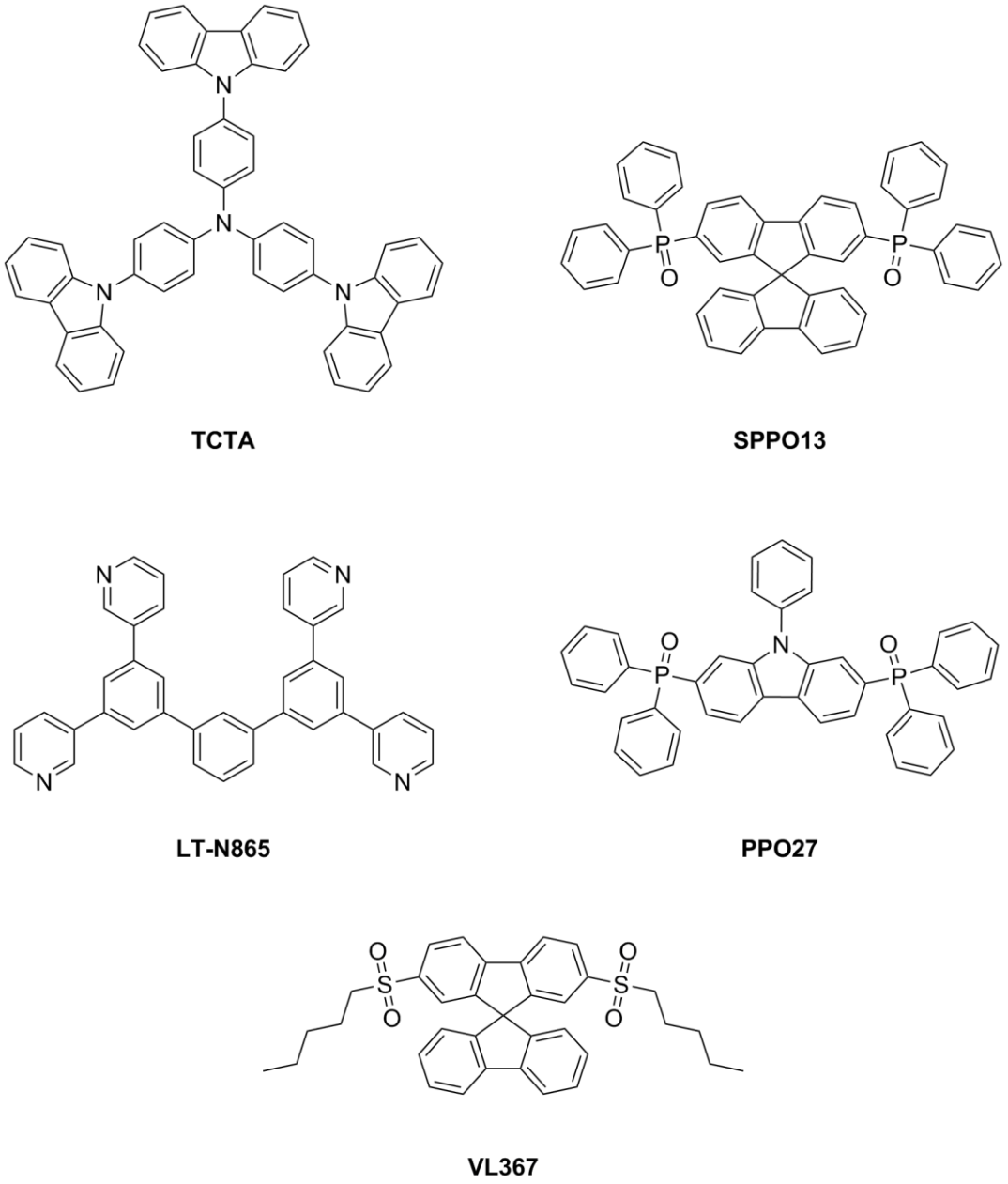

Scheme 3-5: Chemical structures of host materials and additives.

Figure 3-17 shows the PL spectra (excitation spectra are subtracted) in films of **1b** in four different hosts or host blends. The films were excited at 350 nm. The films containing TCTA, SPPO13 and VL367 (Scheme 3-5) show emission maxima at 395 nm, 404 nm and 423 nm. The emission intensities are slightly different. The emission of the film containing the SPPO13:TCTA blend as a host, is red-shifted compared to the others and shows a broader emission band with a maximum at 479 nm.

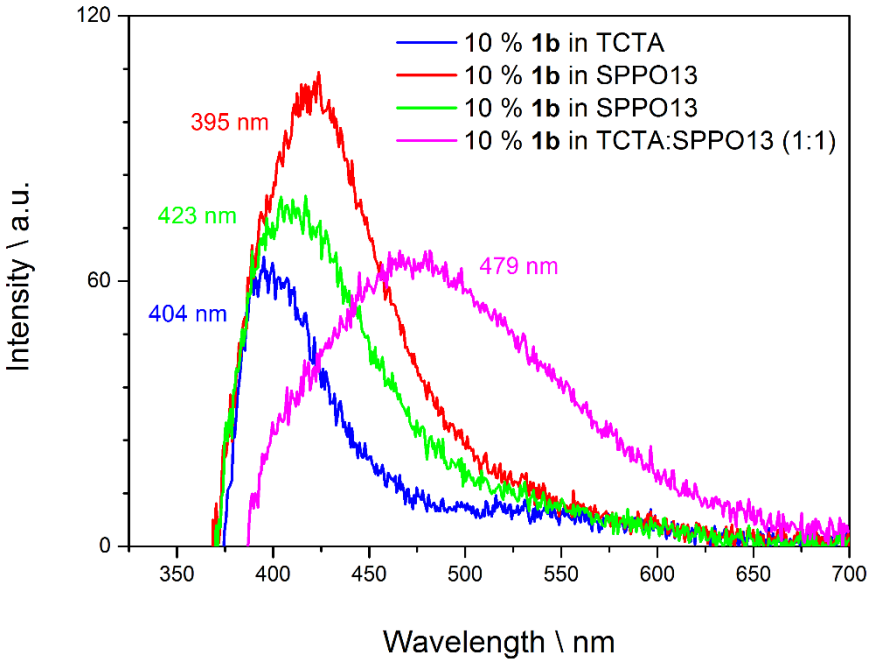

*Figure 3-17: Part of the PL spectra of **1b** in different hosts.*

Table 3-5 shows the corresponding PLQY for **1b** in different host blends. One can immediately see that compound **1b** shows the highest PLQY in a SPPO13 matrix.

Compound	Content	Matrix	QY (PL) \ %
1b	10%	TCTA	14.4
1b	10%	SPPO13	32.6
1b	10%	VL367	19.3
1b	10%	TCTA:SPPO13 (1:1)	11.5

*Table 3-5: Photoluminescence QY of 10% **1b** in different matrix blends.*

3.5.2. Photoluminescence studies of varying concentrations of 1b in TCTA

In a further experiment, the amount of **1b** in the host/guest films was varied to check if this ratio has any influence on the emitted wavelength or on the QY of the mixture. Therefore, TCTA films containing 5%, 10%, 20% and 40% of **1b** were prepared and measured. Figure 3-18 shows that all four different films show their PL emission maxima at approximately the same wavelength at around 400 nm. Since there might be differences in film thickness, it is not possible to draw a conclusion about the differences in the emission intensity.

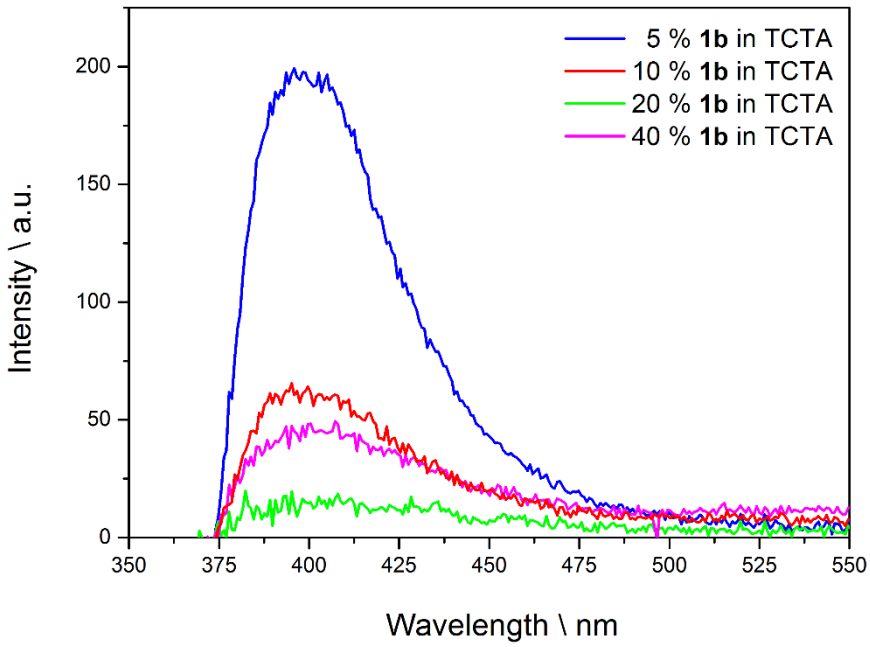

*Figure 3-18: PL emission spectra of different concentrations of **1b** in a TCTA matrix.*

Looking at the PLQY of the samples (Table 3-6), it is clear at first sight that the concentration of **1b** in the host/guest system has a huge influence on the quantum yield of the system. The film with 20% Zn(II) complex content shows a PLQY of 21%, which is more than doubled compared to the sample with only 5% guest-content. The experiment also shows that more emitting substance does not necessarily mean higher quantum yield. The sample containing 40% of the emitting Zn complex shows a significantly lower PLQY, namely 16%.

Compound	Content	Matrix	QY (PL) \ %
1b	5%	TCTA	9.30
1b	10%	TCTA	21.1
1b	20%	TCTA	15.6
1b	40%	TCTA	14.4

*Table 3-6: Photo luminescence QY of different concentrations of **1b** in a TCTA matrix.*

3.5.3. Electroluminescence of OLEDs

3.5.3.1. General remarks

Although the charged nature of the zinc(II) complexes would allow them to be used in a LEC configuration, they are a bit unusual because of their 2+ charge. The compounds that are normally used in LECs are bis-cyclometalated Ir(III) complexes with an overall single charge. These systems have been investigated for a long time and the production type has been optimized towards the Ir(III) complexes. There is still no universal way of building LECs that could be applied for every compound. Thus an OLED architecture was used to further investigate complexes **1b** – **3b** and **5b**, because it allows the usage of hole and electron transport layers as well as hole blocking layers, which could further improve the performance of the investigated zinc(II) complexes.

Scheme 3-6 shows the layered structure of the OLED devices. The thicknesses and composition of the layers mentioned in this section apply to all the devices if not explicitly mentioned to be different. On top of a ITO covered glass substrate a 70 nm thick layer of PEDOT:PSS (Clevios 4083) was spin-coated and annealed (15 min, 150 °C) before a blend of TCTA:SPPO13 containing 25.0 – 28.6 mg/mL (≈ 20%) of compounds **1b** – **3b** and **5b** was spin-coated on top (90 – 100 nm). TCTA and SPPO13 act as hole transporting and electron transporting material, respectively. Finally, LT865 as hole blocking layer (30 – 40 nm) and the metal electrodes (Ba: 5 nm, Ag: 70 – 80 nm and Al: 70 nm) were evaporated on top. For most blends the best of four different devices was selected.

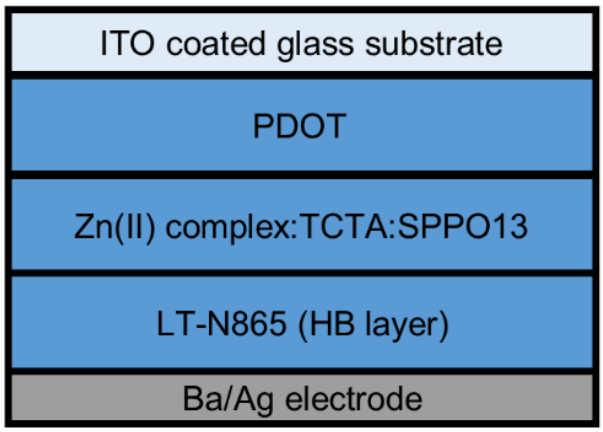

*Scheme 3-6: Layered structure of the prepared OLEDs, incorporating **1b** - **3b** or **5b**.*

3.5.3.2. Optimization of the HT/ET ration in the emitting layer

This experiment is meant to show the dependence of the system on the hole and electron mobility. Therefore, the ratio of TCTA/SPPO13 (HT/ET) was varied to find optimal working conditions. The content of the active compound was held constant at 10%. The layer thickness was not constant in all the following experiments due to the different ratios of hole and electron transporting materials.

3.5.3.2.1. 1b with HT only matrix

A first device was prepared according to the usual build-up protocol but with no SPPO13 in the active layer (total concentration 28.6 mg/mL in anisole). The lack of an electron transporting material leads to a high current density (Figure 3-19) and thus to a low efficacy (Figure 3-20). The observed spikes are outliers and can be disregarded. Nevertheless, this device showed a quite high luminance of 1354 cd/m^2 at 11.6 V (Figure 3-19).

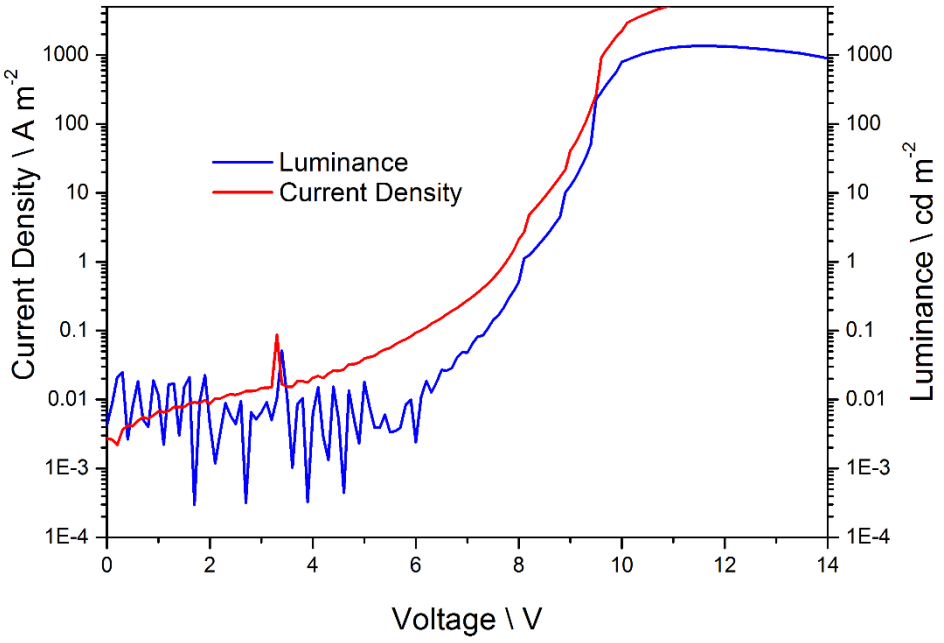

*Figure 3-19: Luminance (blue) and current density (red) curves of **1b** in HT only matrix.*

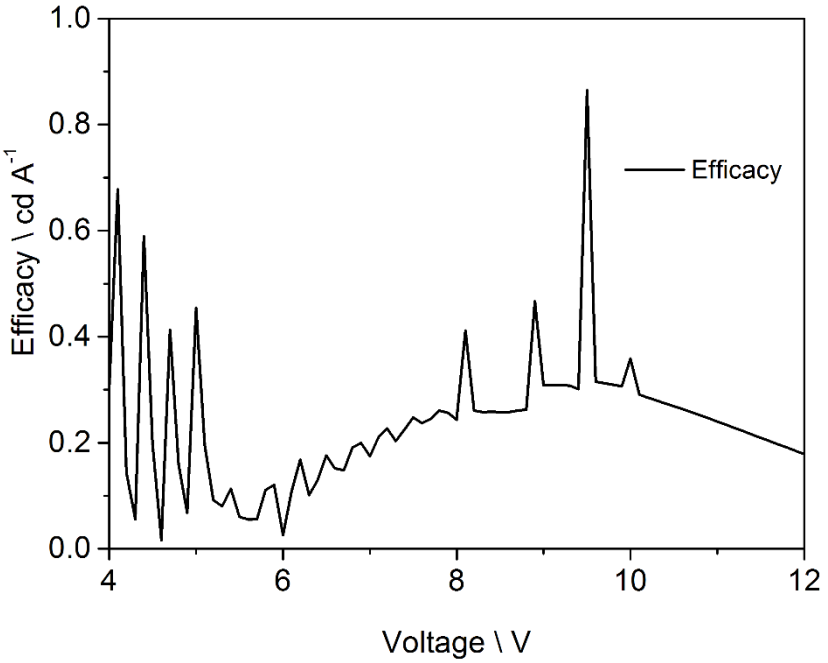

*Figure 3-20: Efficacy curve of **1b** in HT only matrix.*

In Figure 3-21 one can see that three out of four prepared devices show similar efficacies. Again, the spikes in the measured efficacy curves are outliers and can be disregarded. However, the efficacy values for all three working devices are quite poor and lie around 0.3 cd/A at 10 V.

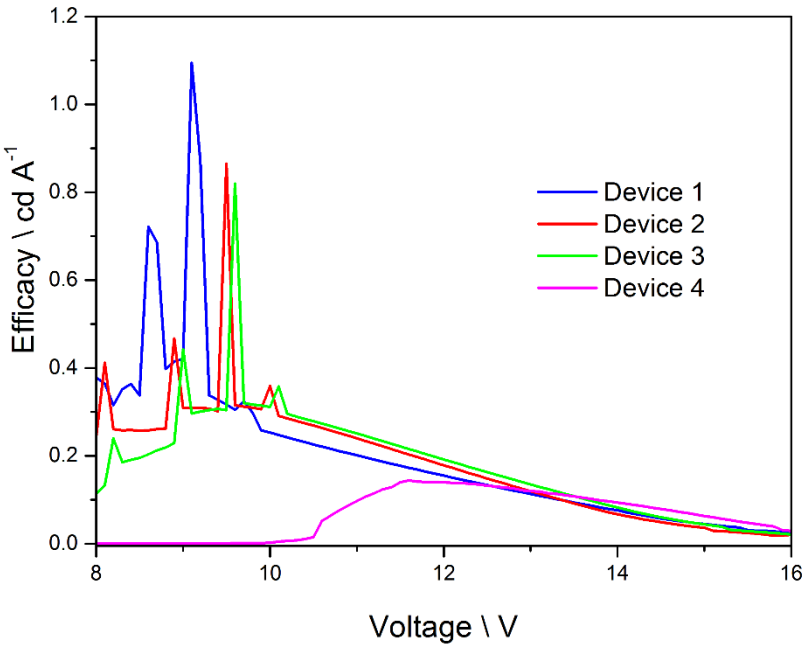

*Figure 3-21: Efficacy curves of the four prepared devices, incorporating **1b** in a HT only matrix.*

3.5.3.2.2. 1b in HT:ET (1:1) matrix

The luminance and current density plots of the three working devices that were prepared using a 1:1 mixture of TCTA and SPPO 13 as a matrix, are shown in Figure 3-22. The highest luminance of 259 cd/m^2 is reached at a driving voltage of 14.8 V, whereas the efficacy reaches its maximum of 1.6 cd/A at 10 V. The spikes can be disregarded, since they are outliers (Figure 3-23).

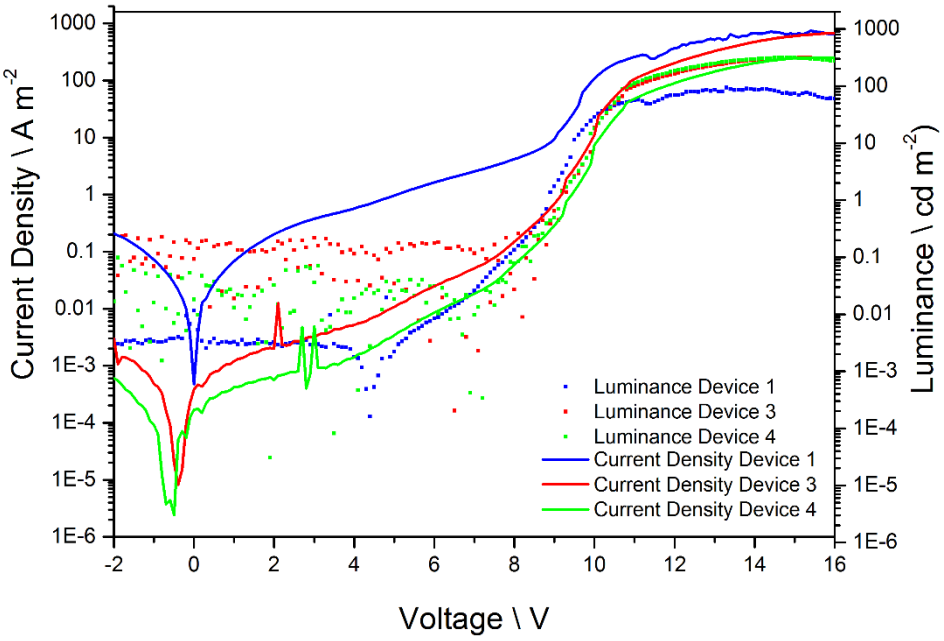

*Figure 3-22: Luminance (dotted) and current density (solid) curves of the 3 working devices, incorporating **1b** in a HT:ET (1:1) matrix.*

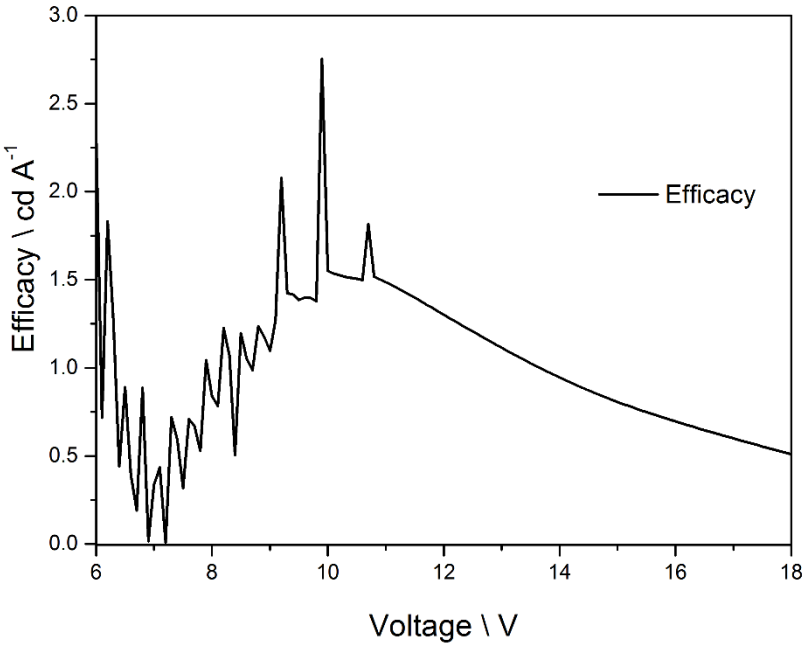

*Figure 3-23: Efficacy curve of the best performing device in this series (**1b** in HT:ET (1:1) matrix).*

3.5.3.2.3. 1b in HT:ET (1:2) matrix

For this device the content of the electron transporting material was increased to result in a 1:2 TCTA:SPPO13 ration. The higher ET content should possibly further lower the current density and thus also increase the efficacy. Figure 3-24 clearly shows that this is not the case at a driving voltage of 10.5 V. The efficacy only reaches a value of about 0.12 cd/A. The spikes in the measured curves can be disregarded, since they are outliers. The maximum luminance of 145 cd/m^2 is reached at 16.7 V, resulting in a current density of about 2860 A/m^2 (Figure 3-25).

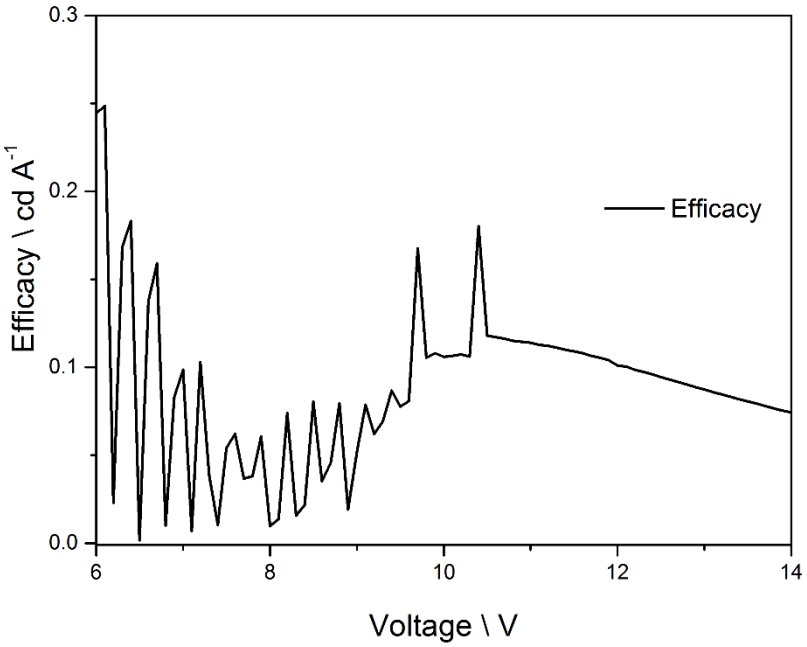

*Figure 3-24: Efficacy curve of **1b** in a HT:ET (1:2) matrix.*

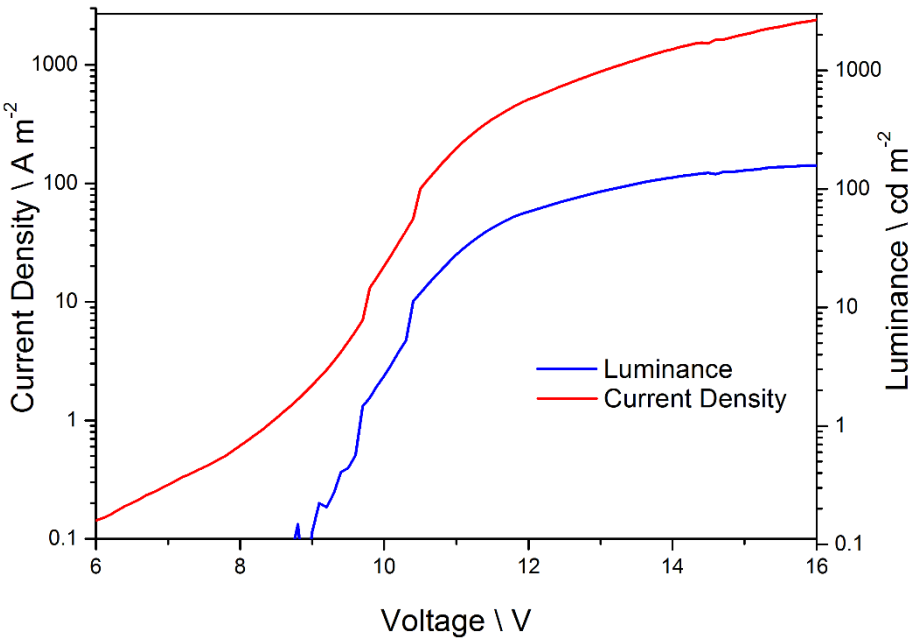

*Figure 3-25: Luminance (blue) and current density (red) plots of **1b** in a HT:ET (1:2) matrix.*

3.5.3.2.4. 1b in ET only matrix

Switching to devices containing an ET only matrix shows that an increasing SPPO13 concentration and thus increased electron transport properties of the matrix has a negative effect on the luminance and also on the efficacy. The prepared device shows a very low luminance of only 2.3 cd/m^2 at a very high driving voltage of 24 V. Also the efficacy of about 0.0005 cd/A (broad, flat peak) at 11 V is almost not measurable. This can probably be attributed to the very high current density (Figure 3-26 and Figure 3-27).

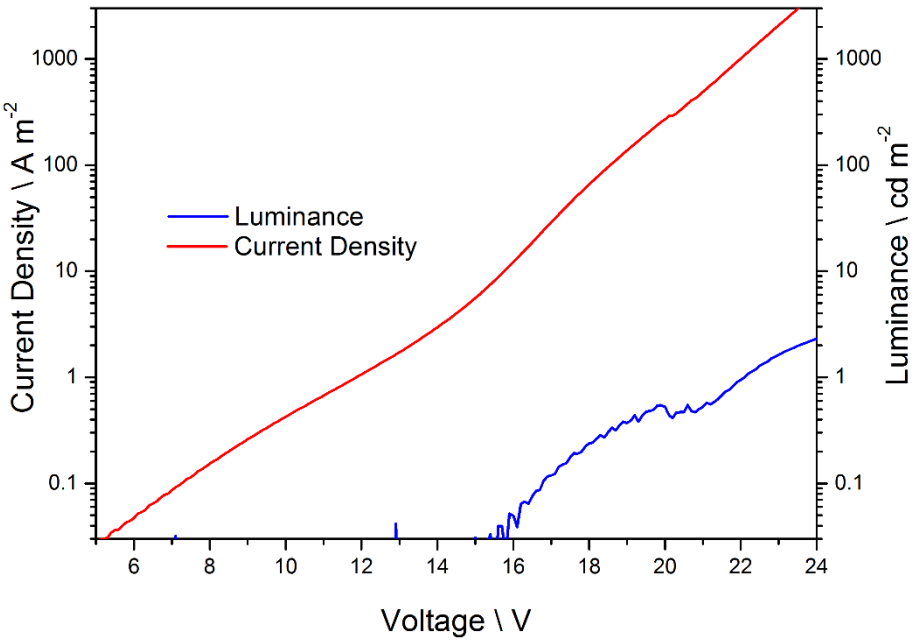

*Figure 3-26: Luminance (blue) and current density (red) curves of **1b** in an ET only matrix.*

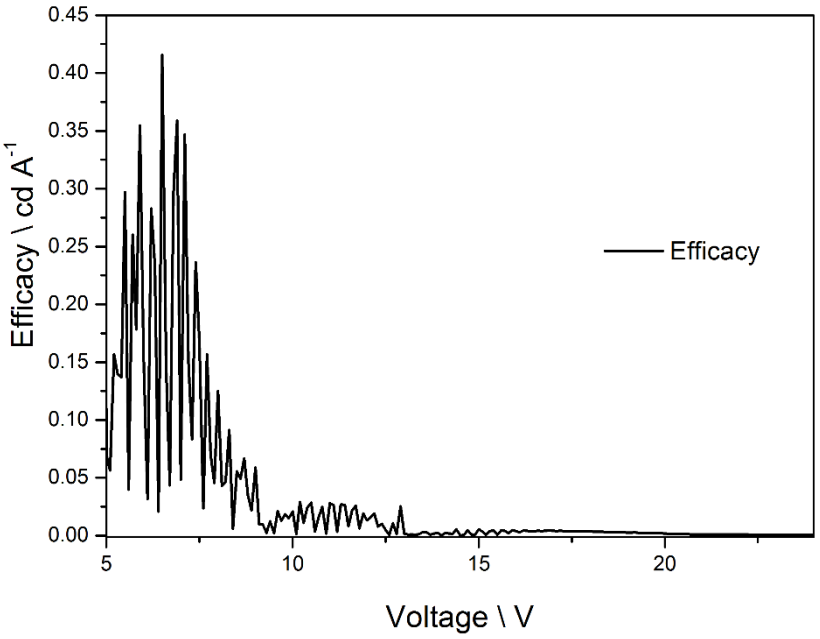

*Figure 3-27: Efficacy curve of **1b** in an ET only matrix.*

3.5.3.2.5. 1b in a bipolar matrix PPO27

PPO27 is a carbazole-based, bipolar host material, which should have improved electron transport properties. The PPO27 could not be dissolved in anisole, therefore 12.5% of chlorobenzene were added. The emitting layer showed a lower thickness of about 53 nm, compared to approximately 100 nm in the other devices, thus resulting in a high current density. The tested device showed a luminance of 57.5 cd/m^2 at 12.5 V driving voltage. Also the current density was fairly high at this potential with 1315 A/m^2 (Figure 3-28).

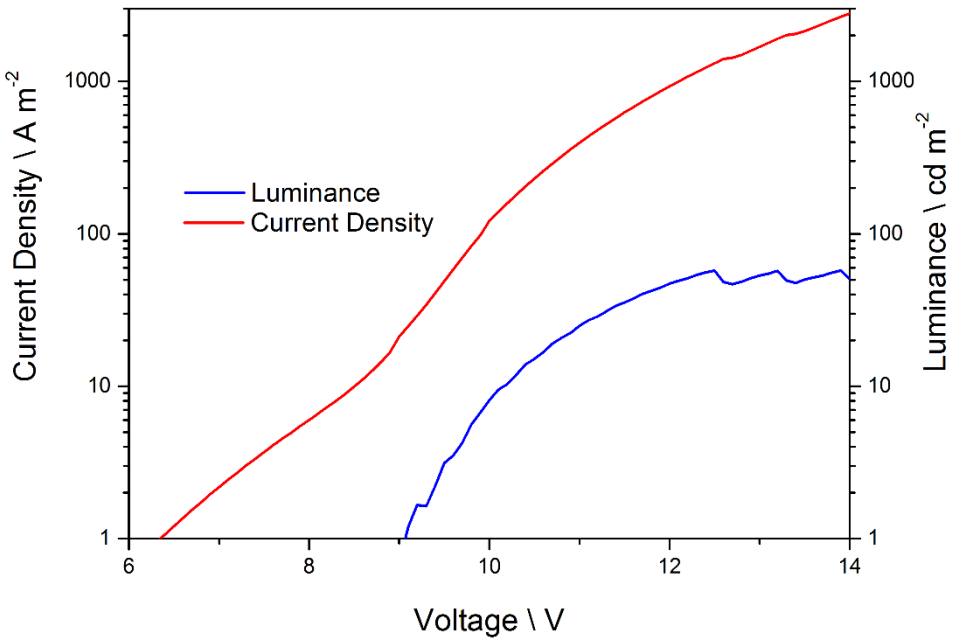

*Figure 3-28: Luminance (blue) and current density (red) curves of **1b** in a bipolar matrix.*

3.5.3.2.6. 1b in HT:ET (1:1) matrix with additional hole injection layer

In this device it was tried to improve the hole injection properties of the device by applying an additional polyvinyl-carbazole (PVK) layer on top of the PEDOT layer. This layer is meant to block electrons at the anode and should also lower the hole-injection barrier.

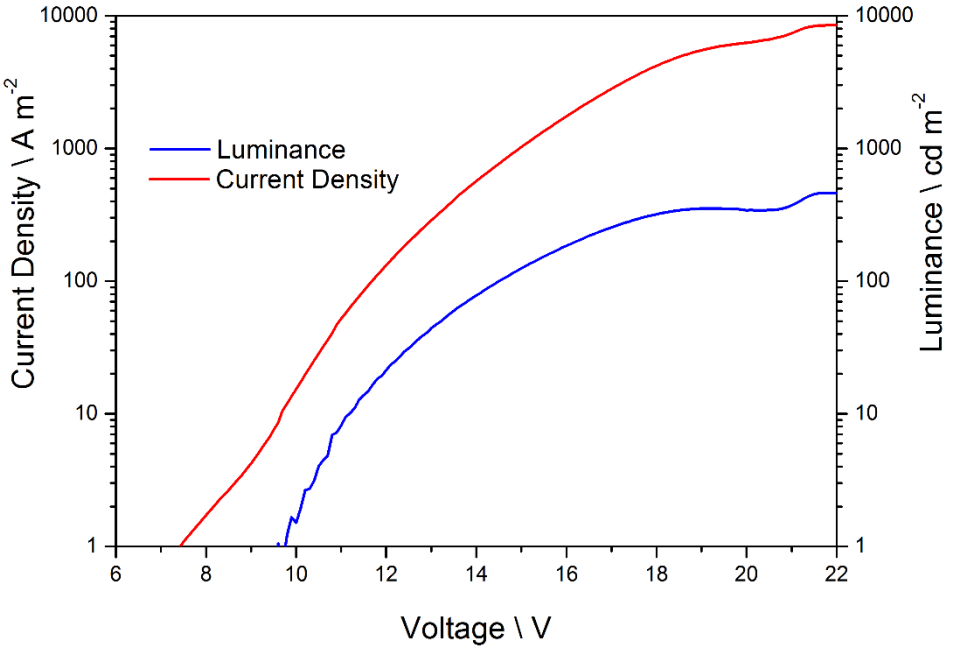

*Figure 3-29: Luminance (blue) and current density (red) curves of **1b** with additional hole-injection layer.*

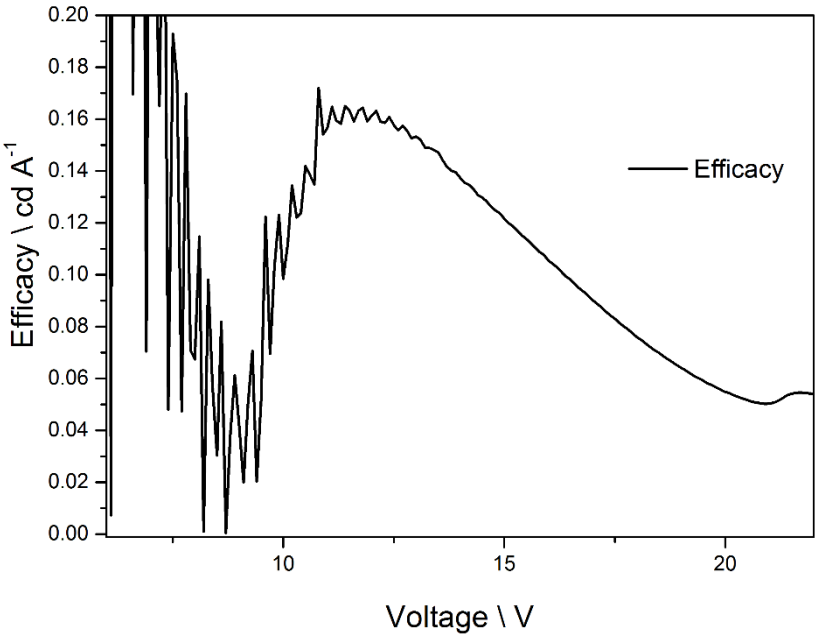

*Figure 3-30: Efficacy curve of **1b** with additional hole-injection layer.*

Compared to the other devices with a HT:ET (1:1) matrix without PVK layer, this device shows a moderate luminance of 463 cd/m^2 at 21.8 V. The efficacy shows a maximum

of 0.16 cd/A at 12.1 V. The PVK layer seems to improve the luminance by approximately 200 cd/m^2, although also the driving voltage has to be increased by 7 V to 21.8 V. The efficacy decreased by a factor of 10 at a comparable driving voltage of 12.1 V, which is 2.1 V higher than in the device without PVK layer (Figure 3-29 and Figure 3-30). The PVK layer also drastically increased the current density to very high 8494 A/m^2, which explains the very poor efficacy.

3.5.3.3. Other Zn(II) bis-terpyridine complexes as emitters in OLED configuration

Complexes **1b**, **2b**, **3b** and **5b** were selected as emitters to be measured in OLED configuration because they showed reasonable quantum yields. If not explicitly mentioned, the content of the active compound in the 1:1 TCTA:SPPO13 matrix was 20%. The layer composition was as follows, layer thicknesses are mentioned in brackets behind the corresponding layer:

ITO | PEDOT | **1b** – **3b**, **5b**:TCTA:SPPO13 | LT865 (30 nm) | Ba (5 nm) | Ag (70 nm)

3.5.3.3.1. Compound 1b

There was again a device measured containing the model compound **1b**. This time its concentration in the matrix was increased to 20%.

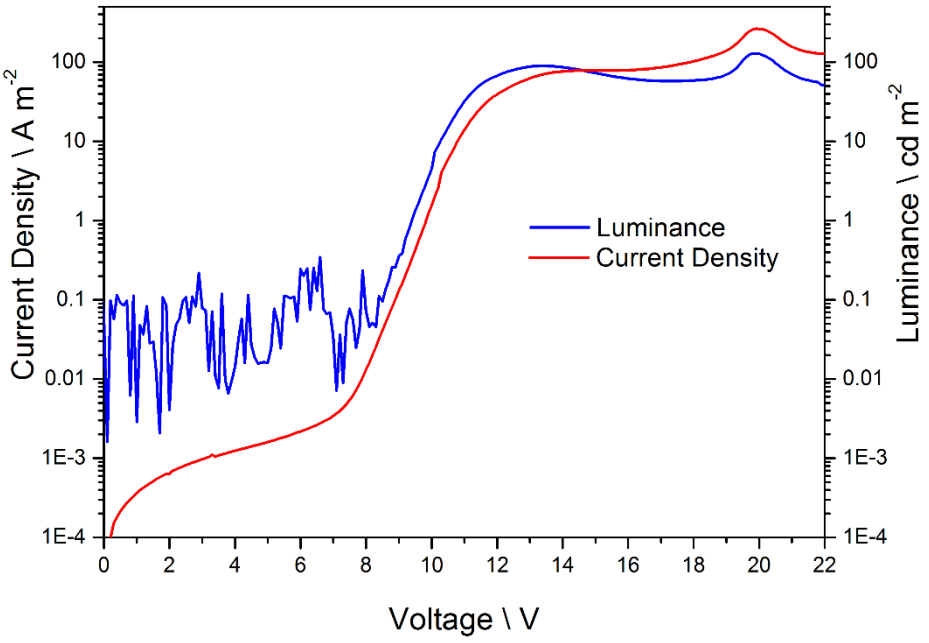

*Figure 3-31: Luminance (blue) and current density (red) curves of 20% **1b** in a HT:ET (1:1) matrix.*

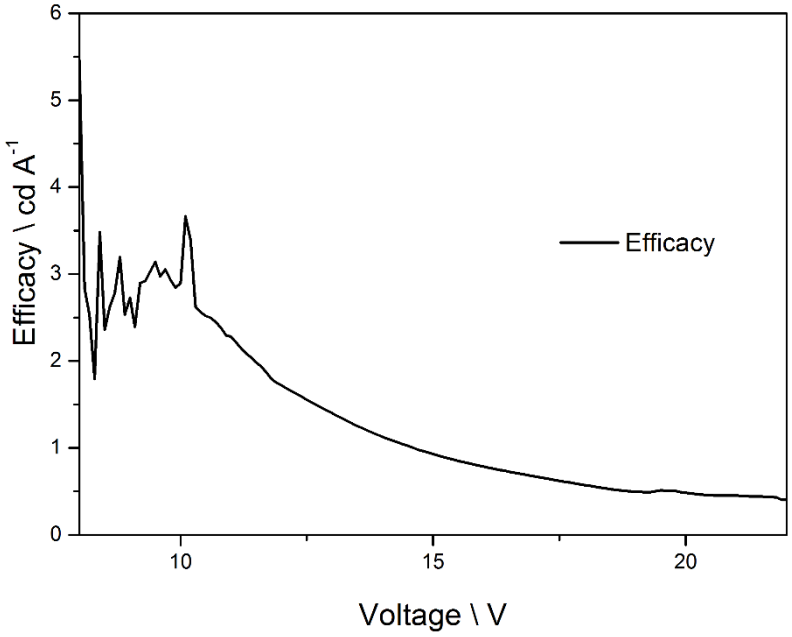

*Figure 3-32: Efficacy curve of 20% **1b** in a HT:ET (1:1) matrix.*

The device shows a low luminance of 129 cd/m^2 at 19.9 V driving voltage and a maximum efficacy of 2.6 cd/A at 10.8 V, corresponding to a luminance of only 10 cd/m^2

(Figure 3-31 and Figure 3-32). Compared to the before measured device with only 10% **1b** in the matrix it seems that the doubling of active compound leads to a reduction of luminance but to a slight increase in efficacy. The emitted light appeared “sky-blue” by eye. The CIE diagram (x = 0.2772; y = 0.3986) shows that the emitted light is in a greenish-white region (Figure 3-33).

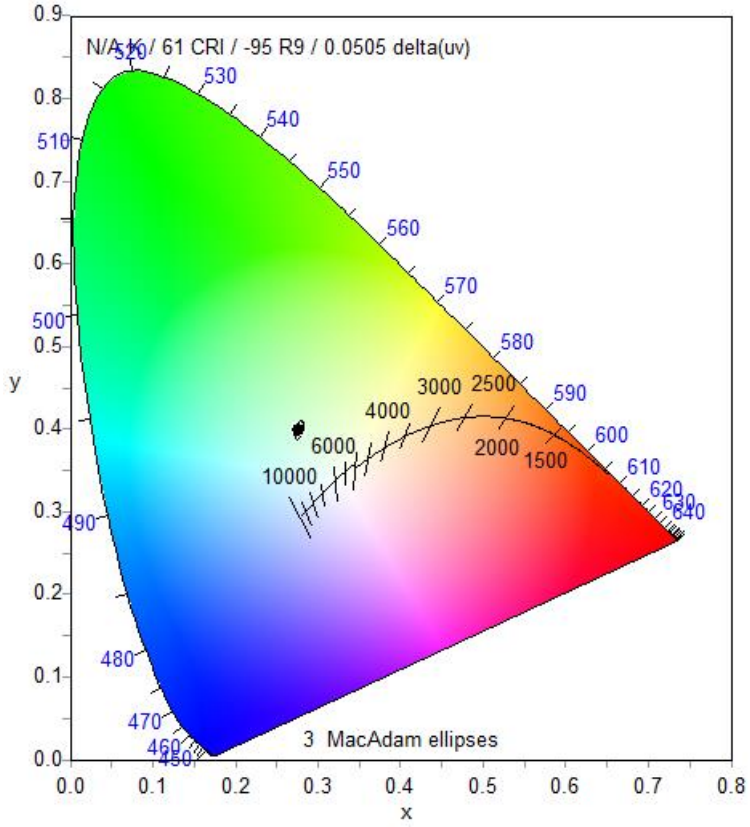

*Figure 3-33: CIE map of device incorporating **1b**.*

3.5.3.3.2. Compound 2b

The device incorporating **2b** as emitter shows properties similar to the previously mentioned one. The highest luminance was observed at 16.1 V and was 277 cd/m^2 (Figure 3-34). The highest efficacy of 0.19 cd/A was reached at a luminance of only 13 cd/m^2 at 9.1 V (Figure 3-35).

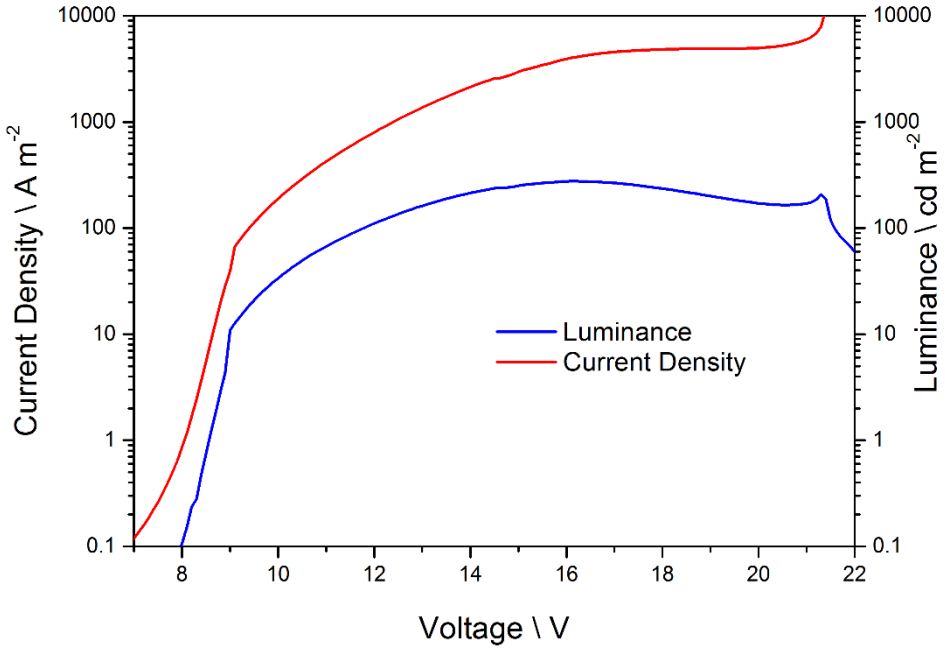

*Figure 3-34: Luminance (blue) and current density (red) curves of 20% **2b** in a HT:ET (1:1) matrix.*

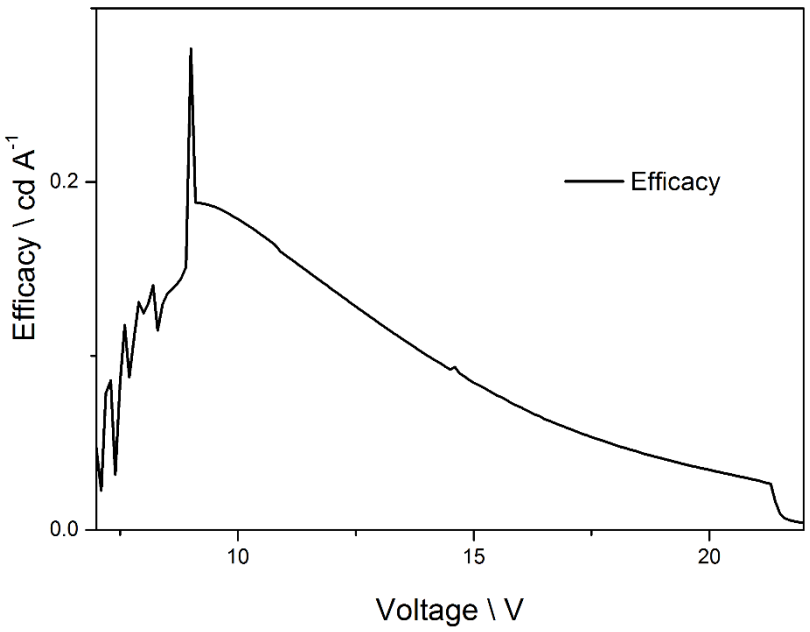

*Figure 3-35: Efficacy curve of 20% **2b** in a HT:ET (1:1) matrix.*

The CIE diagram (x = 0.2794; y = 0.4169) shows again that the emitted light is in the greenish-white region. To the naked eye, the emitted light looks “sky-blue” (Figure 3-36).

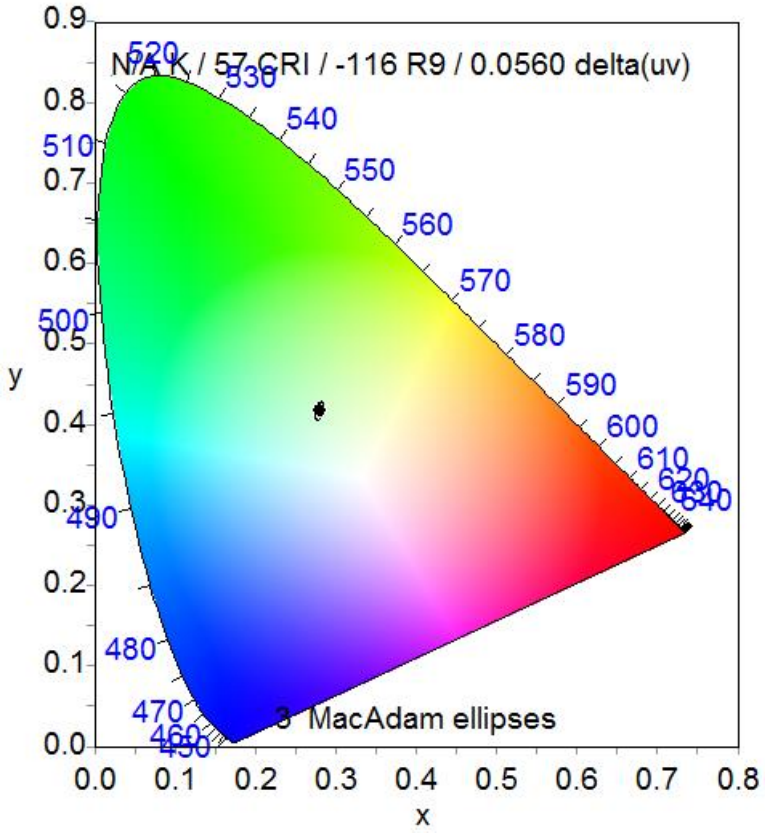

*Figure 3-36: CIE map of device incorporating **2b**.*

Comparing these CIE coordinates to the ones of the before mentioned device it seems clear that the emitted colour is indeed almost the same.

3.5.3.3.3. Compound 3b

The highest luminance for this device was measured as 187 cd/m^2 at 13.1 V. The highest efficacy of 0.31 cd/A (the spike can be disregarded, since it is an artefact) was reached at a luminance of 14.3 cd/m^2 and at 8.9 V driving voltage (Figure 3-37 and Figure 3-38).

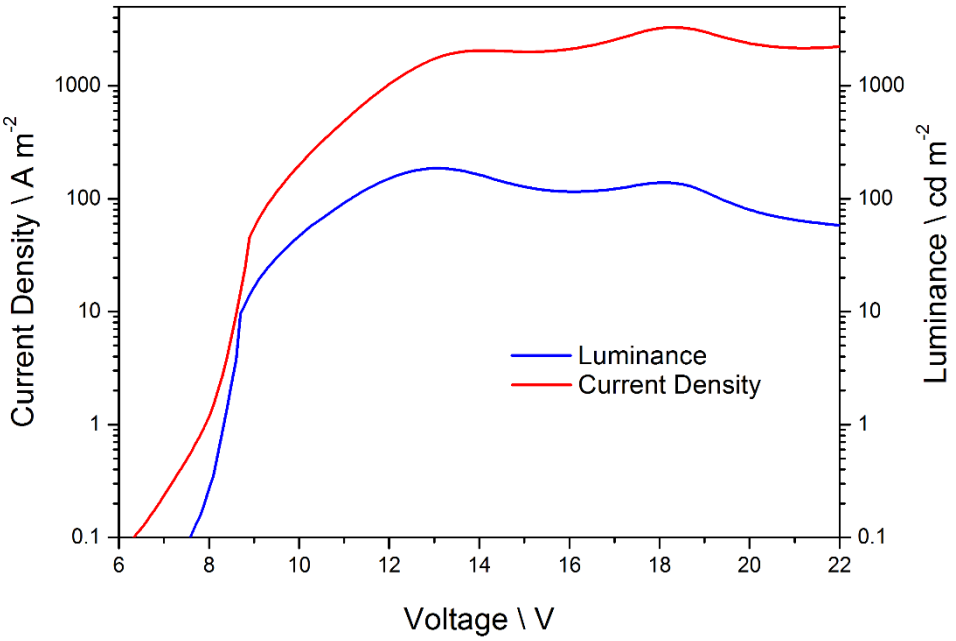

*Figure 3-37: Luminance (blue) and current density (red) curves of 20% **3b** in a HT:ET (1:1) matrix.*

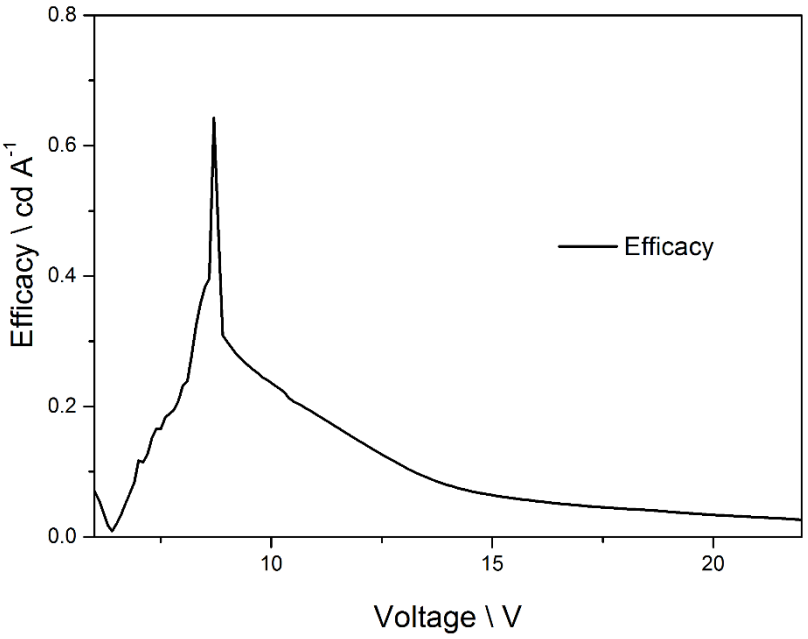

*Figure 3-38: Efficacy curves of 20% **3b** in a HT:ET (1:1) matrix.*

The CIE coordinates (x = 0.3093; y = 4139) lie again in the region of greenish-white light, which appears to the human eye as “sky-blue” (Figure 3-39).

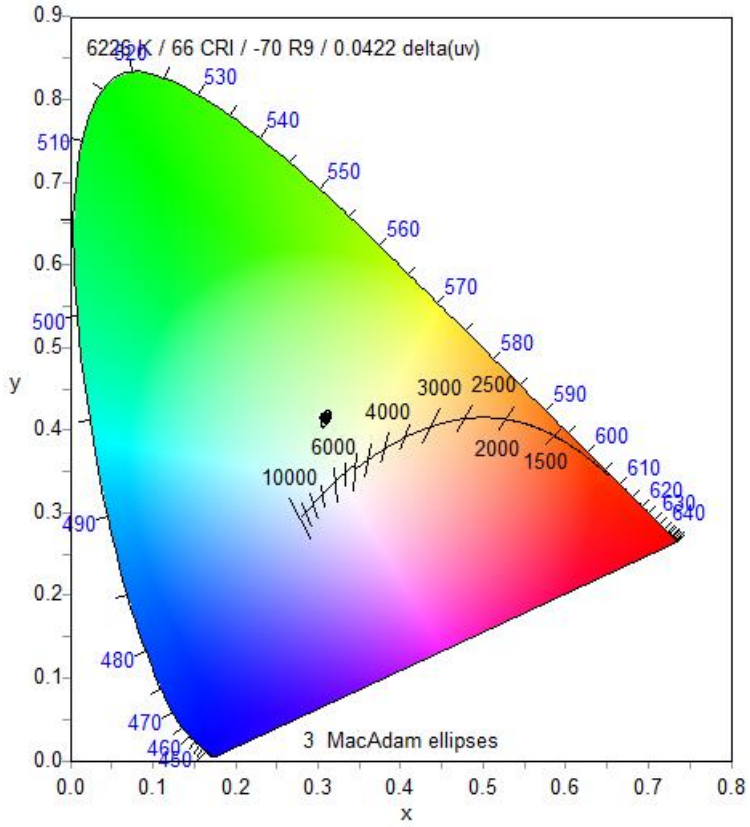

*Figure 3-39: CIE map of device incorporating **3b**.*

3.5.3.3.4. Compound 5b

The device incorporating compound **5b**, shows a luminance of 405 cd/m^2 at 20.5 V, which is one of the highest among this series (Figure 3-40). The maximum efficacy is 0.17 cd/A at a luminance of 8.5 cd/m^2 at 11.1 V (Figure 3-41). What has to be mentioned is the very high current density of 10409 A/m^2 at 20.5 V that was measured for this device. This might be attributed to the different chemical composition of the used ligand. It is the only one in the series that contains a triphenylamine unit which can have certain hole transporting properties. It cannot be said with absolute certainty whether this ability influences the performance of the device in a positive or negative way, but it seems clear that the high current density is a problem that arises from the nature of the ligand.

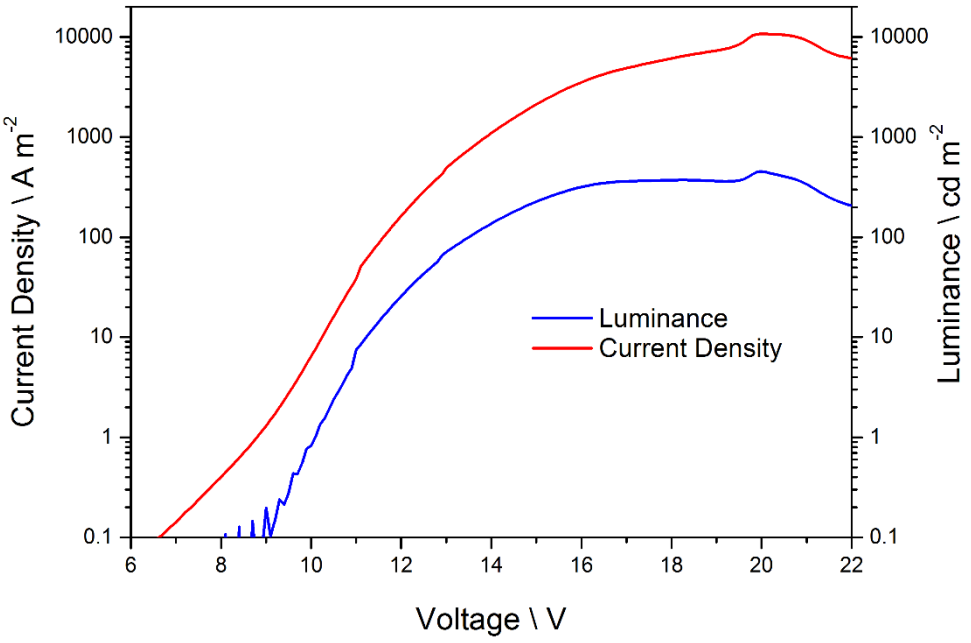

*Figure 3-40: Luminance (blue) and current density (red) curves of 20% **5b** in a HT:ET (1:1) matrix.*

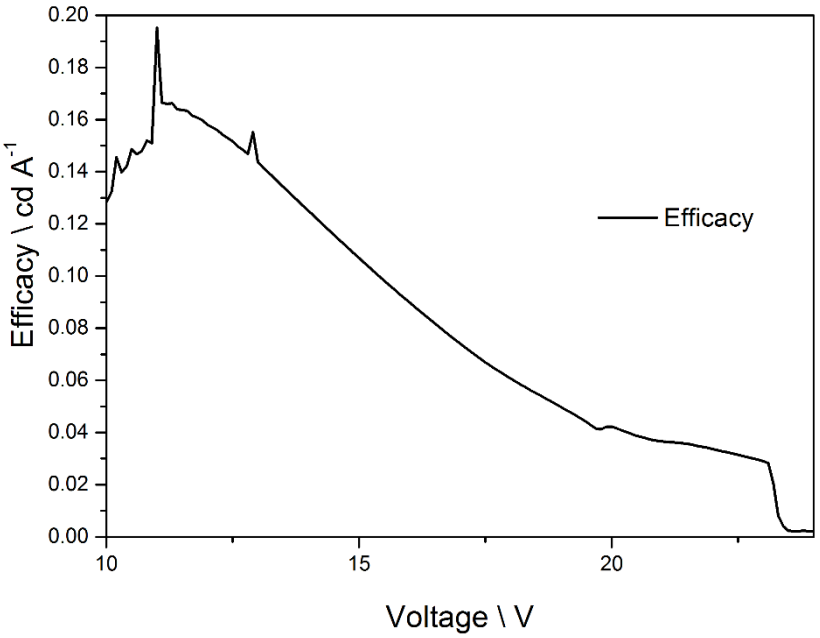

*Figure 3-41: Efficacy curve of 20% **5b** in a HT:ET (1:1) matrix.*

Although the structure of the ligand is different to the others used in the other devices, the CIE coordinates (x = 0.3015; y = 0.4325) of the emitted light are again very similar

to the others observed. The CIE diagram shows that the emitted light lies again in the greenish-white region, although by eye the light looks very whitish (Figure 3-42).

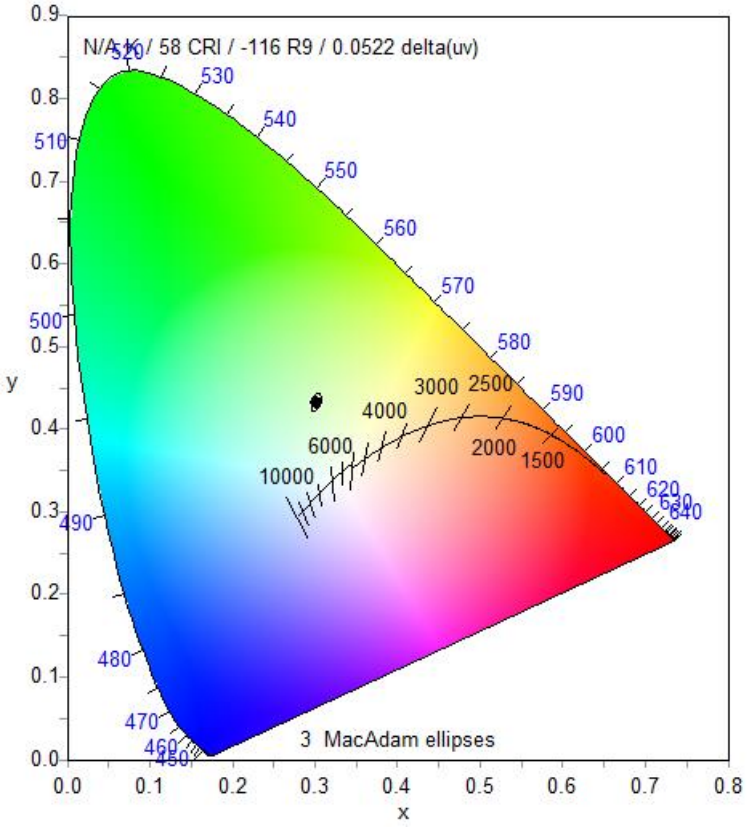

*Figure 3-42: CIE map of device incorporating **5b**.*

3.6. Conclusion and outlook

In conclusion it can be said that 6 ligands and their corresponding Zn(II) complexes have been synthesized in only a few steps and were characterized in terms of their solution electronic properties. HOMO-LUMO gaps obtained from electronic absorption spectra suggest that the substitution pattern in 4'-phenyl-terpyridine-position of the ligands has an effect on these gaps. It can be said that the more electron donating the substituent in 4-position of the 4'-phenyl group is, the smaller the HOMO-LUMO gap gets. It can also be stated that the measured emissions support this theory, since the same trend can be seen. Computational calculations of ground state HOMO and LUMO levels support the trend seen in the UV-Vis spectra.

Compounds **1b** – **6b** were sent to the lab of Dr. Henk Bolink in Valencia, Spain where they were incorporated into LEC and OLED devices by Dr. David Vonlanthen. After a lot of optimization efforts he showed that it is possible to use this kind of complex in such devices. Although the device lifetimes and luminance levels are very poor, it is a proof of concept and it would make sense to further optimize the LEC fabrication process to attune it to 2+ charged compounds like the ones that were tested.

Future work in this field would imply the design of new ligands to further tune the emission properties, as well as further optimizations of the device architecture to better support doubly charged complexes.

3.7. Experimental

3.7.1. 4'-(4-Methoxyphenyl)-2,2':6',2''-terpyridine (1a)[82]

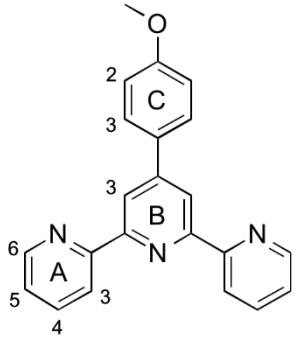

2-Acetylpyridine (5.00 g, 41.2 mmol, 2.0 eq.) was added to ground NaOH (1.65 g, 41.2 mmol) in PEG-300 at 0 °C. The suspension was stirred for 15 min at 0 °C, then *p*-anisaldehyde (2.80 g, 20.6 mmol, 1.0 eq.) was added. After 2 h of stirring at 0 °C, NH_4OH (aq, 25.0 mL, 201 mmol, 10 eq.) was added and the mixture heated to 100 °C for further 2 h. Precipitation of an off-white crystalline solid could be observed. The heating was stopped and the mixture was slowly cooled to RT. It was then filtered. The brown residue was washed with H_2O (50 mL), cold EtOH (15 mL) and Et_2O (50 mL). The now colourless solid was dried on the frit (3.32 g, 9.77 mmol, 47%).

^{1}H NMR (500 MHz, $CDCl_3$) δ / ppm 8.73 (ddd, *J* = 4.8, 1.8, 0.9 Hz, 2H, H^{A6}), 8.71 (s, 2H, H^{B3}), 8.69 – 8.65 (m, 2H, H^{A3}), 7.91 – 7.85 (m, 4H, H^{A4} & H^{C3}), 7.35 (ddd, *J* = 7.5, 4.8, 1.2 Hz, 2H, H^{A5}), 7.05 – 7.01 (d_{AB}, *J* = 8.9 Hz, 2H, H^{C2}), 3.88 (s, 3H, H^{MeO}).

3.7.2. 4'-(4-(Methylthio)phenyl)-2,2':6',2''-terpyridine (2a)[75]

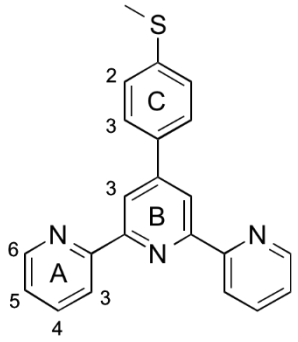

2-Acetylpyridine (5.00 g, 41.2 mmol, 2.0 eq.) was added to KOH (2.77 g, 49.4 mmol, 2.4 eq.) in a EtOH/H_2O (1:1) mixture at 0 °C. The suspension was stirred for 20 min at 0 °C, then 4-(methylthio)benzaldehyd (3.14 g, 20.6 mmol, 1.0 eq.) was added. After 2 h of stirring at 0 °C, NH_4OH (25.0 mL, 201 mmol, 10 eq.) was added and the mixture heated to 100 °C for further 5 h. Formation of a greenish solid material was observed. Heating was stopped and the mixture was slowly cooled to RT. The greenish material was filtered off and washed with H_2O (50 mL), cold EtOH (20 mL) and Et_2O (50 mL). The now light green solid was collected in a round bottomed flask, suspended in Et_2O and sonicated for 15 min. The now almost colourless solid was filtered off, washed with Et_2O (20 mL) and dried on the frit and under high vacuum. The desired product was obtained as colourless solid (3.07 g, 8.64 mmol, 42%).

^{1}H NMR (500 MHz, $CDCl_3$) δ / ppm 8.73 (ddd, *J* = 4.8, 1.8, 0.9 Hz, 2H, H^{A6}), 8.72 (s, 2H, H^{B3}), 8.69 – 8.65 (m, 2H, H^{A3}), 7.89 (dd, *J* = 7.5, 1.8 Hz, 2H, H^{A4}), 7.85 (d_{AB}, *J* = 8.9, 2H, H^{C3}), 7.37 (d_{AB}, *J* = 6.0 Hz, 2H, H^{C2}), 7.36 (ddd, *J* = 7.5, 4.7, 1.3 Hz, 2H, H^{A5}) 2.55 (s, 3H, H^{SMe}).

3.7.3. 4’-(4-Hydroxyphenyl)-2,2':6',2''-terpyridine (4a)[83]

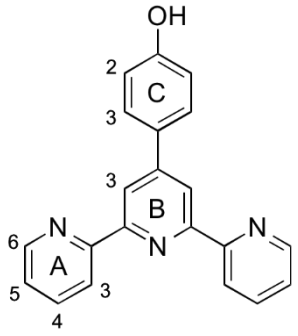

In a 25 cm^3 microwave vessel, **1a** (1.00 g, 2.95 mmol) was mixed with an excess of pyridinium chloride. The reaction mixture was then heated in a microwave reactor for 40 min at 200 °C followed by 10 min at 240 °C. Then the reaction mixture was cooled to room temperature. To the resulting colourless solid water was added and the suspension stirred for 10 min. The precipitate was filtered and washed with H_2O (20 mL), cold EtOH (20 mL) and Et_2O (20 mL). After drying on the frit and under high vacuum, the product was obtained as off-white solid (943 mg, 2.9 mmol, 98%).

^{1}H NMR (500 MHz, DMSO-*d6*) δ / ppm 9.93 (s, 1H, H^{OH}), 8.76 (ddd, *J* = 4.7, 1.7, 0.9 Hz, 2H, H^{A6}), 8.68 – 8.64 (m, 2H, H^{A3}), 8.66 (s, 2H, H^{B3}), 8.05 – 7.99 (m, 2H, H^{A4}), 7.79 (d_{AB}, *J* = 8.7 Hz, 2H, H^{C3}), 7.52 (ddd, *J* = 7.5, 4.7, 1.2 Hz, 2H, H^{A5}), 6.97 (d_{AB}, 2H, H^{C2}).

3.7.4. 4’-(4-Diphenylaminophenyl)-2,2':6',2''-terpyridine (5a)[84],[85]

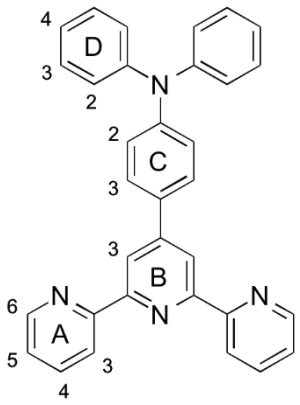

4'-(4-Bromophenyl)-2,2':6',2''-terpyridine (3.88 g, 10.0 mmol, 1.0 eq.) and Ph_2NH (1.69 g, 10.0 mmol, 1.0 eq.) were suspended in toluene (60 mL) under argon, and NaO*t*Bu (1.25 g, 13.0 mmol, 1.3 eq.) was added. A suspension of bis(dibenzylideneacetone)palladium(0) (0.115 g, 0.200 mmol, 0.02 eq.) and P*t*Bu_3 (0.041 g, 0.20 mmol, 0.02 eq.) in toluene (4 mL) was prepared under argon and was added to the reaction mixture. The purple mixture was heated at 100 °C for 16 h, after which time it was filtered while hot and decolorizing charcoal was added to the filtrate. The product was purified by column chromatography (SiO_2, toluene then ethyl acetate), recrystallized from EtOH and isolated as a pale brown solid (3.43 g, 7.24 mmol 72%).

^{1}H NMR (500 MHz, CD_3Cl) δ / ppm 8.73 (ddd, *J* = 7.4, 1.7, 0.8 Hz, 2H, H^{A6}), 8.73 (s, 2H, H^{B3}, 8.68 (dt, *J* = 7.9, 0.9 Hz, 2H, H^{A3}), 7.89 (td, *J* = 7.8, 1.8 Hz, 2H H^{A4}), 7.84 – 7.77 (m, 2H, H^{C3}), 7.36 (ddd, *J* = 7.4, 4.8, 1.1 Hz, 2H, H^{A5}), 7.33 – 7.27 (m, 4H, H^{D3}), 7.20 – 7.13 (m, 6H, H^{C2}, H^{D2}), 7.08 (tt, *J* = 7.6, 1.2 Hz, 2H, H^{D4}).
^{13}C NMR (126 MHz, CD_3Cl) δ / ppm 156.5 (C^{A2}), 156.0 (C^{B2}), 149.9 (C^{C1}), 149.2 (C^{A6}), 148.9 (C^{B4}), 147.5 (C^{D1}), 137.0 (C^{A4}), 131.9 (C^{C4}), 129.5 (C^{D3}), 128.3 (C^{C3}), 124.9 (C^{D2}), 123.9 (C^{A5}), 123.5 (C^{D4}), 123.3 (C^{C2}), 121.5 (C^{A3}), 118.4 (C^{B3}).
MS (EI, *m/z*): 476.2 $[M]^+$ (calc.: 476.2).
UV-Vis (4.0 * 10^{-5} mol/L in MeCN) λ_{abs}/nm 231 (ε / dm^3 mol^{-1} cm^{-1} 51300) = 273 (30300), 281 (32000), 315 (29400) nm; (9.1 * 10^{-4} mol/l in MeCN) λ_{abs}/nm 446 (ε / dm^3 mol^{-1} cm^{-1} 1600) = 503 (1400), 545 sh (500) nm;

CV (MeCN, [^{n}Bu$_4$N][PF$_6$], vs Fc/Fc$^+$): -0.05/-0.11, -1.20/-1.14^{qr}, -2.08/-2.00^{qr}, -2.62^{irr} V.

IR (ATR, $\tilde{\nu}$ / cm^{-1}): 3045(w), 1700 (w), 1581 (m), 1564 (m), 1545 (w), 1517 (m), 1490 (m), 1465 (m), 1441 (m), 1420 (w), 1389 (m), 1328 (m), 1275 (s), 1231 (w), 1116 (w), 1075 (w), 1030 (w), 988 (w), 889 (m), 835 (m), 828 (m), 789 (s), 757 (s), 734 (s), 692 (s), 661 (s), 609 (m).

3.7.5. 4’-(4-Di(4-methoxyphenyl)aminophenyl)-2,2':6',2''-terpyridine (6a)[85]

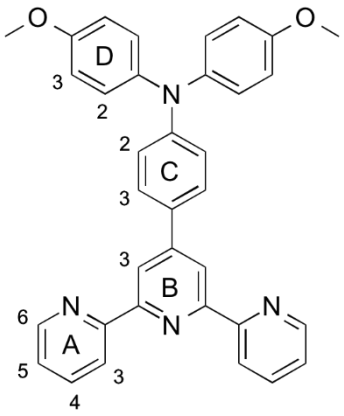

4'-(4-Bromophenyl)-2,2':6',2''-terpyridine (2.90 g, 7.47 mmol, 1.0 eq.) and 4,4'-dimethoxydiphenylamine (1.71 g, 7.47 mmol, 1.0 eq.) were suspended in toluene (60 mL) under argon and NaO^{t}Bu (0.933 g, 9.71 mmol, 1.3 eq.) was added. A suspension of $Pd(dba)_2$ (0.086 g, 0.149 mmol, 0.02 eq.) and $P(^tBu)_3$ (1 mol dm^{-3} solution in toluene, 0.149 mL, 0.20 mmol, 0.02 eq.) in toluene (4 mL) was made up under argon and added to the reaction mixture. The purple mixture was heated at 100 °C for 16 h under argon, and was then filtered hot. The solvent was removed from the filtrate under reduced pressure and the residue was suspended in EtOH (10 mL), filtered and washed with cold EtOH (20 mL). Recrystallization from EtOH yielded **6a** as pale brown solid (3.02 g, 75.3%).

^{1}H NMR (500 MHz, $CDCl_3$) δ / ppm 8.72 (ddd, *J*= 4.8, 1.7, 0.9 Hz, 2H, H^{A6}), 8.69 (s, 2H, H^{B3}), 8.66 (ddd, *J*= 8.0, 1.0, 1.0 Hz, 2H, H^{A3}), 7.89 – 7.84 (m, 2H, H^{A4})), 7.75 (d_{AB}, *J* = 8.8 Hz, 2H, H^{C2}), 7.34 (ddd, *J* = 7.5, 4.8, 1.2 Hz, 2H, H^{A5}), 7.11 (d_{AB}, *J* = 9.0 Hz, 4H, H^{D2}), 7.02 (d_{AB}, *J* = 8.8 Hz, 2H, H^{C3}), 6.87 (d_{AB}, *J*= 9.0 Hz, 4H, H^{D3}), 3.82 (s, 6H, H^{OMe}).

^{13}C NMR (126 MHz, $CDCl_3$) δ / ppm 156.6 (C^{A2}), 156.3 (C^{D4}), 155.9 (C^{B2}), 150.0 ($C^{C4/B4}$), 149.8 ($C^{B4/C4}$), 149.2 (C^{A6}), 140.6 (C^{D1}), 136.9 (C^{A4}), 129.8 (C^{C1}), 128.1 (C^{C2}), 127.1 (C^{D2}), 123.8 (C^{A5}), 121.5 (C^{A3}), 120.1 (C^{C3}), 118.1 (C^{B3}), 114.9 (C^{D3}), 55.6 (C^{OMe}).

MS (EI, m/z): 536.2 $[M]^+$ (calc.: 536.2), 521.2 $[M–Me]^+$ (calc.: 521.2).

UV-Vis (MeCN, 1.04 × 10^{-5} mol dm^{-3}) λ_{abs}/nm 240 (ε / dm^3 $mol^{-1}cm^{-1}$ 31800), 286 (38500), 354 (24700).

CV E^o / V (MeCN, [^{n}Bu$_4$N][PF_6], vs Fc/Fc^+): +1.00^{irr}, +0.42/+0.34^{qr}, –2.42^{irr}.

IR (ATR, $\tilde{\nu}$ / cm^{-1}): 3039 (w), 2950 (w), 2832 (w), 1700 (w), 1601 (m), 1582 (m), 1565 (m), 1501 (s), 1460 (m), 1440 (m), 1391 (m), 1322 (m), 1268 (m), 1236 (s), 1178 (w), 1167 (w), 1105 (m), 1034 (s), 989 (m), 892 (m), 826 (s), 789 (s), 737 (m), 658 (s), 621 (m).

3.7.6. $[Zn(1a)_2][PF_6]_2$ (1b)

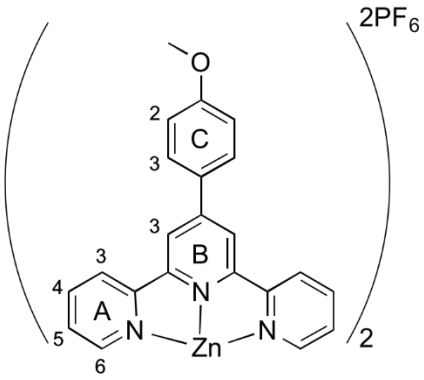

1a (100 mg, 0.295 mmol, 2.0 eq.) and zinc(II) acetate dihydrate (39.6 mg, 0.177 mmol, 1.2 eq.) were suspended in EtOH (5 mL) in a 25 cm^3 microwave vessel and heated in the microwave reactor for 1 h at 120 °C. Then an excess of NH_4PF_6 (aq.) was added, whereupon a colourless solid precipitated, which was filtered, washed with plenty of water and then dried on the frit. Finally, it was washed with Et_2O to yield the desired product as a colourless solid (88.0 mg, 0.085 mmol, 58%).

^{1}H NMR (500 MHz, CD_3CN) δ / ppm 8.93 (s, 4H, H^{B3}), 8.73 – 8.69 (m, 4H, H^{A3}), 8.20 (d_{AB}, *J* = 8.9 Hz, 4H, H^{C3}), 8.18 – 8.14 (m, 4H, H^{A4}), 7.82 (ddd, *J* = 5.1, 1.6, 0.8 Hz, 4H), 7.39 (ddd, *J* = 7.6, 5.1, 1.0 Hz, 4H, H^{A6}), 7.29 (d_{AB}, *J* = 8.9 Hz, 4H, H^{C2}), 3.97 (s, 6H, H^{OMe}).

ESI MS (m/z): 371.3 $[M\text{-}2PF_6]^{2+}$ (calc. 371.1), 887.4 $[M\text{-}PF_6]^+$ (calc. 887.2).

UV-Vis (MeCN, 1.00 × 10^{-5} mol dm^{-3}) λ_{abs}/nm 233 (ε / dm^3 $mol^{-1}cm^{-1}$ 53100), 255 (38500), 266 (43100), 282 (56600), 330 (52600), 339 (53500).

Found: C, 50.38, H, 3.47, N, 8.11; $C_{44}H_{34}F_{12}N_6O_2P_2Zn$ • 0.5 H_2O requires C, 50.66, H, 3.38, N, 8.06.

CV E^o / V (MeCN, $[^nBu_4N][PF_6]$, vs Fc/Fc^+): $+1.44^{irr}$, $–1.76^{irr}$, $-1.87/-1.92^{qr}$.

3.7.7. $[Zn(2a)_2][PF_6]_2$ (2b)

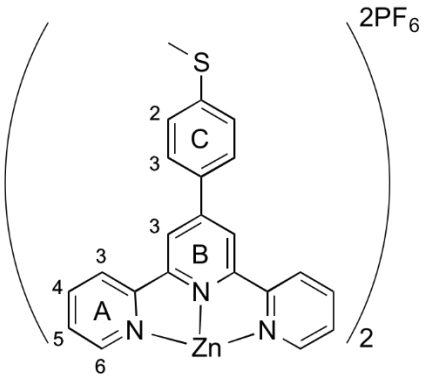

2a (100 mg, 0.281 mmol, 2.0 eq.) and zinc(II) acetate dihydrate (37.8 mg, 0.169 mmol, 1.2 eq.) were suspended in MeOH (5 mL) in a 25 cm^3 microwave vessel and heated in the mw reactor for 1 h at 120 °C. Then an excess of NH_4PF_6 (aq.) was added, whereupon a colourless solid precipitated, which was filtered off, washed with plenty of water and then dried on the frit. Finally, it was washed with Et_2O and dried under high vacuum to yield the desired product as slightly yellow solid (102 mg, 0.096 mmol, 69%).

^{1}H NMR (500 MHz, CD_3CN) δ / ppm 8.95 (s, 4H, H^{B3}), 8.73 – 8.68 (m, 4H, H^{A3}), 8.20 - 8.15 (m, 4H, H^{A4}), 8.14 (d_{AB}, J = 8.6 Hz, 4H, H^{C3}), 7.82 (ddd, *J* = 5.1, 1.6, 0.9 Hz, 4H, H^{A6}), 7.61 (d_{AB}, *J* = 8.6 Hz, 4H, H^{C2}), 7.39 (ddd, *J* = 7.6, 5.1, 1.0 Hz, 4H, H^{A5}), 2.64 (s, 6H, H^{OMe}).

ESI MS (m/z): 387.2 $[M\text{-}2PF_6]^{2+}$ (calc. 387.1), 919.3 $[M\text{-}PF_6]^+$ (calc. 919.1).

UV-Vis (MeCN, 1.00 × 10^{-5} mol dm^{-3}) λ_{abs}/nm 236 (ε / dm^3 $mol^{-1}cm^{-1}$ 61900), 267 (39600), 283 (50000), 332 sh (43200), 343 (46600), 361 sh (36900).

Found: C, 48.64, H, 3.23, N, 7.55; $C_{44}H_{34}F_{12}N_6P_2S_2Zn$ • 1 H_2O requires C, 48.74, H, 3.35, N, 7.75.

CV E^o / V (MeCN, $[^nBu_4N][PF_6]$, vs Fc/Fc^+): $+1.82^{irr}$, $+1.28^{irr}$, $–2.35^{irr}$, -2.73^{irr}, -2.85^{irr}.

3.7.8. $[Zn(3a)_2][PF_6]_2$ (3b)

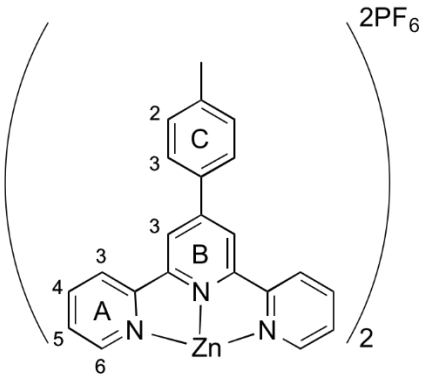

3a (200 mg, 0.618 mmol, 2.0 eq.) and zinc(II) acetate dihydrate (81.4 mg, 0.371 mmol, 1.2 eq.) were suspended in MeOH (10 mL) in a 25 cm^3 microwave vessel and heated in the microwave reactor for 1 h at 120 °C. Then an excess of NH_4PF_6 (aq.) was added, whereupon a colourless solid precipitated and the suspension was stirred for 10 min, then water (30 mL) was added. The solid was filtered off, washed with plenty of water, dried on the frit and then washed with Et_2O to yield the desired product as a colourless solid (285 mg, 0.284 mmol, 92%).

NMR spectroscopic data agree with literature data.[86]

ESI MS (m/z): 355.2 $[M\text{-}2PF_6]^{2+}$ (calc. 355.1), 855.3 $[M\text{-}PF_6]^+$ (calc. 855.2).

UV-Vis (MeCN, 1.00 × 10^{-5} mol dm^{-3}) λ_{abs}/nm 229 (ε / dm^3 $mol^{-1}cm^{-1}$ 49900), 253 (36300), 269 sh (43000), 380 sh (57700), 284 (62000), 314 (43700), 323 (42800), 338 (31700).

CV E^o / V (MeCN, $[^nBu_4N][PF_6]$, vs Fc/Fc^+): –2.47/2.62^{qr}, -2.96^{irr}.

3.7.9. [Zn(4a)$_2$][(PF$_6$]$_2$ (4b)

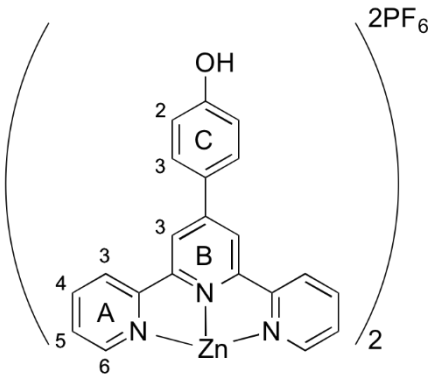

4a (200 mg, 0.615 mmol, 2.0 eq.) and zinc(II) acetate dihydrate (81.0 mg, 0.369 mmol, 1.2 eq.) were suspended in MeOH (10 mL) in a 25 cm^3 microwave vessel and heated in the microwave reactor for 1 h at 120 °C. Then an excess of NH_4PF_6 (aq.) was added, whereupon a colourless solid precipitated and the suspension was stirred for 10 min, then water (30 mL) was added. The solid was filtered off, washed with plenty of water, dried on the frit and then washed with Et_2O to yield the product as a colourless solid (277 mg, 0.275 mmol, 90%).

^{1}H NMR (250 MHz, CD_3CN) δ / ppm 8.90 (s, 4H, H^{B3}), 8.70 (d, *J* = 8.1 Hz, 4H, H^{A3}), 8.25 – 8.04 (m, 8H, H^{A4} & H^{C3}), 7.82 (d, *J* = 4.7 Hz, 4H, H^{A6}), 7.52 – 7.28 (m, 4H, H^{A5}), 7.16 (d, *J* = 8.6 Hz, 4H, H^{C2}).

ESI MS (m/z): 357.2 $[M\text{-}2PF_6]^{2+}$ (calc. 357.1), 859.3 $[M\text{-}PF_6]^+$ (calc. 859.1).

UV-Vis (MeCN, 1.00 × 10^{-5} mol dm^{-3}) λ_{abs}/nm 232 (ε / dm^3 mol^{-1}cm^{-1} 54400), 253 (33300), 265 (34200), 283 (50200), 284 (62000), 318 sh (43800), 329 (52300), 338 (52300).

3.7.10. $[Zn(5a)_2][PF_6]_2$ (5b)[87]

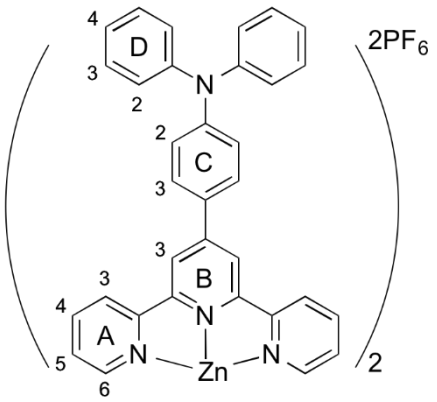

5a (100 mg, 0.210 mmol, 2.0 eq.) and zinc acetate dihydrate (28.2 mg, 0.126 mmol, 1.2 eq.) were suspended in EtOH (5 mL) and the mixture was heated in a microwave reactor for 1 h at 120 °C. The precipitate that formed was dissolved in EtOH (150 mL) and then an excess of aqueous NH_4PF_6 and water (50 mL) was added and an orange precipitate formed. This was separated by filtration, washed with H_2O and Et_2O, and then redissolved in MeCN (20 mL). After removal of solvent under reduced pressure, the desired product was isolated as an orange solid (134 mg, 0.102 mmol, 98%).

^{1}H NMR (500 MHz, CD_3CN) δ / ppm 8.89 (s, 4H, H^{B3}), 8.68 (ddd, *J* = 8.0, 0.9, 0.9 Hz, 4H, H^{A3}), 8.14 (td, *J* = 7.8, 1.6 Hz, 4H, H^{A4}), 8.09 (d_{AB}, *J* = 8.9 Hz, 4H, H^{C2}), 7.81 (ddd, *J* = 5.1, 1.5, 0.8 Hz, 4H, H^{A6}), 7.47 – 7.41 (m, 8H, H^{D3}), 7.40 – 7.36 (m, 4H, H^{A5}), 7.27 – 7.24 (m, 12H, H^{D2} & H^{D4}), 7.22 (d_{AB}, *J* = 8.8 Hz, 4H, H^{C3}).
^{13}C NMR (126 MHz, CD_3CN) δ / ppm 156.3 (C^{B4}), 152.0 (C^{C4}), 150.6 (C^{B2}), 149.0 (C^{A2}), 148.8 (C^{A6}), 147.6 (C^{D1}), 142.1 (C^{A4}), 130.8 (C^{D3}), 130.0 (C^{C2}), 128.4 (C^{C1}), 128.3 (C^{A5}), 126.9 (C^{D2}), 125.8 (C^{D4}), 124.0 (C^{A3}), 121.8 (C^{C3}), 121.0 (C^{B3}).
ESI-MS (m/z) 508.2 $[M - 2PF_6]^{2+}$ (calc. 508.2).
UV-VIS (MeCN, 3.0×10^{-6} mol dm^{-3}) λ_{abs}/nm 205 (ε / $dm^3\,mol^{-1}\,cm^{-1}$ 171000), 243 (70900), 259 (63700), 284 (73100), 311 sh (48700), 325 (43200), 407 (49100).
Found: C, 57.49, H, 3.92, N, 8.27; $C_{66}H_{48}F_{12}N_8P_2Zn \bullet 4H_2O$ requires C, 57.42, H, 4.09, N, 8.12.
CV E^o / V (MeCN, $[^nBu_4N][PF_6]$, vs Fc/Fc^+): $+0.78/+0.70^{qr}$, $–2.42/–2.35^{qr}$.

Found: C, 57.49, H, 3.92, N, 8.27; $C_{66}H_{48}F_{12}N_8P_2Zn.4H_2O$ requires C, 57.42, H, 4.09, N, 8.12.

IR (ATR, $\tilde{\nu}$ / cm^{-1}): 3066 (w), 1584 (m), 1572 (w), 1544 (w), 1516 (m), 1489 (m), 1471 (m), 1414 (m), 1363 (w), 1331 (m), 1262 (w), 1244 (w), 1201 (m), 1163 (w), 1116 (w), 1076 (w), 1024 (w), 1015 (w), 830 (s), 789 (s), 757 (m), 732 (m), 695 (s), 688 (s), 659 (m).

3.7.11. [Zn(6a)$_2$][PF$_6$]$_2$ (6b)

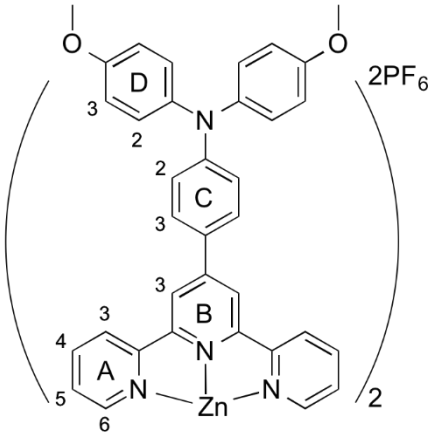

6a (100 mg, 0.186 mmol, 2.0 eq.) and zinc(II) acetate dihydrate (24.5 mg, 0.112 mmol, 1.2 eq.) were suspended in EtOH (5 mL) and the mixture was heated in a microwave reactor for 1 h at 120 °C. The precipitate that formed was dissolved in EtOH (150 mL) and then an excess of aqueous NH_4PF_6 and water (50 mL) was added and an orange precipitate formed. This was separated by filtration, washed with H_2O and Et_2O, and then redissolved in MeCN (20 mL). Solvent was removed under reduced pressure to give an orange glassy solid. This was dissolved in CH_2Cl_2 (20 mL) and then toluene (10 mL) was added. The solvents were evaporated under reduced pressure and the desired product was isolated as an orange solid (130 mg, 0.102 mmol, 98%).

^{1}H NMR (500 MHz, CD_3CN) δ / ppm 8.85 (s, 4H, H^{B3}), 8.66 (dt, *J* = 8.3, 0.8 Hz, 4H, H^{A3}), 8.13 (td, *J* = 7.9, 1.6 Hz, 4H, H^{A4}), 8.03 (d_{AB}, *J* = 9.0 Hz, 4H, H^{C2}), 7.79 (ddd, *J* = 5.1, 1.5, 0.8 Hz, 4H, H^{A6}), 7.38 – 7.34 (m, 4H, H^{A5}), 7.24 (d_{AB}, *J* = 9.0 Hz, 8H, H^{D2}), 7.03 – 6.99 (m, 12H, H^{D3} & H^{C3}), 3.83 (s, 12H, H^{OMe}).
^{13}C NMR (126 MHz, CD_3CN) δ / ppm 158.5 (C^{D4}), 156.5 ($C^{B4/C4}$), 153.1 ($C^{B4/C4}$), 150.5 (C^{A2}), 149.2 (C^{B2}), 148.9 (C^{A6}), 142.1 (C^{A4}), 140.2 (C^{D1}), 129.9 (C^{C2}), 129.2 (C^{D2}), 128.3 (C^{A5}), 126.2 (C^{C1}), 123.9 (C^{A3}), 120.6 (C^{B3}), 118.6 (C^{C3}), 116.1 (C^{D3}), 56.2 (C^{OMe}).
ESI-MS (m/z) 568.2 $[M - 2PF_6]^{2+}$ (calc. 568.2), 537.3 [**6a** + H]$^+$ (base peak, calc. 537.2).
UV-VIS (MeCN, 3.0 × 10^{-6} mol dm^{-3}) λ_{abs} / nm 231 (ε / dm^3 mol^{-1} cm^{-1} 65200), 283 (71000), 313 sh (49700), 325 (44200), 420 (48300).

Found: C, 57.41; H, 4.13; N, 7.65; $C_{70}H_{56}F_{12}N_8O_4P_2Zn \bullet 2H_2O$ requires C, 57.52; H, 4.24; N,7.78.

CV E^o / V (MeCN, [^{n}Bu$_4$N][PF$_6$], vs Fc/Fc$^+$) +1.03^{irr}, +0.49/+0.40^{qr}, –2.44^{irr}.

IR (ATR, $\tilde{\nu}$ / cm^{-1}): 1700 (w), 1595 (m), 1572 (w), 1502 (s), 1474 (m), 1465 (w), 1437 (w), 1418 (w), 1366 (w), 1325 (w), 1285 (w), 1237 (s), 1198 (w), 1162 (w), 1106 (w), 1069 (w), 1015 (w), 824 (s), 788 (s), 744 (w), 730 (s), 667 (w), 659 (s), 639 (w).

Part 2

Chapter 4

Part 2: Zinc complexes as dyes in DSCs

Chapter 4: Zinc complexes in DSCs

As already known from the previous chapter, the absorption behaviour of Zn(II) complexes is mainly ligand dependent. The homoleptic complexes **5b** and **6b** (Scheme 4-1) show electronic absorption bands in the visible range and are therefore interesting candidates to be tested in dye sensitized solar cells (DSCs). These two complexes were synthesized using the first generation (G1) ligands **5a** and **6a**. Figure 4-1 shows the absorption spectra of **5b** and **6b**.

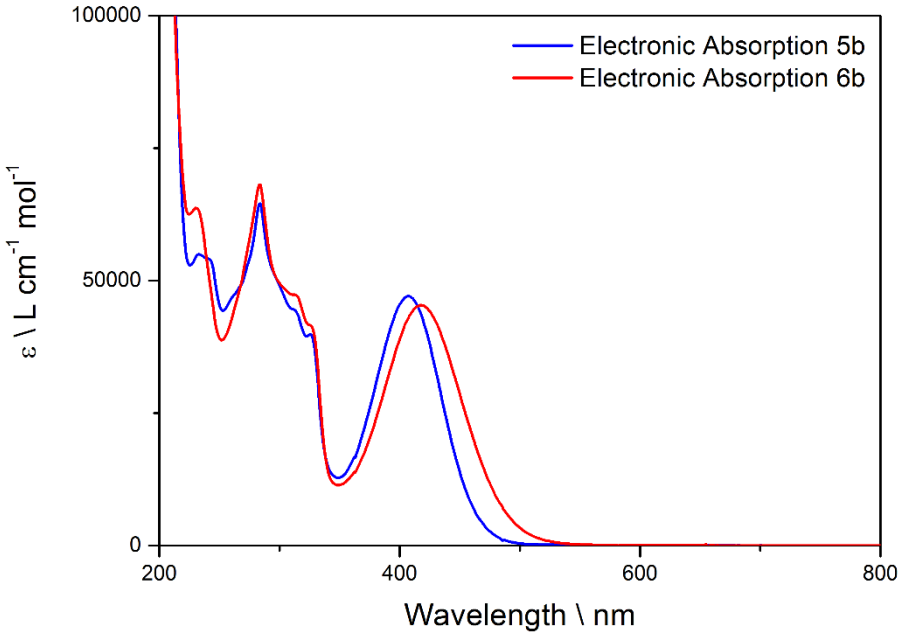

*Figure 4-1: Electronic absorption spectra (MeCN, 1 × 10^{-5} M) of **5b** (blue) and **6b** (red).*

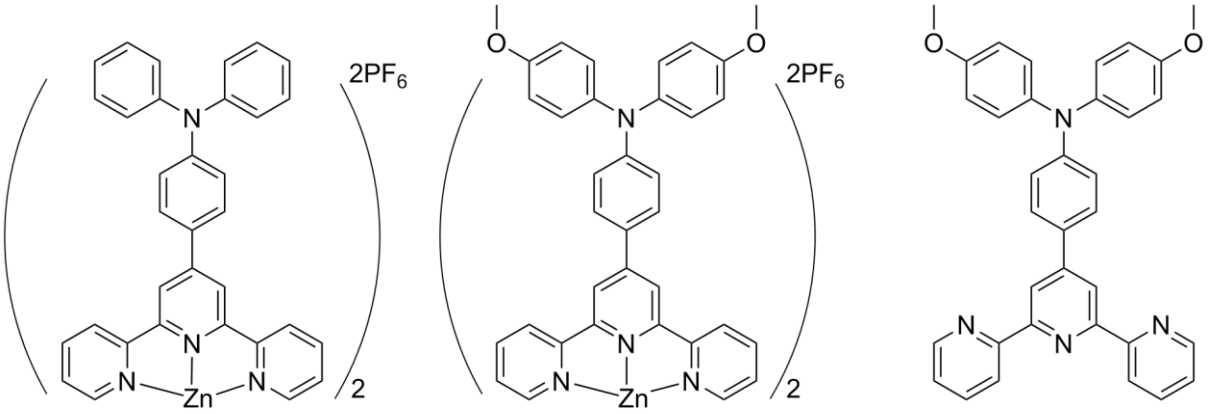

5b **6b** **6a**

*Scheme 4-1: Chemical structure of complexes **5b**, **6b** and ligand **6a**.*

It can clearly be seen that the complexes exhibit high energy transitions as well as the ILCT bands with maxima at 407 nm and 420 nm, respectively. They extend nicely into the visible region, which is very important, since an efficient dye should cover as much of the solar spectrum as possible. To possibly further expand the absorption into the red region, a second generation (G2) ligand was synthesized (Scheme 4-2).

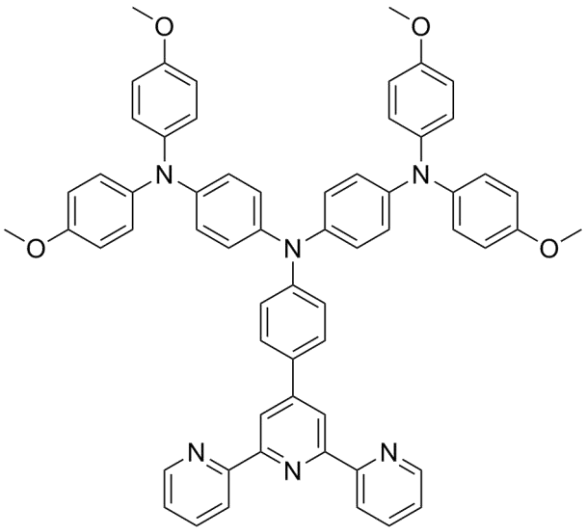

7

*Scheme 4-2: Second-generation (G2) ligand **7**.*

To attach the dyes on the semiconductor surface a functional group is needed which is able to interact with the surface in a way that it anchors the dye to the surface. Very frequently used anchoring groups are hydroxyl, carboxylate or phosphonate groups. To reach high charge injection efficiencies it is important to have groups such as these. Carboxylate and phosphonate groups in particular have been shown, via studies with a variety of Ru and Cu dyes, to be effective anchors.[88][60]
Anchoring ligands (**8**, **9** and **10**) were therefore selected for the investigation of **5b** and **6b** (Scheme 4-3).

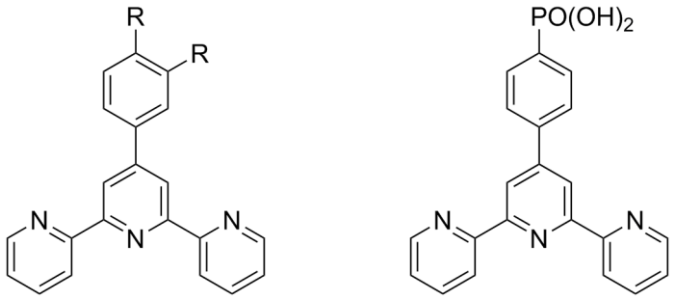

8 R = CO_2H
9 R = OH

10

*Scheme 4-3: The used anchoring ligands **8**, **9** and **10**.*

In the case of ruthenium sensitizers it is possible to synthesize heteroleptic dyes directly, because Ru(II) tris-chelate complexes show very high stability constants. In the case of zinc(II) bis-terpyridine complexes, on the other hand, the synthesis of heteroleptic complexes is not trivial. Therefore a method was used to attach the dye on the surface, which was developed in our group for copper based dye sensitized solar cells.[89][90]

4.1. Classical approach

The classical approach that was developed in our group[89][90] is based on the lability of copper(I) complexes.[91] An electrode consisting of a semiconductor layer on a conducting glass plate is immersed in a solution of an anchoring ligand (AL) for a certain amount of time. In a second step the electrode with the anchoring ligand attached to the surface is immersed into a solution of a homoleptic copper(I) complex. Due to the lability of the homoleptic complex $[CuL_2]^+$, a ligand exchange reaction takes place immediately, leading to a heteroleptic Cu(I) complex on the surface $[CuL(AL)]^+$. This approach is very straightforward, since the ligand exchange is very fast. On the other hand, it demands the prior synthesis of the homoleptic complex and the exchange process always leaves one ligand "unused" (Figure 4-2).

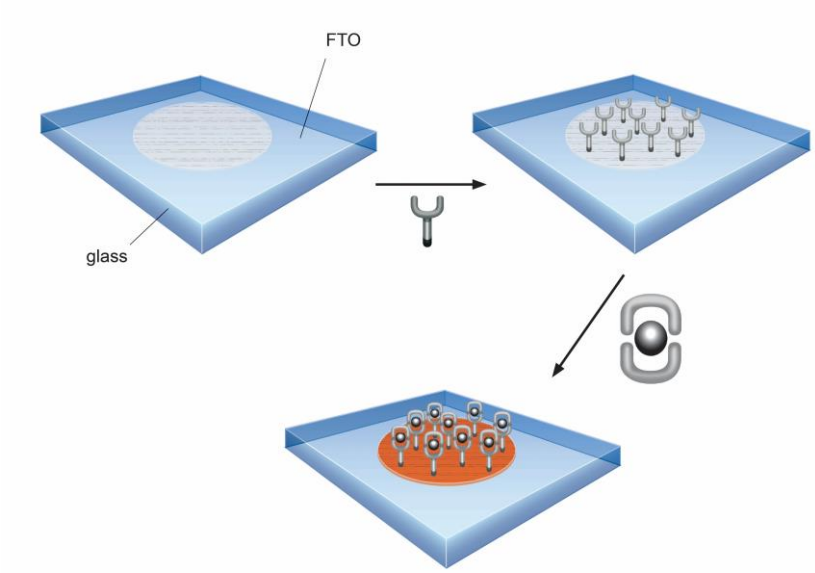

Figure 4-2: Schematic representation of the classical approach (Illustrated by Danielle Hayoz).

This method works as well for the zinc(II) bis-terpyridine complexes discussed in this chapter, but it is by far not ideal. These zinc complexes are much less labile than the copper complexes and the ligand exchange reaction therefore takes much longer. This behaviour was studied in a proton NMR experiment. Scheme 4-4 shows the ligands with which the homoleptic Zn(II) bis-terpyridine model compounds were synthesized.

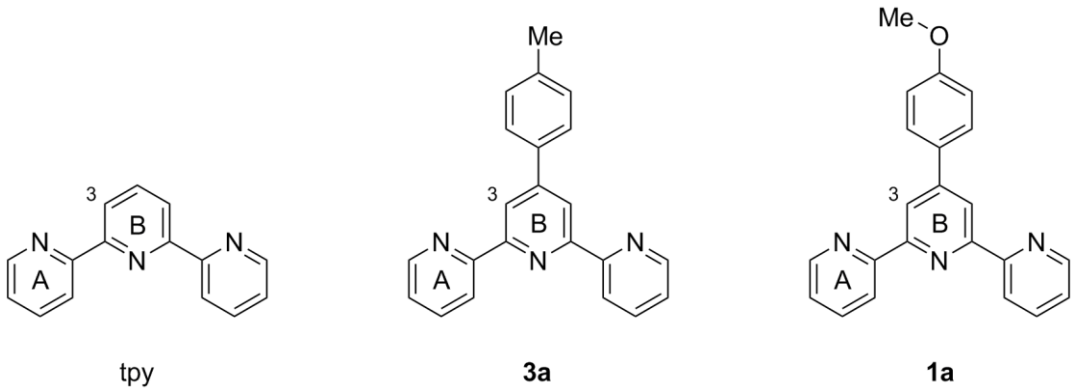

Scheme 4-4: Ligands used to synthesize homoleptic Zn(II) complexes for the NMR experiment.

For the NMR experiment the following complexes were used: $[Zn(tpy)_2][PF_6]_2$, $[Zn(\mathbf{3a})_2][PF_6]_2$, $[Zn(\mathbf{1a})_2][PF_6]_2$. An NMR sample of the same concentration (≈ 10^{-3} M) in MeCN-*d3* of each compound was prepared and a 500 MHz proton NMR was recorded.

Figure 4-3 shows the NMR spectra of $[Zn(\mathbf{3a})_2][PF_6]_2$, $[Zn(\mathbf{1a})_2][PF_6]_2$ and at the bottom a spectrum of a 1:1 mixture of the two compounds after standing for 1 h at room temperature.

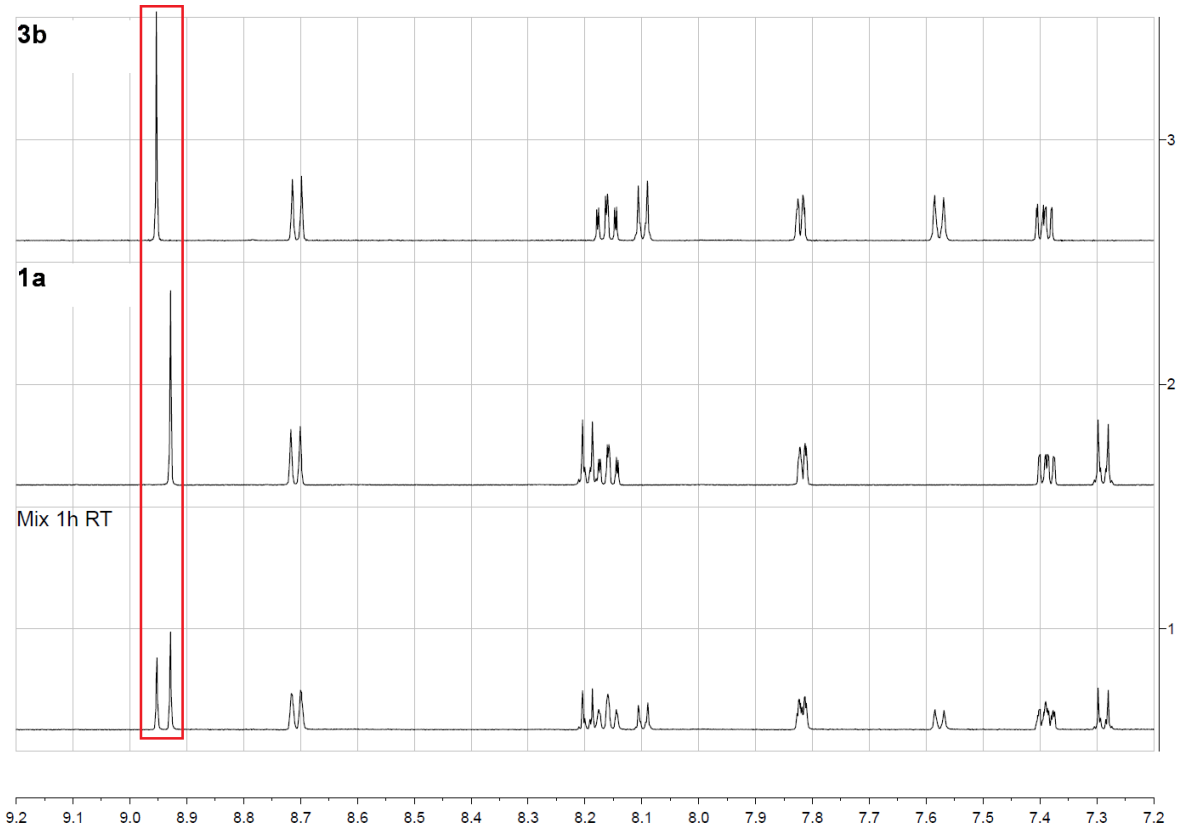

Figure 4-3: NMR spectra of $[Zn(\mathbf{3a})_2][PF_6]_2$ and $[Zn(\mathbf{1a})_2][PF_6]_2$ and the mixture of the two after 1 h at RT (500 MHz, MeCN-d3).

At first sight, it looks like a simple mixture of the two compounds, since no change in chemical shifts or extra peaks are observed. In an expansion (Figure 4-4) of the H^{B3} proton signals of the mixture it can be seen that each peak arising from the H^{B3} protons, shows small split-ups, which suggests that ligand exchange is indeed taking place.

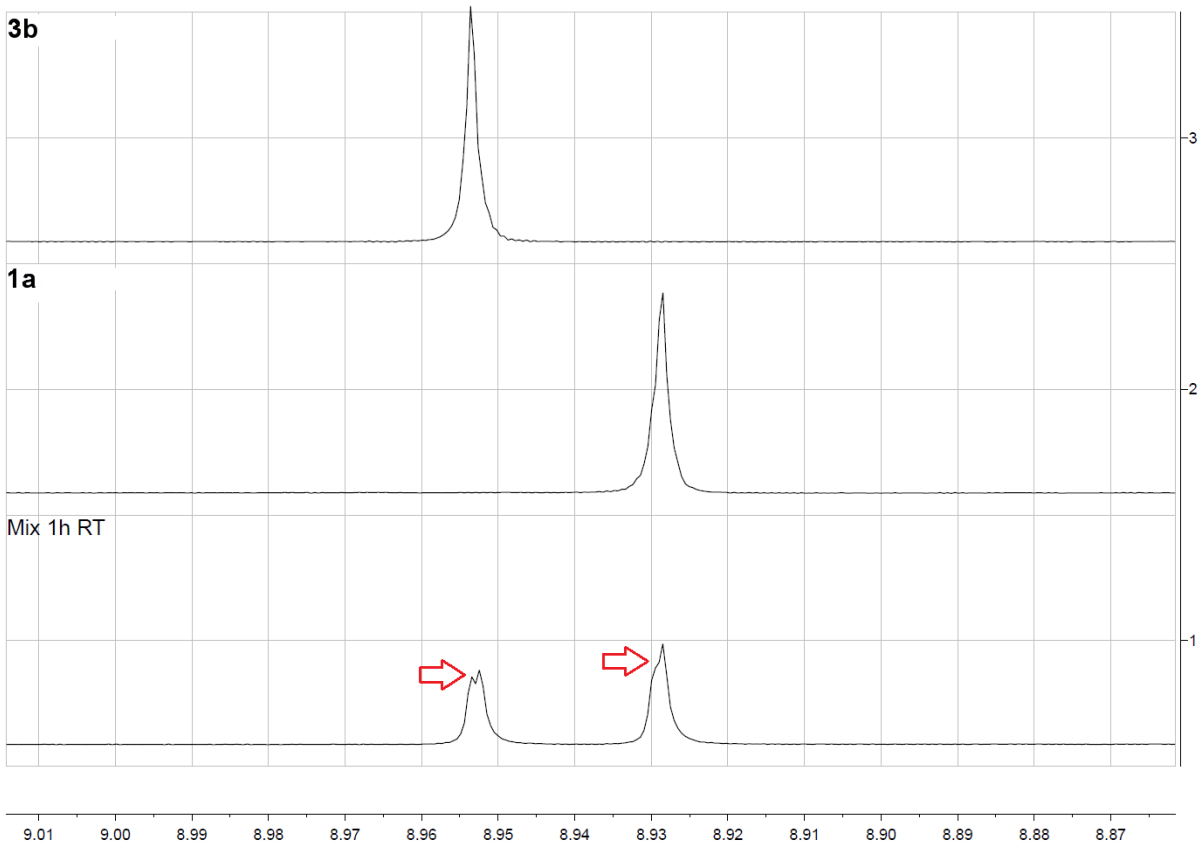

Figure 4-4: Expansion of the H^{B3} protons of of $[Zn(\mathbf{3a})_2][PF_6]_2$ and $[Zn(\mathbf{1a})_2][PF_6]_2$ and the mixture of the two after 1 h at RT (500 MHz, MeCN-d3).

Although this seems to prove the theory of a slower ligand exchange it is not entirely satisfying. Therefore a second NMR experiment was performed, this time with the pair of compounds $[Zn(tpy)_2][PF_6]_2$ and $[Zn(\mathbf{1a})_2][PF_6]_2$. The H^{B3} proton of $[Zn(tpy)_2][PF_6]_2$ has a different chemical shift than the H^{B3} proton of $[Zn(\mathbf{3a})_2][PF_6]_2$, which hopefully makes the observation of the ligand exchange easier to monitor than in the previous experiment. The top two spectra in Figure 4-5 are of the two pure samples. From bottom to top the spectra of the 1:1 mixture of the two compounds after standing for periods of 15 min to 29 h at room temperature are shown.

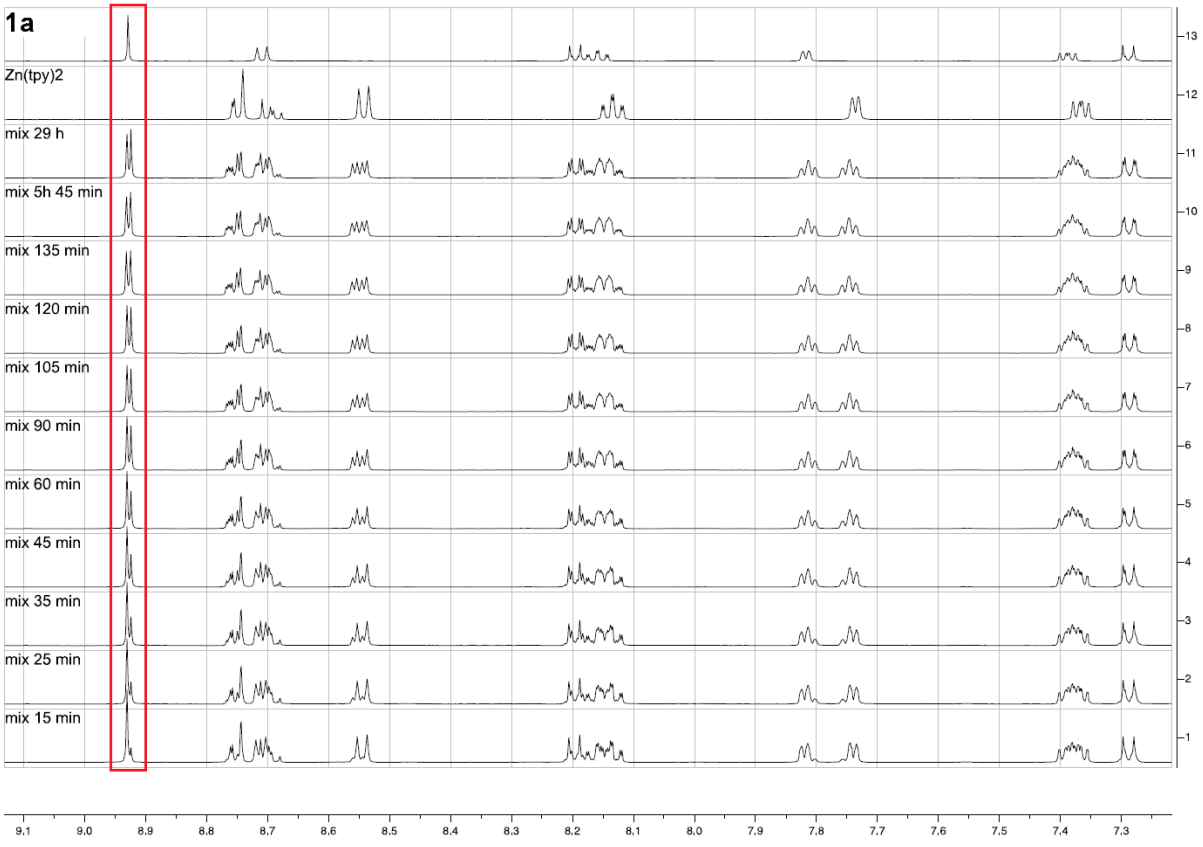

Figure 4-5: NMR spectra of $[Zn(tpy)_2][PF_6]_2$ and $[Zn(\mathbf{1a})_2][PF_6]_2$ and the mixture of the two after periods of 15 min to 29 h at RT (500 MHz, MeCN-d3).

It is easily seen that this experiment also supports ligand exchange and Figure 4-6 provides better insight into the interesting region around the signals for the two H^{B3} protons. One can nicely see how the original H^{B3} proton signal at 8.93 ppm decreases and a new signal at 8.92 ppm arises; this new signal belongs to the heteroleptic complex [(**1a**)Zn(tpy)][PF_6]$_2$. After approximately 2 h an equilibrium between the three compounds is established. Compared to the copper complexes, which exchange immediately, 2 h are a quite long time, therefore a new strategy was developed for the zinc dyes.[60]

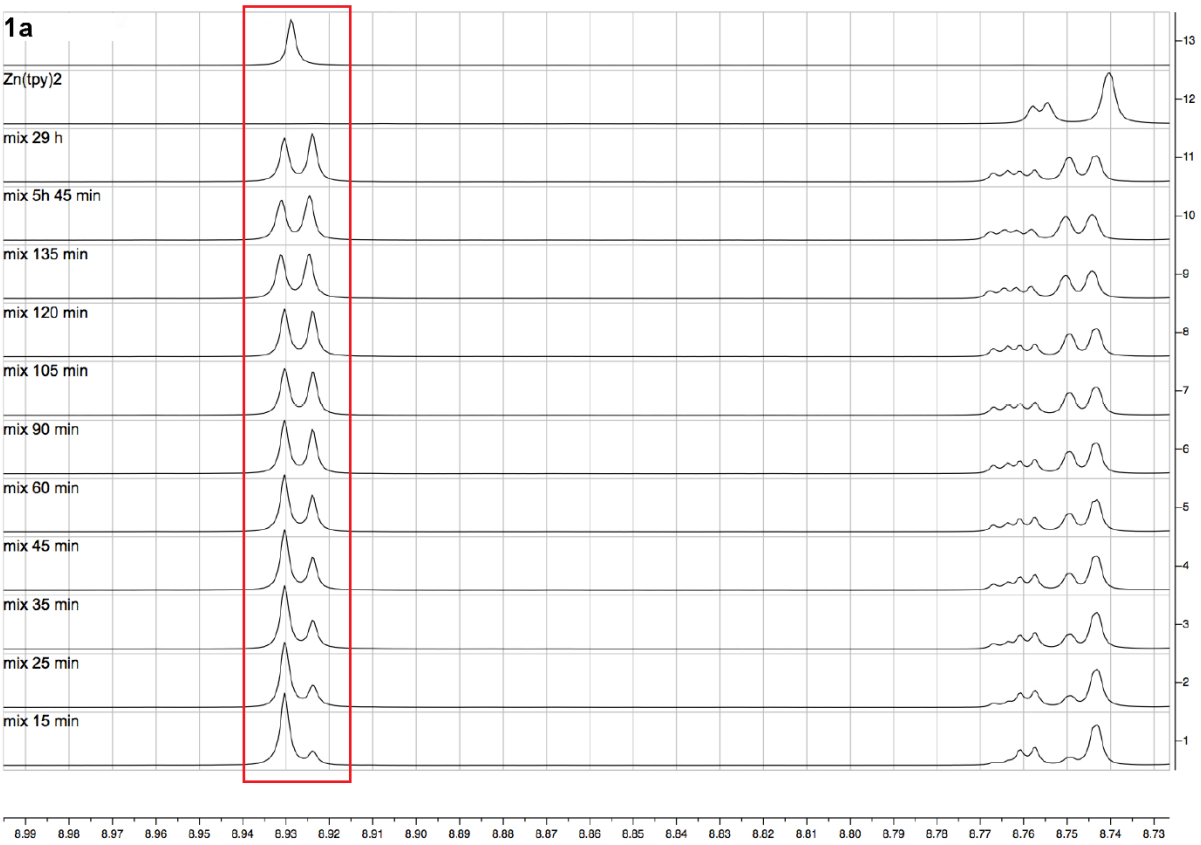

Figure 4-6: Expansion of the region for signals for the H^{B3} protons of of $[Zn(tpy)_2][PF_6]_2$ and $[Zn(\mathbf{1a})_2][PF_6]_2$ and the mixture of the two after periods of 15 min to 29 h at RT (500 MHz, MeCN-d3).

4.2. Step-wise approach

As the title indicates, the method of DSC dye assembly is based on a step-wise protocol. This protocol also starts with an electrode consisting of a semiconductor layer on a conducting glass plate, which is immersed in a solution of an anchoring ligand. It is then immersed in a solution of a zinc(II) salt. The soluble zinc(II) salts choosen were $Zn(OAc)_2$ dihydrate and $ZnCl_2$. This probably leads to the formation of a first neutral, heteroleptic complex consisting of the anchoring ligand, the metal centre and the acetates or chlorides. After 24 h, the electrode is put into a solution of the ancillary ligand (CL). In this final step the octahedral bis-terpyridine complex $[(AL)Zn(CL)]X_2$ is formed, either with acetate or chloride counter anion (X), depending on which was used in the second step (Figure 4-7).

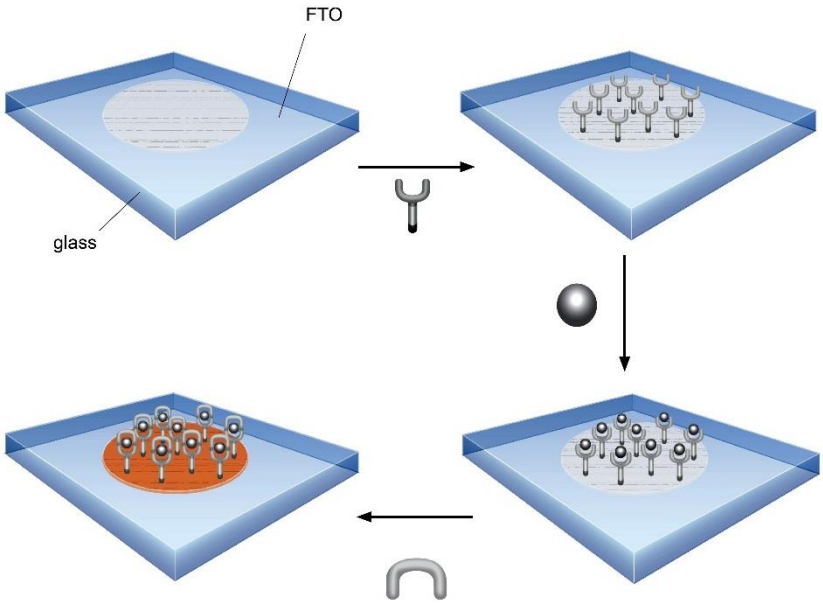

Figure 4-7: Schematic representation of the step-wise approach (Illustrated by Danielle Hayoz).

4.3. Results and discussion

4.3.1. First generation (G1) dyes based on ancillary ligands 5a and 6a

4.3.1.1. Solid state electronic absorption

Before the cells were sealed, electronic absorption spectra were recorded of ligands **8**, **9** and **10** (Scheme 4-3) anchored on the TiO_2 surface, after treatment with $Zn(OAc)_2$ dihydrate or $ZnCl_2$ and ancillary ligand **6a**. In Figure 4-8 the spectra are named in the following way: $[(AL)Zn(CL)]X_2$, where the counter ion also stands for the zinc salt that was used in the second step of the cell dyeing process (Figure 4-7).

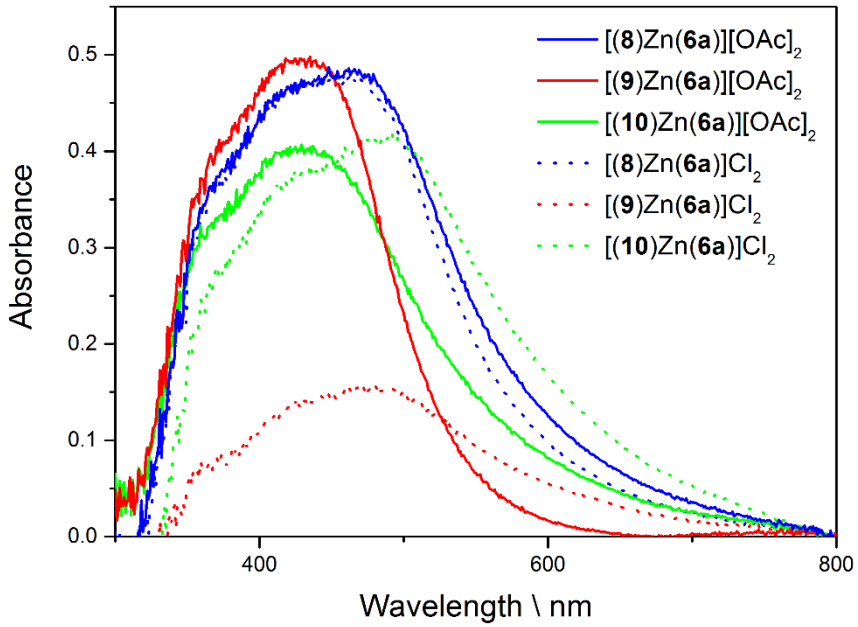

Figure 4-8: Solid electronic absorption spectra of TiO_2 anchored dyes of the scheme: $[(AL)Zn(CL)][AI]_2$.

It is not easy to obtain unambiguous information from the solid absorption spectra, since they are not related to the dye content on the semiconductor surface. All spectra show broad absorptions between 320 nm and 750 nm, except for dye [(**9**)Zn(**6a**)][OAc]$_2$, which absorbs from 320 nm to 650 nm.

4.3.1.2. Solar cell measurements

DSC efficiencies are shown in Table 4-1. They were measured two days and seven days after the sealing, without cell masking[92].

Comparing the data in Table 4-1 suggests that the system [(**8**)Zn(**5a**)]Cl_2 works most efficiently. It shows 0.71% percent efficiency, 7 days after sealing of the cell, this corresponds to a 9.7% efficiency compared to the N719 reference cell. [(**9**)Zn(**6a**)][OAc]$_2$ shows the highest fill factor of 68%, 7 days after sealing. The highest open circuit voltage of 571 mV was measured for the cell [(**8**)Zn(**5a**)]Cl_2 2 days after sealing of the cell. Although the system [(**8**)Zn(**5a**)]Cl_2 showed the highest efficiency, the differences between the measured values of the cells are not significant enough to allow one to draw clear conclusions. Nevertheless it is a proof of principle and leaves room for improvements.

Zinc(II) salt	Ancillary ligand	Anchoring ligand	J_{SC} \ A cm^{-2}	V_{OC} \ mV	FF \ %	η \ %	η rel. to N719 \ %
			2 days after sealing of the cells				
$Zn(OAc)_2$	**5a**	**8**	0.002	545	49	0.55	7.54
$ZnCl_2$	**5a**	**8**	0.002	527	55	0.68	9.33
$Zn(OAc)_2$	**6a**	**8**	0.002	555	61	0.54	7.41
$ZnCl_2$	**6a**	**8**	0.001	498	63	0.46	6.31
$Zn(OAc)_2$	**6a**	**9**	0.001	**571**	66	0.53	7.27
$ZnCl_2$	**6a**	**9**	0.001	458	58	0.33	4.53
$ZnCl_2$	**6a**	**10**	0.002	530	62	0.63	8.64
			7 days after sealing of the cells				
$Zn(OAc)_2$	**5a**	**8**	0.002	538	52	0.59	8.09
$ZnCl_2$	**5a**	**8**	0.003	546	52	**0.71**	**9.74**
$Zn(OAc)_2$	**6a**	**8**	0.002	544	66	0.56	7.68
$ZnCl_2$	**6a**	**8**	0.001	521	64	0.46	6.31
$Zn(OAc)_2$	**6a**	**9**	0.001	529	**68**	0.41	5.62
$ZnCl_2$	**6a**	**9**	0.001	521	54	0.34	4.66
$ZnCl_2$	**6a**	**10**	0.002	536	61	0.55	7.54
			Standard dye				
	N719		0.018	718	58	7.29	100

Table 4-1: Summary of measured solar cell properties, 2 days and 7 days after sealing.

4.3.2. Second generation (G2) dyes based on ancillary ligand 7

4.3.2.1. Solid state electronic absorption

Figure 4-9 shows the electronic absorption spectra of the dyes containing ancillary ligand **7** (Scheme 4-2) in combination with anchoring ligands **8** and **10** (Scheme 4-3). Comparing these measurements to the ones discussed in section 4.3.1.1 reveals that expansion of the absorption into the red region of the spectrum has failed. Taking into account that the absorption intensity is not the same for the dyes containing ancillary ligands **6a** (Scheme 4-1) and **7**, it seems that the absorption range of all four measurements is more or less the same. It is difficult to draw clear conclusions about this fact, but one explanation could be that the Ph_2N-arene rings introduced in **7** are twisted with respect to the plane of the adjacent arene rings, relieving proton-proton repulsion between the adjacent rings. Therefore the extended conjugation is not established as planned[93].

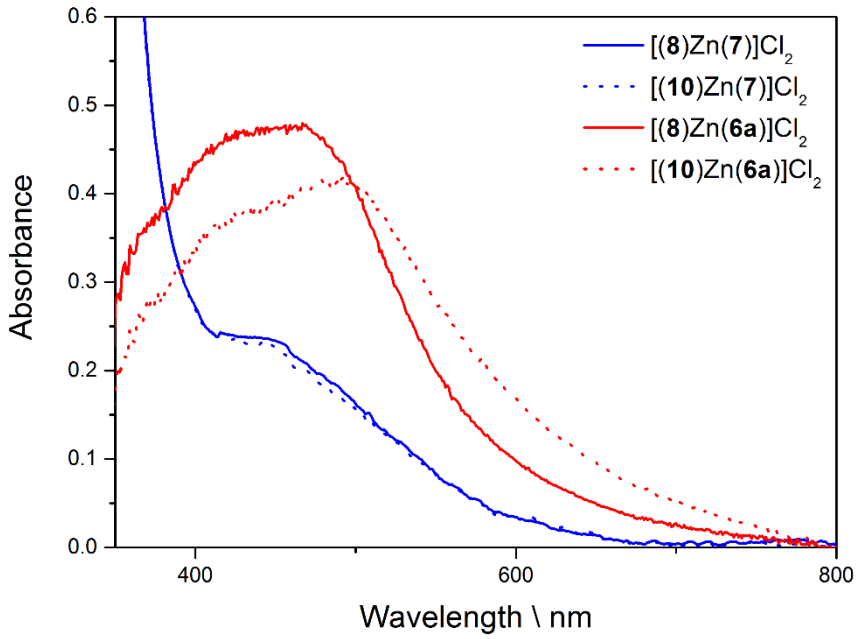

*Figure 4-9: Solid state electronic absorption spectra of [(**8**)Zn(**7**)]Cl_2 (solid blue), [(**10**)Zn(**7**)]Cl_2 (dotted blue), [(**8**)Zn(**6a**)]Cl_2 (solid red) and [(**10**)Zn(**6a**)]Cl_2 (dotted red).*

4.3.2.2. Solution electronic absorption

A comparison of the solution electronic absorption spectrum of **7** with spectra of **5a** and **6a**, shows that the extension of the π–system slightly extends the absorption to the red region. The extended conjugation of **7** also manifests itself in the higher extinction coefficients (ε). Nevertheless, since these kinds of compounds tend to show solvatochromic effects and the compounds were not measured in the same solvent, this observation is speculative.

The maxima in the spectrum of **7** can be attributed to π*←π and π*←n transitions within the ligand.[78] Using the formula introduced in the previous chapter, the optical HOMO-LUMO gap was calculated to be 2.53 eV.

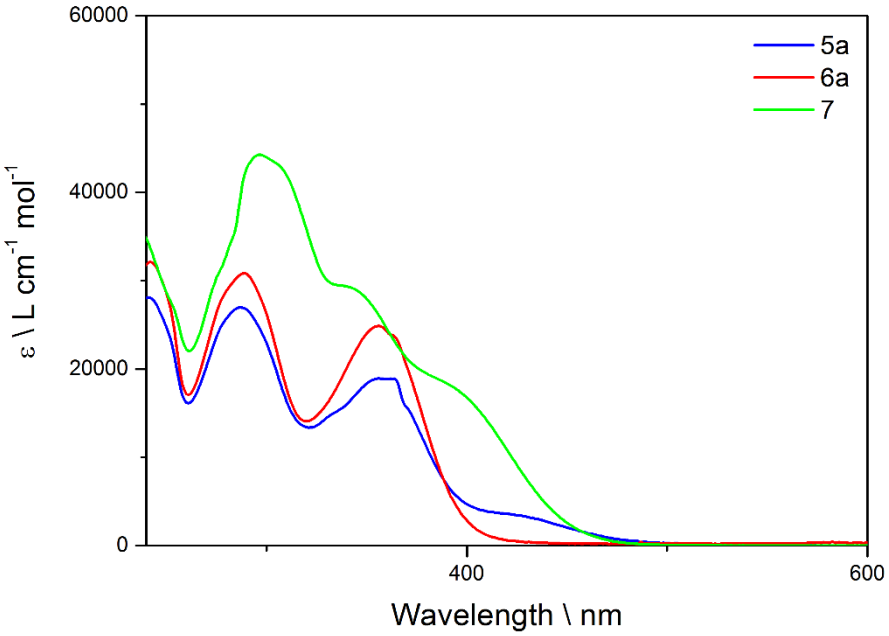

*Figure 4-10: Electronic absorption spectra of **5a** and **6a** in MeCN and **7** in THF.*

4.3.2.3. Solar cell measurements

The cells were measured on the assembly day, 3 days and 10 days after, while masked, to avoid false values because of scattered light[92] (average measured area: 0.06012 cm^2). The J_{SC}, V_{OC}, fill factor and efficiency are close to constant throughout the measuring period. Also the identical cells behave in a consistent way. In general all the cells show a very low efficiency: the cell with dye [(**10**)Zn(**7**)]Cl_2 shows the highest efficiency, 3 and 10 days after the sealing of the cell. It also shows the highest measured fill factor of 70% 10 days after sealing.

The fill factors of all cells lie around 70% which is good. The same dye exhibits the highest values for J_{SC} of 0.82 mA/cm^2 on the day of sealing and V_{OC} of 427 mV, 3 days after sealing, respectively. A summary of all the measured values can be found in Table 4-2. A comparison of the measured cell parameters, shown in Table 4-1 and Table 4-2 reveals certain differences, mainly lower J_{SC} values in the measurements for cells containing ancillary ligand **7**, which also influence the cell efficiency. The lower J_{SC} values can most probably be attributed to the fact that these cells were made from commercially available electrodes.

Anchored dye	J_{SC} \ mA cm^{-2}	V_{OC} \ mV	FF \ %	η \ %	η rel. to N719 \ %
Day of sealing of the cells					
[(**8**)Zn(**7**)]Cl_2 1	0.53	380	67	0.14	1.82
[(**8**)Zn(**7**)]Cl_2 2	0.55	375	68	0.14	1.82
[(**10**)Zn(**7**)]Cl_2 1	**0.82**	415	68	0.23	2.99
[(**10**)Zn(**7**)]Cl_2 2	**0.82**	408	68	0.23	2.99
N719	17.17	635	70	7.68	100
3 days after sealing of the cells					
[(**8**)Zn(**7**)]Cl_2 1	0.44	377	69	0.11	1.39
[(**8**)Zn(**7**)]Cl_2 2	0.45	374	69	0.12	1.51
[(**10**)Zn(**7**)]Cl_2 1	0.81	**427**	69	**0.24**	3.02
[(**10**)Zn(**7**)]Cl_2 2	0.70	407	67	0.19	2.39
N719	16.72	674	71	7.94	100
10 days after sealing of the cells					
[(**8**)Zn(**7**)]Cl_2 1	0.43	375	68	0.11	1.36
[(**8**)Zn(**7**)]Cl_2 2	0.45	380	69	0.12	1.48
[(**10**)Zn(**7**)]Cl_2 1	0.81	428	**70**	**0.24**	2.96
[(**10**)Zn(**7**)]Cl_2 2	0.71	407	68	0.20	2.47
N719	16.71	690	70	8.11	100

Table 4-2: Summary of measured solar cell properties, on the day of sealing and 3 and 10 days after sealing.

4.3.2.4. External quantum efficiency (EQE)

The EQE spectra of cells containing dyes [(**8**)Zn(**7**)]Cl_2, [(**10**)Zn(**7**)]Cl_2, are shown in Figure 4-11. For each dye two independent cells were assembled and measured. The maximum photon to current conversion efficiency of approximately 3%, was reached by the dye, [(**10**)Zn(**7**)]Cl_2. The lowest value of around 1.7% was measured for the dye containing anchoring ligand **8**. All of the measured cells show photon to current conversion up to 690 nm, although the maxima for all dyes lie around 470 nm. The very low EQE reflects the poor efficiency of the cell discussed in 4.3.2.3.

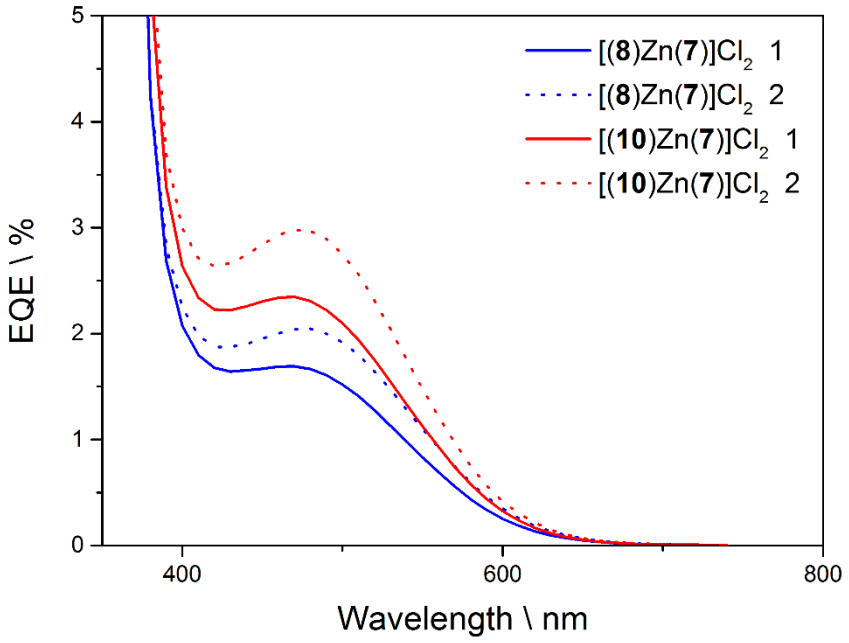

*Figure 4-11: EQE spectra of cells with dyes [(**8**)Zn(**7**)]Cl_2 (blue) and [(**10**)Zn(**7**)]Cl_2 (red).*

4.4. Conclusion

In this chapter, a new step-wise protocol was introduced, to assemble dyes on the semiconductor surface. Furthermore, it was found that $ZnCl_2$ is the zinc source of choice in this assembling process. It could as well be proven that zinc(II) based dyes show photon to current conversion, although it is not very efficient. Nevertheless, efficiencies up to 0.71% were measured with unmasked cells.

Additionally, a new second generation ancillary ligand (**7**) was synthesized. Unfortunately, the dyes based on this ligand did not show the expected improvement in DSC performance. The extension of the π-system did not have the planned effect of red shifting the absorption. One reason for this might be that the Ph_2N-arene rings are twisted with respect to the plane of the adjacent arene rings, relieving proton-proton repulsion between the adjacent rings.

4.5. Experimental

4.5.1. *N*1-(4-([2,2':6',2''-Terpyridin]-4'-yl)phenyl)-*N*1-(4-(bis(4-methoxyphenyl)amino)phenyl)-*N*4,*N*4-bis(4-methoxyphenyl)benzene-1,4-diamine (7)

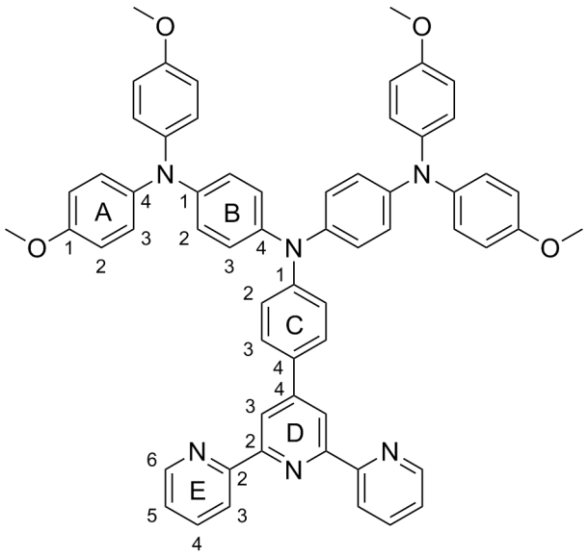

A round bottomed flask was charged with *N*1-(4-(bis(4-methoxyphenyl)amino)phenyl)-*N*4,*N*4-bis(4-methoxyphenyl)benzene-1,4-diamine (150 mg, 0.234 mmol, 1.1 eq.), 4'-(4-bromophenyl)-2,2':6',2''-terpyridine (83.2 mg, 0.214 mmol, 1.0 eq.), NaO^{t}Bu (67.9 mg, 0.707 mmol, 3.3 eq.) and $Pd(dba)_2$ (4.93 mg, 8.57 µmol, 0.04 eq.) under an N_2 atmosphere. Then dry and degassed toluene (10 mL) and P(^{t}Bu)$_3$ (8.57 µL, 8.57 µmol, 0.04 eq.) were added to the mixture. The reaction mixture was stirred for 3 d at 100 °C. The solvent was then removed under reduced pressure and the remaining solid was recrystallized from acetone. The yellow solid was dissolved in CH_2Cl_2 (30 mL), washed with 6 M KOH (aq, 2 x 15 mL) and water (3 x 20 mL) and then dried over $MgSO_4$. The solvent was again removed under reduced pressure and the product was obtained as a yellow solid (95.0 mg, 0.102 mmol, 43%).

^{1}H NMR (500 MHz, THF-*d8*) δ / ppm 8.80 (s, 2H, H^{D3}), 8.71 – 8.68 (m, 2H, H^{E3}), 8.66 (ddd, *J* = 4.8, 1.8, 0.9 Hz, 2H, H^{E6}), 7.91 – 7.85 (m, 2H, H^{E4}), 7.74 (d_{AB}, *J* = 8.8 Hz, 2H, H^{C3}), 7.34 (ddd, *J* = 7.5, 4.7, 1.2 Hz, 2H, H^{E5}), 7.10 (d_{AB}, *J* = 8.8 Hz, 2H, H^{C2}), 7.03 (d_{AB}, *J* = 9.0 Hz, 8H, H^{A3}), 7.00 (d_{AB}, *J* = 9.1 Hz, 4H, H^{B3}), 6.87 (d_{AB}, *J* = 8.9 Hz, 4H, H^{B2}), 6.82 (d_{AB}, *J* = 9.0 Hz, 8H, H^{A2}), 3.74 (s, 12H, H^{MeO}).

^{13}C NMR (126 MHz, THF-*d8*) δ / ppm 157.2 (C^{E2}), 157.1 (C^{A1}), 156.9 (C^{D2}), 150.7 (C^{C1}), 150.5 (C^{D4}), 150.0 (C^{E6}), 146.2 (C^{B1}), 142.1 (C^{A4}), 141.1 (C^{B4}), 137.4 (C^{E4}), 130.9 (C^{C4}), 128.5 (C^{C3}), 127.08 (C^{B3}), 127.05 (C^{A3}), 124.6 (C^{E5}), 122.7 (C^{B2}), 121.6 (C^{E3}), 121.4 (C^{C2}), 118.4 (C^{D3}), 115.5 (C^{A2}), 55.6 (C^{MeO}).

ESI MS (m/z): 930.9 $[M+H]^+$ (calc.: 931.4).

MALDI-TOF MS (m/z): 931.1 $[M+H]^+$ (calc. 931.4)

UV-Vis (THF, c = 2.4 × 10^{-5} mol dm^{-3}) λ_{abs} / nm 296 (ε / dm^3 mol^{-1} cm^{-1} 44700), 335 sh (29800), 382 sh (19200).

Chapter 5

Chapter 5: The influence of different alkyl chains on the ancillary ligand on the performance of the DSC

As seen in the previous chapter, it is possible to use Zn(II) bis-terpyridine complexes as dyes in DSCs and an easy and atom economical step-wise approach of dyeing was established. Nevertheless the tested cells cannot compete with state of the art ruthenium dyes that are often used as references e.g. N719, due to their very efficient light harvesting properties. Dye sensitized solar cells show certain problems which arise from their basic working principle. There are several pathways that contribute to losses in the efficiency of a DSC (Figure 5-1). One of them is the loss of electrons from the semiconductor. After the dye is excited and the electron injected into the TiO_2, the desired route for the electron is to migrate through the semiconductor to the back electrode into the external circuit. Since the electron travels through the TiO_2 in the order of milliseconds, there is plenty of time for other processes to happen, which take place faster or equally fast. Mainly there are two ways in which charge can be lost. Firstly, there is the recombination of an electron with the oxidized redox mediator that is known to happen in the order of 10^{-2} s, which lies in the same range as the residence time of the electron in the semiconductor. The second pathway is the recombination of an electron with the oxidized dye. The time domain of this process is on the order of 10^{-4} s, which is 10 times faster than the time it takes for the electron to travel through the TiO_2 surface. The minimization of these losses is the focus of this chapter.[94],[47]

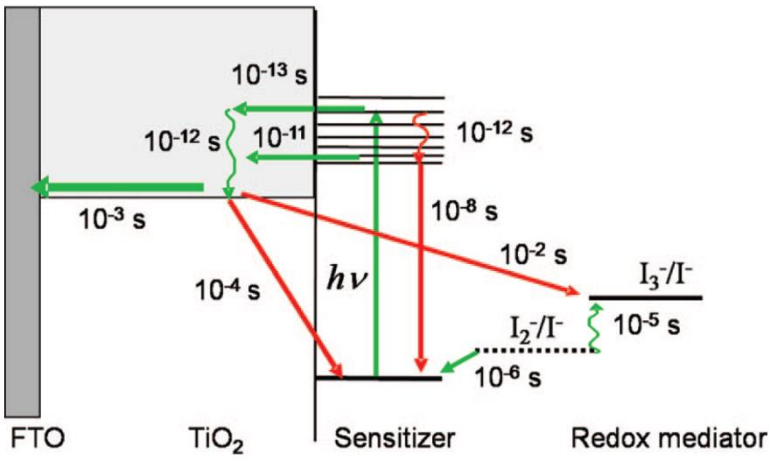

Figure 5-1: Wanted (green) and unwanted (red) processes in a dye sensitized solar cell.[45]

In order to further increase the efficiency of the dyes shown in the previous chapter, ancillary ligands were introduced that have built-in features to minimize the loss of electrons through the two channels described above. For this purpose ligands were synthesized that are based on the compound **6a**, but feature longer alkoxy chains in place of the methoxy groups. The non-polar chains are meant to shield the dye from its environment in a way that the charge recombination from the semiconductor to the dye or electrolyte is hindered.[95],[96]

The compounds **13**, **14** and **15** (Scheme 5-1) exhibit *iso*-butoxy, octyloxy and n-butoxy functionalities on the diphenylamine domain. Theoretically, these can, once incorporated into the anchored dye on the TiO_2 surface, interact with each other in an intra- or intermolecular way to establish a recombination blocking shell. In this process, the long alkyl chains interact through van der Waals forces and align next to one another.

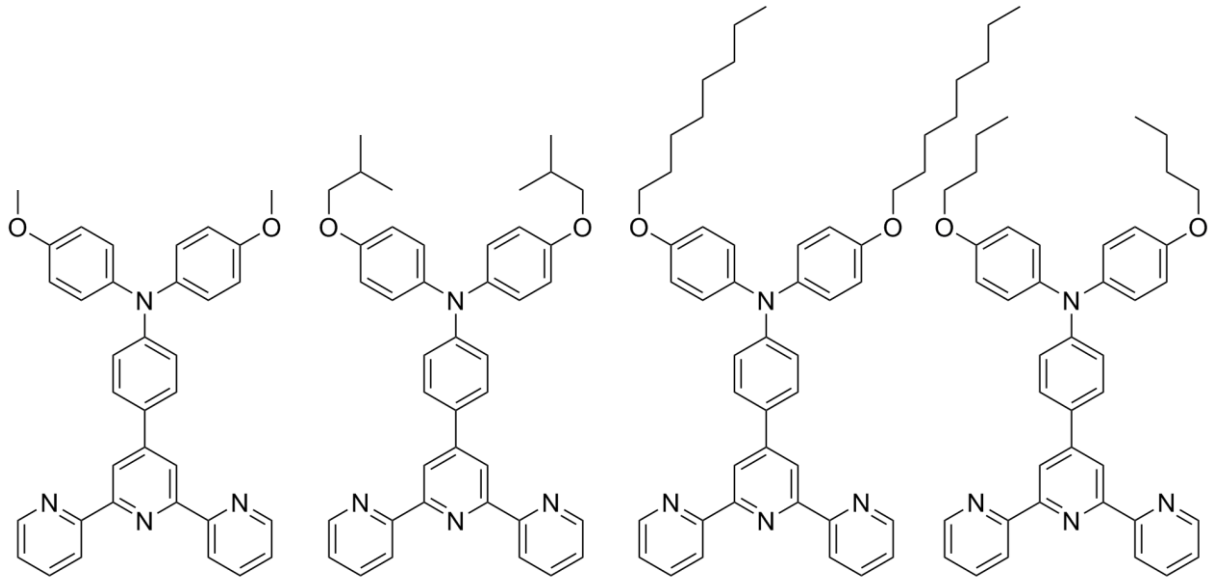

*Scheme 5-1: Alkoxy substituted ancillary ligands **13**, **14**, **15** which are successor ligands to **6a**.*

In Scheme 5-1 one can see the ligands with possible recombination blocking abilities. Compound **14** is the ligand which offers the most potential, since its long chains provide the biggest contact surface for hydrophobic interactions.

5.1. Ligand synthesis

The synthesis of the ligands started with the alkylation of 4-bromophenol and 4-acetamidophenol to the corresponding alkoxy derivatives using the Williamson ether synthesis under the conditions shows in Scheme 5-2.

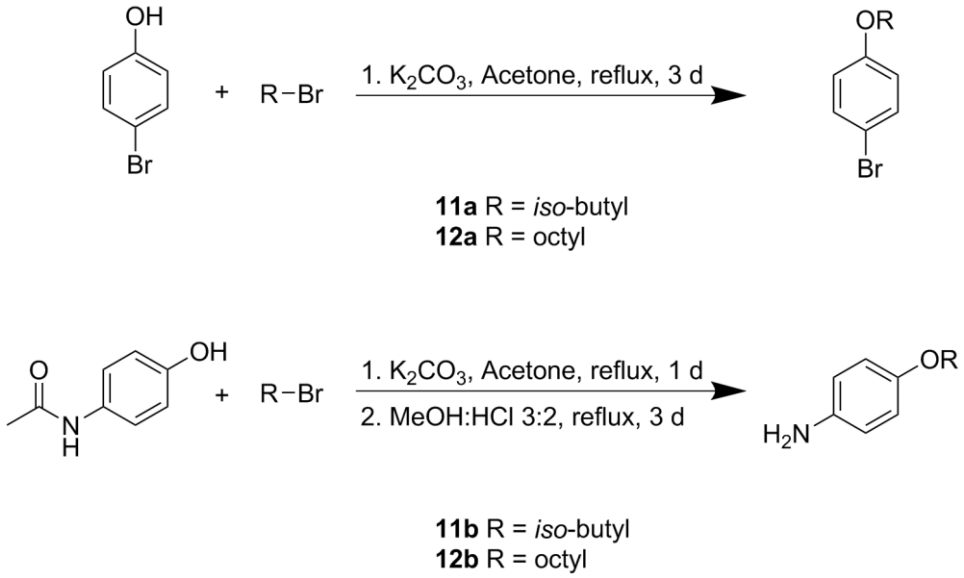

*Scheme 5-2: Williamson ether synthesis for precursors **11a**, **11b**, **12a** and **12b**.*

The compounds **11a**, **11b**, **12a** and **12b**, now exhibiting the desired alkoxy substituents in the 4 position, were coupled together in a second step, using an Ullmann-type reaction, involving CuI and L(-)-proline as a catalyst. The conditions are shown in Scheme 5-3.

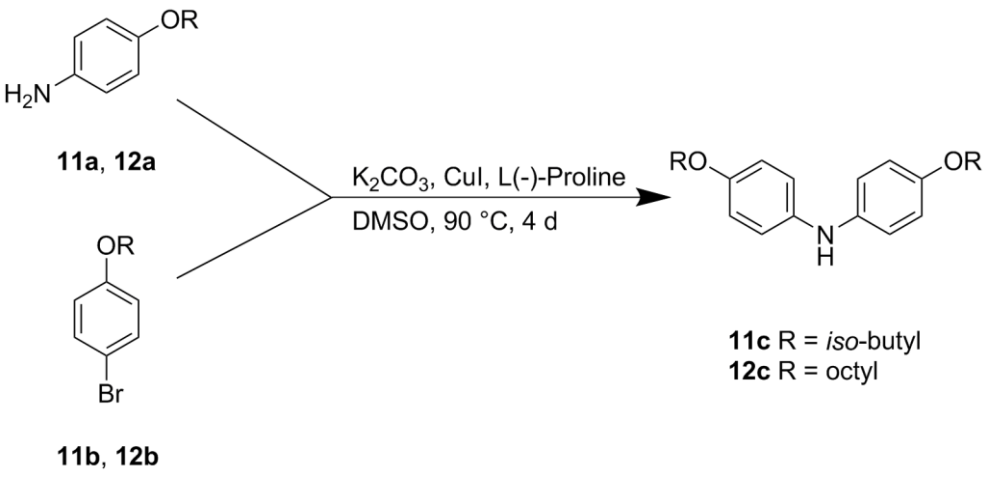

*Scheme 5-3: Ullmann-type reaction to give secondary amines **11c** and **12c**.*

In a final step the secondary amines (**11c** and **12c**) were reacted with 4'-(4-bromophenyl)-2,2':6',2''-terpyridine in a Hartwig-Buchwald reaction, using $Pd(dba)_2$ and $P(^tBu)_3$ as catalyst, giving ancillary ligands **13** and **14** (Scheme 5-4). Ligand **15** was synthesized using the same reaction type. The *n*-butyl substituted secondary amine was provided by Sebastian Fürer.

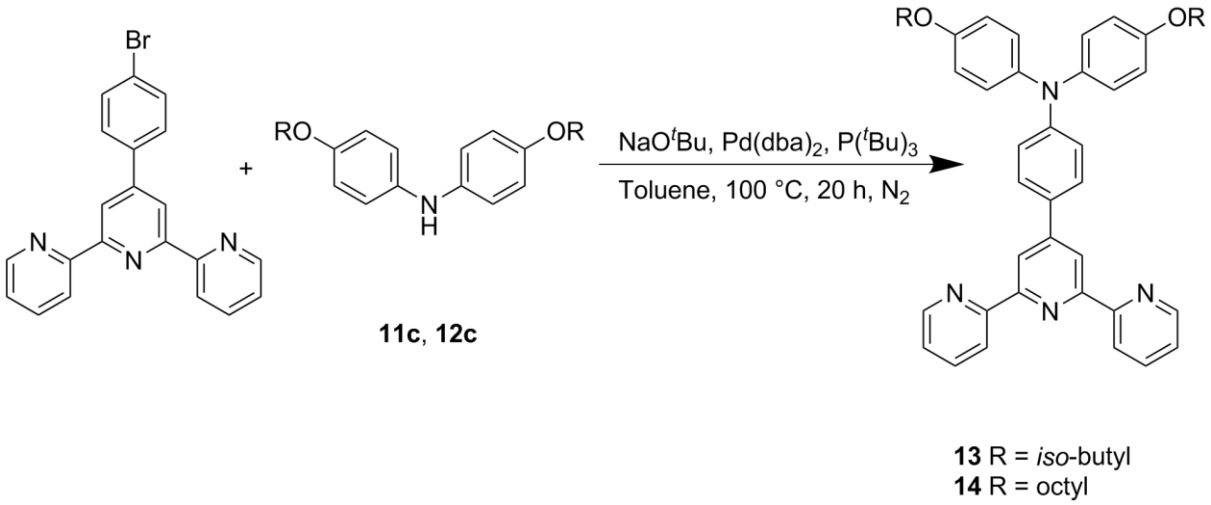

*Scheme 5-4: Hartwig-Buchwald coupling to obtain ancillary ligands **13** and **14**.*

5.2. Results and discussion

5.2.1. Solid state electronic absorption

Based on the results presented in the previous chapter, only $ZnCl_2$ was used as a zinc(II) source in the dyeing process of the solar cells.

Scheme 5-5 shows the used anchoring ligands **8** and **10**, exhibiting carboxylic and phosphonic acid anchoring groups.

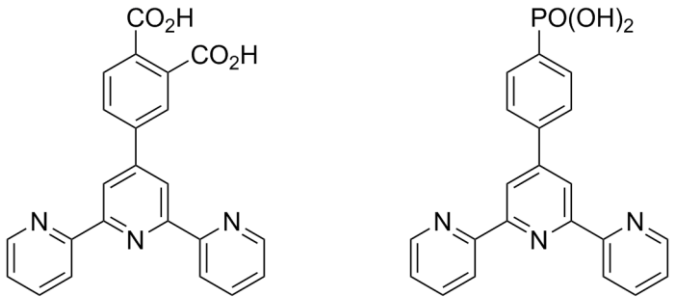

8 **10**

*Scheme 5-5: The used anchoring ligands **8** and **10**.*

Figure 5-2 shows the solid state electronic absorption spectra of [(**8**)Zn(**13**)]Cl_2 and [(**10**)Zn(**13**)]Cl_2 on the TiO_2 surface. Both spectra are of a similar shape and show a broad absorption between 375 nm and 550 nm. Below this range the TiO_2 starts to absorb light as well, which explains the very strong absorption band arising below 375 nm. The broad ILCT bands with maxima around 440 nm show different absorption intensities. For the dye [(**10**)Zn(**13**)]Cl_2 the intensity is lower. The onset of the lowest absorption is at 553 nm, corresponds to an optical HOMO – LUMO gap of 2.24 eV.

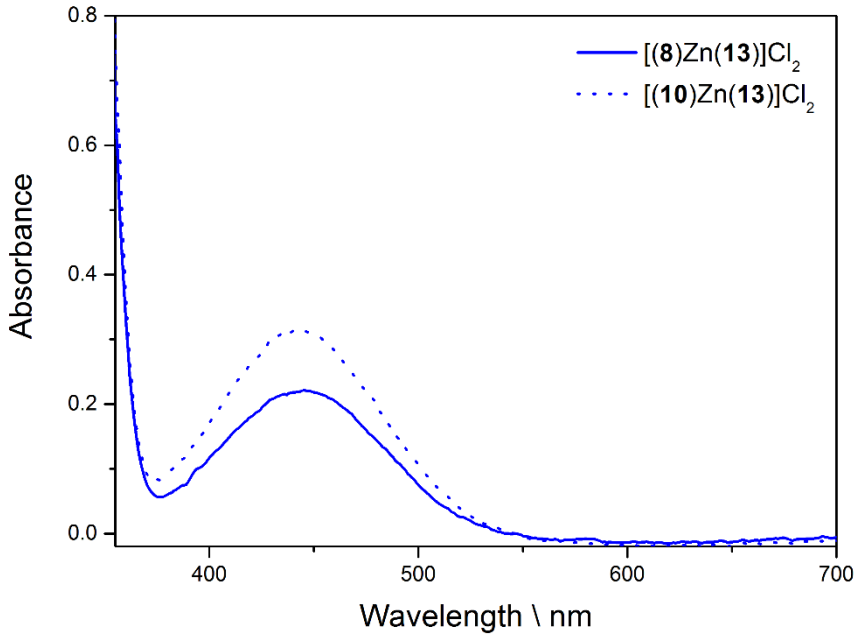

*Figure 5-2: Solid state electronic absorption spectra of [(**8**)Zn(**13**)]Cl_2 and [(**10**)Zn(**13**)]Cl_2.*

Spectra for dyes [(**8**)Zn(**14**)]Cl_2 and [(**10**)Zn(**14**)]Cl_2 on TiO_2 are shown in Figure 5-3 and are very similar to the above spectra. Again there is a broad absorption between 375 nm (where the TiO_2 starts to absorb) and 550 nm. This can again be attributed to an ILCT. Also in these spectra it is clearly visible that the dye using anchoring ligand **10**, shows a more intense absorption at 440 nm. The onset of the most red-shifted absorption lies at 555 nm and corresponds to a HOMO – LUMO gap of 2.23 eV.

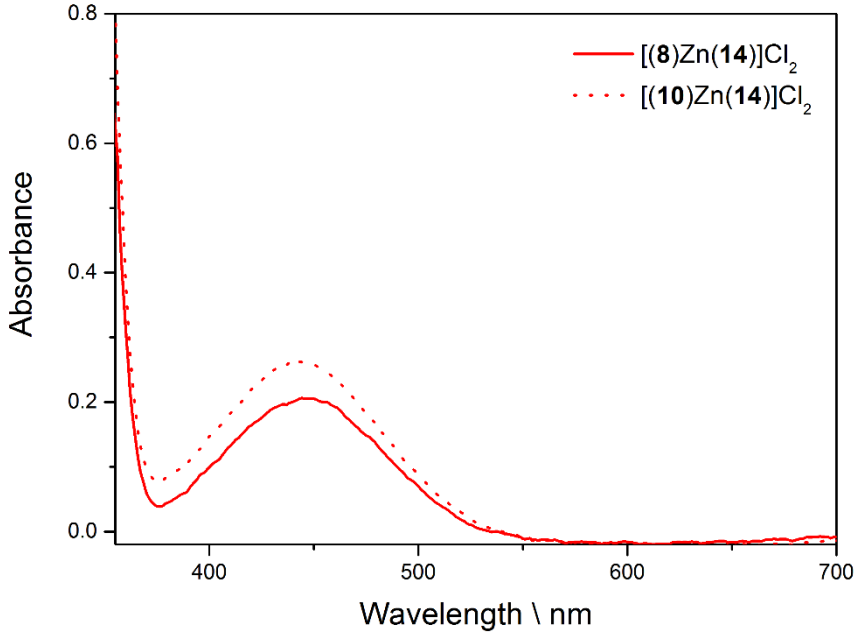

*Figure 5-3: Solid state electronic absorption spectra of [(**8**)Zn(**14**)]Cl_2 and [(**10**)Zn(**14**)]Cl_2.*

Dyes [(**8**)Zn(**15**)]Cl_2 and [(**10**)Zn(**15**)]Cl_2 showed similar trends (Figure 5-4). The spectra show an intense absorption below 375 nm (where the TiO_2 starts to absorb) and a broad ILCT absorption band between 375 nm and 550 nm. Again the intensity of the broad absorption band is more intense for the dye containing anchoring ligand **10**. The onset of the lowest energy transition is at 559 nm and corresponds to a HOMO – LUMO gap of 2.21 eV.

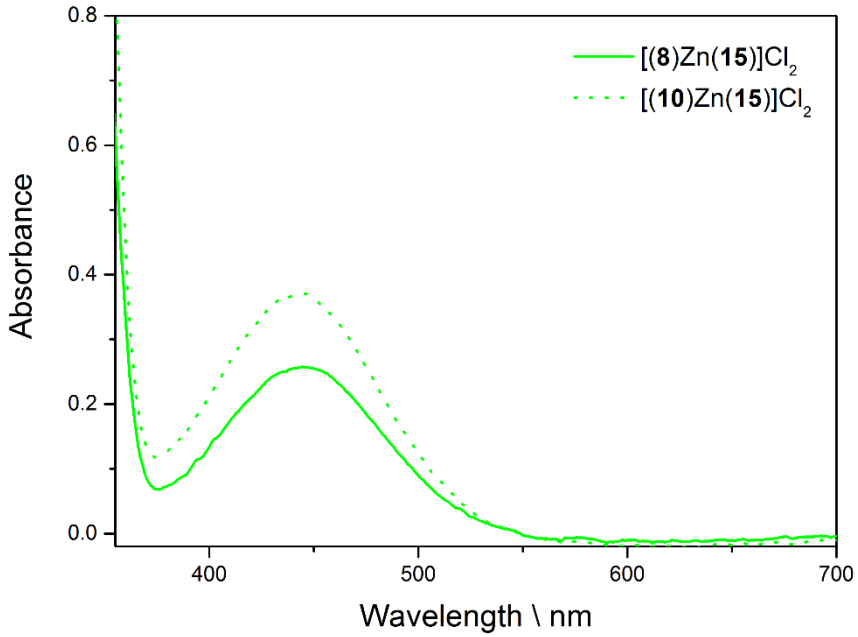

*Figure 5-4: Solid state electronic absorption spectra of [(**8**)Zn(**15**)]Cl₂ and [(**10**)Zn(**15**)]Cl₂.*

Figure 5-5 and Figure 5-6 show a comparison of the solid state absorption spectra for the dyes containing anchoring ligand **8** and **10**, respectively. This comparison suggests for both anchoring ligands, the complexes show the highest absorption with ancillary ligand **15** and the weakest with ligand **14**. The same trend is seen for both anchoring ligands, which suggests this underlays a certain pattern. A reason for this trend might be the size of the ancillary ligands. Ligand **15** exhibits n-butyl substituents and, in comparison to the bulky ligand **14** with octyl chains, allows more dye molecules to adsorb on the TiO_2 surface. Ligand **13** lies between the other two.

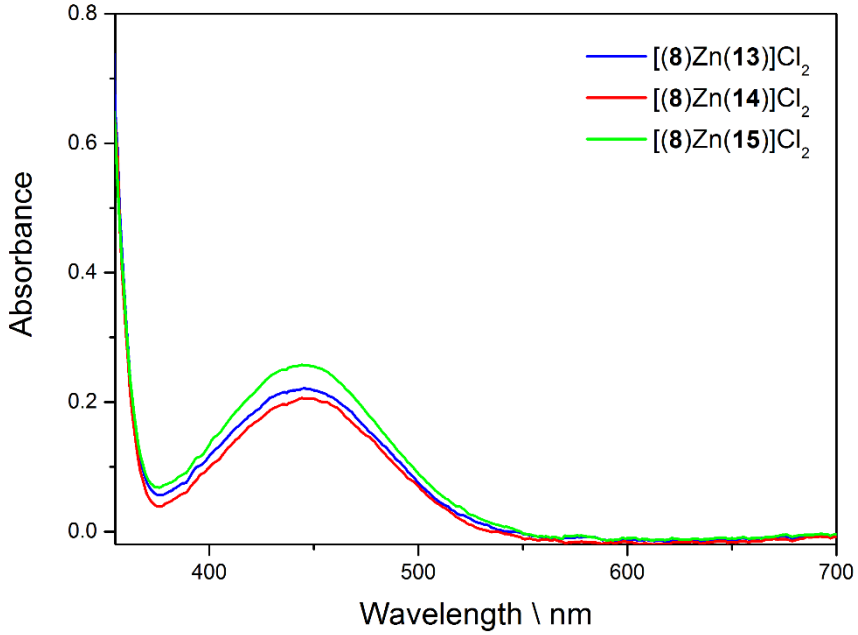

*Figure 5-5: Comparison of solid electronic absorption spectra of dyes containing anchoring ligand **8**.*

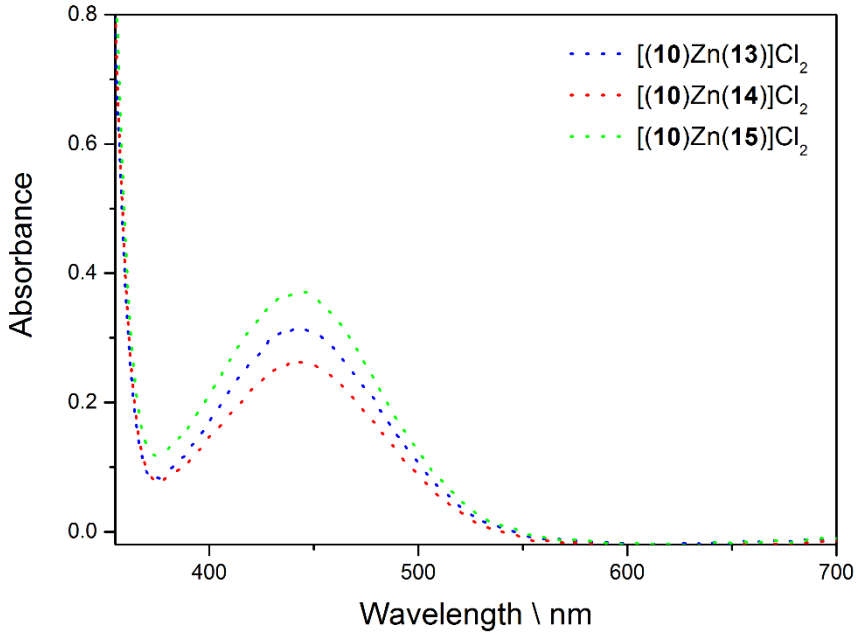

*Figure 5-6: Comparison of solid electronic absorption spectra of dyes containing anchoring ligand **10**.*

Figure 5-8 shows all measured spectra and it makes clear that the different alkoxy substituents do not have an influence on the electronic properties or energy levels of the dyes, since all the solid state electronic absorption spectra show identical absorption ranges. The only variable is the absorption intensity, which can be explained by the different length of the alkyl chains on the dyes, anchored on the TiO_2 surface. The bulkier the ancillary ligand is, the less dye molecules can form on the surface, assuming that there is the same number of available anchoring ligands on the surface for each sample. However, it is not possible to easily remove the dye from the surface to quantify the amount of material, e.g. by using a quartz microbalance.

Not only does the size of the ancillary ligand seem to matter, but a difference between the two anchoring ligands (**8** and **10**) can also be noticed. Namely dyes containing anchoring ligand **10** show higher absorption intensities.[60] This might be due to the fact that the phosphonic anchoring group offers three binding sites to connect to the semiconductor surface, which is one more than ligand **8**.[97] The top of Figure 5-7 illustrates how the phosphonate anchor can bind to the TiO_2 surface. Although the phosphonate anchor is able to offer three binding sites, it is more likely that it anchors with two (bottom of Figure 5-7).[98]

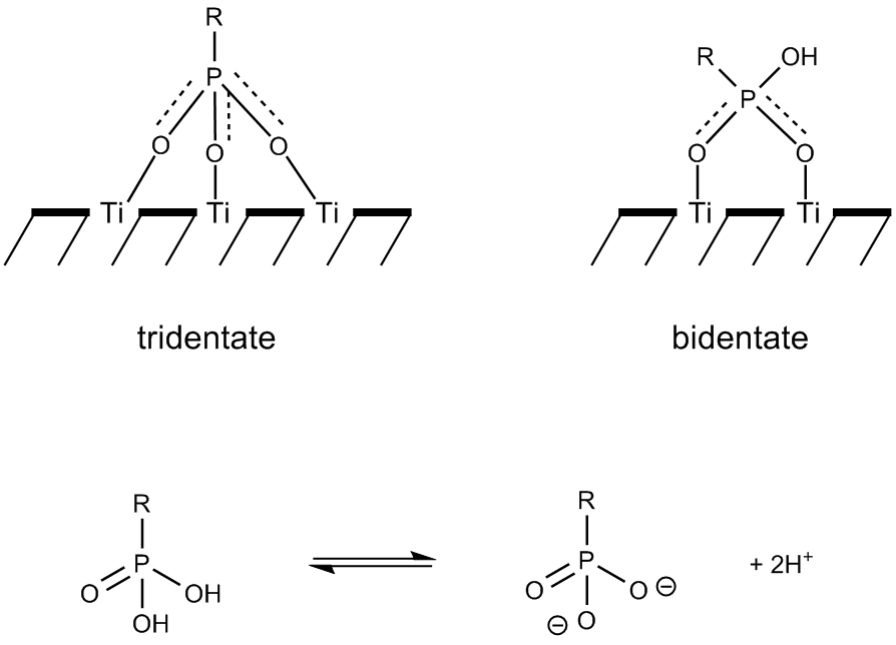

Figure 5-7: Illustration of the possible binding modes of the phosphonate anchor.[98]

Nevertheless, this fact could lead to a more stable linkage to the TiO_2 in the case of ligand **10** and thus to more available free binding sites for the Zn(II) in the second step of the dyeing protocol, which could ultimately lead to more dye molecules on the surface, resulting in the higher absorption intensities.

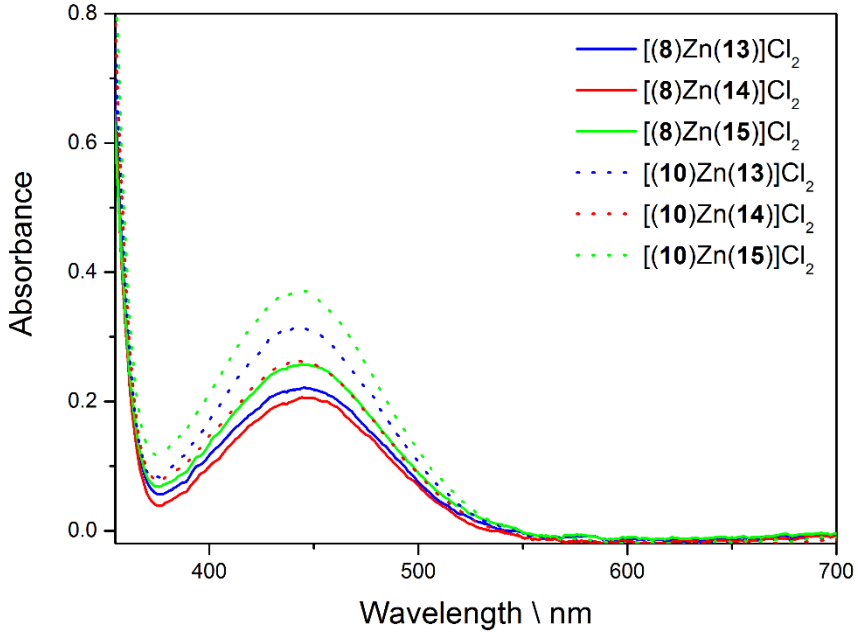

Figure 5-8: Solid state electronic absorption spectra of all the measured anchoring ligand-ancillary ligand combinations.

5.2.2. External quantum efficiency (EQE)

Figure 5-9 shows the external quantum efficiency of dyes [(**8**)Zn(**13**)]Cl_2 and [(**10**)Zn(**13**)]Cl_2. It is easy to see that, compared to N719, these dyes show lower light harvesting properties. For reasons of clarity dyes [(**8**)Zn(**14**)]Cl_2, [(**10**)Zn(**14**)]Cl_2, [(**8**)Zn(**15**)]Cl_2 and [(**10**)Zn(**15**)]Cl_2 are not included in this figure. The EQEs of those dyes lie in the same range as the ones shown below and will be discussed later in this section.

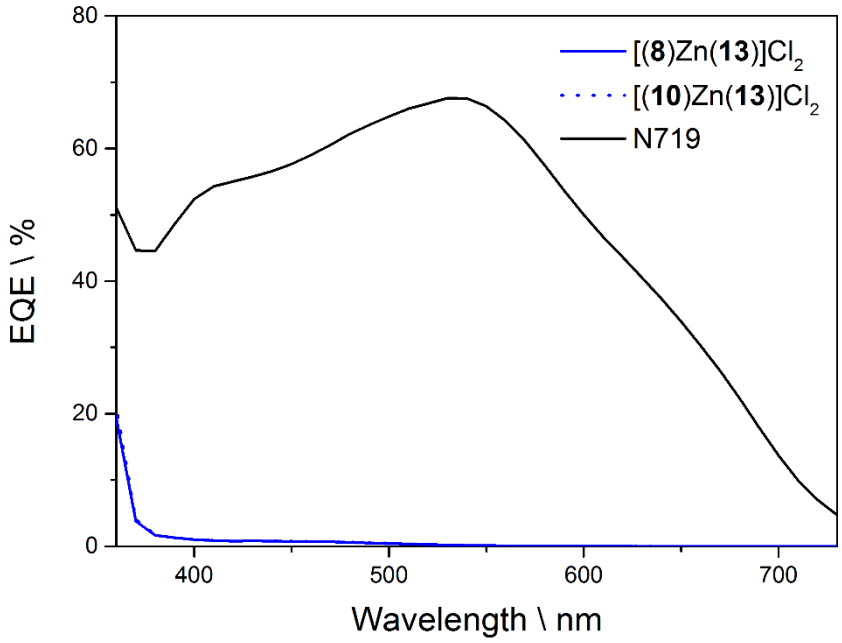

*Figure 5-9: EQE spectra of [(**8**)Zn(**13**)]Cl_2 and [(**10**)Zn(**13**)]Cl_2 compared to N719.*

In Figure 5-10 an expansion of the EQEs of dyes [(**8**)Zn(**13**)]Cl_2 and [(**10**)Zn(**13**)]Cl_2 is shown. The difference between the two spectra is minimal, which suggests that the photon to electron conversion is more or less the same for both dyes, although it is also very weak for both. The maximum EQE lies at about 0.8%. The range at which the dye converts light into electrons tails out to 620 nm. Below 400 nm the TiO_2 contributes as well.

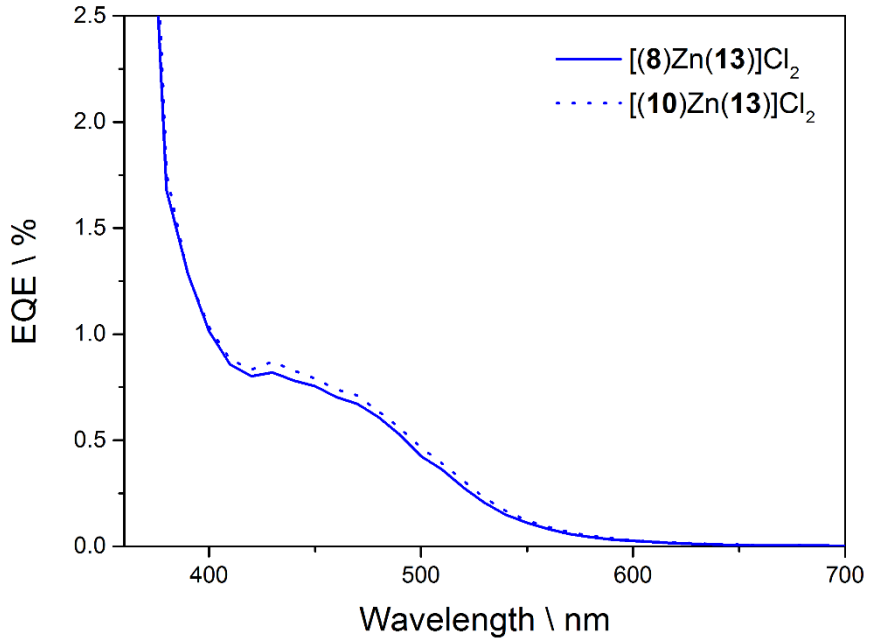

*Figure 5-10: EQE spectra of [(**8**)Zn(**13**)]Cl₂ and [(**10**)Zn(**13**)]Cl₂.*

To compare how the conversion range seen in the EQE spectra correlates with the absorption spectrum of the dye attached on the semiconductor, the EQE and solid state electronic absorption spectra of [(**10**)Zn(**13**)]Cl₂ are presented in Figure 5-11.

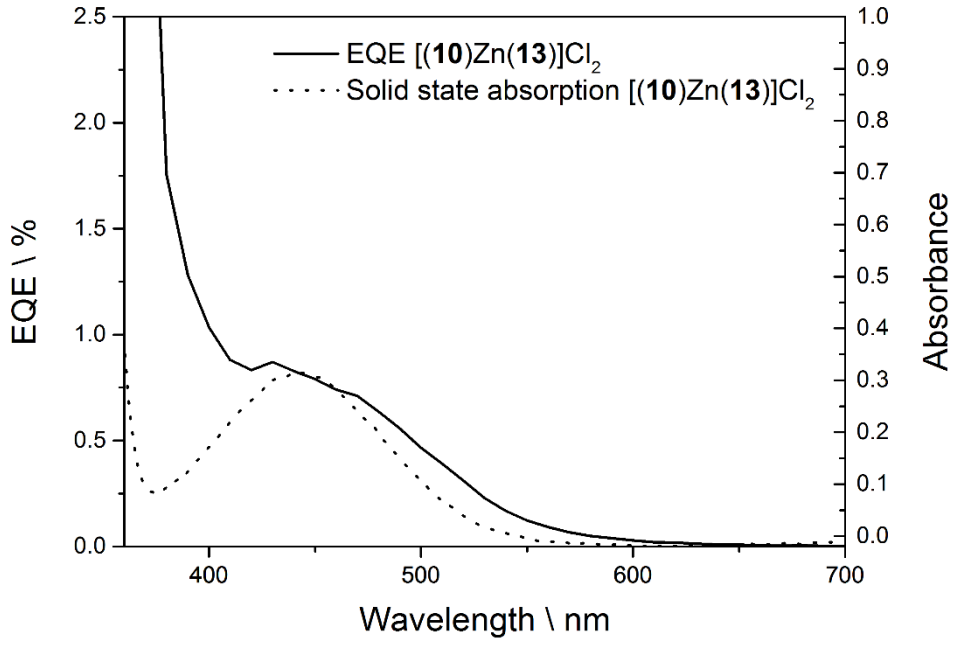

*Figure 5-11: Comparison of EQE and solid electronic absorption spectra of [(**10**)Zn(**13**)]Cl₂.*

It shows that these two match quite well in terms of absorption and conversion range, respectively. It may look like a correlation between the absorption intensity and the EQE value exists, but there is no direct connection between the two.
No further comparisons of this manner are shown for the other dyes in this series, because they all behave in a very similar way.

Figure 5-12 shows the EQE spectra of [(**8**)Zn(**14**)]Cl_2 and [(**10**)Zn(**14**)]Cl_2. They look very similar to the ones shown before, with both the conversion range and the conversion efficiency being comparable.

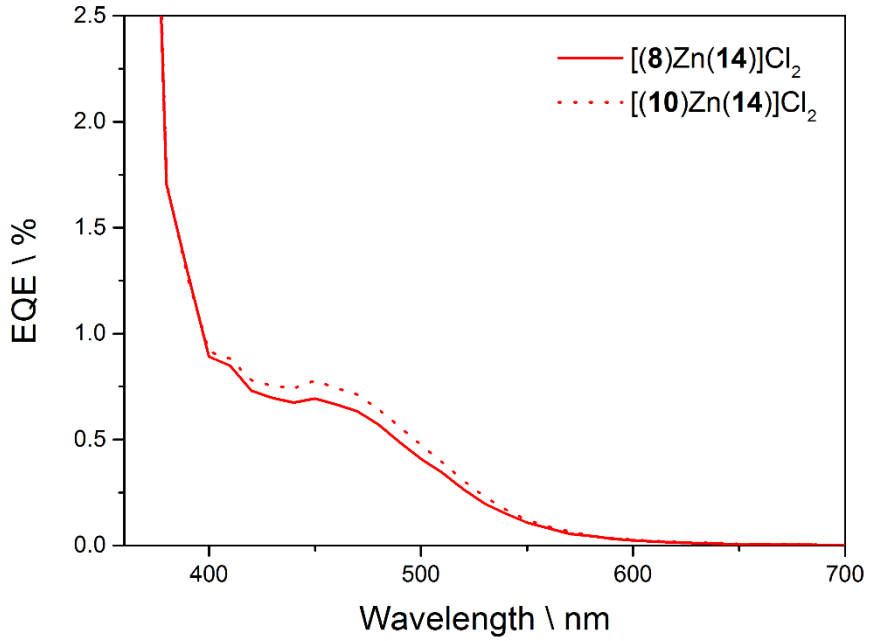

*Figure 5-12: EQE spectra of [(**8**)Zn(**14**)]Cl_2 and [(**10**)Zn(**14**)]Cl_2.*

For the dyes [(**8**)Zn(**15**)]Cl_2 and [(**10**)Zn(**15**)]Cl_2, the corresponding EQE spectra are shown in Figure 5-13. Although the conversion range is the same as for the dyes containing ancillary ligands **13** and **14**, there is a more pronounced difference between spectra where the two anchoring ligands **8** and **10** were used. The dye containing anchoring ligand **10** shows a maximum EQE of 1.3%, whereas the **8** containing dye only shows an EQE of about 1.0%. The difference is only very little and may be within experimental error, which makes it hard to draw a clear conclusion about why the difference between these two dyes is bigger in this case than for the two pairs discussed before. Nevertheless, the trend is the same for all three dye pairs.

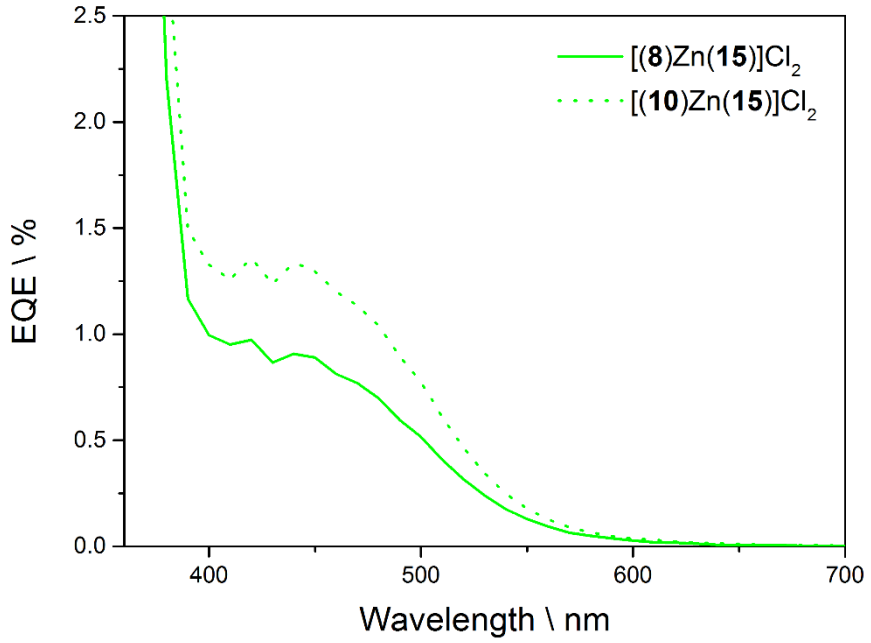

*Figure 5-13: EQE spectra of [(**8**)Zn(**15**)]Cl₂ and [(**10**)Zn(**15**)]Cl₂.*

Figure 5-14 shows the EQE spectra of dyes [(**8**)Zn(**6a**)]Cl₂ and [(**10**)Zn(**6a**)]Cl₂. This series of cells was dyed and assembled according to the same protocol as the others in this chapter.

One can easily see that the photon to current conversion efficiency is very low for both dyes. For dye [(**8**)Zn(**6a**)]Cl₂ the highest observed EQE was 0.6% and for dye [(**10**)Zn(**6a**)]Cl₂ 0.8%. Although the measured EQEs are very low, the dye containing anchoring ligand **10** is still more efficient, which corresponds to the trend observed for the other cells in this chapter.

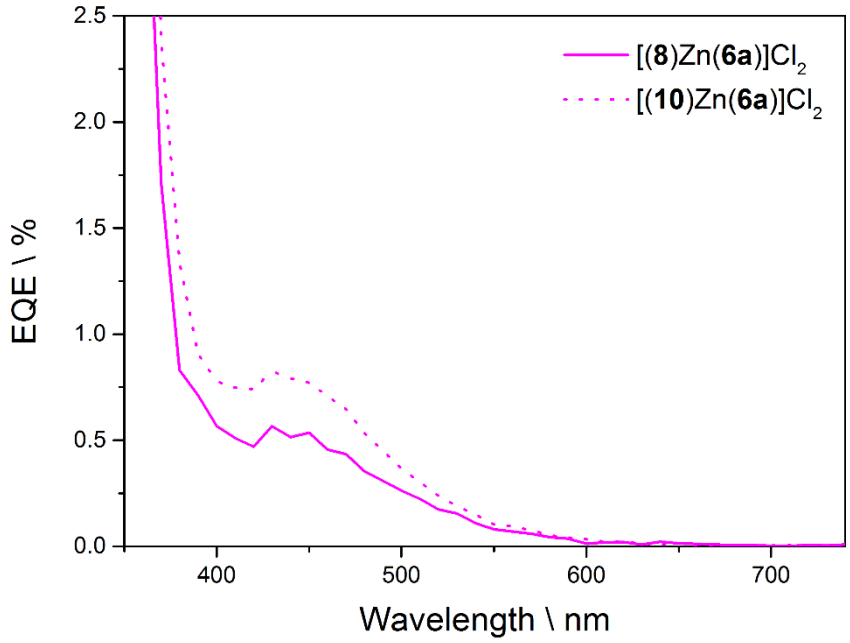

*Figure 5-14: EQE spectra of [(**8**)Zn(**6a**)]Cl₂ and [(**10**)Zn(**6a**)]Cl₂.*

5.2.3. Solar cell measurements

The results are summarized in Table 5-1, Table 5-2 and Table 5-3. They show the measured values on the day of sealing, as well as 3 and 16 days after sealing of the cells. All cells were measured while masked (average measured area: 0.06012 cm^2) to avoid false values because of scattered light.

5.2.3.1. Dyes [(8)Zn(13)]Cl₂ and [(10)Zn(13)]Cl₂

Table 5-1 shows the results of the solar cell measurements of dyes [(**8**)Zn(**13**)]Cl₂ and [(**10**)Zn(**13**)]Cl₂. Looking at the efficiencies one can immediately see that these cells do not perform particularly well, and this is consistent with the EQE measurements in section 5.2.2.

The highest J_{SC} was 0.45 mA/cm^2 obtained on the day of sealing by both cells containing [(**10**)Zn(**13**)]Cl₂. It was also one of these cells that showed the highest V_{OC} (428 mV), and efficiency (0.13%) on the same day. From day 0 to day 16 a slight decrease in J_{SC} is observed. V_{OC} and fill factors show only minor changes and even increase slightly over time for some of the cells. The efficiency slightly drops over time,

which can be attributed to the loss in J_{SC}. Furthermore, there is an observable difference in all factors, except for the fill factor, between the dyes containing anchoring ligand **8** and **10**. Dyes containing the latter show slightly better values. The fill factors for all cells are good. The JV-curves (Figure 5-15) illustrate quite nicely the reproducibility of the cells and the differences in J_{SC} and V_{OC} between the dyes with different anchoring ligands.

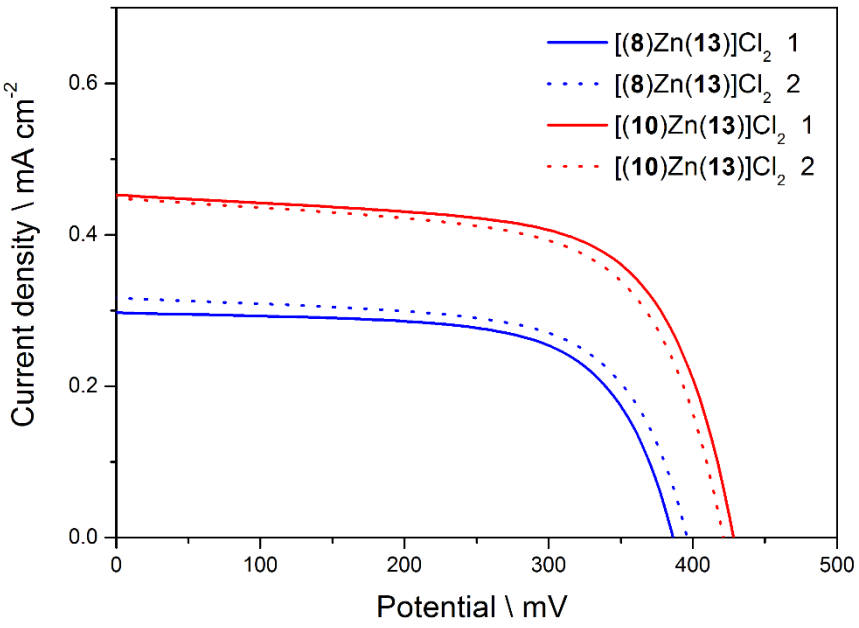

*Figure 5-15: JV-curves of cells containing dyes [(**8**)Zn(**13**)]Cl₂ and [(**10**)Zn(**13**)]Cl₂, measured on the day of sealing.*

Anchored dye	J_{SC} \ mA cm^{-2}	V_{OC} \ mV	FF \ %	η \ %	η rel. to N719 \ %
Day of sealing of the cells					
[(**8**)Zn(**13**)]Cl_2 1	0.30	386	66	0.08	1.12
[(**8**)Zn(**13**)]Cl_2 2	0.32	396	64	0.08	1.12
[(**10**)Zn(**13**)]Cl_2 1	**0.45**	**428**	66	**0.13**	1.82
[(**10**)Zn(**13**)]Cl_2 2	**0.45**	421	64	0.12	1.68
N719	15.27	652	72	7.13	100
3 days after sealing of the cells					
[(**8**)Zn(**13**)]Cl_2 1	0.26	375	65	0.06	0.76
[(**8**)Zn(**13**)]Cl_2 2	0.28	393	65	0.07	0.88
[(**10**)Zn(**13**)]Cl_2 1	0.42	425	65	0.12	1.51
[(**10**)Zn(**13**)]Cl_2 2	0.40	410	63	0.10	1.26
N719	16.72	674	71	7.94	100
16 days after sealing of the cells					
[(**8**)Zn(**13**)]Cl_2 1	0.26	396	66	0.07	1.07
[(**8**)Zn(**13**)]Cl_2 2	0.25	389	64	0.06	0.92
[(**10**)Zn(**13**)]Cl_2 1	0.37	**428**	**68**	0.11	1.68
[(**10**)Zn(**13**)]Cl_2 2	0.35	412	65	0.09	1.38
N719	14.23	653	70	6.53	100

Table 5-1: Summary of measured solar cell properties, on the day of sealing and 3 and 16 days after sealing.

5.2.3.2. Dyes [(8)Zn(14)]Cl_2 and [(10)Zn(14)]Cl_2

In Table 5-2 the results for the dyes [(**8**)Zn(**14**)]Cl_2 and [(**10**)Zn(**14**)]Cl_2 are summarized. One cell with dye [(**10**)Zn(**14**)]Cl_2 shows a J_{SC} of 0.41 mA/cm^2, a V_{OC} of 436 mV and an efficiency of 0.12% on the day of sealing.

J_{SC}, and efficiencies show again a decreasing trend going from day 0 to day 16. The V_{OC} and the fill factors stay quite constant over the period of 16 days. Again, there is a difference between the two anchoring groups, although in this series the dye containing anchoring ligand **10** is only very slightly better.

The whole series does not perform very well in terms of efficiency, which can again be attributed to the very poor J_{SC}. Fill factors are good. Also for this series the difference between the two anchoring ligands is quite nicely visible in the JV-plot (Figure 5-16). Here it can also be observed that there is a bigger difference in J_{SC} and V_{OC} between the two cells using ancillary ligand **10**.

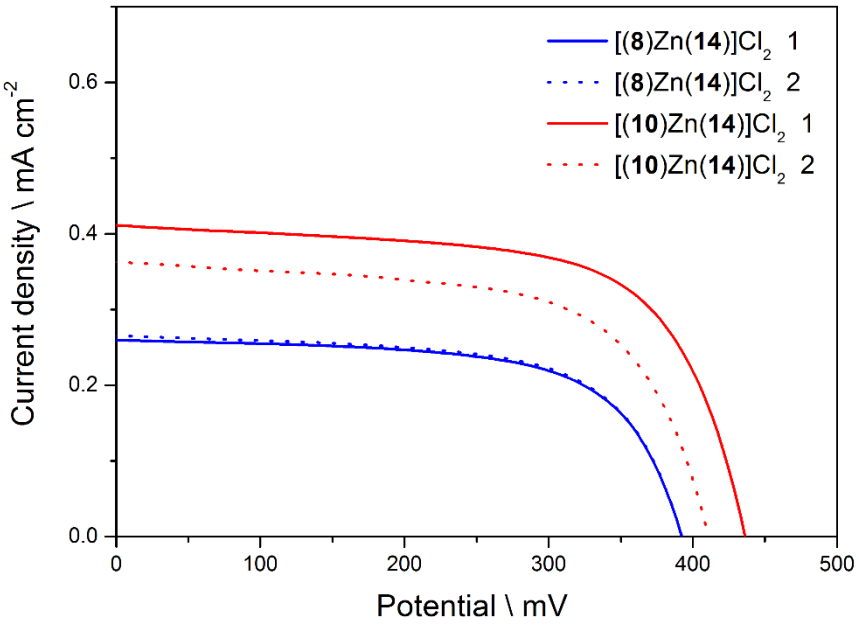

*Figure 5-16: JV-curves of cells containing dyes [(**8**)Zn(**14**)]Cl_2 and [(**10**)Zn(**14**)]Cl_2, measured on the day of sealing.*

Anchored dye	J_{SC} \ mA cm^{-2}	V_{OC} \ mV	FF \ %	η \ %	η rel. to N719 \ %
		Day of sealing of the cells			
[(**8**)Zn(**14**)]Cl_2 1	0.26	392	64	0.07	0.98
[(**8**)Zn(**14**)]Cl_2 2	0.27	392	64	0.07	0.98
[(**10**)Zn(**14**)]Cl_2 1	**0.41**	**436**	65	**0.12**	1.68
[(**10**)Zn(**14**)]Cl_2 2	0.36	411	63	0.09	1.26
N719	15.27	652	72	7.13	100
		3 days after sealing of the cells			
[(**8**)Zn(**14**)]Cl_2 1	0.23	382	62	0.06	0.76
[(**8**)Zn(**14**)]Cl_2 2	0.23	390	63	0.06	0.76
[(**10**)Zn(**14**)]Cl_2 1	0.31	405	64	0.08	1.01
[(**10**)Zn(**14**)]Cl_2 2	0.28	393	62	0.07	0.88
N719	16.72	674	71	7.94	100
		16 days after sealing of the cells			
[(**8**)Zn(**14**)]Cl_2 1	0.23	398	65	0.06	0.92
[(**8**)Zn(**14**)]Cl_2 2	0.21	403	65	0.05	0.77
[(**10**)Zn(**14**)]Cl_2 1	0.32	429	**67**	0.09	1.38
[(**10**)Zn(**14**)]Cl_2 2	0.26	401	65	0.07	1.07
N719	14.23	653	70	6.53	100

Table 5-2: Summary of measured solar cell properties, on the day of sealing and 3 and 16 days after sealing.

5.2.3.3. Dyes [(8)Zn(15)]Cl_2 and [(10)Zn(15)]Cl_2

The DSC parameters for dyes [(**8**)Zn(**15**)]Cl_2 and [(**10**)Zn(**15**)]Cl_2 are shown in Table 5-3. As expected, these dyes behave similarly to [(**8**)Zn(**13**)]Cl_2, [(**10**)Zn(**13**)]Cl_2, [(**8**)Zn(**14**)]Cl_2 and [(**10**)Zn(**14**)]Cl_2. Cell 2 containing dye [(**10**)Zn(**15**)]Cl_2 shows the best parameters. It exhibits 0.72 mA/m^2 in J_{SC}, 467 mV in V_{OC} and 0.23% efficiency, measured on the day of sealing. The highest fill factor of 68% was achieved by the same cell, 16 days after sealing of the cell. V_{OC} and fill factors are more or less stable for all cells during the 16 day period, whereas J_{SC} and efficiency decrease going from day of sealing to day 16. Overall the fill factors are in an acceptable range, but the efficiencies are very poor also for this series. Probably, the very low J_{SC} is the main reason for the poor performance. Figure 5-17 shows the JV-curves that have been measured for this series. Obviously, cell 2 containing dye [(**10**)Zn(**15**)]Cl_2 shows a significantly higher J_{SC} than all the other cells. It can be assumed that the second cell containing this dye is the outlier in this series. With this assumption, the difference between the two anchoring ligands can again be seen.

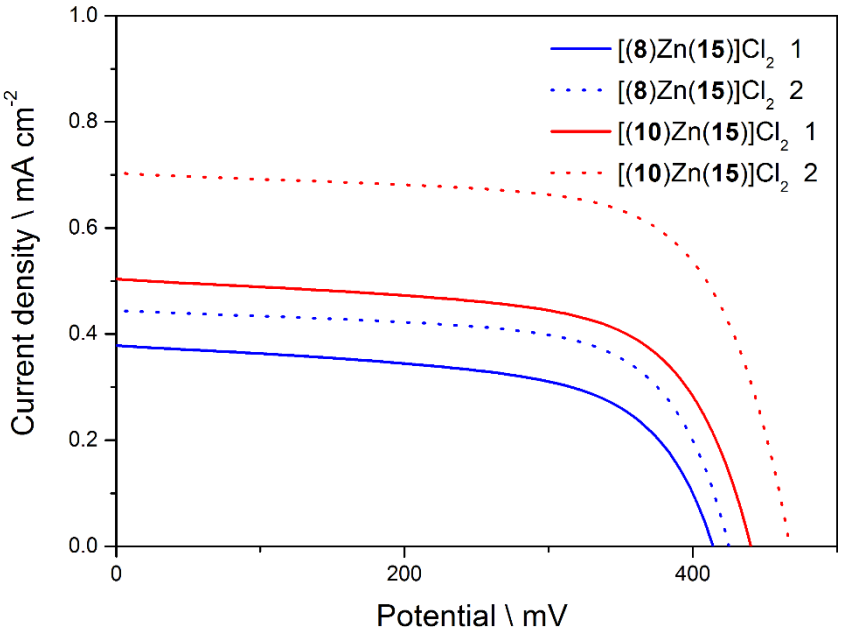

*Figure 5-17: JV-curves of cells containing dyes [(**8**)Zn(**15**)]Cl_2 and [(**10**)Zn(**15**)]Cl_2, measured on the day of sealing.*

Anchored dye	J_{SC} \ mA cm^{-2}	V_{OC} \ mV	FF \ %	η \ %	η rel. to N719 \ %
		Day of sealing of the cells			
[(**8**)Zn(**15**)]Cl_2 1	0.38	414	60	0.09	1.26
[(**8**)Zn(**15**)]Cl_2 2	0.45	425	65	0.13	1.82
[(**10**)Zn(**15**)]Cl_2 1	0.51	440	63	0.14	1.96
[(**10**)Zn(**15**)]Cl_2 2	**0.72**	**467**	67	**0.23**	3.23
N719	15.27	652	72	7.13	100
		3 days after sealing of the cells			
[(**8**)Zn(**15**)]Cl_2 1	0.27	380	56	0.06	0.76
[(**8**)Zn(**15**)]Cl_2 2	0.32	406	65	0.09	1.13
[(**10**)Zn(**15**)]Cl_2 1	0.41	432	62	0.11	1.39
[(**10**)Zn(**15**)]Cl_2 2	0.53	447	66	0.16	2.02
N719	16.72	674	71	7.94	100
		16 days after sealing of the cells			
[(**8**)Zn(**15**)]Cl_2 1	0.25	403	57	0.06	0.92
[(**8**)Zn(**15**)]Cl_2 2	0.27	404	64	0.07	1.07
[(**10**)Zn(**15**)]Cl_2 1	0.36	439	63	0.10	1.53
[(**10**)Zn(**15**)]Cl_2 2	0.38	440	**68**	0.11	1.68
N719	14.23	653	70	6.53	100

Table 5-3: Summary of measured solar cell properties, on the day of sealing and 3 and 16 days after sealing.

5.2.3.4. Dyes [(8)Zn(6a)]Cl_2 and [(10)Zn(6a)]Cl_2

Figure 5-18 shows the JV-measurements of the dyes [(**8**)Zn(**6a**)]Cl_2 and [(**10**)Zn(**6a**)]Cl_2. This series was dyed and assembled using the same protocol as the other three presented in this chapter.

Table 5-4 shows the DSC parameters and one can see that the efficiencies are very low on both days they were measured. This can be attributed to the very low J_{SC} and the poor fill factors. The V_{OC} values are constant, but also very low. One cell incorporating dye [(**10**)Zn(**6a**)]Cl_2 showed the best values for J_{SC} (0.21 mA/cm^2), V_{OC} (379 mV), fill factor (64%) and efficiency (0.05%).

In Figure 5-18 one can see the JV-curves of the measured cells. Although the DSC performance is very poor, there is still a difference in J_{SC} observable between the dyes with different anchoring ligands.

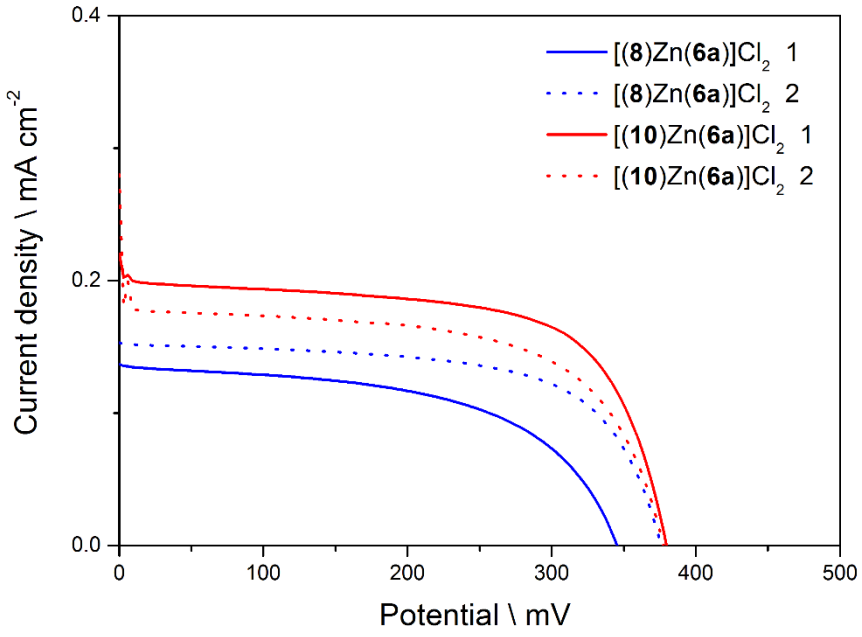

*Figure 5-18: JV-curves of cells containing dyes [(**8**)Zn(**6a**)]Cl_2 and [(**10**)Zn(**6a**)]Cl_2, measured on the day of sealing.*

Anchored dye	J_{SC} \ mA cm^{-2}	V_{OC} \ mV	FF \ %	η \ %	η rel. to N719 \ %
Day of sealing of the cells					
[(**8**)Zn(**6a**)]Cl_2 1	0.14	345	55	0.03	0.47
[(**8**)Zn(**6a**)]Cl_2 2	0.15	376	**64**	0.04	0.62
[(**10**)Zn(**6a**)]Cl_2 1	**0.21**	**379**	**64**	**0.05**	0.78
[(**10**)Zn(**6a**)]Cl_2 2	0.20	377	55	0.04	0.62
N719	14.59	609	73	6.44	100
2 days after sealing of the cells					
[(**8**)Zn(**6a**)]Cl_2 1	0.13	349	55	0.02	0.30
[(**8**)Zn(**6a**)]Cl_2 2	0.14	364	62	0.03	0.46
[(**10**)Zn(**6a**)]Cl_2 1	0.17	354	62	0.04	0.61
[(**10**)Zn(**6a**)]Cl_2 2	0.17	345	55	0.03	0.46
N719	14.76	616	72	6.58	100

Table 5-4: Summary of measured solar cell properties, on the day of sealing and 2 days after sealing.

5.3. Conclusion

Three new ancillary ligands (**13**, **14** and **15**) were synthesized and used for the step-wise dye assembly on a TiO_2 surface, with anchoring ligands **8** and **10**. Using these ligands and $ZnCl_2$, three sets of zinc(II) based DSCs were prepared and characterized. These measurements show that there is indeed a difference between the different dyes, containing ancillary ligands with alkyl chains of different lengths. Although this may sound promising, the difference is only small in JV-measurements of the cells. Only one cell containing ancillary ligand **15**, shows a significantly higher J_{SC} than the other cells, which might be a sign that the octyl chain indeed has an influence on the recombination of electrons from the TiO_2 to the oxidised dye or electrolyte. Namely there are more electrons actually flowing through the semiconductor to the back electrode, leading to a higher current. On the other hand the efficiencies of all the cells are so low that there is only very little room for interpretation. The main reason for the very low efficiencies can be found in the low J_{SC} values. Concerning the efficiencies, one might argue that these are so low that the cell is not actually working, but the EQEs show that certain photon to current conversion does occur, although it is very inefficient. The comparison of the DSC parameters of dyes containing ancillary ligands **13**, **14** and **15** and the dye containing **6a** suggests that the introduction of alkyl chains has a positive effect on the dye performance. EQE and JV-measurements show improved values for dyes containing ligands **13**, **14** and **15**.

What is clear is the fact that dyes containing anchoring ligand **10** are in all cases performing better than those containing **8**. Furthermore, all the cells show aging effects during the measuring period of 16 days, mainly expressed in decreasing J_{SC} and efficiencies.

In summary these experiments show that long, pendant alkoxy chains probably have an influence on the recombination and hence lead to more efficient cells, but the dyes themselves are not optimized enough to reveal this effect in an unambiguous way.

5.4. Experimental

5.4.1. 1-Bromo-4-isobutoxybenzene (11a)[99]

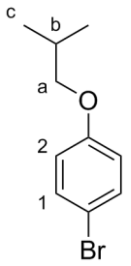

4-Bromophenol (5.00 g, 28.9 mmol, 1.0 eq.) was dissolved in 60 mL of acetone and K_2CO_3 (7.99 g, 57.8 mmol, 2.0 eq.) was added. The white suspension was stirred for 5 min, then 1-bromo-2-methylpropane (4.76 mL, 43.4 mmol, 1.5 eq.) was added and the mixture heated to reflux for 3 d. After the mixture was allowed to cool to RT, it was filtered and the filtrate concentrated in vacuo to give a colourless oil. This was dissolved in CH_2Cl_2 and washed with NaOH (3 x 50 mL, 2.0 M, aq.) and water (2 x 50 mL). Then it was dried over $MgSO_4$, filtered and the filtrate concentrated under reduced pressure to yield the desired product as a light yellow oil (1.78 g, 7.75 mmol, 27%)

^{1}H NMR (500 MHz, $CDCl_3$) δ / ppm 7.36 (d, *J* = 9.1 Hz, 2H, H^1), 6.77 (d, *J* = 9.0 Hz, 2H, H^2), 3.68 (d, *J* = 6.6 Hz, 2H, H^a), 2.07 (dh, *J* = 13.3, 6.7 Hz, 1H, H^b), 1.01 (d, *J* = 6.7 Hz, 6H, H^c).

5.4.2. 4-Isobutoxyaniline (11b)[99]

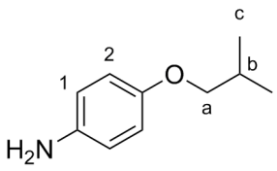

4-Acetamidophenol (5.00 g, 33.1 mmol, 1.0 eq.) was suspended in 60 mL of acetone, then K_2CO_3 (9.14 g, 66.2 mmol, 2.0 eq.) was added and the white suspension was stirred for 5 min. After that, 1-bromo-2-methylpropane (5.45 mL, 49.6 mmol, 1.5 eq.) was added and the mixture heated to reflux overnight. Another 2.00 g (26.5 mmol, 0.8 eq.) of K_2CO_3 and 1 mL (9.10 mmol, 0.28 eq.) 1-bromo-2-methylpropane were added to the mixture, which was further reacted for another 6 h. The mixture was then poured into water (30 mL) and stirred for 30 min. Because no precipitation was observed, the aqueous phase was extracted with CH_2Cl_2 (3 x 50 mL) and the organic phase dried over $MgSO_4$. The solvent was removed under reduced pressure and the light pink solid formed was suspended in hexane and stirred for 30 min. The solid was subsequently filtered, dried on the frit and then dissolved in a MeOH:HCl (conc.) 60:40 mixture. After refluxing overnight the mixture was allowed to cool down to RT and was then poured into water. The pH was adjusted to 6 - 7 adding NaOH (2.0 M, aq.). The light brown solution was extracted with EtOAc (4 x 50 mL) and dried over $MgSO_4$. After removal of the solvent under reduced pressure, the desired product was obtained as a brown oil (1.94 g, 11.7 mmol, 35%).

^{1}H NMR (250 MHz, $CDCl_3$) δ / ppm 6.75 (d, *J* = 9.0 Hz, 2H, H^1), 6.64 (d, *J* = 9.0 Hz, 2H, H^2), 3.65 (d, *J* = 6.6 Hz, 2H, H^a), 3.24 (s (br), 2H, H^{NH2}), 2.05 (dh, *J* = 13.3, 6.8 Hz, 1H, H^b), 1.00 (d, *J* = 6.7 Hz, 6H, H^c).

5.4.3. Bis(4-isobutoxyphenyl)amine (11c)

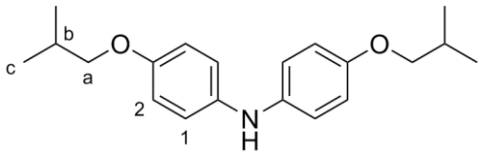

A round bottomed flask was charged with K_2CO_3 (1.21 g, 8.73 mmol, 2.0 eq.), CuI (83.1 mg, 0.436 mmol, 0.1 eq.) and L(-)-proline (100 mg, 0.873 mmol, 0.2 eq.) under an N_2 atmosphere. Then DMSO (20 mL) was added and stirred until most of the solid had dissolved. Then **11a** (1.50 g, 6.55 mmol, 1.5 eq.) and **11b** (721 mg, 4.36 mmol, 1.0 eq.) were added and the mixture heated to 90 °C for 3 d. Then water (50 mL) was added and extracted with EtOAc (3 x 25 mL). The combined organic phases were washed with brine and dried over $MgSO_4$. The solvent was removed under reduced pressure and the obtained brown oil subjected to column chromatography (SiO_2, Hexane:EtOAc 10:1 → 10:2 → 10:3 → 0:1) and then recrystallized from hexane. The brown oil so-obtained still contained some minor impurities, but was used without further purification (103 mg, 329 mmol, 7.6%).

^{1}H NMR (500 MHz, $CDCl_3$) δ / ppm 6.92 (d, *J* = 8.0 Hz, 4H, H^1), 6.81 (d, *J* = 8.9 Hz, 4H, H^2), 3.68 (d, *J* = 6.7 Hz, 4H, H^a), 2.05 (dh, *J* = 13.2, 6.6 Hz, 2H, H^b), 1.02 (d, *J* = 6.7 Hz, 12H, H^c).
MALDI-TOF MS (m/z): 313.0 $[M]^+$ (calc. 313.2), 314.0 $[M+H]^+$ (calc. 314.2).

5.4.4. 1-Bromo-4-(octyloxy)benzene (12a)[99]

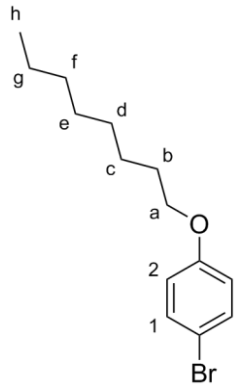

4-Bromophenol (5.00 g, 28.9 mmol, 1.0 eq.) was dissolved in 60 mL of acetone and K_2CO_3 (7.99 g, 57.8 mmol, 2.0 eq.) was added, the suspension was then stirred for 5 min until 1-bromooctane (6.03 mL, 34.7 mmol, 1.2 eq.) was added and the mixture heated to reflux for 3 d. After the mixture was allowed to cool to RT it was filtered and the solid remaining on the frit washed with acetone (3 x 25 mL). Then the solvent of the combined organic phases was removed under reduced pressure. Column chromatography (SiO_2, hexane 100%) yielded the desired product as a colourless oil; it still contained small amounts of 1-bromooctane, but was used without further purification (7.81 g, 27.4 mmol, 95%).

^{1}H NMR (400 MHz, $CDCl_3$) δ / ppm 7.36 (d, *J* = 9.0 Hz, 2H, H^1), 6.77 (d, *J* = 9.0 Hz, 2H, H^2), 3.91 (t, *J* = 6.6 Hz, 2H, H^a), 1.82 – 1.68 (m, 2H, H^b), 1.52 – 1.19 (m, 12H, $H^{c+d+e+f+g}$), 0.89 (t, *J* = 7.0 Hz, 3H, H^h).

5.4.5. 4-(Octyloxy)aniline (12b)[99]

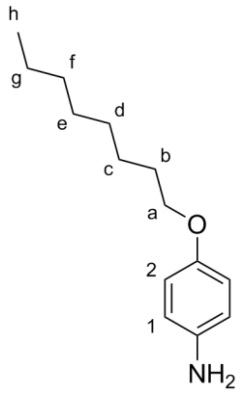

4-Acetamidophenol (5.00 g, 33.1 mmol, 1.0 eq.) was dissolved in 60 mL of acetone and K_2CO_3 (9.14 g, 66.2 mmol, 2.0 eq.) was added. The mixture was stirred for 15 min, then 1-bromooctane (6.91 mL, 39.7 mmol, 1.2 eq.) was added and the mixture heated to reflux for 3d. The mixture was allowed to cool to RT and was poured into 150 mL of water. The precipitate was filtered and washed with water. After being dried on the frit for 10 min, the solid was suspended in a MeOH:HCl (conc.) 60:40 mixture and heated at reflux for 1 d. The solution was subsequently poured into 200 mL of water while stirring and the pH was adjusted to 7, which lead to the precipitation of a white solid. The precipitate was filtered and washed with water (3 x 50 mL). The solid was recrystallized from acetone to yield a pale purple, crystalline solid (5.89 g, 26.6 mmol, 80%).

^{1}H NMR (400 MHz, $CDCl_3$) δ / ppm 6.90 (d, *J* = 8.9 Hz, 2H, H^1), 6.66 (d, *J* = 8.9 Hz, 2H, H^2), 3.78 (t, *J* = 6.6 Hz, 2H, H^a), 1.78 – 1.58 (m, 2H, H^b), 1.47 – 1.35 (m, 2H, H^c), 1.35 – 1.20 (m, 8H, $H^{d + e + f + g}$), 0.88 (t, *J* = 6.9 Hz, 3H, H^h).

5.4.6. Bis(4-(octyloxy)phenyl)amine (12c)

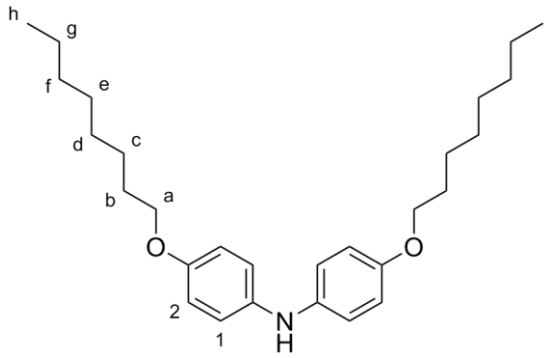

A round bottomed flask was charged with **12b** (1.50 g, 6.78 mmol, 1.0 eq.), K_2CO_3 (1.87 g, 13.6 mmol, 2.0 eq), CuI (129 mg, 0.678 mmol, 0.1 eq.) and L(-)-proline (156 mg, 1.36 mmol, 0.2 eq.) under an N_2 atmosphere. Then DMSO (20 mL) was added and stirred until most of the solid had dissolved. **12a** (2.90 g, 10.2 mmol, 1.5 eq.) was added and the mixture was heated at 90 °C for 4 d. Then water (50 mL) was added and extracted with EtOAc (3 x 25 mL). The combined organic phases were washed with brine and dried over $MgSO_4$. The solvent was removed under reduced pressure and the brown oil was subjected to column chromatography (SiO_2, Hexane:EtOAc 1:0 → 20:1 → 10:1 → 10:2 → 0:1) and twice recrystallized from hexane. The product was obtained as a white solid (320 mg, 0.752 mmol, 11%).

^{1}H NMR (400 MHz, $CDCl_3$) δ / ppm 6.92 (d, *J* = 8.9 Hz, 4H, H^1), 6.81 (d, *J* = 8.9 Hz, 4H, H^2), 3.91 (t, *J* = 6.6 Hz, 4H, H^a), 1.82 – 1.69 (m, 4H, H^b), 1.51 – 1.38 (m, 4H, H^c), 1.39 – 1.23 (m, 16H, $H^{d + e + f + g}$), 0.88 (t, *J* = 6.9 Hz, 6H, H^h).
LC-ESI (m/z): 426.4 $[M+H]^+$ (calc. 426.3).

5.4.7. 4-([2,2':6',2''-Terpyridin]-4'-yl)-*N*,*N*-bis(4-isobutoxyphenyl)aniline (13)

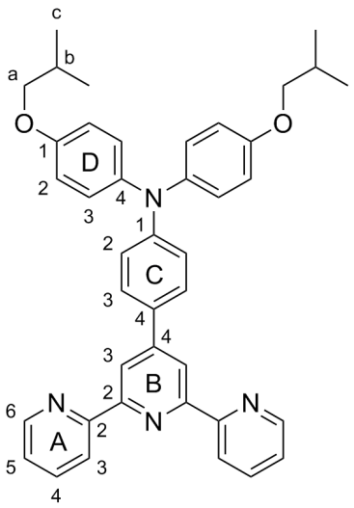

A round bottomed flask was charged with 4'-(4-bromophenyl)-2,2':6',2''-terpyridine (113 mg, 0.290 mmol, 1.0 eq.), **11c** (100 mg, 0.319 mmol, 1.1 eq.) and NaO^{t}Bu (36.2 mg, 0.377 mmol, 1.3 eq.) under an N_2 atmosphere. Toluene (20 mL) was added and the mixture vigorously stirred for 5 min to remove O_2. $Pd(dba)_2$ (3.34 mg, 5.80 µmol, 0.02 eq.) and P(^{t}Bu)$_3$ (6 µL, 5.80 µmol, 0.02 eq.) were added and the mixture heated at 100 °C for 20 h under N_2. The hot mixture was filtered into a hot Erlenmeyer flask to give a reddish filtrate. The solvent was removed under reduced pressure and the obtained solid subjected to column chromatography (SiO_2, toluene:EtOAc 1:0 → 20:1 → 10:1 → 10:2 → 2:1 → 1:1 → 0:1) to yield the desired product as a light yellow solid (81.0 mg, 0.130 mmol, 45%).

^{1}H NMR (500 MHz, THF-d_8) δ / ppm 8.79 (s, 2H, H^{B3}), 8.72 – 8.69 (m, 2H, H^{A3}), 8.67 (ddd, J = 4.8, 1.9, 0.9 Hz, 2H, H^{A6}), 7.91 – 7.86 (m, 2H, H^{A4}), 7.73 (d_{AB}, J = 8.7 Hz, 2H, H^{C3}), 7.35 (ddd, J = 7.4, 4.7, 1.2 Hz, 2H, H^{A5}), 7.09 (d_{AB}, J = 9.0 Hz, 4H, H^{D3}), 7.03 (d_{AB}, J = 8.7 Hz, 2H, H^{C2}), 6.88 (d_{AB}, J = 9.0 Hz, 4H, H^{D2}), 3.73 (d, J = 6.4 Hz, 4H, H^a), 2.13 – 1.99 (m, J = 6.7 Hz, 2H, H^b), 1.04 (d, J = 6.7 Hz, 12H, H^c).

^{13}C NMR (126 MHz, THF-d_8) δ / ppm 157.0 (C^{A2}), 157.0 (C^{D1}), 156.6 (C^{B2}), 150.8 (C^{C4}), 150.3 (C^{C1}), 149.8 (C^{A6}), 141.1 (C^{D4}), 137.2 (C^{A4}), 130.4 (C^{B4}), 128.3 (C^{C2}), 127.6 (C^{D2}), 124.3 (C^{A5}), 121.4 (C^{A3}), 120.6 (C^{C3}), 118.2 (C^{B3}), 115.9 (C^{D3}), 75.0 (C^a), 29.2 (C^b), 19.4 (C^c).

ESI MS (m/z): 621.6 $[M+H]^+$ (calc. 621.3).

HR ESI-MS (m/z): 621.3223 $[M+H]^+$ (calc. 621.3224).

5.4.8. 4-([2,2':6',2''-Terpyridin]-4'-yl)-*N*,*N*-bis(4-(octyloxy)phenyl)aniline (14)

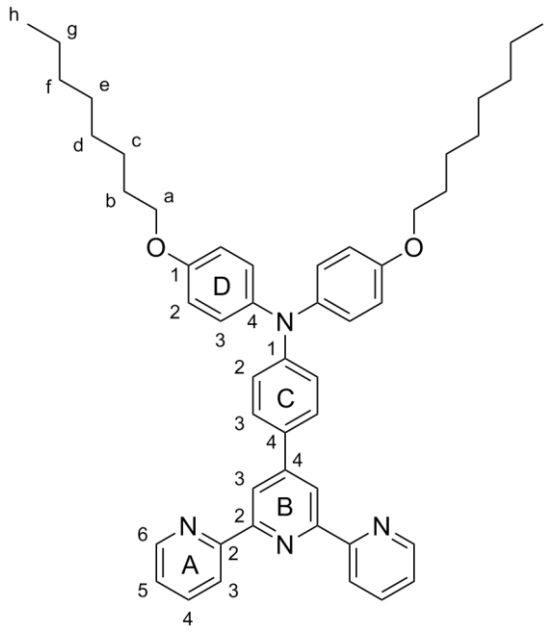

A round bottomed flask was charged with 4'-(4-bromophenyl)-2,2':6',2''-terpyridine (166 mg, 0.427 mmol, 1.0 eq.), **12c** (200 mg, 0.470 mmol, 1.1 eq.) and NaO^{t}Bu (53.4 mg, 0.555 mmol, 1.3 eq.) under N_2 atmosphere. Toluene (20 mL) was added and the mixture vigorously stirred for 5 min to remove O_2. $Pd(dba)_2$ (4.91 mg, 8.54 µmol, 0.02 eq.) and P(^{t}Bu)$_3$ (8 µL, 8.54 µmol, 0.02 eq.) were added and the mixture heated at 100 °C for 20 h under N_2. The hot mixture was filtered into a hot Erlenmeyer flask to give a reddish filtrate. The solvent was removed under reduced pressure and the obtained solid subjected to column chromatography (SiO_2, toluene:EtOAc 1:0 → 10:1 → 10:4 → 2:1 → 1:1 → 0:1) to yield the desired product as a light yellow solid (250 mg, 0.341 mmol, 80%).

^{1}H NMR (500 MHz, $CDCl_3$) δ / ppm 8.72 (ddd, *J* = 4.8, 1.8, 0.9 Hz, 2H, H^{A6}), 8.68 (s, 2H, H^{B3}), 8.67 – 8.64 (m, 2H, H^{A3}), 7.90 – 7.83 (m, 2H, H^{A4}), 7.74 (d_{AB}, *J* = 8.8 Hz, 2H, H^{C3}), 7.34 (ddd, *J* = 7.5, 4.8, 1.2 Hz, 2H, H^{A5}), 7.10 (d_{AB}, *J* = 8.9 Hz, 4H, H^{D3}), 7.01 (d_{AB}, *J* = 8.8 Hz, 2H, H^{C2}), 6.85 (d_{AB}, *J* = 8.9 Hz, 4H, H^{D2}), 3.95 (t, *J* = 6.6 Hz, 4H, H^a), 1.84 – 1.75 (m, 4H, H^b), 1.52 – 1.42 (m, 4H, H^c), 1.40 – 1.26 (m, 16H, $H^{d + e + f + g}$), 0.93 – 0.87 (m, 6H, H^h).

^{13}C NMR (126 MHz, $CDCl_3$) δ / ppm 156.7 (C^{A2}), 155.91 ($C^{D1/B2}$), 155.90 ($C^{B2/D1}$), 150.0 (C^{C1}), 149.86 (C^{C4}), 149.2 (C^{A6}), 140.4 (C^{D4}), 137.0 (C^{A4}), 129.6 (C^{B4}), 128.0 (C^{C2}), 127.1 (C^{D2}), 123.8 (C^{A5}), 121.5 (C^{A3}), 120.0 (C^{C3}), 118.1 (C^{B3}), 115.5 (C^{D3}), 68.4 (C^{a}), 32.0 ($C^{d/e/f/g}$), 29.6 ($C^{d/e/f/g}$), 29.5 (C^{b}), 29.4 ($C^{d/e/f/g}$), 26.3 (C^{c}), 22.8 ($C^{d/e/f/g}$), 14.3 (C^{h}).
ESI MS (m/z): 733.7 $[M+H]^+$ (calc. 733.4), 755.7 $[M+Na]^+$ (calc. 755.4).
HR ESI-MS (m/z): 733.4482 $[M+H]^+$ (calc. 733.4476), 755.4300 $[M+Na]^+$ (calc. 755.4295).

5.4.9. 4-([2,2':6',2''-Terpyridin]-4'-yl)-*N*,*N*-bis(4-butoxyphenyl)aniline (15)

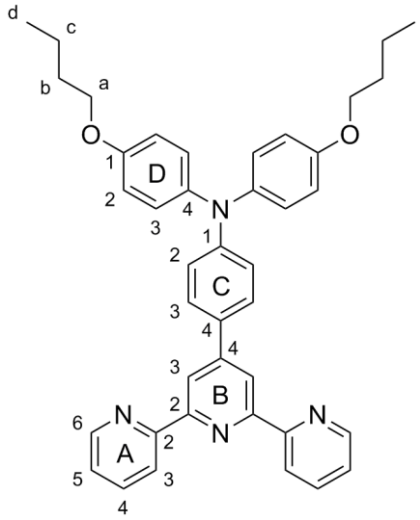

A round bottomed flask was charged with 4'-(4-bromophenyl)-2,2':6',2''-terpyridine (500 mg, 1.29 mmol, 1.0 eq.), bis(4-*n*-butoxyphenyl)amine (404 mg, 1.29 mmol, 1.0 eq.) and NaO^{t}Bu (161 mg, 1.67 mmol, 1.3 eq.) under an N_2 atmosphere. Toluene (20 mL) was added and the mixture vigorously stirred for 5 min to remove O_2. $Pd(dba)_2$ (14.8 mg, 25.8 µmol, 0.02 eq.) and $P(^tBu)_3$ (26 µL, 25.8 µmol, 0.02 eq.) were added and the mixture heated at 100 °C for 20 h under N_2. The hot mixture was filtered into a hot Erlenmeyer flask to give a reddish filtrate. The solvent was removed under reduced pressure and the obtained solid recrystallized from EtOH and then subjected to column chromatography (basic Al_2O_3, hexane:EtOAc 10:1) to yield the desired product as a light yellow solid (152 mg, 0.245 mmol, 19%).

^{1}H NMR (500 MHz, $CDCl_3$) δ / ppm 8.72 (ddd, *J* = 4.8, 1.9, 1.0 Hz, 2H, H^{A6}), 8.68 (s, 2H, H^{B3}), 8.67 – 8.64 (m, 2H, H^{A3}), 7.89 – 7.84 (m, 2H, H^{A4}), 7.74 (d, *J* = 8.8 Hz, 2H, H^{C3}), 7.34 (ddd, *J* = 7.4, 4.8, 1.2 Hz, 2H, H^{A5}), 7.10 (d, *J* = 8.9 Hz, 4H, H^{D3}), 7.01 (d, *J* = 8.8 Hz, 2H, H^{C2}), 6.85 (d, *J* = 9.0 Hz, 4H, H^{D2}), 3.96 (t, *J* = 6.5 Hz, 4H, H^{a}), 1.82 – 1.74 (m, 4H, H^{b}), 1.56 – 1.46 (m, 4H, H^{c}), 0.99 (t, *J* = 7.4 Hz, 6H, H^{d}).

^{13}C NMR (126 MHz, $CDCl_3$) δ / ppm 156.6 (C^{A2}), 155.9 ($C^{D1/B2}$), 155.9 ($C^{D1/B2}$), 150.0 (C^{C4}), 149.9 (C^{C1}), 149.2 (C^{A6}), 140.4 (C^{D4}), 137.0 (C^{A4}), 129.6 (C^{B4}), 128.0 (C^{C3}), 127.1 (C^{D3}), 123.8 (C^{A5}), 121.5 (C^{A3}), 120.0 (C^{C2}), 118.1 (C^{B3}), 115.5 (C^{C2}), 68.1 (C^{a}), 31.6 (C^{b}), 19.4 (C^{c}), 14.0 (C^{d}).

ESI MS (m/z): 621.4 $[M+H]^+$ (calc. 621.3).

HR ESI-MS (m/z): 621.3226 $[M+H]^+$ (calc. 621.3224).

Chapter 6

Chapter 6: Design of new sensitizers for DSCs, based on the BTZ building block

In the previous two chapters it was shown that DSCs using Zn(II) bis-terpyridine complexes do indeed work, although not very efficiently. The aim of the work presented in this chapter was to design and synthesize a ligand that shows more efficient light harvesting properties on one hand and a broader absorption range on the other. This can be achieved by either expanding the π-system[100] or by the use of so-called push-pull systems[101], which consist of donor or acceptor subunits within the molecule, or both.

The newly designed molecule should consist of three main parts. First of all there is a need for a suitable ligating part. In this case it was planned to use zinc(II) dyes again, so a terpyridine unit was chosen, which was well established in the earlier chapters. To construct a push-pull system it was also important to find a donor molecule which is also easy to handle. Using the knowledge from previous studies a diphenylamine donor was chosen. The main focus was on the choice of an acceptor building block which was already known in the literature and easy to integrate synthetically. A very promising candidate was the benzothiadiazole (BTZ) unit which is commercially available as 4,7-dibromobenzo[c][1,2,5]thiadiazole and offers two sites for further coupling reactions. Furthermore, SciFinder® delivers almost 8000 publications in which the BTZ building block was used as a reagent or reactant and almost 7000 of them from the year 2009 until now (as at October 09th 2014). This confirms the importance of this unit.

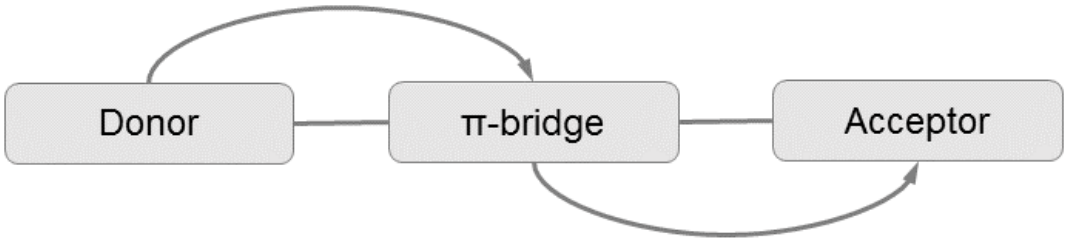

Figure 6-1: Scheme of a Donor-π-Acceptor system.

In a donor acceptor system (Figure 6-1) one tries to connect an electron rich donor to an electron poor acceptor. Very often these two units are connected via a π-bridge that spatially separates the donor from the acceptor while still keeping them connected

electronically. π-Bridges can have an influence on the electronic properties of the whole molecule, influencing the energy levels of both donor and acceptor, and hence also the absorption properties of the molecule.[102]

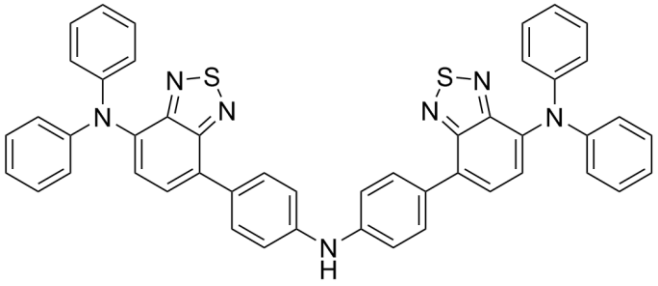

21

*Scheme 6-1: Targeted, very versatile donor-acceptor molecule (**21**).*

A straightforward synthetic route was developed to produce a molecule that includes both donor and acceptor moieties. Furthermore, the targetted molecule must be very easily attachable to ligating or anchoring groups and therefore offers a certain variability.

Scheme 6-1 shows the proposed molecular unit. It combines a diphenylamine donor with a BTZ acceptor unit and, due to the secondary amine, is very easily subjected to palladium catalysed coupling reactions.

6.1. Ligand synthesis

Scheme 6-2 shows the first step of the synthetic route to target molecule **21**. Diphenylamine is reacted with 4,7-dibromobenzo[c][1,2,5]thiadiazole in a palladium catalysed Hartwig-Buchwald reaction to give building block **16**.

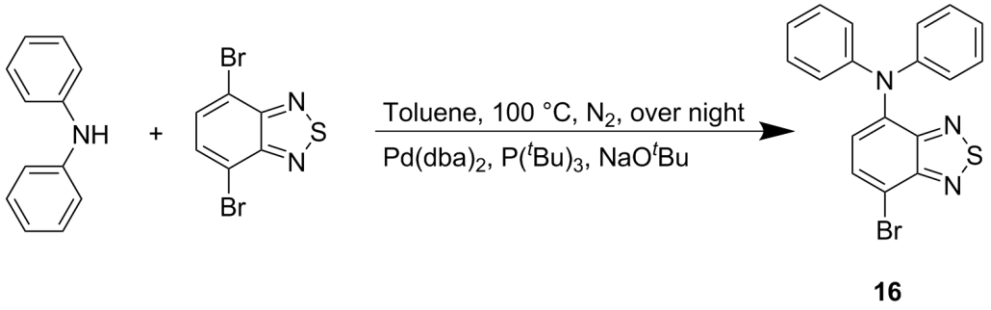

*Scheme 6-2: First synthetic step towards target molecule **16**.*

As the second step, it was planned to convert **16** into the corresponding boronic acid pinacol ester using *n*-BuLi to perform a halogen-lithium-exchange. The activated BTZ derivative could then be reacted with 2-isopropoxy-4,4,5,5-tetramethyl-1,3,2-dioxaborolane to form building block **17** (Scheme 6-3). Unfortunately this step did not lead to the desired product. It is possible that the homocoupled product was formed instead of the desired compound.

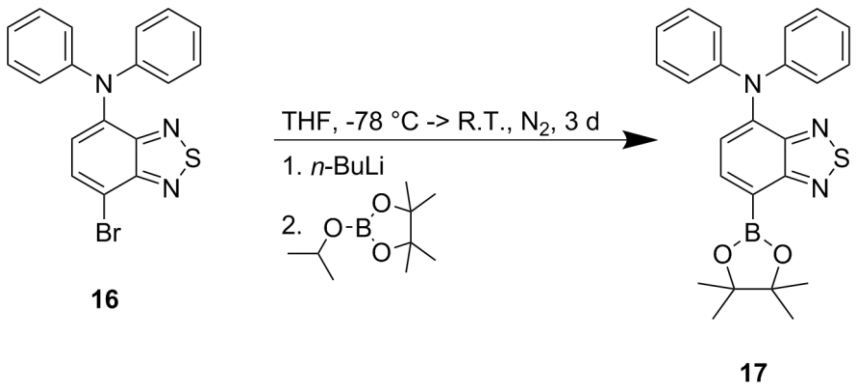

*Scheme 6-3: Unsuccessful synthetic step to **17**.*

To overcome this problem, the strategy was altered in a way that **16** does not have to be further modified. This means that the boronic acid pinacol ester has to be inserted into its reaction partner, namely the diphenylamine, as Scheme 6-4 shows. In a first step the bis(4-bromophenyl)amine was *N*-protected with Boc to obtain compound **18**. This was done by the reaction of bis(4-bromophenyl)amine with Boc_2O in dry THF and DMAP as catalyst. In a second step, the protected amine was subjected to a borylation as described above to obtain compound **19** (Scheme 6-4)

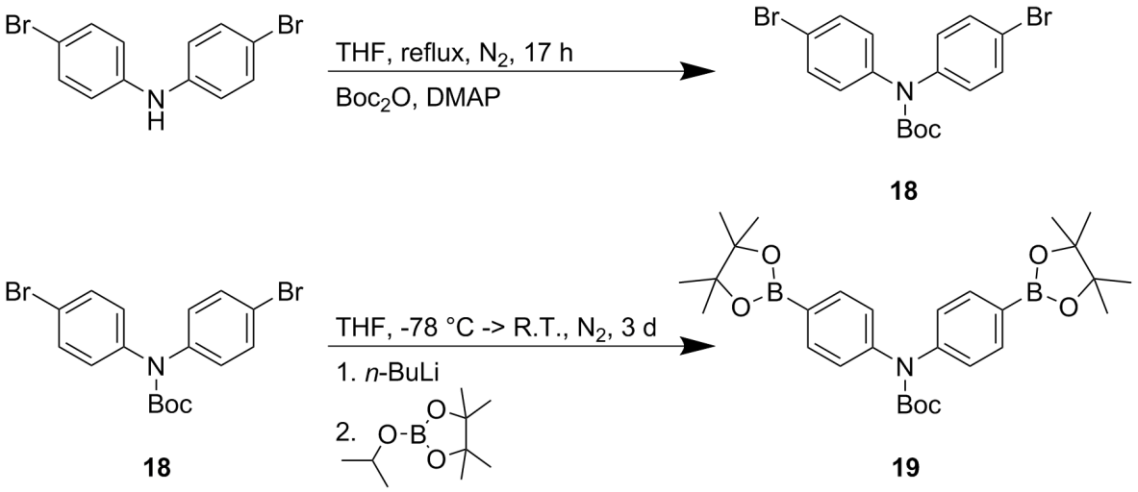

*Scheme 6-4: Synthesis of **18** and **19**.*

The next step of the synthesis was the coupling of **16** and **19** using a Hartwig-Buchwald reaction.[77] Compounds **16** and **19** were reacted under basic conditions in toluene catalysed by $Pd(dba)_2$ and $P(^tBu)_3$ (Scheme 6-5).

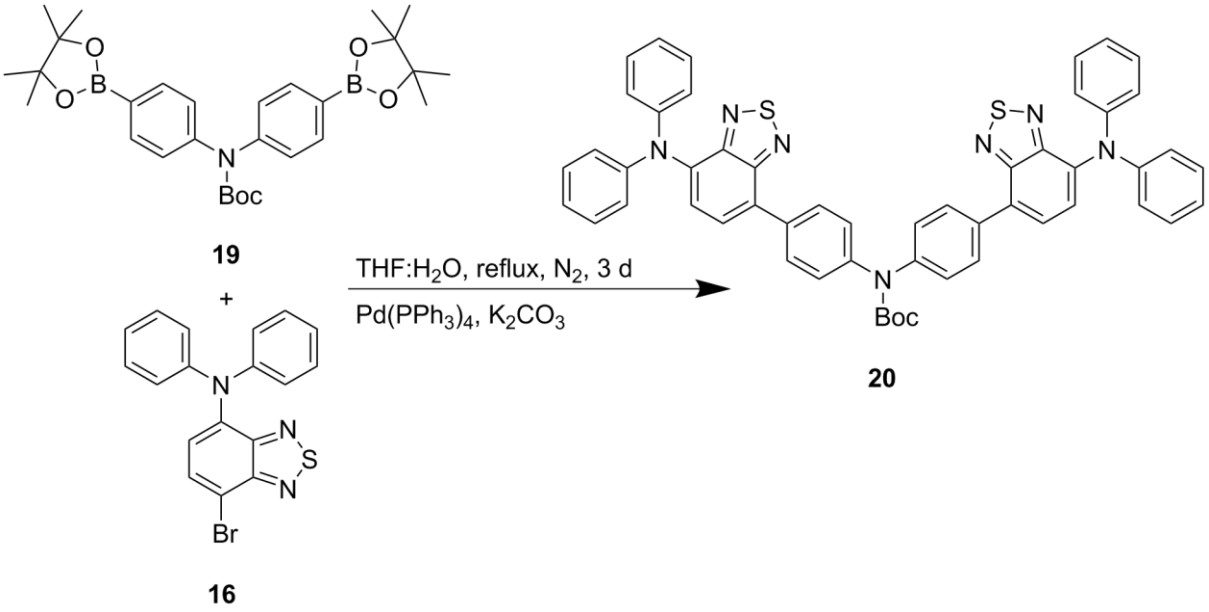

*Scheme 6-5: Hartwig-Buchwald[77] reaction to synthesize **20**.*

To synthesize compound **21** (Scheme 6-1) it was necessary to deprotect compound **20**. Several different methods were evaluated.

Table 6-1 shows the different deprotection reaction conditions used for the synthesis of **20**. Three different reactions with different reaction times and different amounts of TFA were tried. None of these was successful.

Solvent	Temperature	eq. TFA	Reaction time
Acetone	RT	450	Over night
Acetone	RT	10	Over night
Acetone	RT	10	3 d
Ph_2O	200 °C	0	18 h
-	210 °C	0	1 h

*Table 6-1: Tested deprotecting methods for **20**.*

The thermal deprotection in Ph_2O was successful, but the workup turned out to be rather time-consuming, because of the high boiling point of the Ph_2O. Finally, a solvent-free thermal deprotection in an oven at 210 °C proved to be successful. This process has the advantage of taking only 1 h.

Compound **21** was reacted in a Hartwig-Buchwald coupling[77] with 4'-(4-bromophenyl)-2,2':6',2''-terpyridine to produce ligand **22** (Scheme 6-6). This ligand can be combined with zinc(II) ions and an anchoring ligand to obtain a metal containing dye that can be built according to the step-wise protocol, introduced in Chapter 4.

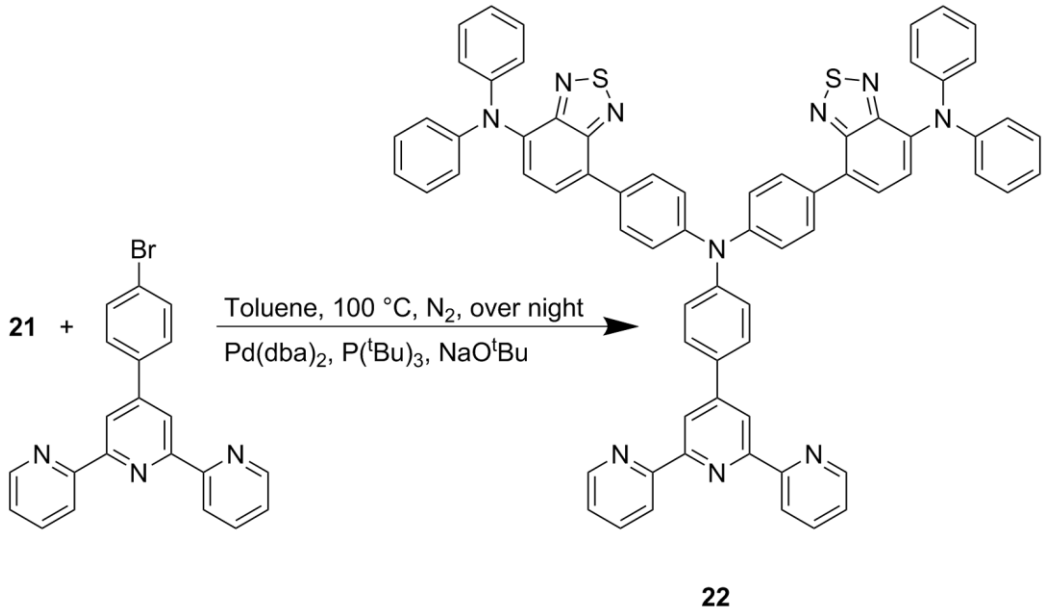

*Scheme 6-6: Synthesis of **22**.*

Alternatively, **21** could be reacted[77] with 4-bromobenzaldehyde to give compound **23** (Scheme 6-7). This compound offers an aldehyde functionality, which can easily undergo various condensation reactions.

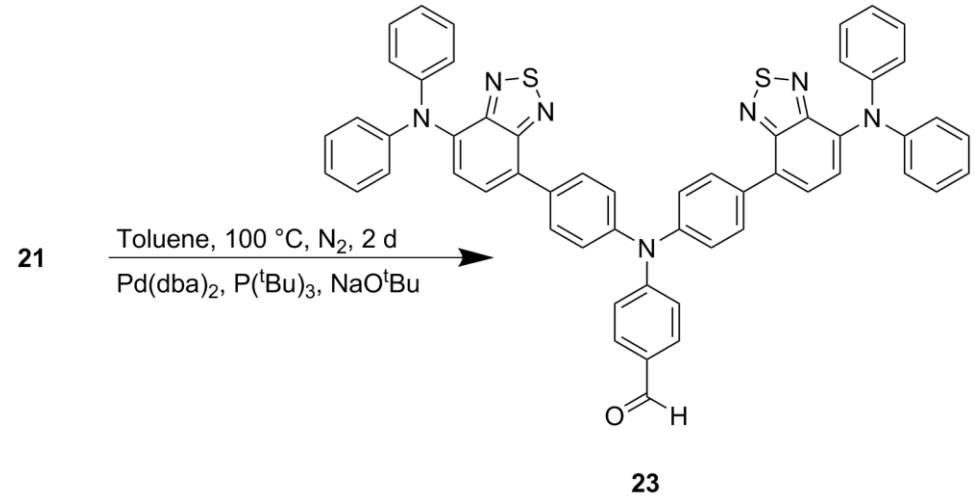

*Scheme 6-7: Synthesis of aldehyde **23**.*

Compound **23** was then reacted with 2-cyanoacetic acid in a piperidine catalyzed Knoevenagel condensation to give the organic dye **24** with a cyanoacrylic acid anchoring group, which is widely used as an anchoring group for organic dyes.[45]

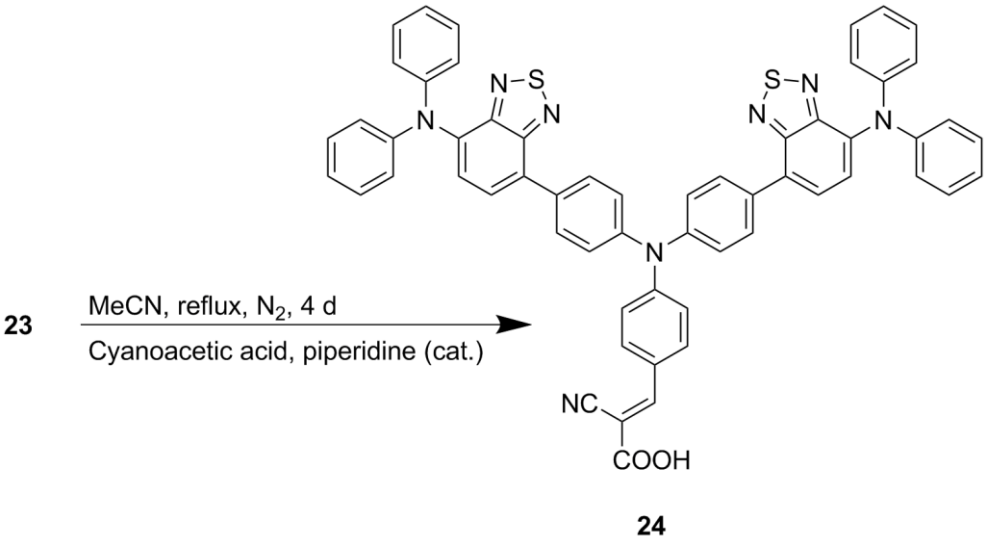

*Scheme 6-8: Knoevenagel condensation to produce organic dye **24**.*

6.2. Crystal structure

Figure 6-2 shows an X-ray structure of compound **16**. It is easy to see that the diphenylamine arene rings are not in the same plane as the BTZ unit. The angle between the two planes is 54.6°. Hydrogen atoms were omitted for clarity.

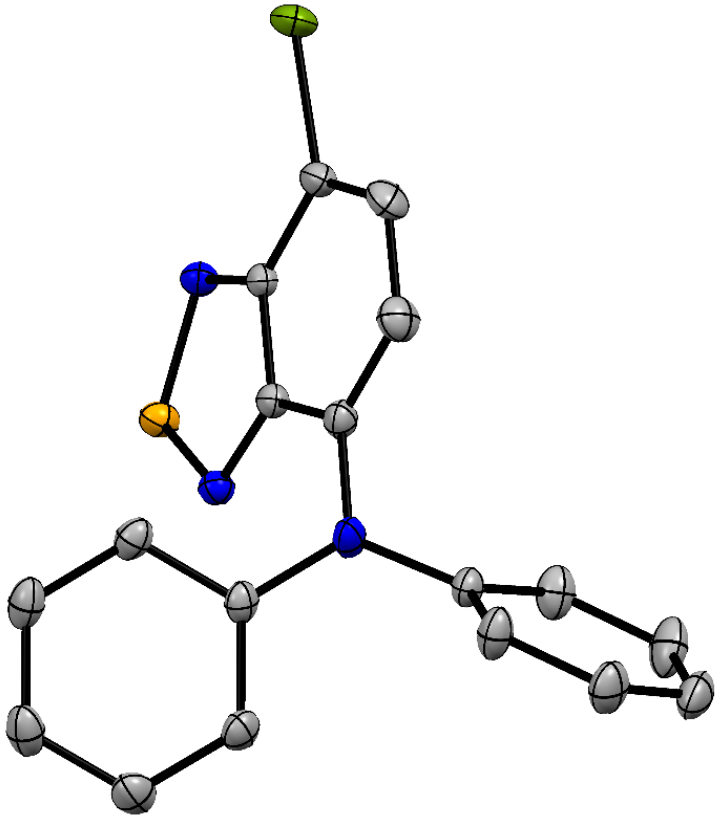

*Figure 6-2: X-ray structure of **16**.*
Monoclinic, $P2_1/c$, a = 8.6692(11), b = 19.013(3), c = 9.9653(14) Å, β = 104.512(7)°. Bond lengths and angles are unexceptional.

6.3. Results and discussion

6.3.1. Computational energy level calculations

The molecular orbital compositions of the ligand **22** and the corresponding zinc(II) dye with anchoring ligand **10**, were investigated using semi empirical (PM3) computational calculations carried out by Prof. Dr. Catherine E. Housecroft to get an impression of the energy levels, mainly about the localisation of the HOMO and LUMO in the compounds.

Figure 6-3 shows the distribution of the HOMO in compound **22**. It is mainly located on the central triphenylamine unit.

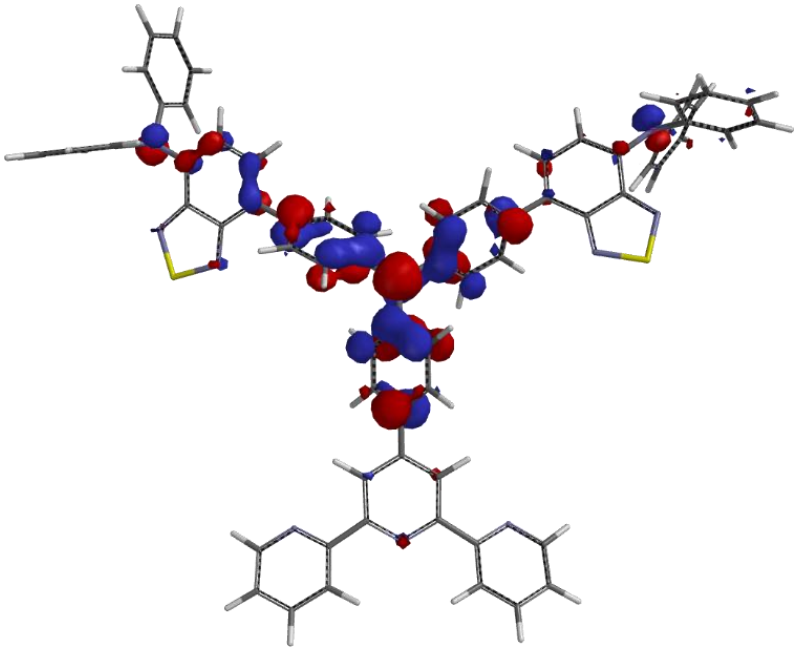

*Figure 6-3: Distribution of the HOMO in **22**.*

In Figure 6-4 one can see the distribution of the LUMO and LUMO+1 in compound **22**. The two orbitals are completely located on the BTZ unit. This makes sense because the BTZ is meant to be the electron acceptor in this compound. This observation shows that in compound **22** LUMO and LUMO+1 lie where they would be expected. These calculations do not give any information about the energy level distribution in a dye configuration. Furthermore, they do not allow conclusions about the energy level distribution in the excited state.

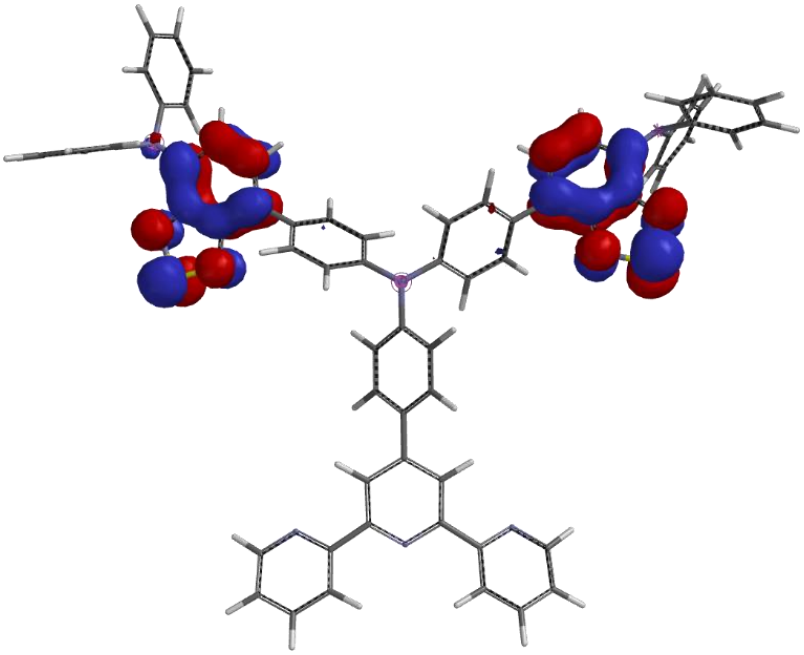

*Figure 6-4: Distribution of the LUMO and LUMO+1 in **22**.*

The calculations done on compound [(**10**)Zn(**22**)]Cl_2 show a much more realistic picture of the energy distribution in this dye, since it takes the influences of the anchoring ligand into account. However, it has to be noted that potential influences of the semiconductor surface on these energy levels are not taken into account. In Figure 6-5 the HOMO and HOMO+1 of compound [(**10**)Zn(**22**)]Cl_2 are depicted and it can be seen that they are located on the peripheral diphenylamine unit and partially on the BTZ unit.

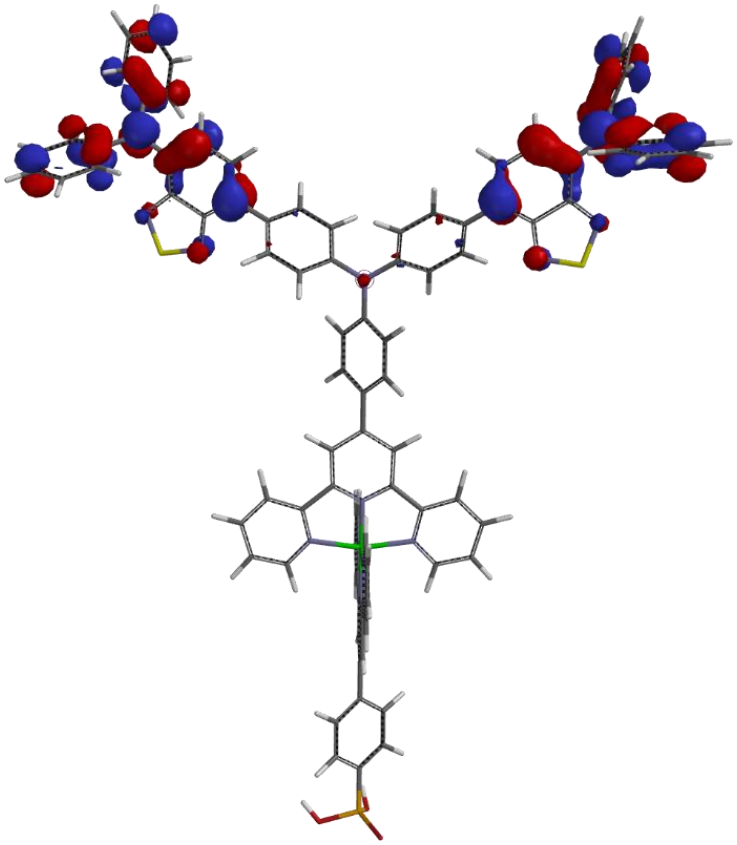

*Figure 6-5: Distribution of the HOMO plus HOMO+1 in [(**10**)Zn(**22**)]Cl_2.*

Figure 6-6 reveals that the LUMO in (**10**)Zn(**22**)]Cl_2 is located on the terpyridine unit of anchoring ligand **10**. This shows that theoretically the LUMO is located on the side of the anchoring ligand, which is as one would expect. For solar cell applications, it is important that the LUMO lies on the anchoring ligand and guarantees that the excited photon is directed towards the semiconductor surface where it can be injected.

From these calculations it can be assumed that in [(**10**)Zn(**22**)]Cl_2 the energy levels are distributed in an appropriate manner. As already mentioned, these calculations do not show the influence on the energy levels induced by the anchoring of the molecule on the TiO_2 surface.

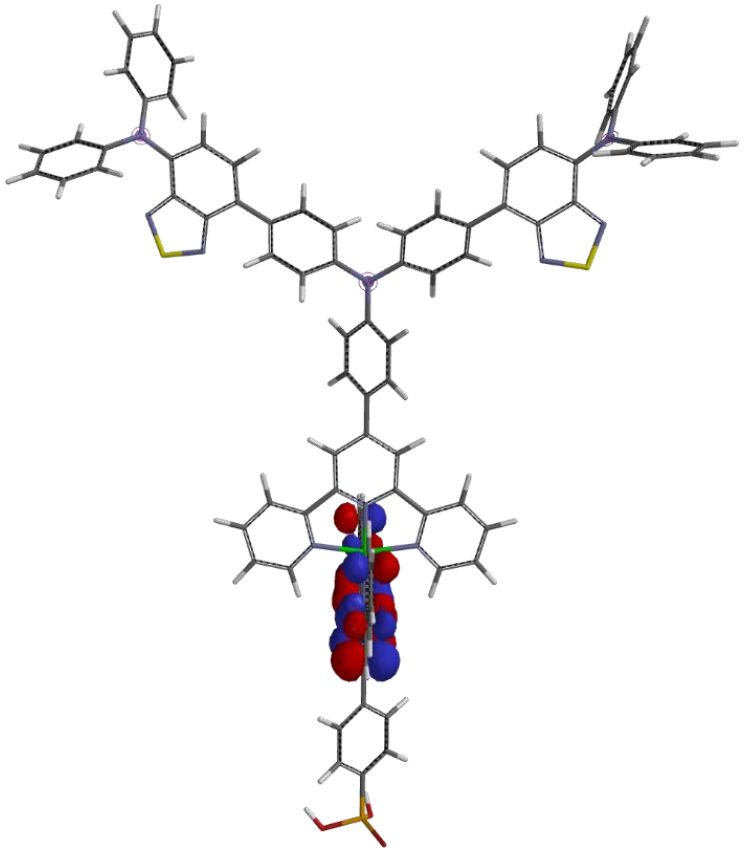

*Figure 6-6: Distribution of the LUMO in [(**10**)Zn(**22**)]Cl_2.*

6.3.2. Solid state electronic absorption

Figure 6-7 shows the solid state electronic absorption spectra of [(**8**)Zn(**22**)]Cl_2, [(**10**)Zn(**22**)]Cl_2 and N719 as a comparison. The absorption spectrum of N719 indicates a broad and intensive absorption over almost the whole visible range. Dyes [(**8**)Zn(**22**)]Cl_2 and [(**10**)Zn(**22**)]Cl_2 show also a quite nice absorption range between approximately 600 nm and 400 nm. Below 400 nm the TiO_2 starts to absorb light as well. Although the two dyes containing different anchoring ligands show almost the same absorption behaviour it seems that one can again find the trend already observed in previous chapters, namely that anchoring ligand **10** performs slightly better than **8**. Figure 6-7 shows that the investigated zinc(II) complexes, in contrast to N719, lack a broad enough absorption range.

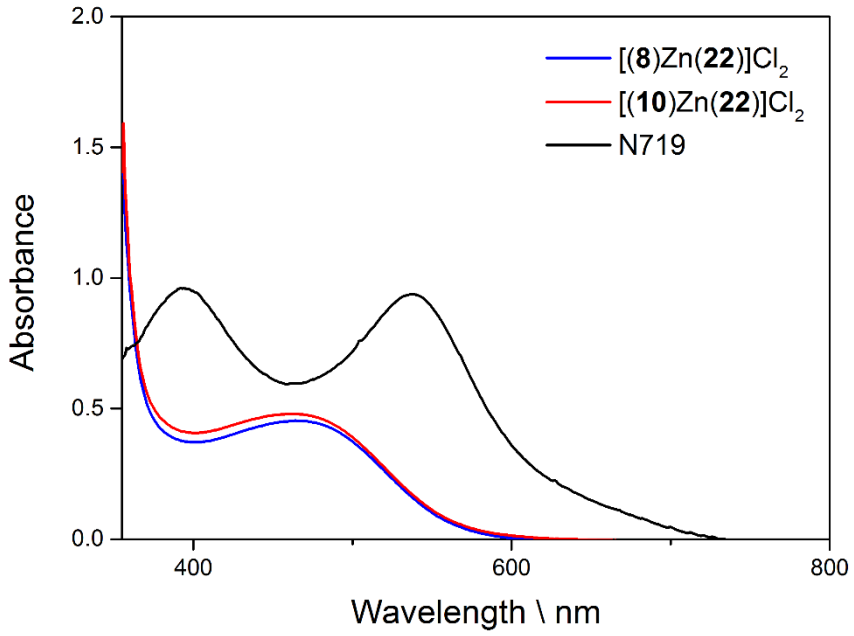

*Figure 6-7: Solid state electronic absorption spectra of [(**8**)Zn(**22**)]Cl_2, [(**8**)Zn(**22**)]Cl_2 and N719.*

Figure 6-8 shows the solid state electronic absorption spectrum of **24**, compared to N719. Reasons for the noisy spectrum of **24** could be that more of the organic dye is adsorbed on the semiconductor surface compared to the zinc(II) containing dyes. This could be because of a difference in the size and hence a different arrangement on the surface. It is also possible that not only a monolayer is formed. The very high dye

loading then leads to the absorption of almost all the photons over the absorption range of the dye, which brings the spectrophotometer to its detection limit.
Dye **24** also shows an absorption range between 400 nm and 600 nm.

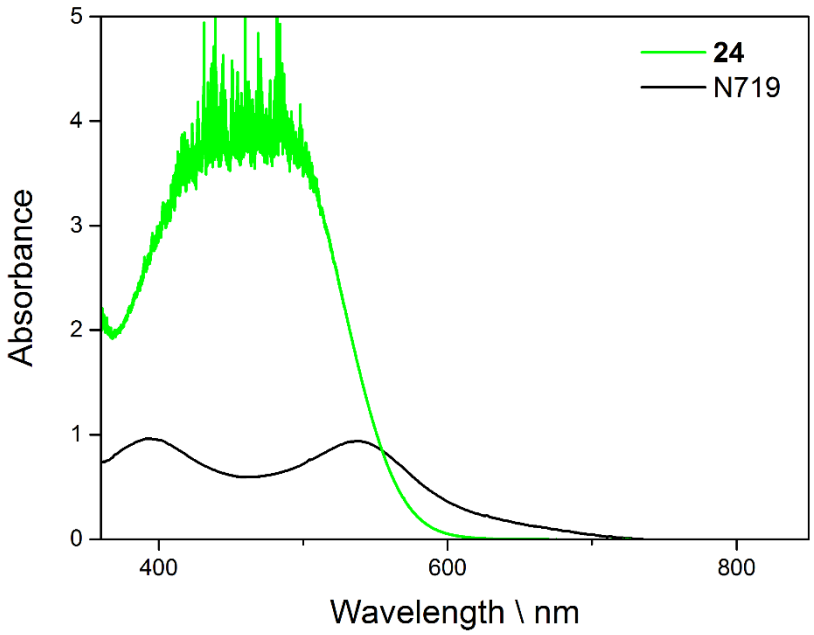

*Figure 6-8: Solid state electronic absorption spectra of **24** and N719.*

6.3.3. Solution electronic absorption

The electronic absorption spectrum of **22** (Figure 6-9) in CH_2Cl_2 shows local maxima, at 252 nm and 303 nm. These bands most probably arise from high energy intramolecular π* ← π transitions. The maximum at 488 nm is the lowest in energy. Looking at the computational calculations of ligand **22** this suggests it being a transition from the electron rich central triphenylamine to the electron poor and therefore electron accepting BTZ unit. This intramolecular charge transfer transition (π* ← n) tails out to about 600 nm and is also responsible for the red colour of the compound. The shoulder at 360 nm may be attributed to another π* ← n transition. It looks very similar to the transition at 488 nm and the computational calculations show that the HOMO-1 and HOMO-2 lie on the peripheral diphenylamine units. This might suggest that it is a charge transfer from the diphenylamine lone pair to the LUMO which is situated on the electron accepting BTZ unit. This being a charge transfer from the HOMO-1 or HOMO-2 to the LUMO leads to a transition higher in energy. These assumptions are based on the computational calculations, based on PM3 level.

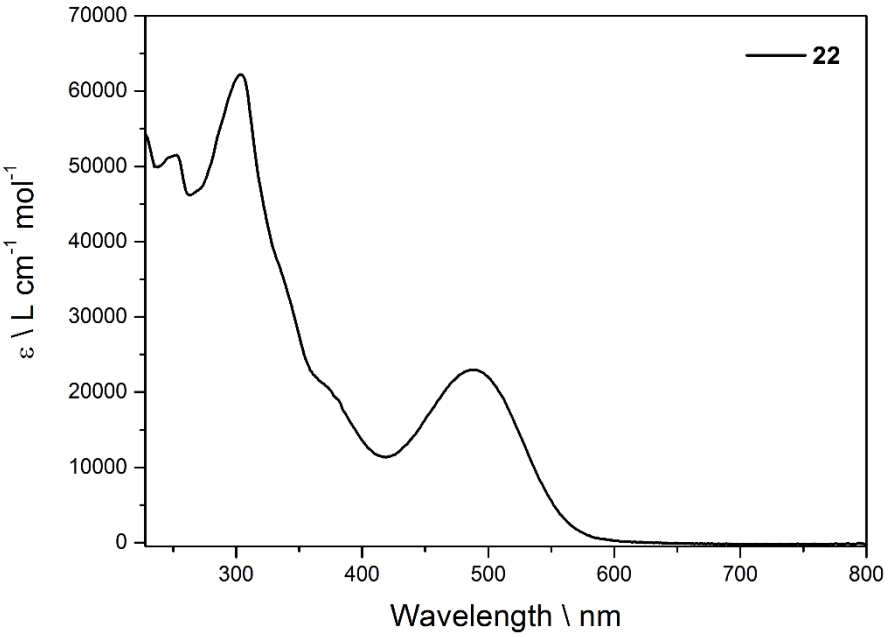

*Figure 6-9: Solution electronic absorption spectrum of **22** in CH_2Cl_2 (conc. = 3 x 10^{-6} mol L^{-1}).*

Figure 6-10 shows the solution electronic absorption spectrum of organic dye **24**. It shows high energy π* ← π transitions between 300 nm and 360 nm. The visible range of the spectrum shows maxima at 439 nm and 474 nm. Since there are no computational data available for this compound there are no hints where these transitions originate from, but from the calculations for compound **22** and their structural similarity it can be claimed that their origin is of similar nature. The absorption at 474 nm is the lowest in energy that is found in the spectrum. It can be speculated that the LUMO again lies on the BTZ and the HOMO on one of the polyphenylamine units. This is very speculative and the strongly electron withdrawing cyanoacrylic acid anchoring group undoubtedly has a strong influence on the energy levels in the molecule.

The low energy absorption tails out to about 600 nm and is again responsible for the red colour of the compound.

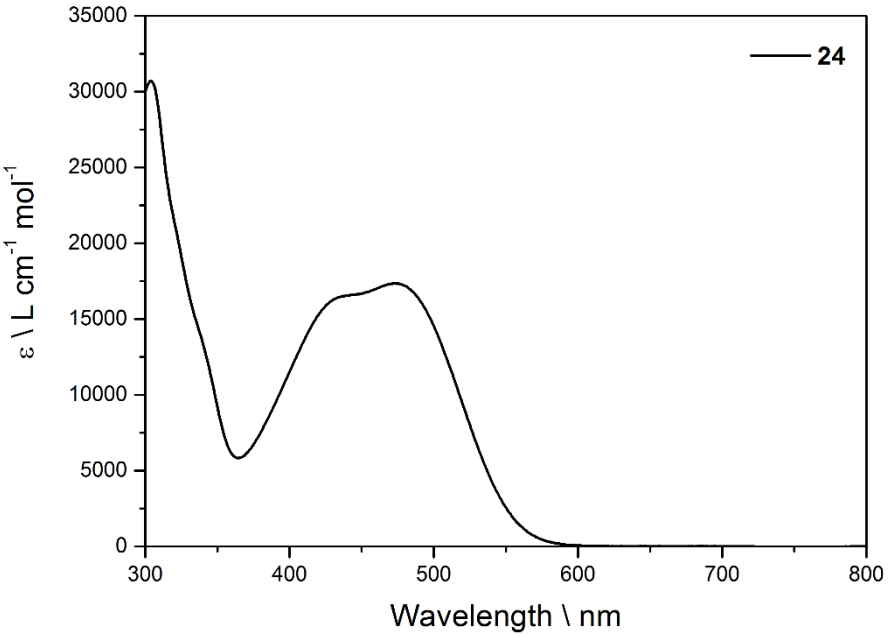

*Figure 6-10: Solution electronic absorption spectrum of **24** in THF (conc. = 5 x 10^{-5} mol L^{-1}.).*

6.3.4. Solar cell measurements

Picture 6-1 shows electrodes without scattering layer containing dyes [(**10**)Zn(**22**)]Cl_2 and **24**. One can immediately see the colour difference between the two samples, which supports the observations made in the solid state electronic absorption spectra of these dyes.

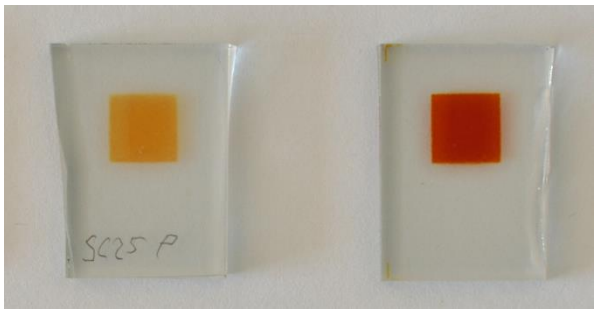

*Picture 6-1: Image of electrodes incorporating [(**10**)Zn(**22**)]Cl_2 (left) and **24** (right). Picture taken by Danielle Hayoz.*

All cells were measured while masked, to avoid false values because of scattered light (average measured area: 0.06012 cm^2). The cells with dye containing ancillary

ligand **22** were measured on the assembly day, 3 days and 17 days after. The cells containing dye **24** were measured on the assembly day, two days and 14 days after. The results of the solar cell measurements of dyes [(**8**)Zn(**22**)]Cl_2, [(**10**)Zn(**22**)]Cl_2 and **24** are shown in Table 6-2 and Table 6-3.

6.3.4.1. Dyes [(8)Zn(22)]Cl_2 and [(10)Zn(22)]Cl_2

The cells containing dyes [(**8**)Zn(**22**)]Cl_2 and [(**10**)Zn(**22**)]Cl_2 perform very poorly. The highest efficiency is around 0.13%, reached by dye [(**8**)Zn(**22**)]Cl_2 on the day of assembly and [(**10**)Zn(**22**)]Cl_2 on the third day after assembly. The highest J_{SC} is gained by the dye containing anchoring ligand **8** on the day of assembly. The highest V_{OC} is reached on the 17th day after the cells were assembled, by a cell containing anchoring ligand **10**. The fill factors are good and lie around 70% for all the cells. In summary it can be said that all the cells perform very poorly. Especially J_{SC} and efficiencies are very low and, in contrast to zinc(II) containing dyes discussed in previous chapters, there is no obvious difference in the efficiencies between cells containing the two anchoring ligands. However, one must take into account that the cells perform so poorly that this observation may be within experimental error.
The JV-measurements (Figure 6-11) on the day of assembly show that this time the cells containing anchoring ligand **8** show higher J_{SC}. This is in contrast to the trends seen in the previous chapters. Since the cell performance is so poor, this information may as well be within experimental error. What can nicely be seen is the parity of the J_{SC} values of the cells using the same anchoring ligand. Over all the efficiencies of the cells stayed more or less constant on a very low level during the measuring period. The J_{SC} values dropped slightly over this period and the V_{OC} increased for some of the cells. Fill factors also slightly increased over the 17 days period.

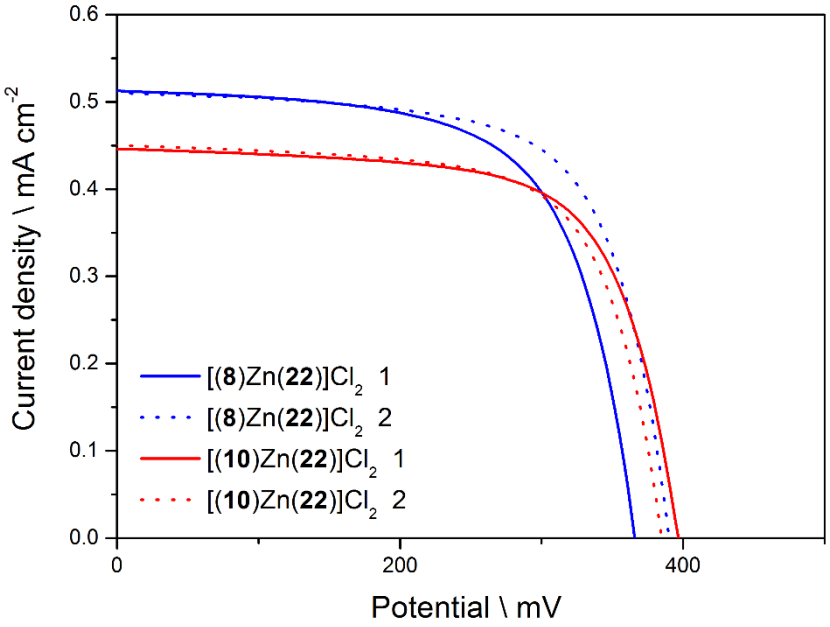

*Figure 6-11: JV-curves of cells containing dyes [(**8**)Zn(**22**)]Cl_2 and [(**10**)Zn(**22**)]Cl_2 measured on the assembly day.*

Anchored dye	J_{SC} \ mA cm^{-2}	V_{OC} \ mV	FF \ %	η \ %	η rel. to N719 \ %
		Day of sealing of the cells			
[(**8**)Zn(**22**)]Cl_2 1	**0.52**	366	64	0.12	1.69
[(**8**)Zn(**22**)]Cl_2 2	**0.52**	390	67	**0.13**	1.83
[(**10**)Zn(**22**)]Cl_2 1	0.45	396	67	0.12	1.69
[(**10**)Zn(**22**)]Cl_2 2	0.46	385	67	0.12	1.69
N719	15.32	667	69	7.09	100
		3 days after sealing of the cells			
[(**8**)Zn(**22**)]Cl_2 1	0.43	385	68	0.11	1.60
[(**8**)Zn(**22**)]Cl_2 2	0.43	382	70	0.11	1.60
[(**10**)Zn(**22**)]Cl_2 1	0.43	412	70	**0.13**	1.89
[(**10**)Zn(**22**)]Cl_2 2	0.43	388	69	0.11	1.60
N719	14.79	661	70	6.88	100
		17 days after sealing of the cells			
[(**8**)Zn(**22**)]Cl_2 1	0.38	382	70	0.10	1.67
[(**8**)Zn(**22**)]Cl_2 2	0.38	383	70	0.10	1.67
[(**10**)Zn(**22**)]Cl_2 1	0.40	**416**	**72**	0.12	2.00
[(**10**)Zn(**22**)]Cl_2 2	0.41	400	70	0.11	1.83
N719	13.48	648	69	6.00	100

Table 6-2: Summary of measured solar cell properties, on the day of sealing and 3 and 17 days after sealing.

6.3.4.2. Organic dye 24

The organic dye **24** (Scheme 6-8) shows decent light harvesting properties and a DSC efficiency of about 4.5%. The two measured cells show similar J_{SC} values, with the highest value of 10.23 mA/m^2 being reached on the day of assembly. The V_{OC} is slightly different between the two cells, one reaching a value almost as high as the V_{OC} of the N719 reference cell. The highest V_{OC} value measured was 624 mV on the second day after the assembly. The cells showed high fill factors of 73% even after 14 days. On day 2 after the assembly one cell shows the highest measured efficiency of 4.57%, which corresponds to 70.1% relative to the efficiency of the N719 reference cell. Over a 14 day measuring period the cell efficiencies drop slightly, which can be traced back to the slight drop in J_{SC} over the same period of time. V_{OC} only dropped slightly and fill factors stay constant or even increase slightly.

The JV-curves in Figure 6-12 point out the remarkable and reproducible performance of dye **24** compared to N719.

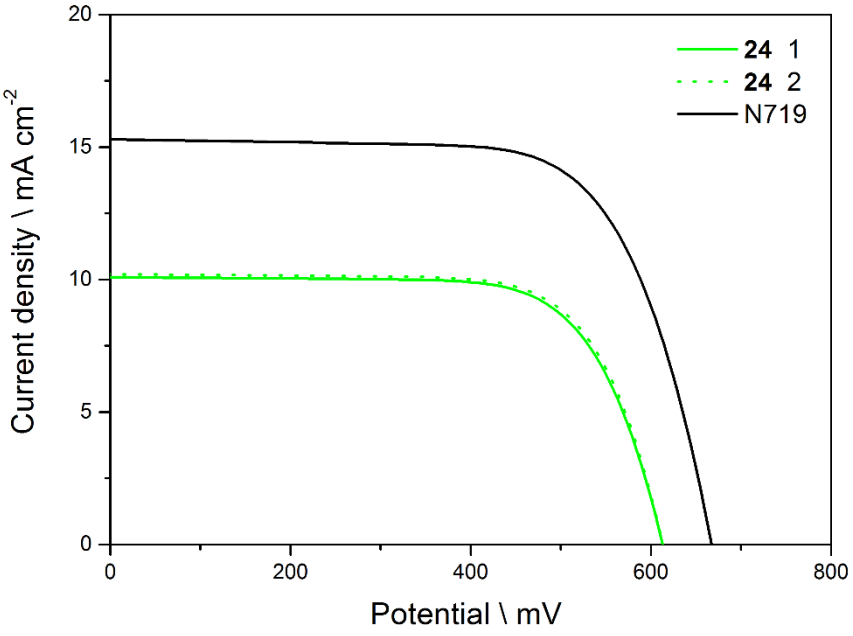

*Figure 6-12: JV-curves of cells containing dye **24** measured on the assembly day.*

Anchored dye	J_{SC} \ mA cm^{-2}	V_{OC} \ mV	FF \ %	η \ %	η rel. to N719 \ %
		Day of sealing of the cells			
24 1	10.12	613	71	4.40	68.54
24 2	**10.23**	613	71	4.48	69.78
N719	14.93	632	68	6.42	100
		2 days after sealing of the cells			
24 1	9.73	599	72	4.21	64.57
24 2	10.16	**624**	72	**4.57**	70.09
N719	14.82	646	68	6.52	100
		14 days after sealing of the cells			
24 1	9.04	598	**73**	3.93	63.90
24 2	9.55	610	72	4.21	68.46
N719	13.96	643	69	6.15	100

Table 6-3: Summary of measured solar cell properties, on the day of sealing and 2 and 14 days after sealing.

6.3.5. External quantum efficiency

Figure 6-13 compares the EQE curves of [(**8**)Zn(**22**)]Cl_2 and [(**10**)Zn(**22**)]Cl_2 to that of N719. It is obvious that the photon to current conversion of the zinc(II) dyes is not very efficient at all. The same fact was already observed for the dyes discussed in the previous chapter.

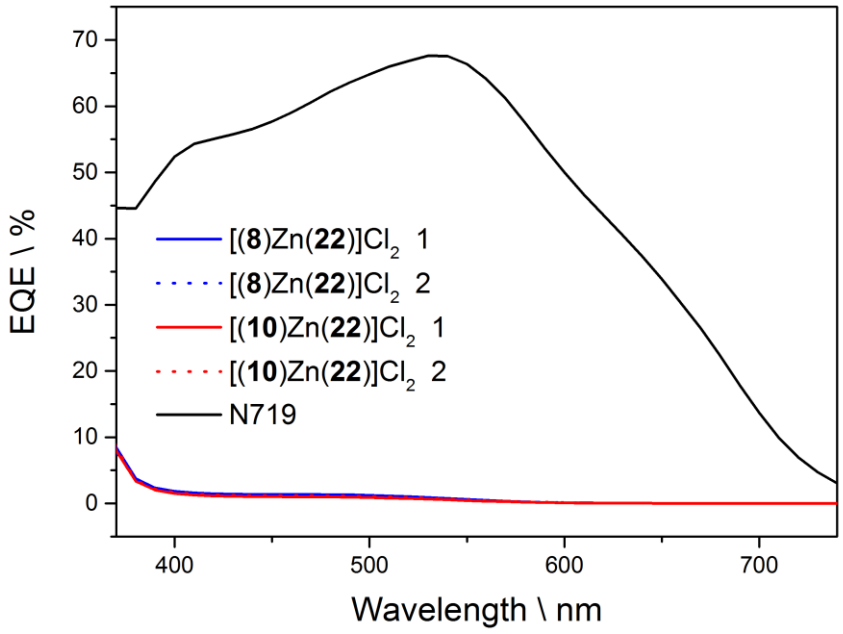

*Figure 6-13: EQE spectra of [(**8**)Zn(**22**)]Cl_2 and [(**10**)Zn(**22**)]Cl_2 compared to N719.*

In Figure 6-14 a zoom in on the EQE spectra of [(**8**)Zn(**22**)]Cl_2 and [(**10**)Zn(**22**)]Cl_2 is shown. One can see that for all the measured cells the photon to current conversion efficiency is very low, meaning that the best cell does not even reach 1.5%. It is observed that ligand **22**, in combination with anchoring ligand **8**, gives slightly better results. But still the differences are so small that this observation does not necessarily mean that this is a significant difference. Between the two measured cells containing the same dye only a slight difference is observable, which is evidence for the reproducibility of the cells. The spectral range the dyes cover in the EQE measurements is in good agreement with the solid state electronic absorption spectra shown in Figure 6-7 and extends from 640 nm to 400 nm.

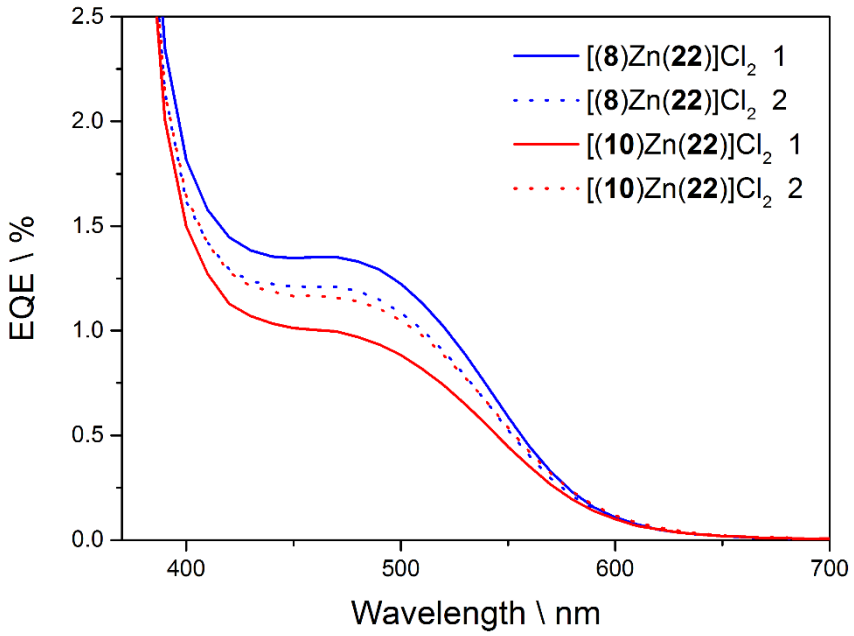

*Figure 6-14: EQE spectra of [(**8**)Zn(**22**)]Cl₂ and [(**10**)Zn(**22**)]Cl₂.*

The EQE spectra of duplicate cells containing organic dye **24** are shown in Figure 6-15. Comparing EQE curves of **24** to the one of N719, one can see that dye **24** shows a very high photon to current conversion efficiency of over 50% between 400 nm and 530 nm. This makes it very competitive to N719, which absorbs about 100 nm more into the red. Both measurements emphasize the reproducibility of the cells. The highest reached EQE value is 56.6% and the conversion range lies between 650 nm and 350 nm. Below this the semiconductor starts to absorb light as well. Also in this case the EQE measurements are in good agreement with the solid state electronic absorption spectra shown in Figure 6-8.

It is not easy to understand why there is such a huge difference between the organic and the zinc(II) containing dye, although both use basically the same chromophore. The most obvious difference between the two systems is the type of dye that was used, namely the missing zinc(II) ion in **24** and it is not clear if the zinc(II) possibly causes problems in the “communication” between the ancillary and anchoring ligand, making it impossible to direct the excited electron towards the semiconductor surface.

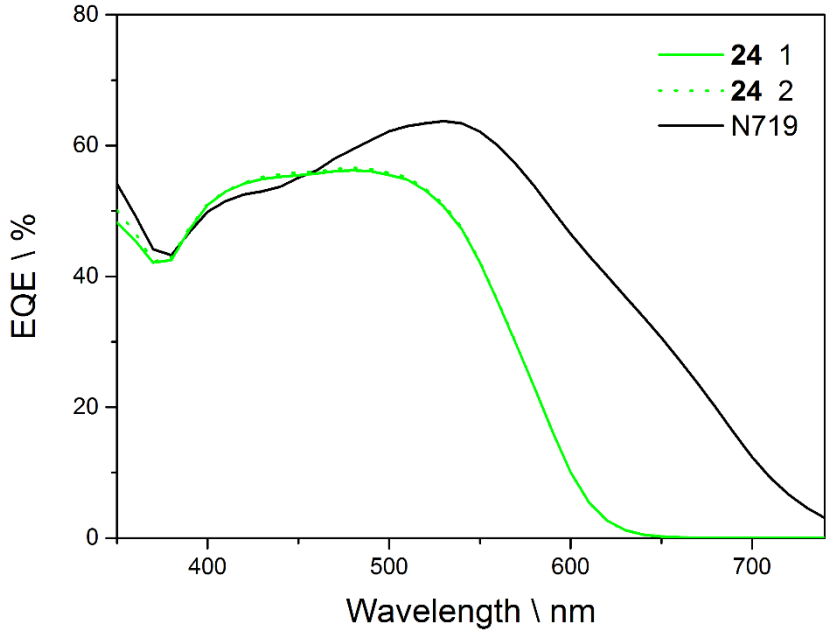

*Figure 6-15: EQE spectra of organic dye **24** and N719.*

6.4. Conclusion

A new set of solar cells has been assembled and measured, containing zinc(II) based dyes [(**8**)Zn(**22**)]Cl_2 and [(**10**)Zn(**22**)]Cl_2. Although computational calculations of [(**10**)Zn(**22**)]Cl_2 show that the HOMO/LUMO energy levels are distributed in the right way throughout the molecule for electron injection, the JV and EQE measurements show very low performance of the cells. All the measured cells show poor efficiencies around 0.12% and EQE values below 1.5%. This proves that there is indeed a photon to current conversion process happening, but some other factors have a dominating negative influence on this process.

Measurements of the organic dye **24** show promising results. It turns out that the combination of chromophore **21** with a cyanoacrylic acid anchoring group gives a fairly efficient dye. It reaches efficiencies of 4.6% and is quite stable over a period of 14 days. Furthermore it shows very high photon to current conversion efficiencies of more than 50% between 400 nm and 530 nm and is therefore comparable to N719 (Figure 6-15).

It is interesting to look at the difference between the zinc(II) containing dyes discussed in this and in the previous chapter and the organic dye **24**. The very obvious structural difference between the two different types is the zinc(II) ion. The zinc(II) complex-

based dyes consist of three main parts: the ancillary ligand, the anchoring ligand and the zinc(II) ion connecting the two ligands. Since computational calculations for [(**10**)Zn(**22**)]Cl_2 showed that the HOMO is located on the ancillary ligand and the LUMO on the anchoring ligand, it is not easy to see where the interruption happens. It could be argued that zinc(II) complexes are not suitable as dyes for DSCs, because they lack sufficient electronic communication between the ligands and the metal. This linkage between ligands and metal centre can be observed, e.g. in copper(I) bis-bipyridine complexes, that show nice MLCT bands as proof for electronic metal-ligand interaction. It is also known that zinc(II) d^{10} ions are very inert with regard to oxidation processes. This is only very speculative but would at least partially explain why all the efforts to find a zinc(II) based dye, that gives satisfactory results, only yielded poorly performing solar cells.

Further work in this direction should involve the development of anchoring ligands containing chromophores to investigate the role of the zinc(II) ion in the complex. If it turns out that the metal centre does not ensure the needed communication between the two other parts of the dye, it might be very hard to find practical ways to obtain efficient zinc(II) bis-terpyridine based DSCs.

6.5. Experimental

6.5.1. 7-Bromo-*N*,*N*-diphenylbenzo[c][1,2,5]thiadiazol-4-amine (16)

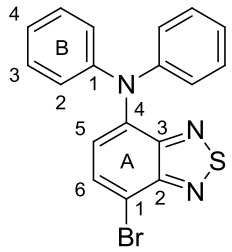

4,7-Dibromo-2,1,3-benzothiadiazole (5.00 g, 17.0 mmol, 1.0 eq.) and diphenylamine (2.88 g, 17 mmol, 1.0 eq.) were dissolved in dry toluene (40 mL) under an N_2 atmosphere and NaO^{t}Bu (2.12 g, 22.1 mmol, 1.3 eq.) was added. To the dark red solution $Pd(dba)_2$ (0.196 g, 0.340 mmol, 0.02 eq.) and P(^{t}Bu)$_3$ (0.279 g, 0.340 mmol, 0.02 eq.) were added. The reaction mixture was then stirred overnight at RT. The solvent was then removed under reduced pressure and the remaining solid purified using column chromatography (SiO_2, hexane:CH_2Cl_2 1:0 - 1:2). The product was obtained as a red oil. Ultrasonic treatment in hexane yielded an orange solid (1.62 g, 4.22 mmol, 25%).

^{1}H NMR (500 MHz, CD_2Cl_2) δ / ppm 7.70 (d, *J* = 8.0 Hz, 1H, H^{A6}), 7.31 – 7.22 (m, 4H, H^{B3}), 7.12 – 7.06 (m, 2H, H^{B4}), 7.05 – 7.02 (m, 4H, H^{B2}), 7.02 (d, *J* = 8.0 Hz, 1H, H^{A5}). **^{13}C NMR** (126 MHz, CD_2Cl_2) δ / ppm 155.2 (C^{A2}), 151.2 (C^{A3}), 148.1 (C^{B1}), 140.4 (C^{A4}), 133.1 (C^{A6}), 129.8 (C^{B3}), 124.8 (C^{B2}), 124.2 (C^{B4}), 124.1 (C^{A5}), 107.9 (C^{A1}).

6.5.2. *tert*-Butyl bis(4-bromophenyl)carbamate (18)

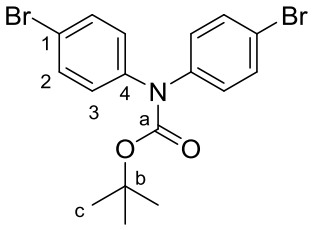

To a solution of bis(4-bromophenyl)amine (2.00 g, 5.93 mmol, 1.0 eq.) and Boc_2O (1.42 g, 6.53 mmol, 1.1 eq.) in dry THF (20 mL), 4-dimethylaminopyridine (0.145 g, 1.19 mmol, 0.2 eq.) was added in one portion and the mixture refluxed for 17 h under an Ar atmosphere. The solvent was then removed under reduced pressure to give a yellowish oil. The addition of hexane caused the precipitation of a white solid, which was collected by filtration and recrystallized from hexane to yield the pure product (1.10 g, 2.58 mmol). The mother liquor was collected and the solvent removed under reduced pressure. The obtained yellow solid was purified using column chromatography (Al_2O_3, $CHCl_3$) to yield the pure product (0.681 g, 1.59 mmol). Total yield: 1.78 g, 4.17 mmol, 70%

^{1}H NMR (500 MHz, $CDCl_3$) δ / ppm 7.43 (d_{AB}, J = 8.8 Hz, 4H, H^3), 7.06 (d_{AB}, J = 8.8 Hz, 4H, H^2), 1.44 (s, 9H, H^c).

^{13}C NMR (126 MHz, $CDCl_3$) δ / ppm 153.3 (C^a), 141.8 (C^1), 132.1 (C^3), 128.6 (C^2), 119.4 (C^4), 82.1 (C^b), 28.3 (C^c).

6.5.3. *tert*-Butyl bis(4-(4,4,5,5-tetramethyl-1,3,2-dioxaborolan-2-yl)phenyl)carbamate (19)

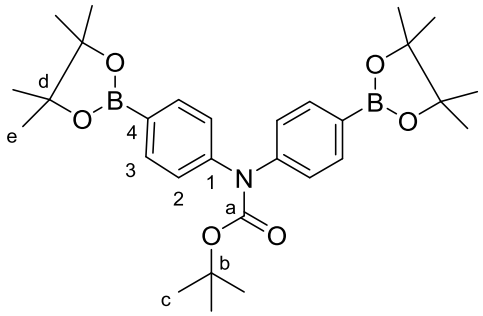

18 (5.00 g, 11.7 mmol, 1.0 eq.) was dissolved in dry THF (20 mL) and cooled to -78 °C under an N_2 atmosphere. Then a 1.6 M solution of *n*-BuLi in hexane (17.6 mL, 28.1 mmol, 2.4 eq.) was added dropwise over a period of 5 min. The mixture was then stirred at -78 °C for 2.5 h. Then 2-isopropoxy-4,4,5,5-tetramethyl-1,3,2-dioxaborolane (5.85 mL, 28.1 mmol, 2.4 eq.) was added in one portion and the mixture allowed to warm to RT. While doing so, the mixture turned cloudy and it was stirred for further 3 d at RT. The precipitate that formed was filtered and the solvent of the mother liquor evaporated. Column chromatography (SiO_2, hexane:EtOAc = 10:1 - 1:1) gave a colourless solid, which was suspended in hexane and filtered off. The product was obtained as a colourless crystalline solid (4.63 g, 8.88 mmol, 76%).

^{1}H NMR (500 MHz, CD_2Cl_2) δ / ppm 7.69 (d, *J* = 8.5 Hz, 4H, H^3), 7.17 (d, *J* = 8.5 Hz, 4H, H^2), 1.44 (s, 9H, H^c), 1.32 (s, 24H, H^e).

^{13}C NMR (126 MHz, CD_2Cl_2) δ / ppm 153.7 (C^a), 146.2 (C^1), 135.6 (C^3), 126.7 (C^2), 84.4 (C^d), 81.9 (C^b), 28.5 (C^c), 25.2 (C^e).

6.5.4. *tert*-Butyl bis(4-(7-(diphenylamino)benzo[c][1,2,5]thiadiazol-4-yl)phenyl)carbamate (20)

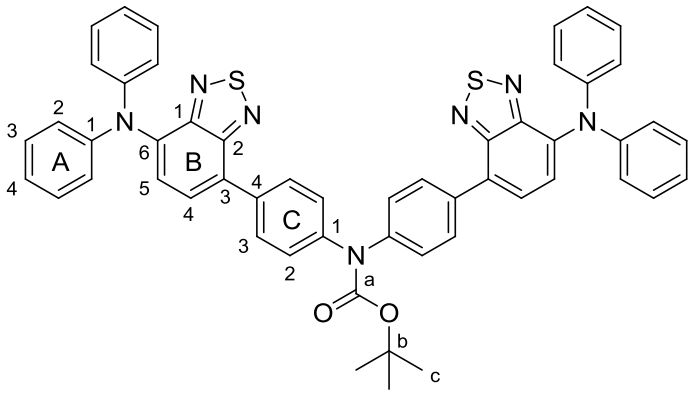

A round bottomed flask was charged with **16** (1.20 g, 3.14 mmol, 2.1 eq.), **19** (0.779 g, 1.49 mmol, 1.0 eq.) and K_2CO_3 (0.826 g, 5.98 mmol, 4.0 eq.) under an N_2 atmosphere, then H_2O and THF were added and the mixture degassed with N_2 for 15 min. After the addition of $Pd(PPh_3)_4$ (0.173 g, 0.149 mmol, 0.1 eq.) the mixture was refluxed for 3 d. Then the solvent was removed under reduced pressure and the resulting solid purified using column chromatography (SiO_2, hexane:EtOAc 10:1 and SiO_2, CH_2Cl_2:hexane 4:1-10:1) to yield the desired product as a red solid (509 mg, 0.584 mmol, 75%).

^{1}H NMR (500 MHz, CD_2Cl_2) δ / ppm 7.94 (d_{AB}, *J* = 8.6 Hz, 4H, H^{C3}), 7.64 (d, *J* = 7.8 Hz, 2H, H^{B4}), 7.41 (d_{AB}, *J* = 8.6 Hz, 4H, H^{C2}), 7.30 – 7.25 (m, 8H, H^{A3}), 7.24 (d, *J* = 7.8 Hz, 2H, H^{B5}), 7.11 – 7.02 (m, 12H, H^{A2} & H^{A4}), 1.52 (s, 9H, H^{c}).
^{13}C NMR (126 MHz, CD_2Cl_2) δ / ppm 155.4 (C^{B2}), 154.0 (C^{a}), 152.2 (C^{B1}), 148.3 (C^{A1}), 143.4 (C^{C1}), 139.6 (C^{B6}), 135.4 (C^{C4}), 129.9 (C^{C3}), 129.7 (C^{A3}), 129.2 (C^{B3}), 129.0 (C^{B4}), 127.6 (C^{C2}), 124.6 (C^{A2}), 124.5 (C^{B5}), 123.9 (C^{A4}), 81.9 (C^{b}), 28.6 (C^{c}).

6.5.5. 7-(4-((4-(7-(Diphenylamino)benzo[c][1,2,5]thiadiazol-4-yl)phenyl)amino)phenyl)-*N*,*N*-diphenylbenzo[c][1,2,5]thiadiazol-4-amine (21)

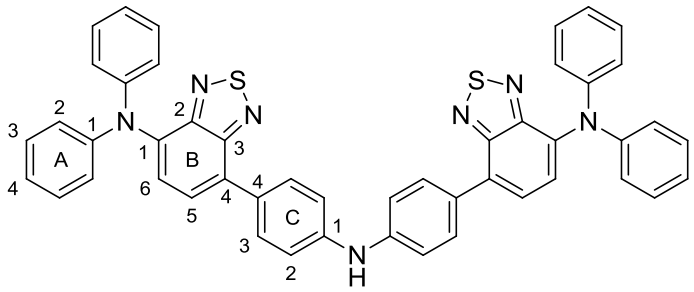

20 (113 mg, 0.13 mmol) was heated to 210 °C for 1 h in an oven. It was then used without further purification or analysis.

6.5.6. 7-(4-((4-([2,2':6',2''-Terpyridin]-4'-yl)phenyl)(4-(7-(diphenylamino)benzo[c][1,2,5]thiadiazol-4-yl)phenyl)amino)phenyl)-*N*,*N*-diphenylbenzo[c][1,2,5]thiadiazol-4-amine (22)

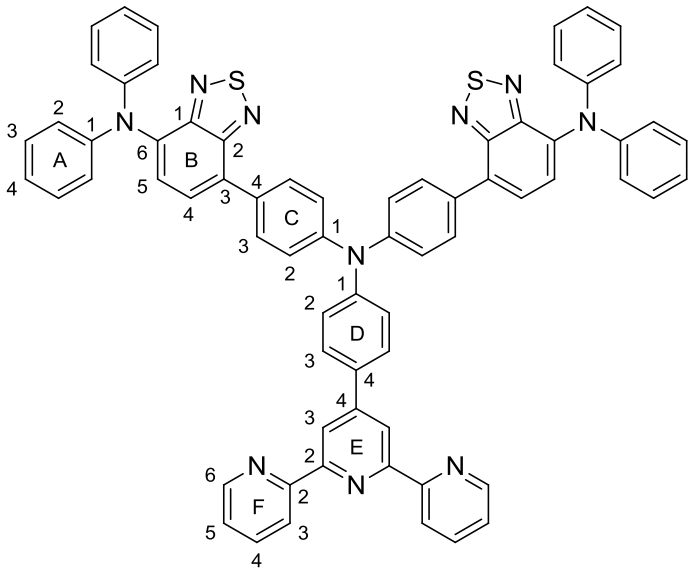

A round bottomed flask was charged with **21** (100 mg, 0.130 mmol, 1.0 eq.), 4'-(4-bromophenyl)-2,2':6',2''-terpyridine (55.3 mg, 0.142 mmol, 1.1 eq.), NaO^{t}Bu (37.3 mg, 0.389 mmol, 3.0 eq.) and Pd(dba)$_2$ (1.50 mg, 2.59 µmol, 0.02 eq.) under an N_2 atmosphere. Then dry and degassed toluene (10 mL) and P(^{t}Bu)$_3$ (2.60 µL, 2.60 µmol, 0.02 eq.) were added to the mixture. The reaction mixture was stirred overnight at 100 °C. The hot reaction mixture was then filtered through a glass sinter frit, which was subsequently rinsed with hot toluene. The solvent was removed under reduced pressure and the remaining solid purified by recrystallization from acetone. The product was obtained as a red solid. (40.0 mg, 37.1 µmol, 29%).

^{1}H NMR (500 MHz, CD_2Cl_2) δ / ppm 8.78 (s, *J* = 3.3 Hz, 2H, H^{E3}), 8.72 (ddd, *J* = 4.7, 1.7, 0.9 Hz, 2H, H^{F6}), 7.71 – 8.67 (m, 2H, H^{F3}), 7.95 (d_{AB}, *J* = 8.8 Hz, 4H, H^{C3}), 7.93 – 7.89 (m, 2H, H^{F4}), 7.83 (d_{AB}, *J* = 8.7 Hz, 4H, H^{D3}), 7.66 (d, *J* = 7.8 Hz, 2H, H^{B4}), 7.41 – 7.35 (m, 8H, H^{F5} & H^{D2} & H^{C2}), 7.30 – 7.25 (m, 8H, H^{A3}), 7.26 (d, *J* = 7.7 Hz, 2H, H^{B5}), 7.11 – 7.05 (m, 12H, H^{A2} & H^{A4}).

^{13}C NMR (126 MHz, CD_2Cl_2) δ / ppm 156.6 (C^{E2}), 156.4 (C^{F2}), 155.3 (C^{B2}), 152.1 (C^{B1}), 149.8 (C^{E4}), 149.6 (C^{F6}), 148.7 (C^{D1}), 148.2 (C^{A1}), 147.3 (C^{C1}), 139.1 (C^{B6}), 137.2 (C^{F4}), 133.2 (C^{D4}), 132.9 (C^{C4}), 130.5 (C^{C3}), 129.6 (C^{A3}), 129.4 (C^{B3}), 128.6 (C^{D3}), 128.4 (C^{B4}), 124.8 (C^{C2}), 124.7 (C^{B5}), 124.6 (C^{D2}), 124.3 (C^{A2}), 124.3 (C^{F5}), 123.6 (C^{A4}), 121.5 (C^{F3}), 118.5 (C^{E3}).

MALDI-TOF MS (*m/z*): 1078.7 $[M]^+$ (calc. 1078.3).

UV-Vis (CH_2Cl_2, 3 x 10^{-6} mol cm^{-3}) λ_{abs}/nm 247 (ε / cm^3 mol^{-1} cm^{-1} 51204), 252 (51524), 304 (62216), 366 sh (21486), 488 (22953); (THF, 3 x 10^{-5} mol cm^{-3}) λ_{abs}/nm 302 (ε / cm^3 mol^{-1} cm^{-1} 70565), 302 (70565), 334 sh (40620), 365 sh (27505), 489 (26121).

6.5.7. 4-(Dis(4-(7-(diphenylamino)benzo[c][1,2,5]thiadiazol-4-yl)phenyl)amino)benzaldehyde (23)

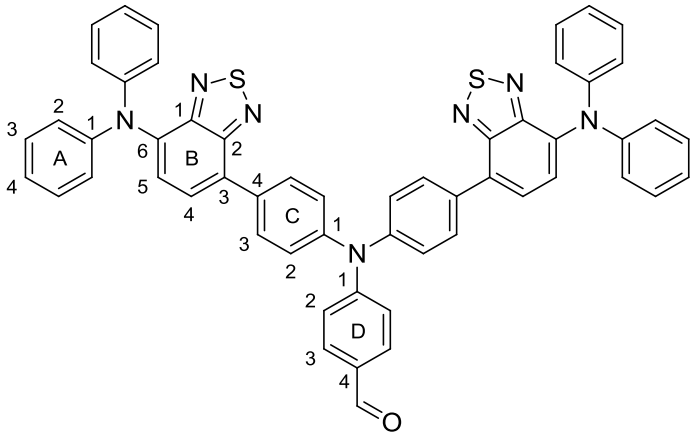

A round bottomed flask was charged with **21** (100 mg, 0.130 mmol, 1.0 eq.), 4-bromobenzaldehyde (28.8 mg, 0.155 mmol, 1.2 eq.), NaO^{t}Bu (37.3 mg, 0.389 mmol, 3.0 eq.) and $Pd(dba)_2$ (1.50 mg, 2.59 µmol, 0.02 eq.) under an N_2 atmosphere. Then dry and degassed toluene (10 mL) and P(^{t}Bu)$_3$ (2.60 µL, 2.60 µmol, 0.02 eq.) were added to the mixture. The reaction mixture was stirred overnight at 100 °C, then again $Pd(dba)_2$ (1.50 mg, 2.59 µmol, 0.02 eq.) and P(^{t}Bu)$_3$ (2.60 µL, 2.60 µmol, 0.02 eq.) were added and the stirring continued for another night. The hot reaction mixture was then filtered through a glass sinter frit, which was subsequently rinsed with hot toluene. The solvent was removed under reduced pressure and the remaining solid purified by column chromatography (SiO_2, CH_2Cl_2:hexane 4:1). The obtained red solid was suspended in hexane and sonicated until no more compound was sticking to the wall of the flask. The solid was then filtered of and dried on the frit. The product was obtained as a red solid. (101 mg, 115 µmol, 89%).

^{1}H NMR (500 MHz, CD_2Cl_2) δ / ppm 9.85 (s, 1H, H^{CHO}), 7.98 (d_{AB}, J = 8.7 Hz, 4H, H^{C3}), 7.76 (d_{AB}, J = 8.8 Hz, 2H, H^{D3}), 7.65 (d, J = 7.8 Hz, 2H, H^{B4}), 7.38 (d_{AB}, J = 8.7 Hz, 4H, H^{C2}), 7.31 – 7.23 (m, 12H, H^{A3} & H^{B5} & H^{D2}), 7.11 – 7.05 (m, 12H, H^{A2} & H^{A4}).
^{13}C NMR (126 MHz, CD_2Cl_2) δ / ppm 190.6 (C^{CHO}), 155.2 (C^{B2}), 153.2 (C^{D1}), 152.0 (C^{B1}), 148.1 (C^{A1}), 146.2 (C^{C1}), 139.4 (C^{B6}), 134.5 (C^{C4}), 131.5 (C^{D3}), 130.7 (C^{C3}), 130.3 (C^{D4}), 129.6 (C^{A3}), 128.9 (C^{B3}), 128.7 (C^{B4}), 126.3 (C^{C2}), 124.43 (C^{A2}), 124.38 (C^{B5}), 123.7 (C^{A4}), 120.9 (C^{D2}).

6.5.8. (Z)-3-(4-(bis(4-(7-(diphenylamino)benzo[c][1,2,5]thiadiazol-4-yl)phenyl)amino)phenyl)-2-cyanoacrylic acid (24)

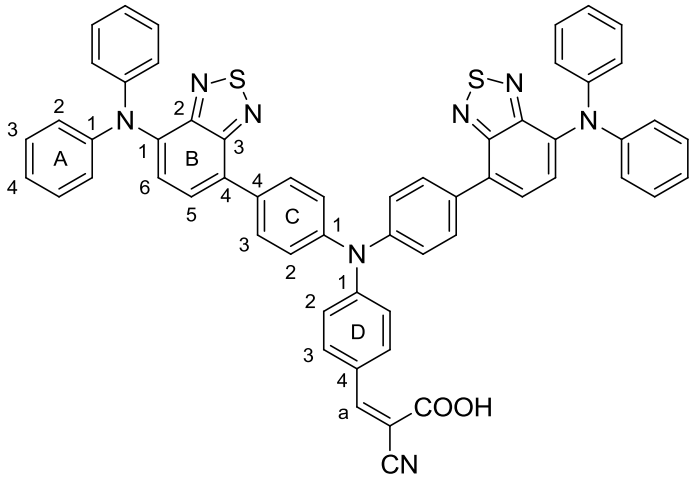

A round bottomed flask was charged with **23** (50.0 mg, 57.1 µmol, 1.0 eq.) and cyanoacetic acid (10.7 mg, 126 µmol, 2.2 eq.) under an N_2 atmosphere. Then MeCN (60 mL) and a few drops of piperidine were added and the mixture heated to reflux for 4 d. Then the solvent was removed under reduced pressure and the remaining red solid purified by column chromatography (SiO_2, CH_2Cl_2:MeOH 10:1). After removal of the solvent the desired product was obtained as red solid (30.0 mg, 31.8 µmol, 56%).

^{1}H NMR (500 MHz, DMSO-*d6*) δ / ppm 8.08 (s, 1H, H^a), 8.03 (d_{AB}, *J* = 8.7 Hz, 4H, H^{C3}), 7.96 (d_{AB}, *J* = 9.0 Hz, 2H, H^{D3}), 7.83 (d, *J* = 7.8 Hz, 2H, H^{B4}), 7.36 (d_{AB}, *J* = 8.7 Hz, 4H, H^{C2}), 7.32 – 7.27 (m, 8H, H^{A3}), 7.26 (d, *J* = 7.7 Hz, 2H, H^{B5}), 7.12 (d_{AB}, *J* = 8.9 Hz, 2H, H^{D2}), 7.10 – 7.04 (m, 4H, H^{A4}), 7.03 – 6.99 (m, *J* = 8.8, 1.7 Hz, 8H, H^{A2}).
^{13}C NMR (126 MHz, DMSO-*d6*) δ / ppm 154.7 (C^{B2}), 151.1 (C^{B1}), 150.3 (C^a), 147.6 (C^{A1}), 145.2 (C^{C1}), 138.8 (C^{B6}), 133.9 (C^{C4}), 132.1 (C^{D3}), 130.9 (C^{C3}), 129.9 (C^{A3}), 129.1 (C^{B4}), 127.9 (C^{B3}), 125.3 (C^{C2}), 124.1 (C^{B5}), 123.5 (C^{A2}), 123.3 (C^{A4}), 120.6 (C^{D2}).
MALDI-TOF MS (*m/z*): 942.1 $[M]^+$ (calc. 942.3).

Chapter 7

Chapter 7: Design of new anchoring ligands

7.1. Strategy

Anchoring ligands are important for the electron communication between the organometallic dye and semiconductor in DSCs. They are responsible for the adsorbing of the dye molecules to the semiconductor surface, the drainage of the excited electrons and the injection of the electrons into the semiconductor. Normally, our concept was to use a simple anchoring ligand and a chromophoric ancillary ligand.[60] An alternative idea was to use building blocks that were used in chromophore **21** and to incorporate them into an anchoring ligand. The most promising building block was the BTZ unit, since it exhibits strong acceptor properties, which is exactly what is needed in an anchoring ligand to direct the electron flow towards the semiconductor. For this reason, two new anchoring ligands were designed that incorporated BTZ as a central unit (Scheme 7-1).

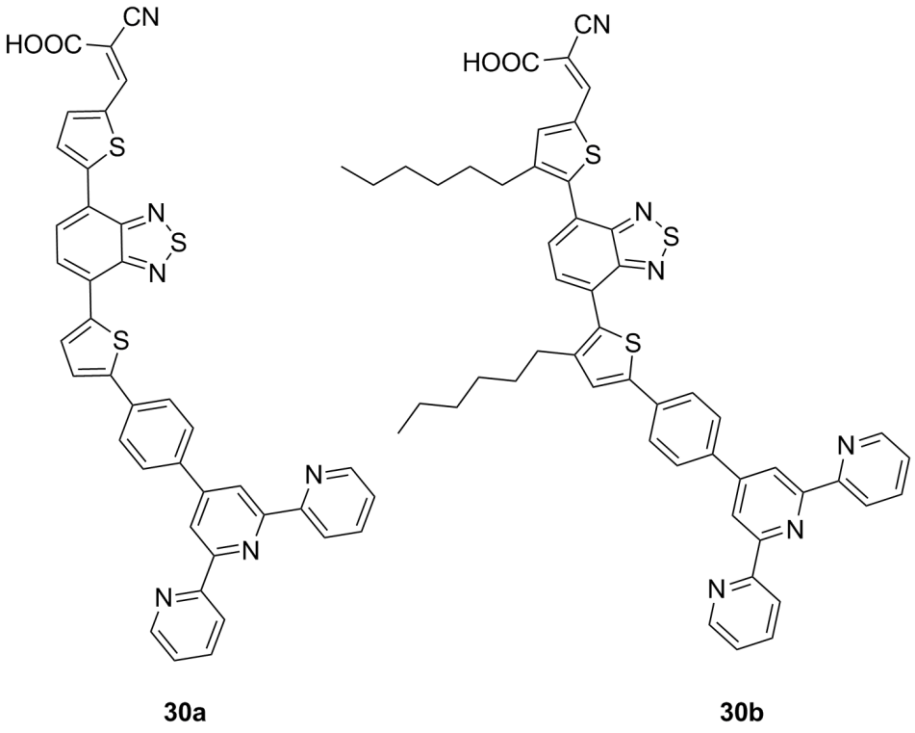

*Scheme 7-1: Newly designed anchoring ligands **30a** and **30b**.*

As the ligating part of the molecule for binding to zinc(II), 2,2':6',2''-terpyridine was chosen. Thiophene units were inserted between the anchor and terpyridine units as π-

bridges. These extend the π-system and may also have an influence on the energy levels of the ligand and the dye. For reasons of recombination blocking (already discussed in chapter 5), hexyl chains were introduced on the thiophene spacers in one of the two new anchoring ligands. These alkyl chains also had an important influence on the solubility of the intermediate compounds during ligand synthesis. As anchoring group, the cyanoacrylic acid functionality was chosen, since it performed well in compound **24**.

The synthesis of both anchoring ligands **30a** and **30b** was carried out in parallel using the following synthetic pathway. The synthesis started with the coupling of 4,7-dibromo-2,1,3-benzothiadiazole and 4,4,5,5-tetramethyl-2-(thiophen-2-yl)-1,3,2-dioxaborolane in a Suzuki-coupling reaction to give compounds **25a** and **25b** (Scheme 7-2).[103]

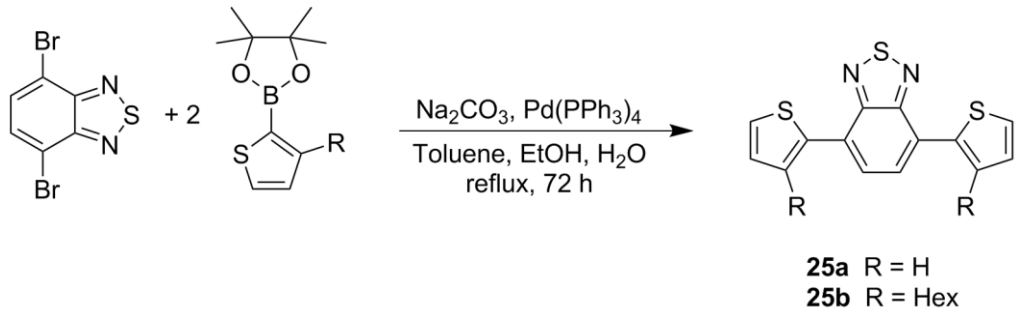

*Scheme 7-2: Suzuki reaction to get compounds **25a** and **25b**.*

The second step involved a Vilsmeier-Haack reaction with $POCl_3$ and DMF to introduce an aldehyde functionality (Scheme 7-3). To avoid overreaction to the dialdehyde, only 1.1 equivalents of DMF were used.

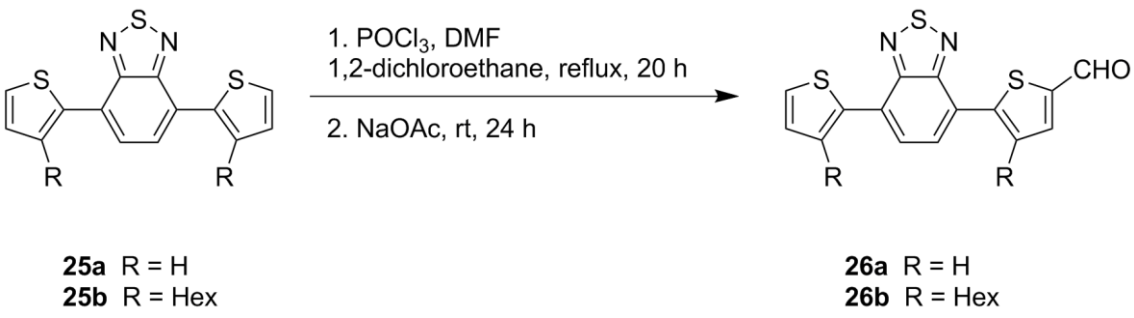

*Scheme 7-3: Vilsmeier-Haack reaction to produce compounds **26a** and **26b**.*

The next step involved a straightforward reaction already discussed in chapter 3. This route introduced by Hanan[75] involves the reaction of an aromatic aldehyde with two equivalents of 2-acetylpyridine under basic conditions, to obtain a terpyridine (Scheme 7-4).

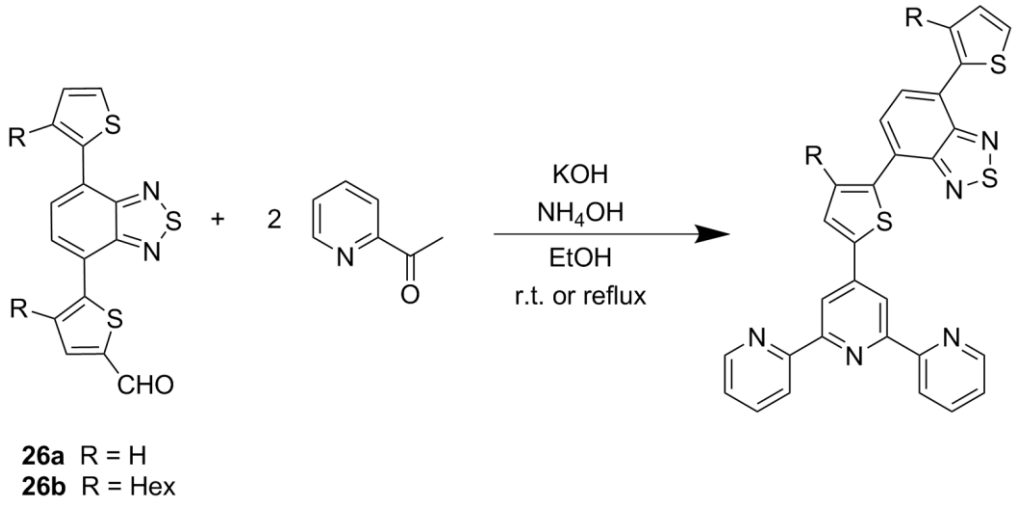

Scheme 7-4: Failed attempt to make the terpyridine using the Hanan[75] approach.

This step was tried several times but was never successful. If it had worked, the plan was to continue with another Vilsmeier-Haack reaction on the unsubstituted thiophene to obtain a second aldehyde functionality. This aldehyde could then undergo a Knoevenagel condensation with cyanoacetic acid to complete the anchoring ligands with the cyanoacrylic acid anchoring groups. If this pathway had been successful the resulting ligands would have differed from those shown in Scheme 7-1, by lacking the phenyl spacer in the 4'-position of the terpyridine. Due to the change in the synthetic route, it was inevitable that this additional phenyl ring was introduced. When selecting an alternative, it was important to make use of the already synthesized compounds **26a** and **26b**, if possible. The idea to use 4'-(4-bromophenyl)-2,2':6',2''-terpyridine seemed promising. This compound can easily be synthesized by the Hanan[75] method, and then be converted to the corresponding boronic acid pinacol ester using a palladium catalysed Miyaura borylation reaction.[104]

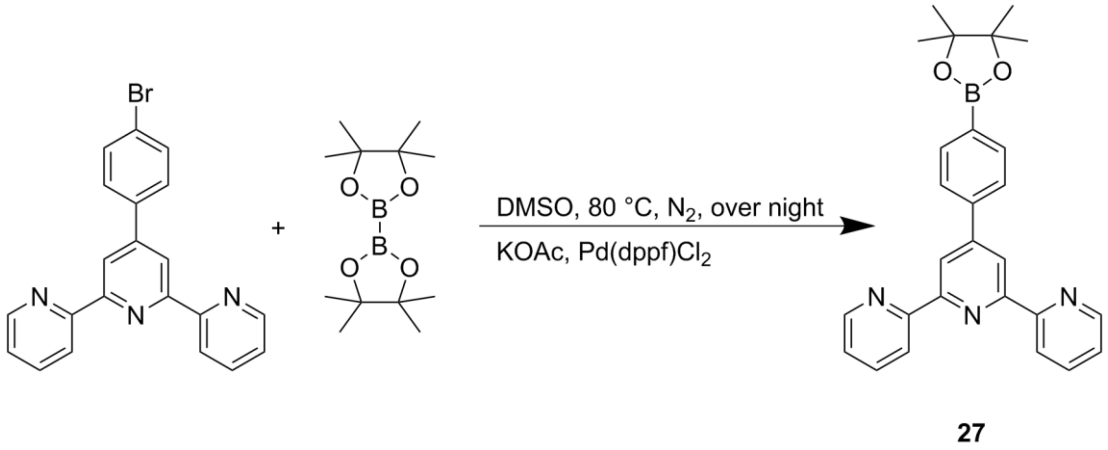

*Scheme 7-5: Synthesis of **27** via a Miyaura borylation reaction.*

To provide a coupling partner for **27**, compounds **26a** and **26b** were brominated on the unsubstituted thiophene using NBS (Scheme 7-6).

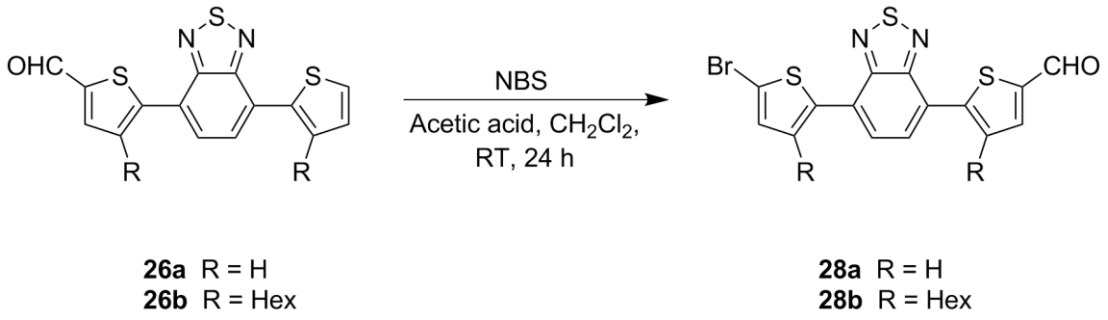

*Scheme 7-6: Bromination of **26a** and **26b** with NBS.*

Compounds **28a** and **28b** were then coupled to **27** in another palladium catalysed Suzuki-coupling reaction to produce the terpyridines **29a** and **29b**. Unfortunately only small amounts of these could be isolated and the time was too short to repeat the synthesis. No-further work on these compounds was carried out; I acknowledge the efforts of Cedric Wobill who worked on these syntheses during his Wahlpraktikum.

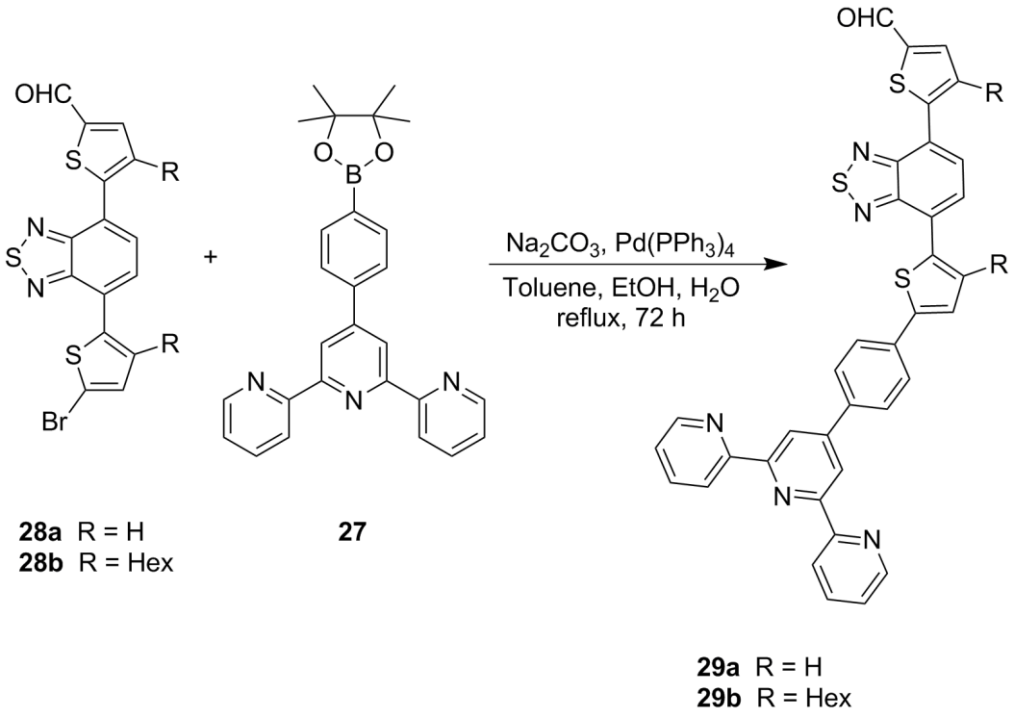

*Scheme 7-7: Suzuki-coupling reaction to **29a** and **29b**.*

7.2. Conclusion and suggestions for extension of this work

It could be shown that the revised synthetic strategy works until the second last step. If the synthesis could be scaled up and the yield be improved, it would be possible to synthesize the anchoring ligands **30a** and **30b**. However, compound **29a** is very insoluble, which makes **29b** a more suitable candidate. Future work would therefore consist of a scale up of the synthesis of **30b**. If this step is successful, it should be tested for its suitability as anchoring ligand. The best would be to use the step wise dye assembling protocol (introduced in chapter 4) and very simple ancillary ligands such as **5a** or **6a**. If this would lead to better efficiencies than with anchoring ligands **8 – 10**, the testing could be expanded to more complex molecules such as **22** (introduced in chapter 6). If this proof-of-principle is provided, one could consider modifications in the anchoring ligand structure. It would be interesting to use more and/or different π-bridges (e.g. furans, selenophenes, phenyls etc.) to adjust the energy levels within the ligand and the dye. Further it would also be possible to replace the terpyridine unit by any other ligating species, to use it for different metal ions with different coordination numbers. It would even be possible to follow a similar strategy as for **24** (introduced in chapter 6), namely to couple **28a** or **28b** to a donor molecule such as diphenylamine

and, in a second step, to convert the aldehyde into a cyanoacrylic acid anchoring group for use as an organic dye.

7.3. Experimental

7.3.1. 4,7-Di(thiophen-2-yl)benzo[c][1,2,5]thiadiazole (25a)[103]

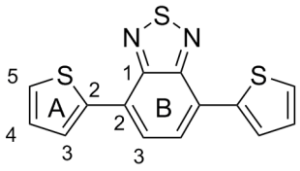

4,7-Dibromo-2,1,3-benzothiadiazole (4.00 g, 13.6 mmol, 1.0 eq.), 2-thiophene boronic pinacol ester (6.00 g, 28.6 mmol, 2.1 eq.), Na_2CO_3 (3.03 g, 28.6 mmol, 2.1 eq.) and $Pd(PPh_3)_4$ (768 mg, 0.682 mmol, 0.05 eq.) were added to a mixture of toluene (60 mL), EtOH (40 mL) and H_2O (40 mL) under an N_2 atmosphere. The suspension was refluxed for 72 h and then cooled to RT. The solvent was removed under reduced pressure and afterwards H_2O (100 mL) and CH_2Cl_2 (100 mL) were added. The phases were separated and the aqueous phase was extracted with CH_2Cl_2 (3 x 50 mL). The combined organic phases were dried over $MgSO_4$, filtered and the solvent was removed under reduced pressure. The desired product was obtained by recrystallization from EtOH and subsequent column chromatography (SiO_2, CH_2Cl_2:hexane 1:2) as a red-orange solid (810 mg, 2.70 mmol, 20%). Spectroscopic data agreed with the literature.

^{1}H-NMR (500 MHz, $CDCl_3$) δ / ppm 8.12 (dd, *J* = 3.7, 1.2 Hz, 2H, H^{A3}), 7.87 (s, 2H, H^{B3}), 7.46 (dd, *J* = 5.1, 1.1 Hz, 2H, H^{A5}), 7.22 (dd, *J* = 5.1, 3.7 Hz, 2H, H^{A4}).
^{13}C-NMR (126 MHz, $CDCl_3$) δ / ppm 152.8 (C^{B1}), 139.5 (C^{A2}), 128.2 (C^{A4}), 127.6 (C^{A3}), 127.0 (C^{A5}), 126.1 (C^{B2}), 125.9 (C^{B3}).

7.3.2. 4,7-Bis(3-hexylthiophen-2-yl)benzo[c][1,2,5]thiadiazole (25b)[105]

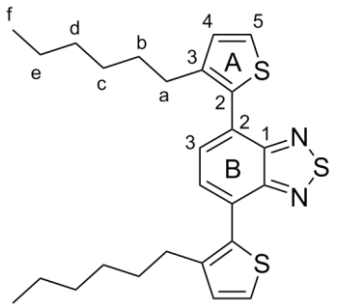

4,7-Dibromo-2,1,3-benzothiadiazole (4.50 g, 15.3 mmol, 1.0 eq.), 2-(3-hexylthiophen-2-yl)-4,4,5,5-tetramethyl-1,3,2-dioxaborolane (9.48 g, 30.6 mmol, 2.0 eq.), Na_2CO_3 (3.24 g, 30.6 mmol, 2.0 eq.) and $Pd(PPh_3)_4$ (765 mg, 0.765 mmol, 0.05 eq.) were added to a mixture of toluene (90 mL), EtOH (60 mL) and H_2O (60 mL). The suspension was refluxed for 48 h and then cooled to RT. The solvent was removed under reduced pressure, then H_2O (100 mL) and CH_2Cl_2 (200 mL) were added. After separation of the phases, the aqueous phase was extracted with CH_2Cl_2 (3 x 50 mL). The combined organic phases were dried over $MgSO_4$, filtered and then the solvent was removed in vacuo. The product was purified by column chromatography (SiO_2, CH_2Cl_2:hexane 1:4) and isolated as a yellow-orange oil (3.39 g, 7.24 mmol, 50%). Spectroscopic data agreed with the literature.

^{1}H-NMR (500 MHz, $CDCl_3$) δ / ppm 7.65 (s, 2H, H^{B3}), 7.44 (d, *J* = 5.2 Hz, 2H, H^{A5}), 7.11 (d, *J* = 5.2 Hz, 2H, H^{A4}), 2.70 – 2.63 (m, 4H, H^{a}), 1.66 - 1.58 (m, 4H, H^{b}), 1.29 – 1.14 (m, 12H, H^{c} & H^{d} & H^{e}), 0.81 (t, *J* = 6.9 Hz, 6H, H^{f}).
^{13}C-NMR (126 MHz, $CDCl_3$) δ / ppm 154.4 (C^{B1}), 141.8 (C^{A3}), 132.3 (C^{A2}), 130.0 (C^{B3}), 129.4 (C^{A4}), 127.6 (C^{B2}), 126.0 (C^{A5}), 31.7 (C^{d}), 30.8 (C^{b}), 29.5 (C^{a}), 29.2 (C^{c}), 22.7 (C^{e}), 14.2 (C^{f}).

7.3.3. 5-(7-(Thiophen-2-yl)benzo[c][1,2,5]thiadiazol-4-yl)thiophene-2-carbaldehyde (26a)[106]

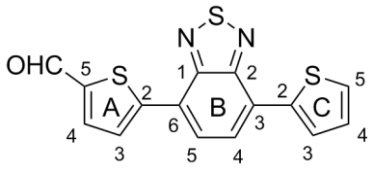

A solution of **25a** (810 mg, 2.7 mmol, 1.0 eq.) and DMF (207 mg, 2.83 mmol, 1.1 eq.) in 1,2-dichloroethane (30 mL) was cooled to 0 °C. After a dropwise addition of phosphorus oxychloride (434 mg, 2.83 mmol, 1.1 eq.), the solution was warmed to RT and then refluxed for 20 h. After cooling down to RT, an aqueous solution of sodium acetate (1.0 M, 100 mL) was added and the mixture was stirred at RT for 24 h. After separation of the phases, the aqueous phase was extracted with CH_2Cl_2 (2 x 50 mL). The combined organic phases were dried over $MgSO_4$, filtered and the solvent was removed in vacuo. Purification by column chromatography (SiO_2, CH_2Cl_2:hexane 2:3) gave the product as an orange solid (210 mg, 639 µmol, 24%).

^{1}H-NMR (500 MHz, $CDCl_3$) δ / ppm 9.97 (s, 1H, H^{CHO}), 8.20 (d, *J* = 4.0 Hz, 1H, H^{A3}), 8.17 (dd, *J* = 3.7, 1.2 Hz, 1H, H^{C3}), 7.99 (d, *J* = 7.6 Hz, 1H, H^{B5}), 7.91 (d, *J* = 7.7 Hz, 1H, H^{B4}), 7.84 (d, *J* = 4.0 Hz, 1H, H^{A4}), 7.51 (dd, *J* = 5.1, 1.1 Hz, 1H, H^{C5}), 7.23 (dd, *J* = 5.1, 3.7 Hz, 1H, H^{C4}).

^{13}C-NMR (126 MHz, $CDCl_3$) δ / ppm 183.2 (C^{CHO}), 152.6 (C^{B2}), 152.6 (C^{B1}), 148.7 (C^{A2}), 143.6 (C^{A5}), 139.0 (C^{C2}), 137.0 (C^{A4}), 128.5 (C^{C3}), 128.4 (C^{C4}), 128.2 (C^{B3}), 128.1 (C^{A3}), 127.9 (C^{C5}), 127.6 (C^{B5}), 125.4 (C^{B4}), 124.5 (C^{B6}).

7.3.4. 4-Hexyl-5-(7-(3-hexylthiophen-2-yl)benzo[c][1,2,5]thiadiazol-4-yl)thiophene-2-carbaldehyde (26b)[106]

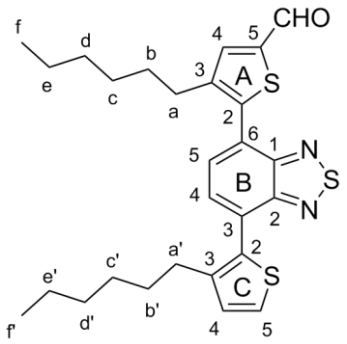

A solution of **25b** (3.39 g, 7.24 mmol, 1.0 eq.) and DMF (582 mg, 7.96 mmol, 1.1 eq.) in 1,2-dichloroethane (50 mL) was cooled to 0 °C. Afterwards phosphorus oxychloride (1.22 g, 7.95 mmol, 1.1 eq.) was added dropwise. The solution was warmed to RT and then refluxed for 24 h. After cooling to RT, an aqueous solution of sodium acetate (1.0 M, 200 mL) was added and the mixture was stirred at RT for 24 h. After separation of the phases, the aqueous phase was extracted with CH_2Cl_2 (3 x 50 mL), the combined organic phases were dried over $MgSO_4$ and the solvent was removed under reduced pressure. The desired product was obtained by column chromatography (SiO_2, CH_2Cl_2:hexane 1:2) as a yellow oil (1.23 g, 2.48 mmol, 34%).

^{1}H-NMR (500 MHz, $CDCl_3$) δ / ppm 9.95 (s, 1H, H^{CHO}), 7.71 (d, *J* = 7.2 Hz, 1H, H^{B5}), 7.68 (d, *J* = 7.2 Hz, 1H, H^{B4}), 7.46 (d, *J* = 5.2 Hz, 1H, H^{C5}), 7.12 (d, *J* = 5.2 Hz, 1H, H^{C4}), 2.70 – 2.64 (m, 4H, H^{a} & $H^{a'}$), 1.67 – 1.59 (m, 4H, H^{b} & $H^{b'}$), 1.29 – 1.14 (m, 12H, H^{c} & $H^{c'}$ & H^{d} & $H^{d'}$ & H^{e} & $H^{e'}$), 0.84 – 0.79 (m, 6H, H^{f} & $H^{f'}$).

^{13}C-NMR (126 MHz, $CDCl_3$) δ / ppm 183.1 (C^{CHO}), 154.3 (C^{B2}), 153.7 (C^{B1}), 143.2 (C^{A3}), 143.0 (C^{A5}), 142.6 (C^{A2}), 142.2 (C^{C3}), 137.9 (C^{A4}), 131.9 (C^{C2}), 130.5 (C^{B5}), 129.7 (C^{B4}), 129.5 (C^{C4}), 129.2 (C^{B3}), 126.4 (C^{C5}), 126.0 (C^{B6}), 31.7 ($C^{d/d'}$), 31.6 ($C^{d/d'}$), 30.8 ($C^{b/b'}$), 30.5 ($C^{b/b'}$), 29.5 ($C^{a/a'}$), 29.4 ($C^{a/a'}$), 29.2 ($C^{c/c'}$), 29.1 ($C^{c/c'}$), 22.7 ($C^{e/e'}$), 22.6 ($C^{e/e'}$), 14.2 ($C^{f/f'}$), 14.1 ($C^{f/f'}$).

7.3.5. 4'-(4-(4,4,5,5-Tetramethyl-1,3,2-dioxaborolan-2-yl)phenyl)-2,2':6',2''-terpyridine (27)[104]

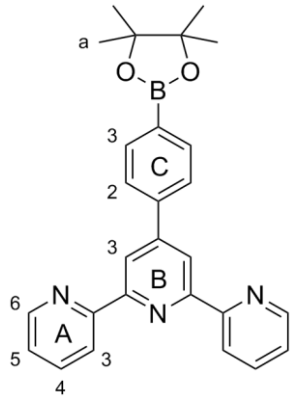

A round bottomed flask was charged with 4'-(4-bromophenyl)-2,2':6',2''-terpyridine (2.00 g, 5.15 mmol, 1.0 eq.), bis(pinacolato)diboron (1.45 g, 5.67 mmol, 1.1 eq.), $Pd(dppf)Cl_2 \bullet CH_2Cl_2$ (126 mg, 155 µmol, 0.03 eq.) and KOAc (1.52 g, 15.5 mmol, 3.0 eq.) under an N_2 atmosphere. Dry, degassed DMSO was added (20 mL) and the mixture stirred at 80 °C over night. Then the still hot mixture was poured into toluene and washed with water several times. After that the organic phase was dried over $MgSO_4$, and the solvent removed under reduced pressure. The obtained solid was suspended in EtOH (~25 mL), sonicated, filtered off and washed with EtOH. After drying on the frit the product was obtained as white solid (1.21 g, 2.78 mmol, 54%).

^{1}H NMR (400 MHz, $CDCl_3$) δ / ppm 8.79 (s, 2H, H^{B3}), 8.77 (d, *J* = 4.0 Hz, 2H, H^{A6}), 8.70 (d, *J* = 8.0 Hz, 2H, H^{A3}), 7.99 – 7.87 (m, 6H, H^{A4} & H^{C2} & H^{C3}), 7.40 (ddd, *J* = 7.5, 4.8, 0.8 Hz, 2H, H^{A5}), 1.38 (s, 12H, H^{a}).
^{11}B NMR (128 MHz, $CDCl_3$) δ / ppm 31.4.

7.3.6. 5-(7-(5-Bromothiophen-2-yl)benzo[c][1,2,5]thiadiazol-4-yl)thiophene-2-carbaldehyde (28a)[107]

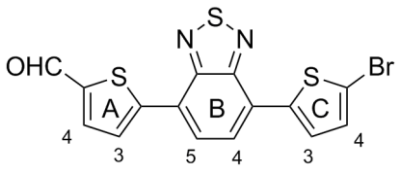

A solution of **26a** (90.0 mg, 274 µmol, 1.0 eq.) in acetic acid (10 mL) and CH_2Cl_2 (10 mL) was stirred at RT. NBS (53.7 mg, 301 µmol, 1.1 eq.) was added in small portions over 20 min. The solution was stirred for 24 h at RT. The precipitate was filtered off and washed with toluene (10 mL), EtOH (10 mL) and diethyl ether (10 mL) and dried in vacuo. The crude product was obtained as a dark purple solid (33.6 mg, 82.5 µmol, 30%).

^{1}H-NMR (500 MHz, DMSO-*d6*) δ / ppm 10.01 (s, 1H, H^{CHO}), 8.39 – 8.36 (m, 1H, H^{B5}), 8.33 – 8.30 (m, 1H, H^{A3}), 8.25 – 8.23 (m, 1H, H^{B4}), 8.15 (d, *J* = 4.1 Hz, 1H, H^{A4}), 8.04 (d, *J* = 4.0 Hz, 1H, H^{C3}), 7.44 (d, *J* = 4.1 Hz, 1H, H^{C4}).

7.3.7. 5-(7-(5-Bromo-3-hexylthiophen-2-yl)benzo[c][1,2,5]thiadiazol-4-yl)-4-hexylthiophene-2-carbaldehyde (28b)

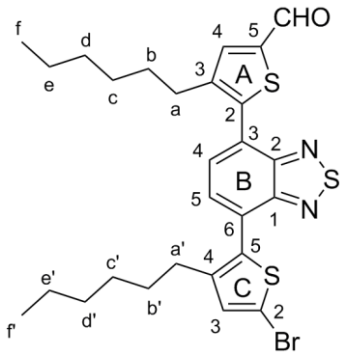

26b (600 mg, 1.21 mmol, 1.0 eq.) was dissolved in a mixture of acetic acid (30 mL) and CH_2Cl_2 (30 mL). While stirring the solution at RT, NBS (236 mg, 1.33 mmol, 1.1 eq.) was added in small portions over 30 min. The mixture was stirred at RT for 24 h, then H_2O (30 mL) was added and the organic phase was washed with H_2O (2 x 10 mL). The organic phase was dried over $MgSO_4$, filtered and the solvent was evaporated. The product was purified by column chromatography (SiO_2, CH_2Cl_2:hexane 1:2) and was isolated as a yellow oil (467 mg). The compound was not obtained pure.

^{1}H-NMR (500 MHz, $CDCl_3$) δ / ppm 9.95 (s, 1H, H^{CHO}), 7.78 (s, 1H, H^{A4}), 7.70 (d, *J* = 7.3 Hz, 1H, H^{B4}), 7.65 (d, *J* = 7.2 Hz, 1H, H^{B5}), 7.07 (s, 1H, H^{C3}), 2.70 – 2.60 (m, 4H, H^{a} & $H^{a'}$), 1.69 – 1.55 (m, 4H, H^{b} & $H^{b'}$), 1.30 – 1.15 (m, 12H, H^{c} & $H^{c'}$ & H^{d} & $H^{d'}$ & H^{e} & $H^{e'}$), 0.84 – 0.79 (m, 6H, H^{f} & $H^{f'}$).

^{13}C-NMR (126 MHz, $CDCl_3$) δ / ppm 183.1 (C^{CHO}), 154.00(C^{B1}), 153.6 (C^{B2}), 143.3 (C^{A3}), 143.1 (C^{A5}), 142.8 (C^{C4}), 142.4 (C^{A2}), 137.9 (C^{A4}), 133.4 (C^{C5}), 132.2 (C^{C3}), 130.4 (C^{B4}), 129.6 (C^{B5}), 127.8 (C^{B6}), 126.5 (C^{B3}), 31.7 ($C^{d/d'}$), 31.6 ($C^{d/d'}$), 30.7 ($C^{b(b')}$), 30.5 ($C^{b/b'}$), 29.6 ($C^{a/a'}$), 29.5 ($C^{a/a'}$), 29.2 ($C^{c/c'}$), 29.1 ($C^{c/c'}$), 22.6 ($C^{e/e'}$), 22.6 ($C^{e/e'}$), 14.2 ($C^{f/f'}$), 14.2 ($C^{f/f'}$).

7.3.8. 5-(7-(5-(4-([2,2':6',2''-Terpyridine]-4'-yl)phenyl)thiophen-2-yl)benzo[c][1,2,5]thiadiazol-4-yl)thiophene-2-carbaldehyde (29a)

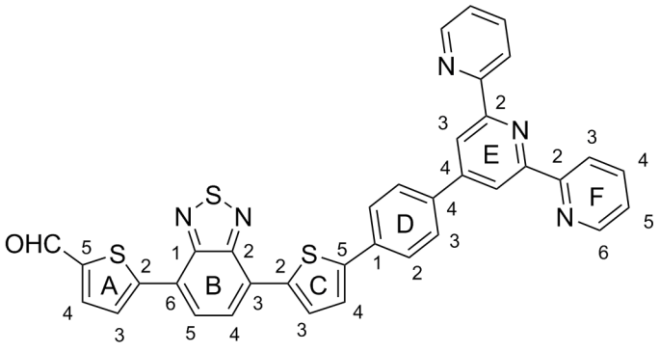

28a (90.0 mg, 221 µmol, 1.0 eq.), **27** (101 mg, 232 µmol, 1.1 eq.), Na_2CO_3 (24.6 mg, 232 µmol, 1.1 eq.) and $Pd(PPh_3)_4$ (7.66 mg, 6.63 µmol, 0.03 eq.) were added to a mixture of toluene (15 mL), EtOH (10 mL) and H_2O (10 mL). The suspension was refluxed for 72 h and then cooled to RT. The solvent was removed under reduced pressure and then $CHCl_3$ (20 mL) was added. The suspension was sonicated for 2 h and afterwards H_2O (40 mL) was added. After removal of $CHCl_3$ under reduced pressure, the precipitate was filtered off and washed with toluene, EtOH and diethylether. The desired product was obtained as a dark red solid (109 mg). The compound was not obtained pure. Due to low solubility in organic solvents, NMR data were recorded in TFA-*d* and refer to the protonated compound.

^{1}H-NMR (500 MHz, CD_2Cl_2, TFA-*d*, D_2O) δ / ppm 9.92 (s, 1H, H^{CHO}), 9.35 (ddd, *J* = 5.9, 1.4, 0.6 Hz, 2H, H^{F6}), 8.87 – 8.77 (m, 4H, H^{F3} & H^{F4}), 8.69 (s, 2H, H^{E3}), 8.23 – 8.18 (m, 4H, H^{A4} & H^{C3} & H^{F5}), 8.08 (d, *J* = 7.7 Hz, 1H, H^{B5}), 8.00 (d, *J* = 7.7 Hz, 1H, H^{B4}), 7.98 – 7.93 (m, 4H. H^{A3} & H^{D2}), 7.90 (d, *J* = 4.0 Hz, 1H, H^{D3}), 7.61 (d, *J* = 3.9 Hz, 1H, H^{C4}).

^{13}C-NMR (126 MHz, CD_2Cl_2, TFA-*d*, H_2O) δ / ppm 187.1 (C^{CHO}), 154.8 (C^{E4}), 152.8 (C^{B2}), 152.8 (C^{B1}), 148.7 (C^{F4}), 147.9 (C^{A2}), 147.4 (C^{F2}), 145.3 (C^{C5}), 143.7 (C^{F6}), 141.0 (C^{A3}), 137.7 (C^{D1}), 134.5 (C^{D4}), 130.4 (C^{C3}), 129.1 (C^{F5}), 128.7 (C^{D3}), 128.6 (C^{B5}), 127.5 (C^{D2}), 126.4 (C^{C4}), 125.8 (C^{B4}), 125.4 (C^{F3}), 123.5 (C^{E3}).

7.3.9. 5-(7-(5-(4-([2,2':6',2''-Terpyridine]-4'-yl)phenyl)-3-hexylthiophen-2-yl)benzo[c][1,2,5]thiadiazol-4-yl)-4-hexylthiophene-2-carbaldehyde (29b)

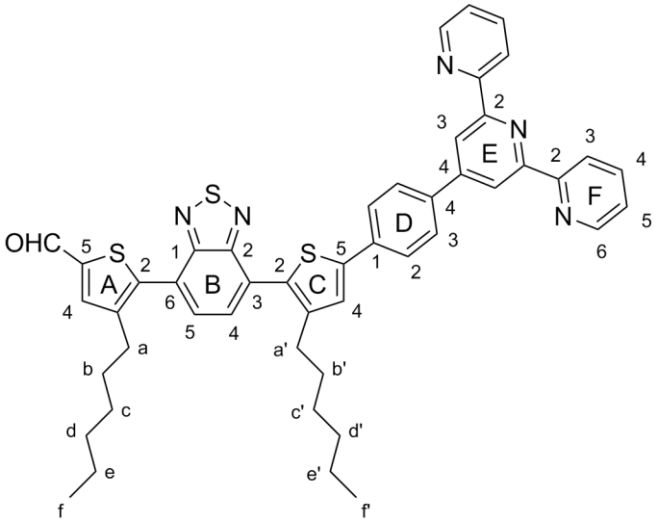

28b (450 mg, 782 µmol, 1.0 eq.), **27** (357 mg, 821 µmol, 1.1 eq.), Na_2CO_3 (87.0 mg, 821 µmol, 1.05 eq.) and $Pd(PPh_3)_4$ (27.1 mg, 23.5 µmol, 0.03 eq.) were added to a mixture of toluene (40 mL), EtOH (25 mL) and H_2O (25 mL). The suspension was refluxed for 72 h and then cooled to RT. The solvent was removed in vacuo and afterwards toluene (30 mL) was added. The mixture was sonicated for 30 min and then H_2O (30 mL) was added. Toluene was removed under reduced pressure and the precipitate that was formed was filtered and washed with toluene, CH_2Cl_2 (10 mL), EtOH (10 mL) and diethyl ether (20 mL). Then hexane was added and the suspension was sonicated. The precipitate was filtered and dried in vacuo. The product was obtained as a red solid (88 mg). The compound was not obtained pure.

^{1}H NMR (400 MHz, CD_2Cl_2) δ / ppm 9.95 (s, 1H, H^{CHO}), 8.82 (s, 2H, H^{B3}), 8.74 (d, *J* = 4.2 Hz, 2H, H^{A6}), 8.71 (d, *J* = 7.9 Hz, 2H, H^{A3}), 7.99 (d, *J* = 8.3 Hz, 2H, H^{D2}), 7.95 – 7.89 (m, 2H, H^{A4}), 7.86 (d, *J* = 8.1 Hz, 2H, H^{D3}), 7.80 (s, 1H, H^{A4}), 7.76 (s, 2H, H^{B4} & H^{B5}), 7.49 (s, 1H, H^{C4}), 7.39 (dd, *J* = 7.5, 4.8 Hz, 2H, H^{A5}), 2.78 – 2.65 (m, 4H, H^{a} & $H^{a'}$), 1.81 – 1.61 (m, 4H, H^{b} & $H^{b'}$), 1.37 – 1.16 (m, 12H, H^{c} & $H^{c'}$ & H^{d} & $H^{d'}$ & H^{e} & $H^{e'}$), 0.93 – 0.80 (m, 6H, H^{f} & $H^{f'}$).

Chapter 8

Chapter 8: The preparation of ZnO electrodes for DSCs

As the previous four chapters showed, TiO_2 is one of the most common n-type semiconductors used in the field of DSCs. Nevertheless, there are several more that are important. Some examples are SnO_2, SiC, WO_3 and ZnO. There are also binary systems under investigation such as TiO_2/CdS[108],[109], SnO_2/CdS[110] and ZnO/ZnS[111]. These materials show different characteristics, i.e. different band gaps and different valence and conduction band energies (Figure 8-1).[47]

This chapter focuses on the fabrication of ZnO electrodes for the application in DSCs combined with zinc(II)-containing dyes. It was necessary to produce different ZnO containing pastes. The intention was to find a semiconductor material, which fits better to the zinc(II) bis-terpyridine based dyes than TiO_2, since it was shown that these systems need certain improvements. ZnO was chosen because it incorporates the same metal ion as the investigated dyes and it shows similar energetic properties to TiO_2 (Figure 8-1).

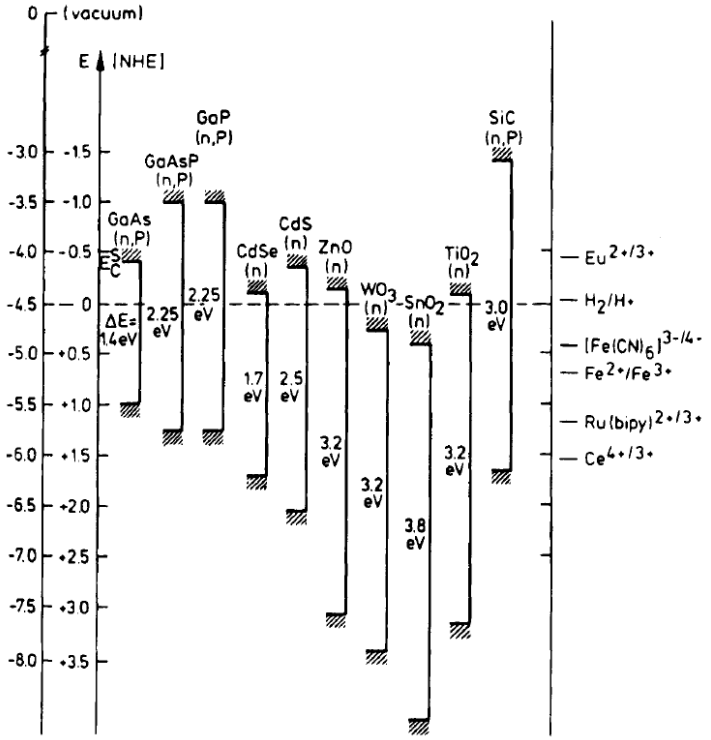

Figure 8-1: Band gaps, valence and conduction bands of different n-type semiconductors.[47]

Different scattering layers were applied to the electrodes to improve the efficiency of the DSCs. For this purpose two different types of SiO_2 nanoparticles were synthesized and pastes produced. Scattering layers consist of nanoparticles of bigger size than those in the semiconductor layer and scatter back the photons that were not absorbed by the dye.

To apply the scattering layer and ZnO to the glass substrate, there are two methods that are fairly cheap and easy to handle in a university chemistry lab, without having to buy large and expensive equipment. One of them is doctor blading, which is a very handy technique to quickly apply a layer of semiconductor paste onto a substrate. The disadvantages are that the layer thickness can only be controlled by the application of a mask on the substrate to set borders with a certain thickness. It is also not possible to apply more than one layer, since the blading process may scratch off parts of the previous layer. Nevertheless pastes for doctor blading experiments were produced and tested with N719.

A slightly more complex method is screen printing. Figure 8-2 shows a schematic interpretation of the screen printing device. This method involves a metal base on which the glass substrate can be locked into the same position again after the printing of each layer. Further it requires a frame with a printing mesh, through which the paste can be transferred onto the glass substrate with a squeegee.

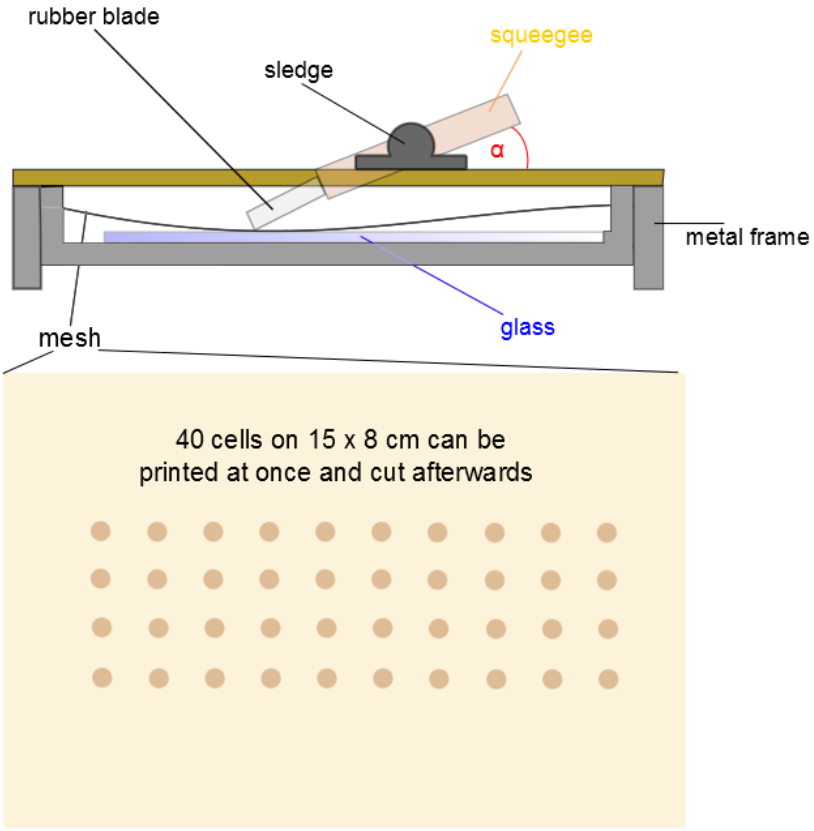

Figure 8-2: Schematic representation of the screen printing device. Figure made by Ewald Schönhofer.

The squeegee is attached to an adjustable sledge on which the angle α can be defined. This angle determines the pressure at which the squeegee pushes the paste through the mesh. The mesh is mounted into a metal frame and is stringed with “SEFAR PET gold”. As one can see in Figure 8-2 and Picture 8-1, the mesh contains 40 printing spots, so that 40 electrodes can be printed at the same time on one big glass plate. A suitable amount of printing paste is then put on the mesh, the sledge with the squeegee (flat angle α) is pushed down on the frame and pulled from left to right (on Figure 8-2), to fill all the holes with paste. In a second step, the previously cleaned glass substrate is fixed on the metal base and the frame with the mesh again mounted on top. The squeegee (steep angle α) is then pulled over the mesh again to transfer the before loaded paste onto the glass substrate.

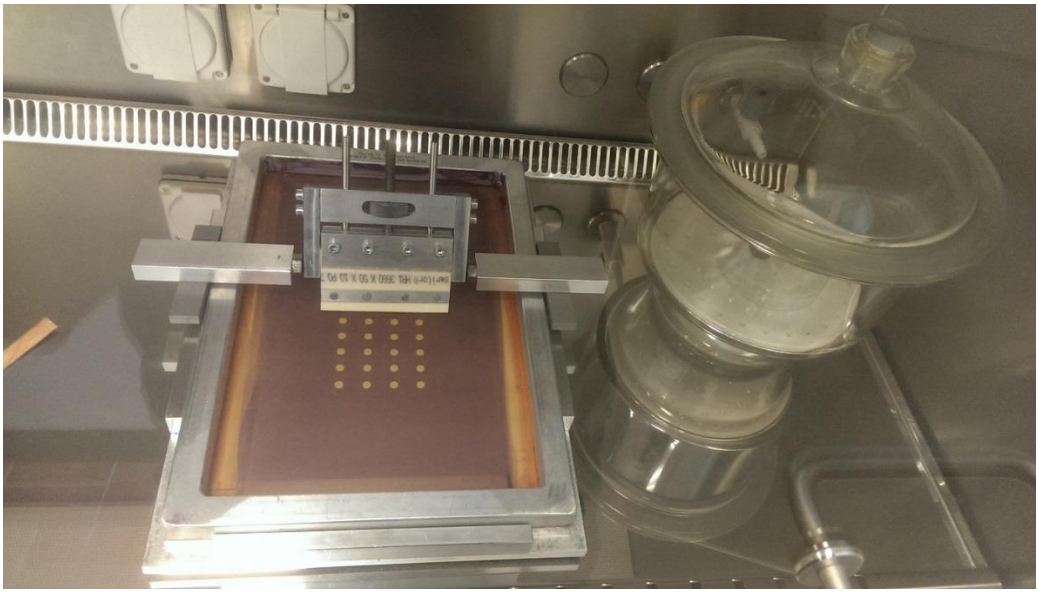

Picture 8-1: Screen printing device with mesh, squeegee and desiccator (for EtOH vapour treatment) inside a clean bench. Photo taken by Ewald Schönhofer.

After this, the glass plate is moved into a desiccator containing an EtOH vapour atmosphere to help the printed paste to relax and form an even surface. Empirical testing shows that for the first layer 1 minute, for the second layer 2 minutes, and for all the later layers 3 minutes are ideal. After removing the glass substrate from the EtOH chamber, it was dried on a hotplate for 6 minutes at 100 °C. The procedure was then repeated for each additional layer. For some of the prepared electrodes, a scattering layer was printed last. These pastes contain particles bigger in diameter, so they are able to backscatter photons that were not absorbed by dye molecules or the semiconductor when they first travelled through the layers. Mostly it is this layer that makes the semiconductor surface look opaque, because the light is scattered on the surface. All of the above described steps were performed inside a clean bench to avoid contamination with dust and other particles.

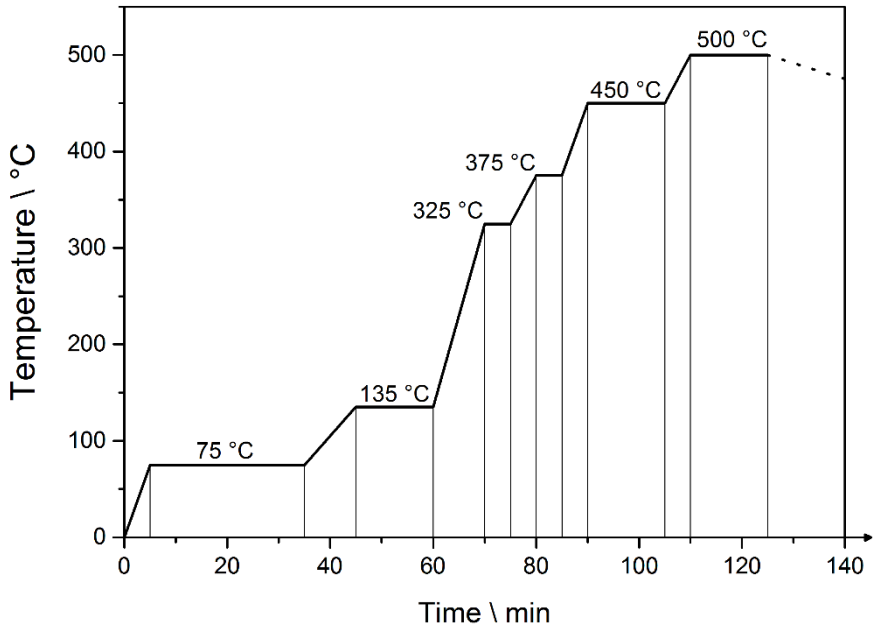

Figure 8-3: Temperature gradient used for the sintering process.

The electrodes were sintered in a Nabertherm N 15/65HA oven, following the protocol shown in Figure 8-3. As one can see the program involves several heating steps as well as holding steps. The main intention is to slowly heat up the electrodes to make sure that the glass does not deform or break. Furthermore it is important that the organic components of the paste evaporate or burn slowly, so that the semiconductor does not get cracks. Therefore each temperature plateau ensures the removal of a specific component of the paste. Heating up to the final 500 °C permits sintering. After sintering the electrodes were cut into their final size of 1.5 cm x 2.0 cm, using a CAMAG smartCUT glass cutter and pincers to break them along the breaking edge (Picture 8-2).

Picture 8-2: CAMAG smartCUT glass cutter and pincers. Photo taken by Ewald Schönhofer

To investigate the screen printed electrodes, the samples were prepared for SEM imaging. After attachment on a sample holder, a layer of gold of a few nanometer thickness was sputtered onto the surface and afterwards the surface connected to the sample holder using conductive silver to guarantee electrical conductivity. Most SEM pictures were recorded on a SEM - FEI Helios Nano Lab 650 dual beam microscope. It features focussed ion beam (FIB) cutting and SEM imaging as well as energy dispersive X-ray spectroscopy (EDX) to investigate the composition of a sample.

The advantage of this dual beam microscope is that the sample can first be manipulated with the FIB gallium ion source and then be observed with standard SEM techniques. In this special case, a cross section of the electrode material was removed using the Ga^+ ion beam. After that the sample could be turned inside the machine to allow the observation of the cross section using SEM. Figure 8-4 shows a schematic representation of the working principle of a FIB SEM microscope. One can see the two parts of the machine, the Ga^+ ion source to manipulate the sample and the electron gun for SEM imaging. The instrument allows detection of secondary electrons as well as back scattered electrons. The latter lead to images with higher material contrast, making it easier to distinguish between areas composed of different elements.[112] The detector, as well as the acceleration potentials, are shown in the respective images.

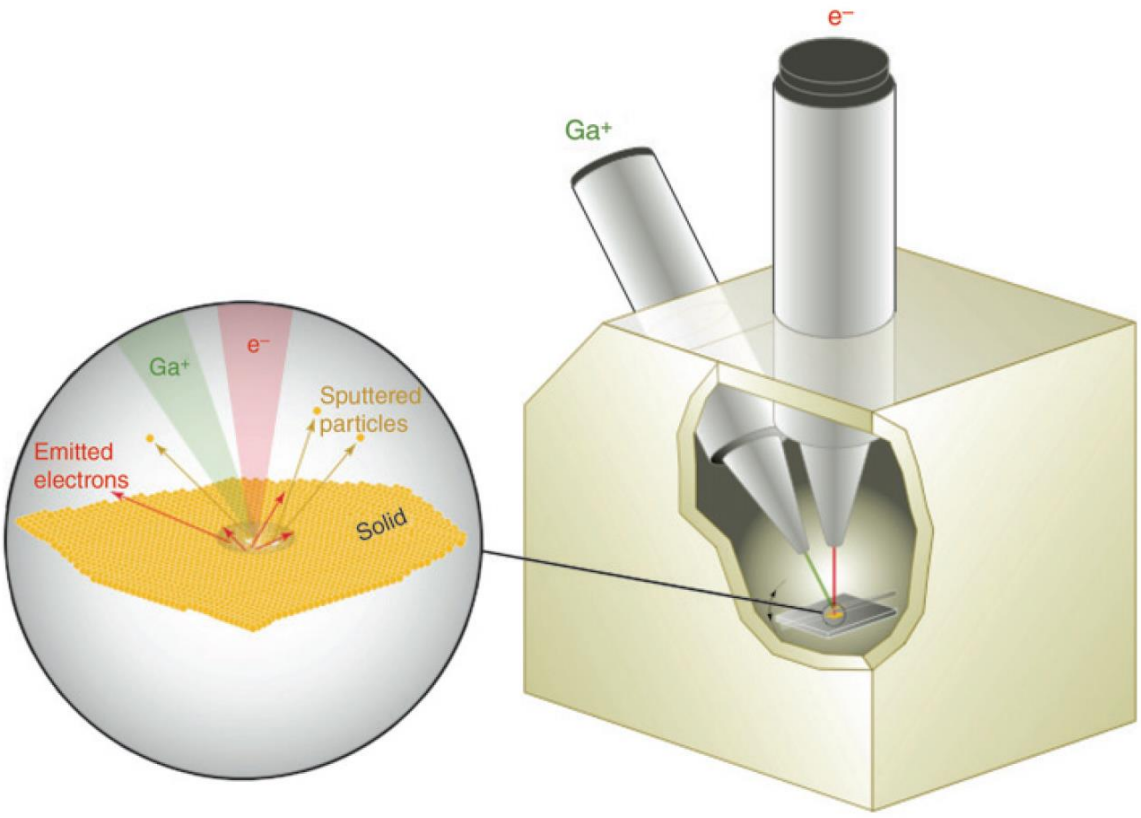

Figure 8-4: Schematic representation of the working principle of a FIB SEM microscope.[112]

8.1. Analysis of the manufactured electrodes

The ZnO pastes described in sections 8.4.2 and 8.4.3 were applied on FTO coated glass using either doctor blading or screen printing. As previous experience in our group has shown, the second method is much more reliable and reproducible, therefore only a few tests were done using the doctor blading method.

A 2.0 cm x 1.5 cm piece of FTO coated glass was cleaned and masked with one layer of scotch tape, to leave only a 0.5 cm broad strip uncovered (Figure 8-5). Then a small amount of the paste was applied on the uncovered part and, using a straight spatula, the paste distributed evenly on the glass plate.

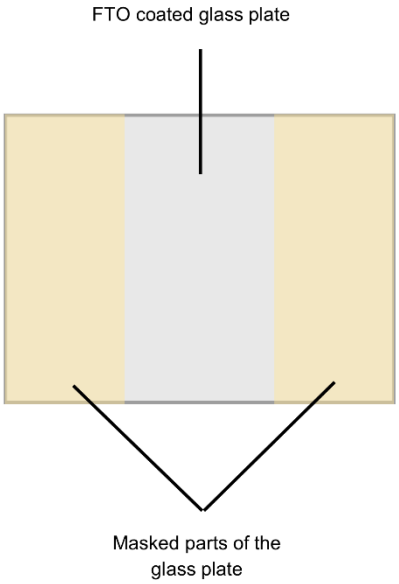

Figure 8-5: Schematic representation of the masked glass plate for doctor blading.

8.1.1. Doctor bladed electrodes

The first attempt to fabricate doctor bladed electrodes was made using paste **DBP1**. Unfortunately, this paste turned out to be too dry and brittle to be evenly distributed on the glass plate, which lead to the slightly altered recipe of **DBP2**, where the ratio of liquid components to ZnO nanoparticles was increased. This lead to a much smoother paste, which could be doctor bladed onto a glass plate. After sintering, the ZnO layer could be very easily removed by only very low mechanical force. Another problem was that the paste dried out very quickly, since the EtOH evaporated within hours. To make the paste slightly more stable and persistent, terpinol was added to **DBP3**. This paste

delivered a nice ZnO layer after doctor blading and sintering. It was therefore used as a sample to be subjected to dyeing with N719 standard dye.

The electrode was immersed in a 0.3 mM solution of N719 in EtOH for 24 h. After that, it was taken out, washed with EtOH and dried. Picture 8-4 and Picture 8-3 show the dyed electrode surface in different magnifications imaged using an optical microscope. The sample is lit from below. One can see that the surface shows certain defects.

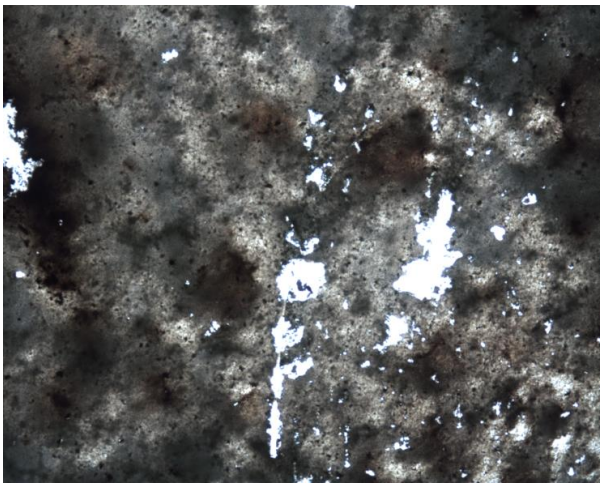

Picture 8-4: Dyed ZnO electrode.

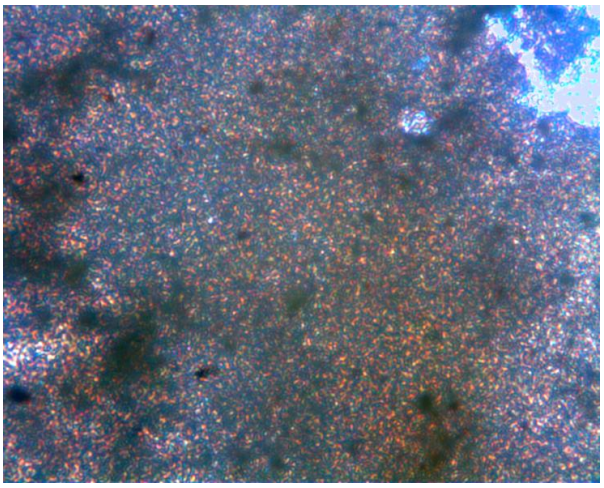

Picture 8-3: Dyed ZnO electrode (zoomed).

In Picture 8-3 one can see the purple colour of the N719 dye. It can not clearly be determined why the ZnO layer peeled off, but it shows that doctor blading is not the method of choice. Thus, screen printing techniques were used in the next experiments.

8.1.2. Screen printed electrodes

Using the equipment described in the introduction of this chapter, ZnO layers were screen printed onto FTO coated glass substrates. Since it is difficult to predetermine the thickness of one layer after sintering and how much over-all thickness every additional layer adds, investigations in this direction had to be made first.

Paste **SPP1** was used to screen print the first electrodes. They were produced following the procedure given in the introduction of this chapter. Picture 8-5 shows a picture of a five layer screen printed ZnO electrode. On can see that the ZnO layer is not opaque, but rather semi-transparent.

Picture 8-5: Sintered electrode consisting of five layers of ZnO.

Electrodes were printed with 1, 3, 5 and 10 layers of paste **SPP1** and the thickness was measured using a profilometer and SEM imaging. The SEM images shown in Picture 8-6 toPicture 8-10 were recorded using a standard SEM instrument. The electrodes were scarified with the CAMAG smartCUT glass cutter and broken right through the semiconductor to obtain a cross section of the electrode on which the imaging was done. A first measurement was done using the profilometer, and the results are presented in Figure 8-6. One can see that one layer adds about 1 µm to the over-all semiconductor thickness, so three printed layers lead to approximately 3 µm thick electrode material. Five layers lead to a layer thickness of about 5 µm to 6 µm. Ten printed layers add up to an over-all thickness of between 9 µm and 11 µm.

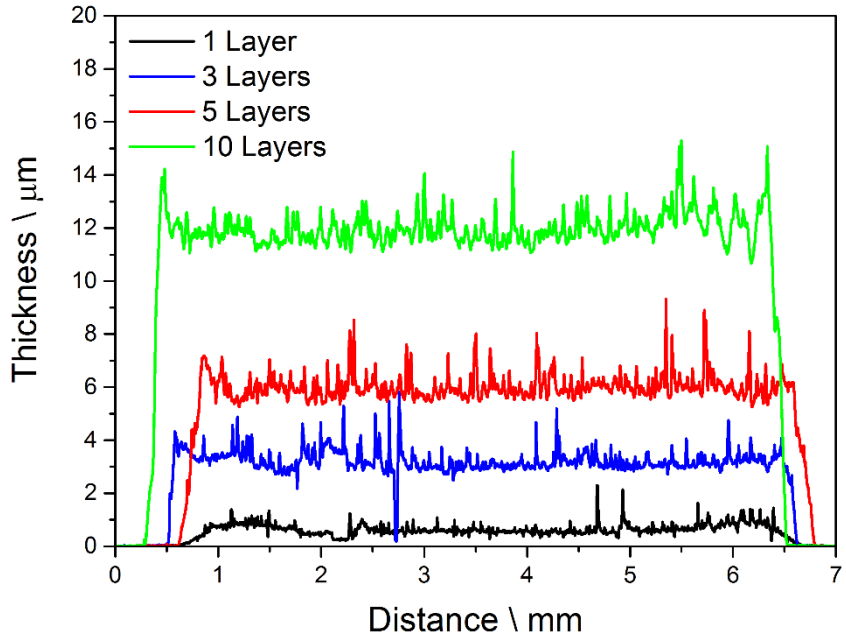

Figure 8-6: Thickness of the sintered semiconductor determined by a profilometer.

Although convenient, the profilometer is not the most accurate method to measure these thicknesses. The way this instrument works is to pull a metal needle over the surface, while a laser detects the vertical movement of the needle to calculate a height profile. It is possible to scratch the sample with the needle and therefore obtain low values. Also, only one straight path through the sample was investigated and this may not be representative of the sample as a whole. On the other hand this method delivers data very quickly and without any sample preparation, which is enough to gain a rough idea about the studied materials. Nevertheless SEM imaging is the method of choice for deeper insights. Picture 8-6 shows an SEM image of one printed layer of **SPP1**. At the very bottom of the image one can see the glass substrate on which an approximately 600 nm thick layer of FTO is attached. On top of the FTO is the printed and sintered ZnO layer of about 2 µm thickness.

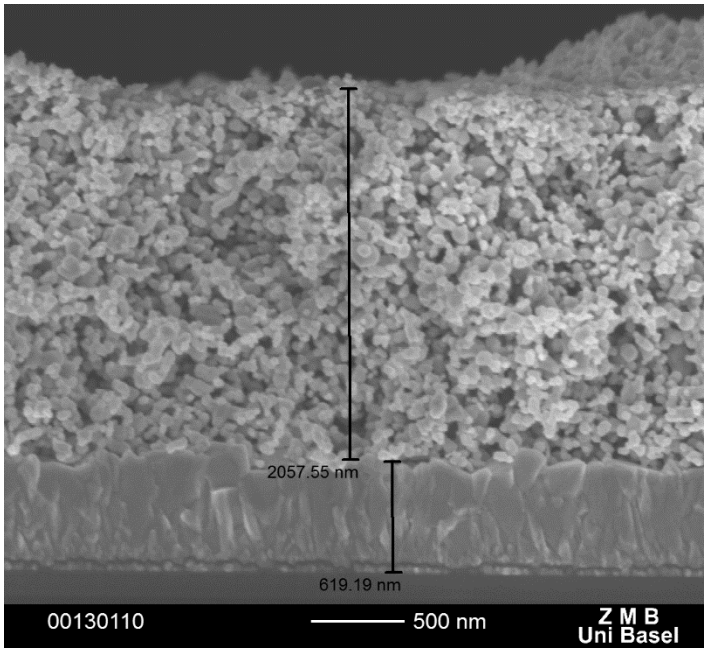

Picture 8-6: SEM image of one layer thick ZnO.

Picture 8-7 shows an image of three printed ZnO layers. Again the glass substrate and the FTO layer are observable. The only noticeable difference is the over-all thickness of the ZnO layer, which lies around 4 µm in this case. In this picture one can see that no individual layer can be observed, which means that the printed layers were all nicely sintered, causing the particles to homogenize.

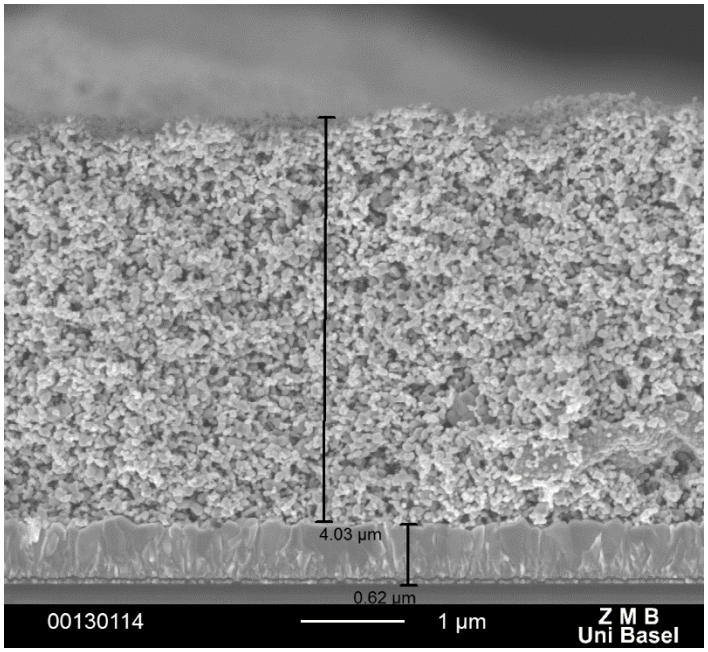

Picture 8-7: SEM image of three layers thick ZnO.

In Picture 8-8 one sees an image of the same sample, but less magnified. It reveals that the over-all layer thickness varies over the whole surface. In this case thicknesses between 4.2 µm and 5.7 µm can be measured.

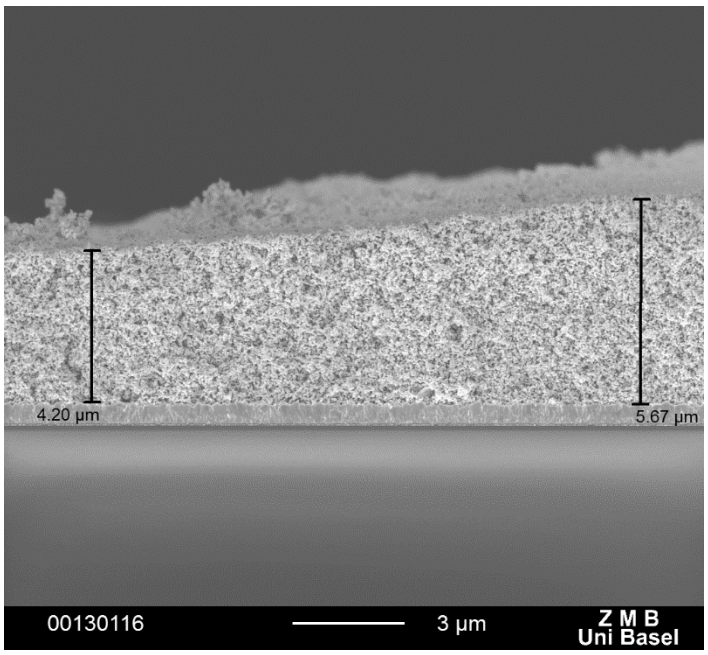

Picture 8-8: SEM image of three layers thick ZnO in lower magnification.

Looking at Picture 8-9 and Picture 8-10 one sees immediately the similarities to Picture 8-6 and Picture 8-8. The only difference here is again the over-all thickness of the ZnO, produced from five printed layers of **SPP1** (~7.6 µm). Again, it appears as one thick layer, rather than five distinguishable layers.

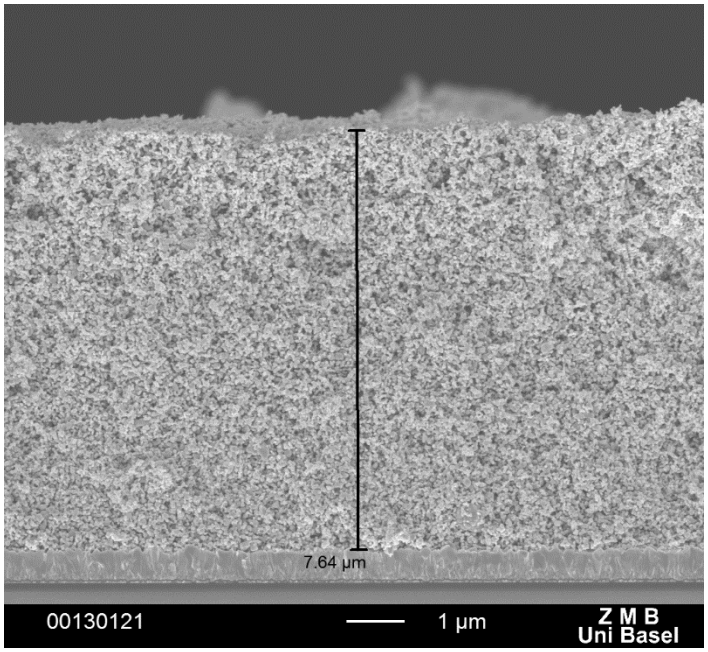

Picture 8-9: SEM image of five layers thick ZnO.

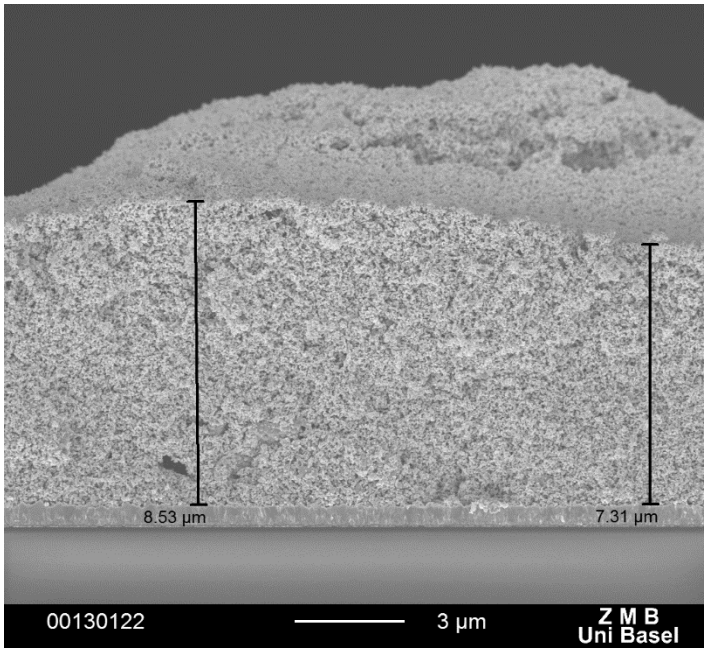

Picture 8-10: SEM image of five layers thick ZnO in lower magnification.

Picture 8-11 was recorded using the dual beam FIB instrument mentioned in the introduction of this chapter. One observes that some of the electrode material has been removed by the gallium ion beam, leaving a cross section that can be imaged using the SEM. The “slug”-like structure on top of the surface is a thin layer of platinum that was added to the top to protect the cutting area from the very abrasive gallium ion

beam. The column-like structures on the cross section are remnants of the ZnO that have not completely been removed by the ion beam. This image shows very nicely the porous structure of the ZnO and also the surprisingly high homogeneity. The thickness of the whole layer is around 13.5 µm.

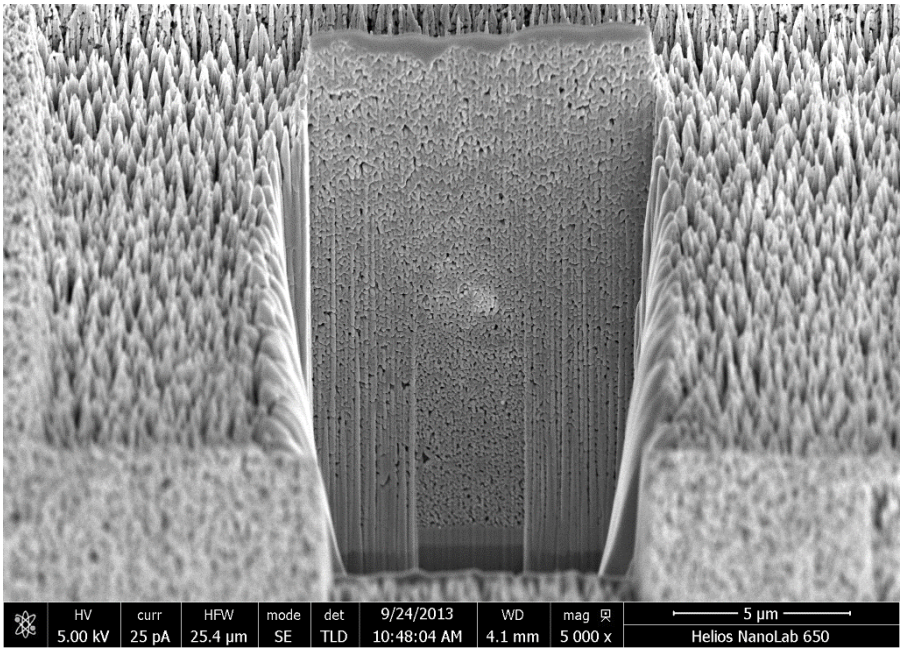

Picture 8-11: SEM - FIB image of ten layers of ZnO.

In Picture 8-12 one can see a close-up on the polished surface of the cross section. It is a 20’000 fold magnification of the cross section shown in Picture 8-11. It is possible to see that the nanoparticles, which comprise the layer are connected with each other. This is very important for efficient charge transport throughout the whole semiconductor. At the bottom, the FTO coated glass substrate is clearly visible as two dark and light grey layer, respectively.

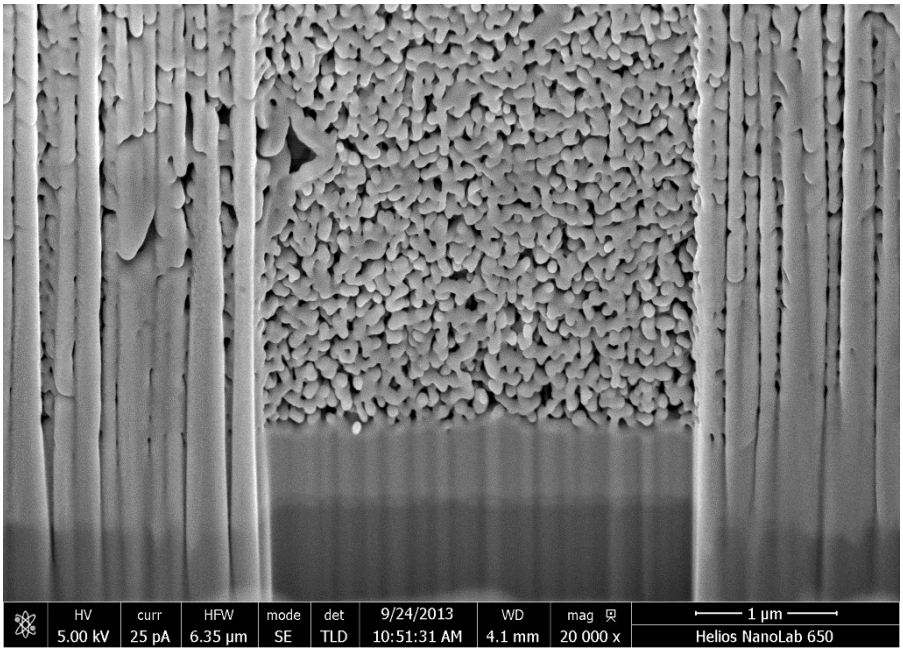

Picture 8-12: 20'000 fold magnification of the cross section shown in Picture 8-11.

8.1.3. Introduction of different types of scattering layers

As already discussed in the introduction of this chapter, not all incident photons are absorbed by the dye and the semiconductor. Some of the photons are scattered back by the surface and are lost or they travel right through the cell without being absorbed and are therefore lost. To overcome at least the second problem it is common to use a covering layer made up from particles of bigger size, since these have the ability to scatter the passing photons back into the cell, where they have another chance to be absorbed.[113]

One way of applying a scattering layer is to screen print it on top of the ZnO layers as a last layer. Since all the solar cell measurements are carried out by irradiating from the backside of the electrode, the top scattering layer will be the last one the incident light passes through. The printing procedure is therefore the same as described in the introduction of the chapter, with the only exception that one additional layer is printed on top of the last ZnO layer. The following SEM – FIB images, recorded after sintering show the results of this approach in terms of layer composition and thickness.

8.1.3.1. TiO_2 scattering layer

The first scattering paste that was tested was WER2-O reflector titania paste purchased from Dyesol. This paste contains TiO_2 particles with an average size between 150 nm and 250 nm. According to the supplier Dyesol, one printed layer should lead to a sintered scattering layer of ~3 µm. On five layers of the **SPP1** ZnO paste, one layer of the before mentioned TiO_2 particle-containing paste was screen printed.

Picture 8-13 shows the different morphologies of the different layers. At the bottom is the glass substrate followed by the FTO layer. On top of this is a 6 µm thick ZnO layer which is covered by an approximately 2 µm thick TiO_2 scattering layer.

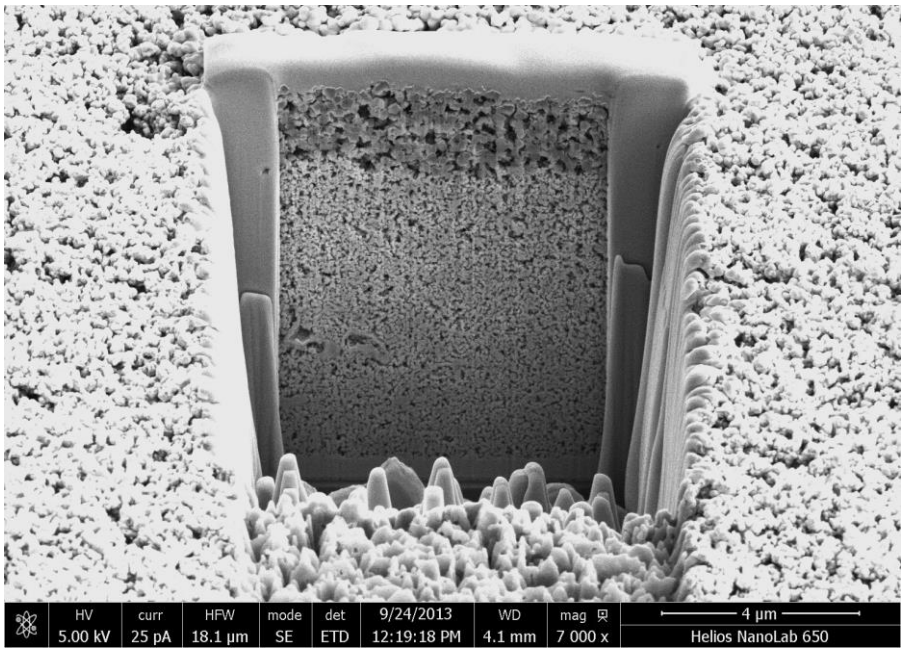

Picture 8-13: SEM - FIB image of five layers ZnO and one layer of TiO_2 scattering particles.

In Picture 8-14 a close-up of the border between the ZnO and the TiO_2 containing layers is shown. The differences in particle size and shape are very easily visible. The ZnO particles have an almost spherical shape, whereas the TiO_2 particle appear more flake-like and have a size between 200 nm and 250 nm. The scattering layer is not as thick as the supplier states, but it is still thick enough to make the electrode surface opaque to the human eye, which proves that indeed light is scattered.

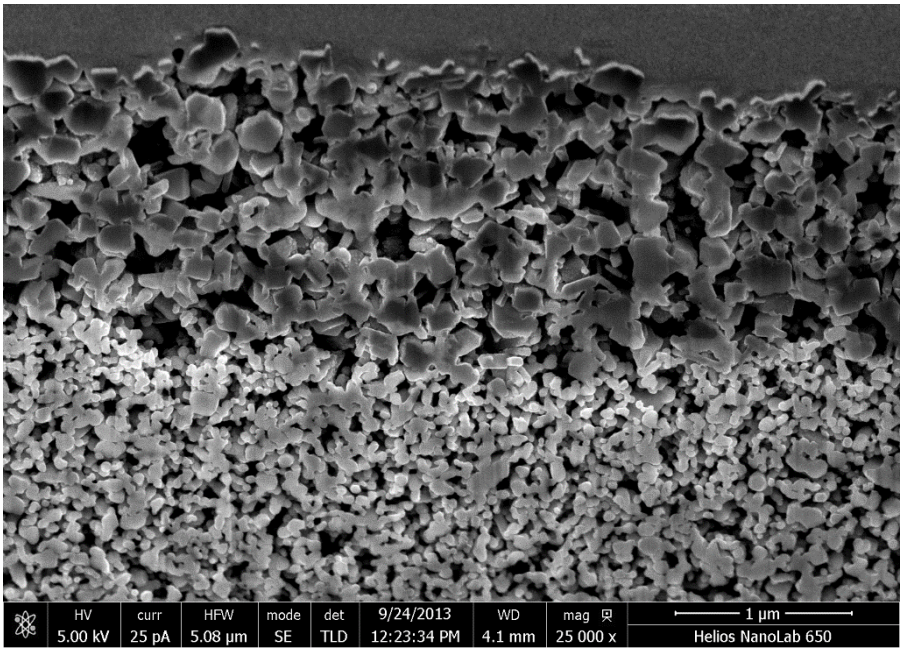

Picture 8-14: SEM - FIB image of five layers ZnO and one layer of TiO_2 scattering particles (close-up).

The sintered electrode is shown in Picture 8-15 and it is obvious that this electrode is much more opaque than the one without a scattering layer (Picture 8-5). Just from this point of view the application of a TiO_2 scattering layer was successful.

Picture 8-15: Photograph of an electrode consisting of 5 layers ZnO and one TiO_2 scattering layer.

8.1.3.2. SiO_2 scattering layers

As described later in section 8.2.3, the TiO_2 scattering layer did not improve the performance of the solar cells. A reason for the lack of improvement might be the fact that TiO_2 is a semiconductor as well as ZnO and therefore they might interfere with each other. An alternative to TiO_2 was found in SiO_2 particles. These can very easily be made with control of their size.[114] And in contrast to the TiO_2, SiO_2 is an insulating material, which should reduce its electronic influence on the cell to a minimum.

One layer of **SPP2** paste was printed on top of five layers of ZnO, screen printed according to the protocol given in the introduction of this chapter. Picture 8-16 illustrates the layer composition of this electrode. From top to bottom one can observe the protecting platinum film, a layer consisting of **SN240** nanoparticles, the ZnO semiconductor layer and the FTO coated glass substrate. What attracts attention is that the layers seem not to be completely separated. It appears as if the bigger SiO_2 particles sank into the adjacent ZnO layer, which is about 6.5 µm thick.

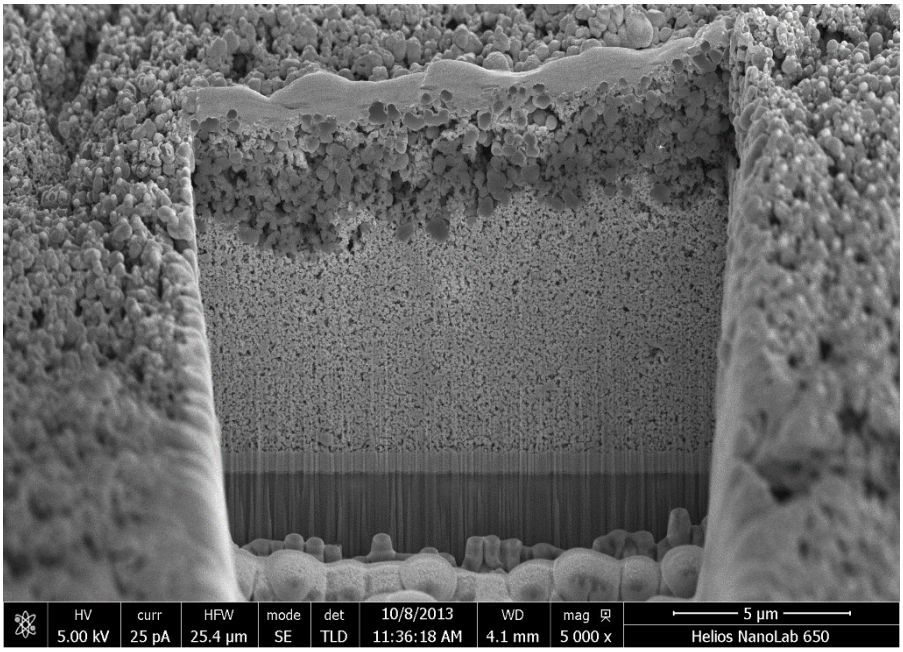

*Picture 8-16: SEM – FIB image of five layers ZnO and one SiO_2 scattering layer (**SPP2** paste).*

Picture 8-17 illustrates that the SiO_2 particles mix with the ZnO particles at the boundary of the layers, but below this the porosity and compactness of the ZnO layer is observable. As expected the SiO_2 particles have sizes between 240 nm and 270 nm, but also aggregates of multiple particles can be observed.

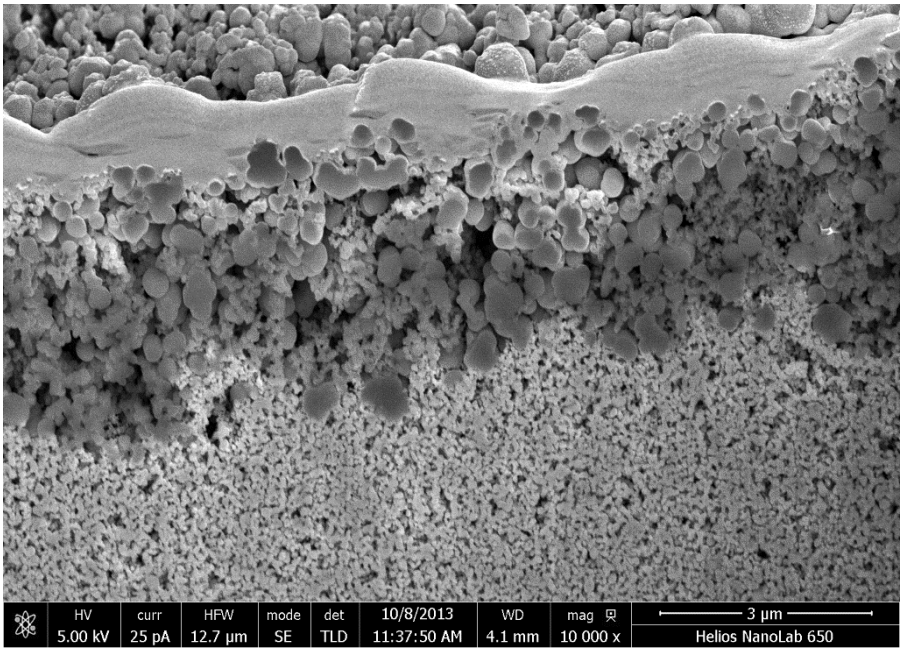

*Picture 8-17: Close-up of the border region between the ZnO and the SiO_2 scattering layer (**SPP2** paste).*

Another set of electrodes was screen printed using **SPP1** and **SPP3** pastes, which contain **SN350** nanoparticles, for the scattering layer. These should be of bigger size than the **SN240** particles, according to the preparation procedure.[114]

In Picture 8-18 one can see a similar layer composition as in Picture 8-16. Again, the scattering layer particles penetrate into the ZnO layer, which is about 7.5 µm thick. The size of the particles in the scattering layer range between 280 µm and 330 µm and are therefore a bit smaller than expected. The ZnO layer is porous and looks quite dense, except for a crack that probably arose from the evaporation of either one of the solvents or the ethyl cellulose used in the paste.

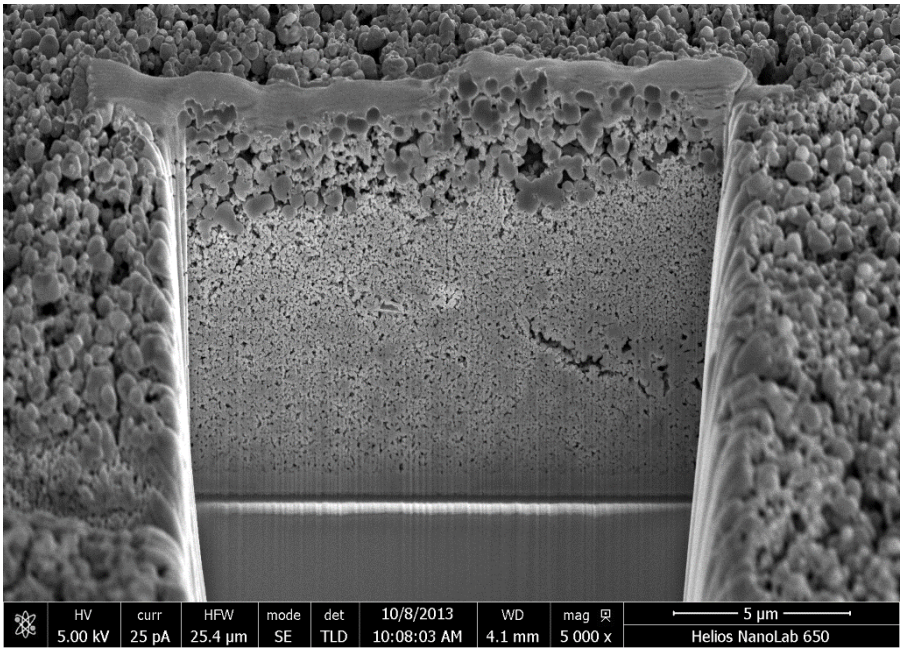

*Picture 8-18: SEM – FIB image of five layers ZnO and one scattering layer (**SPP3** paste).*

A close-up of Picture 8-18 can be seen in Picture 8-19. It is nicely observable how the two different kinds of nanoparticles mix in the top 3 µm. The picture also reveals that there are many aggregated SiO_2 particles in the scattering layer.

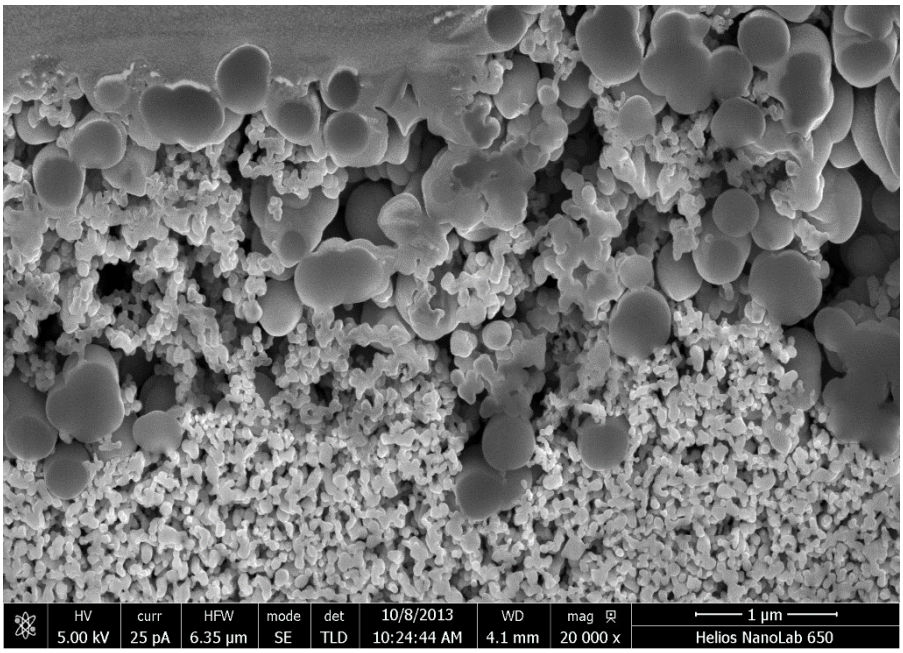

*Picture 8-19: Close-up of the border region between ZnO and SiO_2 scattering layer (**SPP3** paste).*

The electrode on Picture 8-20 consists of 5 layer ZnO and one scattering layer printed with **SPP2**. From an optical point of view, this electrode fulfils the desired criterion that its surface is not transparent.

*Picture 8-20: Photograph of an electrode consisting of 5 layers ZnO and one SiO_2 scattering layer (**SPP2**).*

8.1.3.3. ZnO scattering layers made by acid treatment

For TiO_2 semiconductors it was shown that scattering layers can be generated from the regularly printed nanocrystalline TiO_2 layer by treatment with HNO_3 before sintering. The acid treatment leads to the partial dissolution of the semiconductor layer and the agglomeration of nanoparticles, forming aggregates, which lead to light scattering.[115]

For this experiment 5 layers of ZnO were screen printed, but after the 5th layer the electrodes were immersed into a 2 M HNO_3 (aq) solution for 1, 5, 10, 20, 30 and 60 minutes. One sample was also immersed into milliQ water as a reference and one electrode was not treated at all. All these electrodes were subsequently sintered as mentioned in the introduction of this chapter. The electrodes were then investigated using SEM – FIB imaging and compared by eye.

Picture 8-21 shows the electrodes which have been acid treated for 1, 5, 10, 20 and 30 minutes. As one can see, the longer the electrodes were immersed into the acid, the less material remains on the glass substrate, consistent with reaction between ZnO and HNO_3.

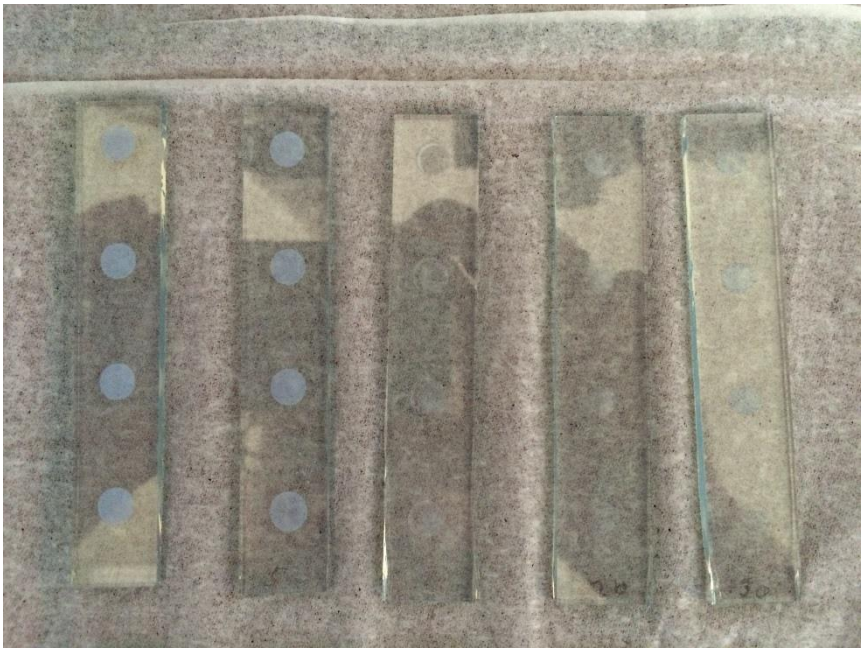

Picture 8-21: Electrodes after acid treatment for 1, 5, 10, 20 and 30 minutes (from left to right).

In comparison Picture 8-22 shows untreated samples (three on the right), which look similar to the one second from left which was immersed in milliQ water for 60 minutes. Also the electrodes acid treated for one minute looks similar.

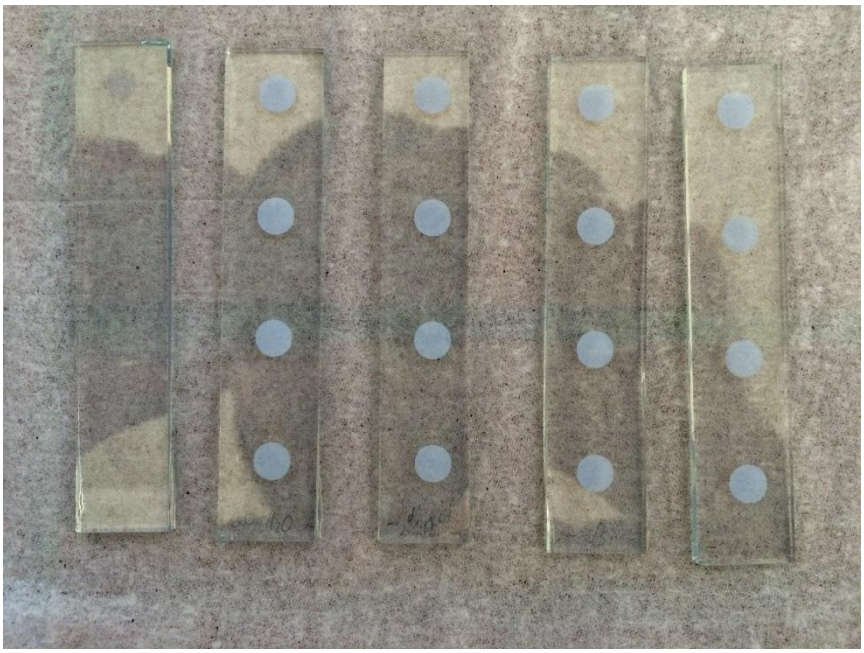

Picture 8-22: Electrodes after acid treatment for 60 minutes (left electrode) and after 60 minutes in milliQ water (second from left). The three samples on the right are not treated at all.

By eye, one can also see that acid treatment for longer than 5 minutes destroys the ZnO layer and removes it completely.
In Picture 8-23, an untreated screen printed ZnO electrode of 2.9 µm thickness is shown.

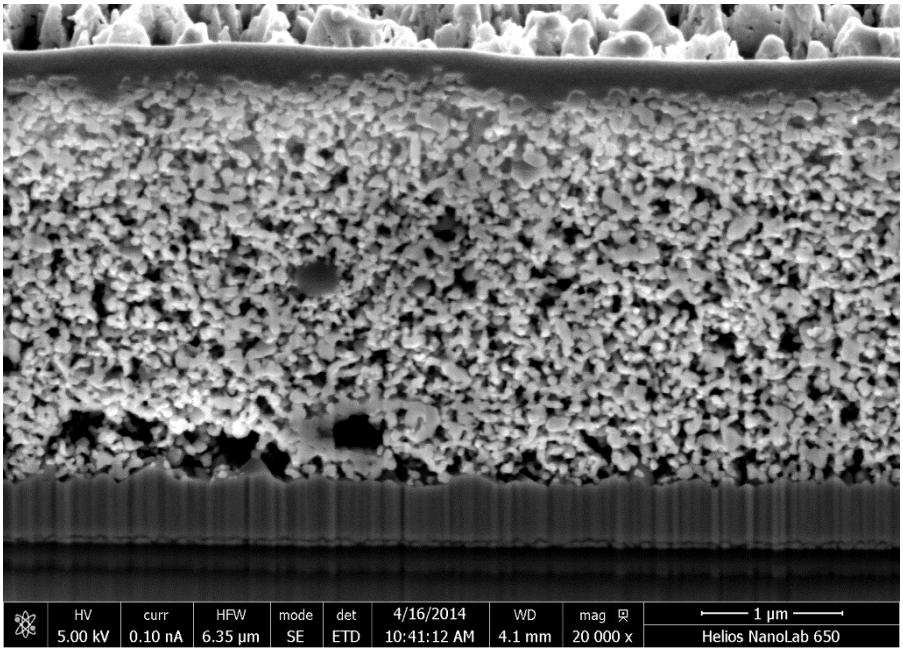

Picture 8-23: SEM – FIB image of an untreated ZnO electrode.

Compared to this, Picture 8-24 shows an image of a ZnO electrode that has been exposed to the acid treatment for 1 minute. It shows a layer thickness of about 2.9 µm, which is the same as the untreated sample. Looking again at Picture 8-21, one can see that the sample treated for 1 minute looks the most similar to the untreated one.

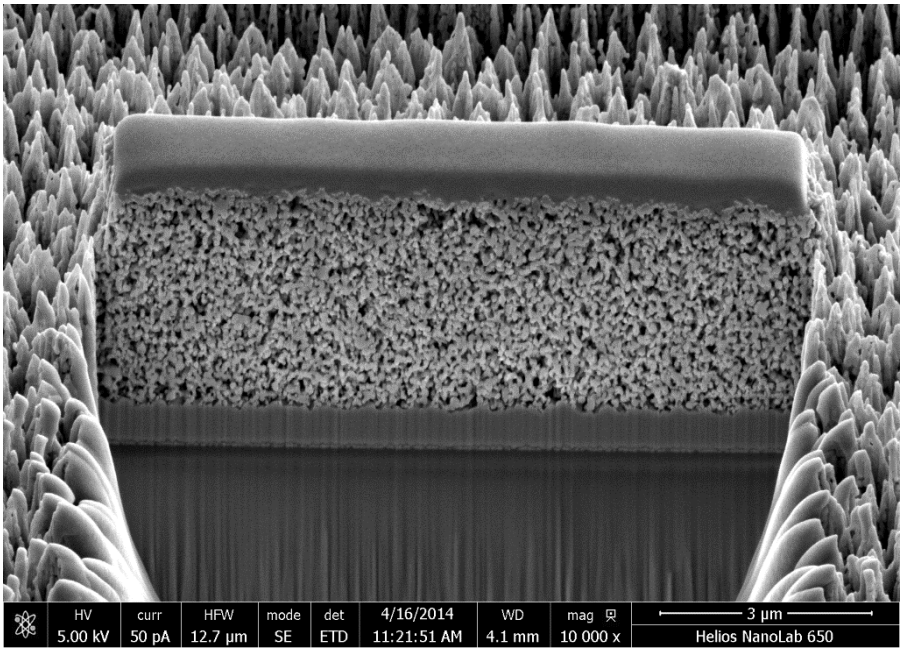

Picture 8-24: SEM- FIB image of ZnO electrode, acid treated for 1 minute.

Picture 8-25 shows a picture of a ZnO electrode immersed in acid for 5 minutes. This layer is only 2.1 µm thick, which indicates that the ZnO layer gets thinner the longer it is exposed to the acid. It is surprising though that the layer does not show any signs of damaging compared to the untreated samples. The thinning of the ZnO layer is consistent with the observations made by eye.

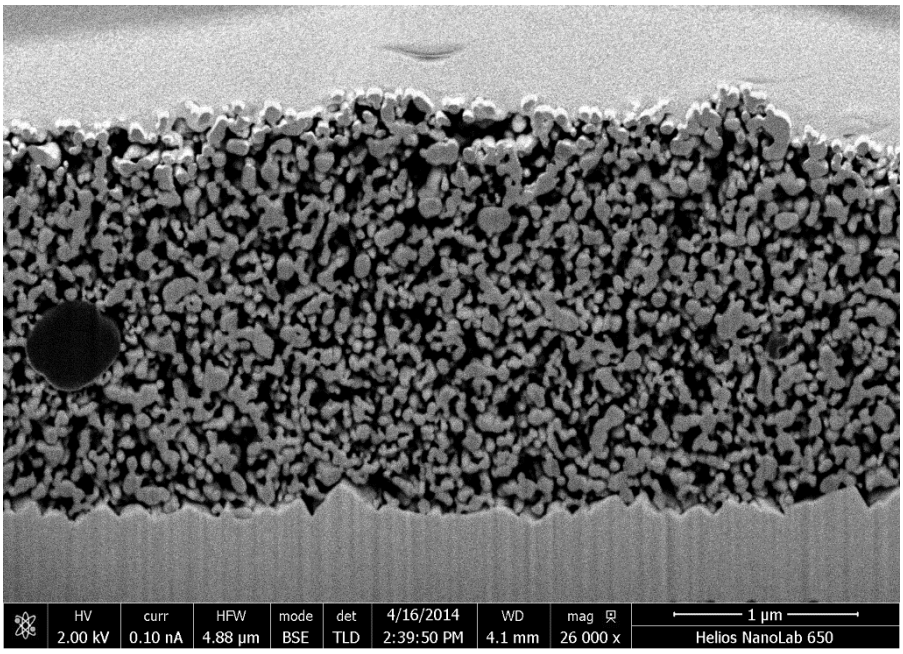

Picture 8-25: SEM- FIB image of ZnO electrode, acid treated for 5 minutes.

The dark spot on the left hand side was proven to be an SiO_2 particle which must have remained in the printing mesh from previous experiments and was imprinted accidently. The composition of the particle was determined by energy dispersive X-ray spectroscopy using the same SEM – FIB microscope (Picture 8-26).

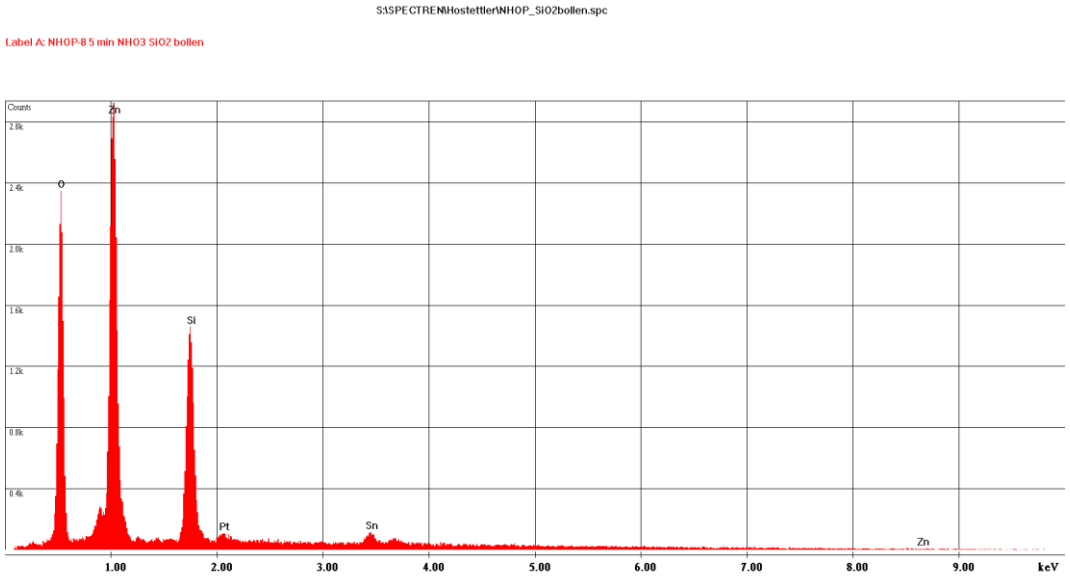

Picture 8-26: EDX spectrum of the SiO_2 particle accidently imprinted into the ZnO layer.

8.2. Solar cell measurements

8.2.1. Dye assembly

The strategy for assembling the dye-functionalized FTO/ZnO electrodes depends on the type of dye. The ruthenium(II)-based N719 is commercially available and contains inherent anchoring groups (CO_2^-). Therefore, for N719, the only parameter that required optimization was the soaking time of the electrode in the dye bath. For zinc(II)-containing dyes, the stepwise procedure described in chapter 4 was used (Figure 8-7).

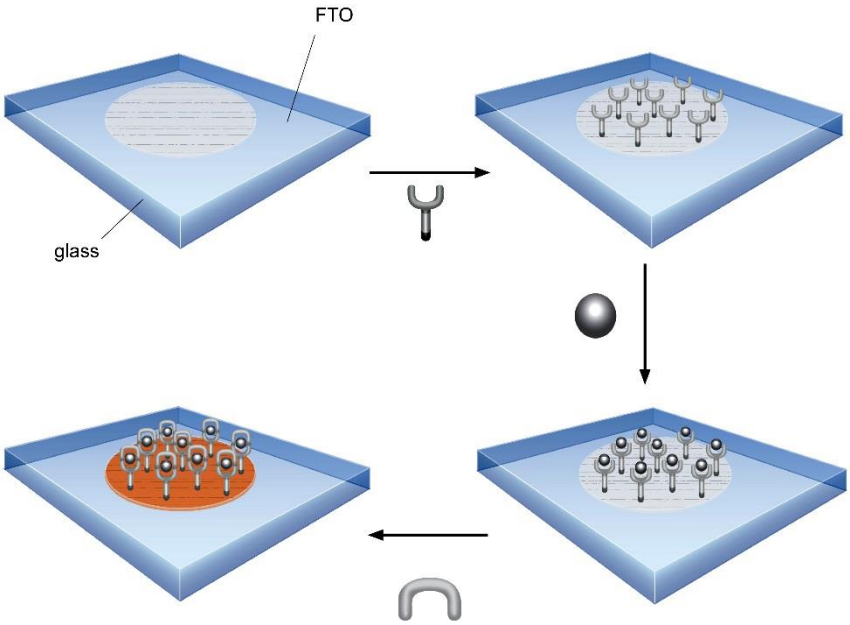

Figure 8-7: Schematic representation of the step-wise procedure. Illustrated by Danielle Hayoz.

For copper(I) containing dyes, an on-surface ligand exchange procedure already established for TiO_2 was used (Figure 8-8).[56],[62],[89],[116]–[118]

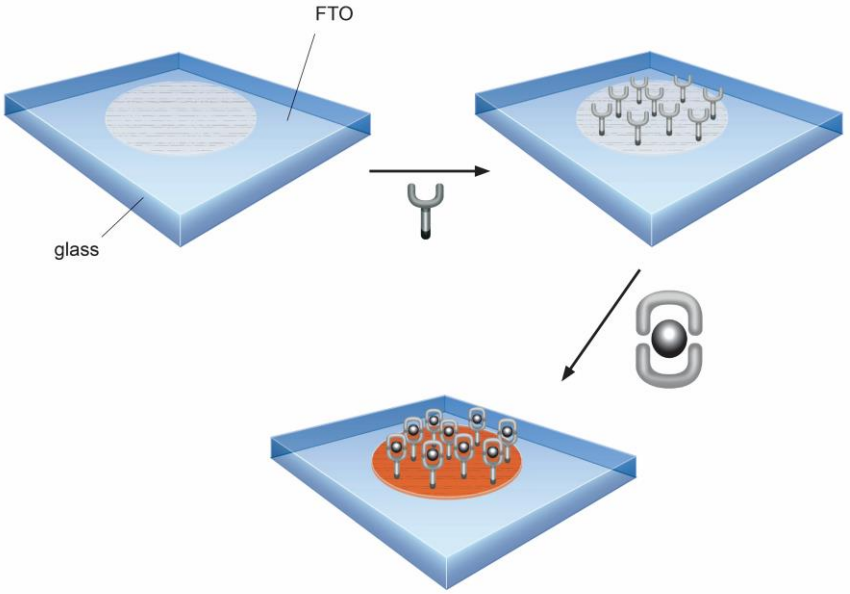

Figure 8-8: Schematic representation of the on-surface ligand exchange procedure. Illustrated by Danielle Hayoz.

8.2.2. Determination of the ideal dipping time for N719

To find out the ideal dipping time for functionalization, 5 layer thick ZnO electrodes were chosen to be dyed with standard dye N719. The electrodes were immersed into a 0.3 mM EtOH solution of N719 for 30 min, 1 h, 19 h and 3 d at room temperature.

The DSC results of the electrodes that were immersed in the dye solution for 30 min are shown in Table 8-1. The best efficiency of 1.82% was reached on the day of sealing of the cell. The same measurement also delivered the highest J_{SC} of 5.15 mA/cm^2 and fill factor of 58%. This value of fill factor is rather low. All the other measurements up to 16 days after the sealing of the cell showed lower performances. V_{OC} on the other hand increased over time.

Anchored dye	J_{SC} \ mA cm^{-2}	V_{OC} \ mV	FF \ %	η \ %
Day of sealing of the cells				
N719_1	**5.15**	603	**58**	**1.82**
2 days after sealing of the cells				
N719_1	5.06	656	51	1.68
4 days after sealing of the cells				
N719_1	5.07	661	46	1.55
8 days after sealing of the cells				
N719_1	5.04	656	45	1.47
16 days after sealing of the cells				
N719_1	4.88	**674**	39	1.28

Table 8-1: Solar cell results of ZnO electrodes immersed in an N719 dye solution for 30 min.

Figure 8-9 shows the JV-curves of the measured cells. It is noticeable that the curves do not have a regular shape and demonstrate a continual worsening of the fill factor over trime. One can also see that over time the J_{SC} drops and V_{OC} increases.

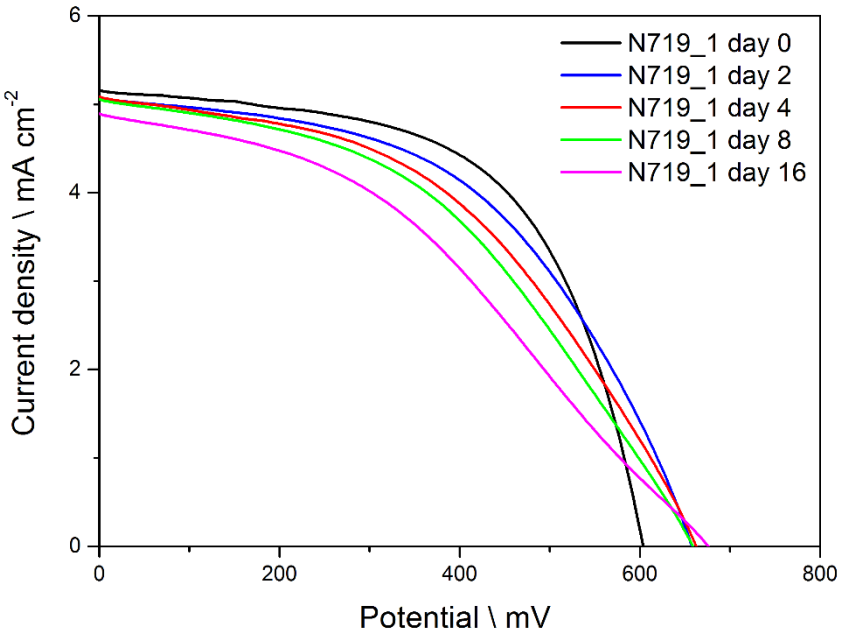

Figure 8-9: JV-curves of solar cells with 30 min dipping time in N719.

The results of the measurements of the cells that were assembled from electrodes immersed in dye solution for 1 h, are shown in Table 8-2. The highest efficiency was reached on day three with 3.66%, although the efficiency stays constant over a period of at least 7 days. On day 17, the efficiency had dropped to 3.32%. Also, the fill factors were quite constant over the whole measuring period. The V_{OC} increased to 712 mV on day 17, from an initial 631 mV. J_{SC} values slightly decreased during the measuring period, namely from 7.86 mA/cm^2 to 7.16 mA/cm^2.

Anchored dye	J_{SC} \ mA cm^{-2}	V_{OC} \ mV	FF \ %	η \ %
Day of sealing of the cells				
N719_2	7.92	641	**71**	3.59
N719_3	7.86	631	69	3.43
1 day after sealing of the cells				
N719_2	7.91	657	70	3.65
N719_3	7.70	662	70	3.57
3 days after sealing of the cells				
N719_2	**7.94**	670	69	**3.66**
N719_3	7.60	671	70	3.55
7 days after sealing of the cells				
N719_2	7.77	691	68	3.63
N719_3	7.48	695	69	3.60
17 days after sealing of the cells				
N719_2	7.41	698	64	3.32
N719_3	7.16	**712**	67	3.41

Table 8-2: Solar cell results of electrodes immersed in dye solution for 1 h.

Figure 8-10 shows the JV-curves of the cells with electrodes that were dipped into the N719 solution for 1 h. If one compares these to the curves measured for the cells with a dipping time of only 30 min, one can see that there is a significant improvement in the fill factor (seen by the curve shape), and also in the better retention of the fill factor over time.

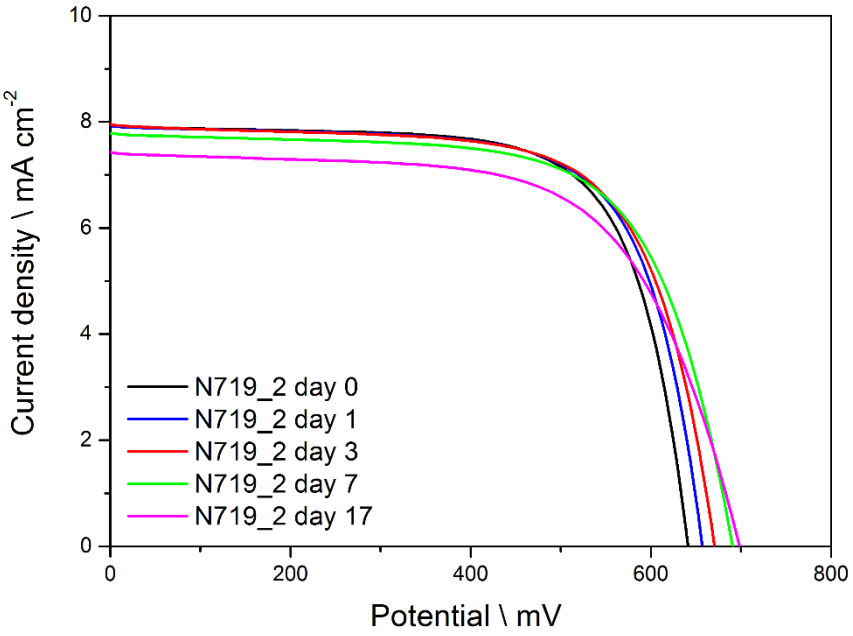

Figure 8-10: JV-curves of solar cells with 1 h dipping time in N719.

Another set of solar cells was assembled from electrodes immersed in the N719 dye solution for 19 h. The results are given in Table 8-3. The highest efficiency of 2.48% was measured on the day of sealing. It decreased over the measuring period of 16 days. The highest fill factor of 60% was achieved on day two. The fill factor for this series laid constantly around this value during the measuring period, although on the day of sealing it was the lowest measured with 54%. V_{OC} increased again slightly from an initial 642 mV to 688 mV on day 16, which is also the highest measured value. J_{SC} showed the highest value of 6.82 mA/cm^2 on the day of sealing and then constantly decreased during the measuring period. The efficiencies are significantly lower than with a 1 hour dipping time.

Anchored dye	J_{SC} \ mA cm^{-2}	V_{OC} \ mV	FF \ %	η \ %
Day of sealing of the cells				
N719_4	**6.82**	636	57	**2.48**
N719_5	7.23	642	54	2.51
2 days after sealing of the cells				
N719_4	6.09	666	59	2.41
N719_5	6.38	675	**60**	2.56
6 days after sealing of the cells				
N719_4	5.89	672	59	2.35
N719_5	6.18	686	61	2.58
16 days after sealing of the cells				
N719_4	5.53	654	58	2.08
N719_5	5.77	**688**	61	2.41

Table 8-3: Solar cell results of ZnO electrodes immersed in N719 dye solution for 19 h.

Figure 8-11 shows the JV-curves of the solar cells that were immersed in the dye solution for 19 h. Again the curve shape supports low fill factors in this series. It is also clearly visible that the J_{SC} decreases over the measuring period and the biggest loss in J_{SC} happened within the first two days.

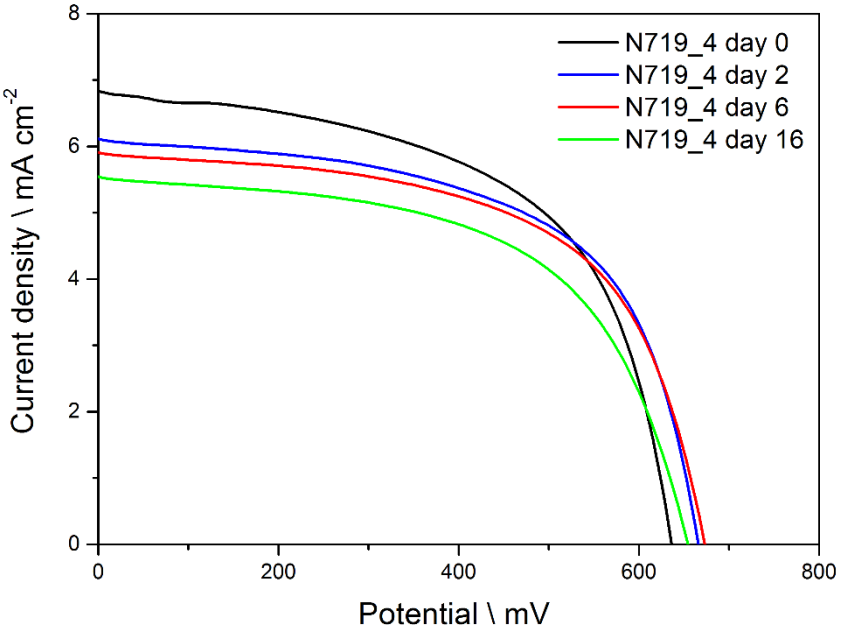

Figure 8-11: JV-curves of solar cells with 19 h dipping time in N719.

Finally, a set of solar cells was assembled with electrodes that were immersed into the dye solution for a longer period of time, namely 3 d. The highest efficiency of 1.98% was reached on the first day after sealing. The efficiencies were over-all quite constant over the measuring period of 11 days. The fill factors increased over the measuring period from an initial 44% to 56%, the latter was the highest measured value, although this is not especially good. V_{OC} slightly increased over time from 624 mV to 658 mV, which was the highest measured value. J_{SC} decreased drastically over time by 1.39 and 1.00 mA/cm^2. The highest measured value was 6.67 mA/cm^2, directly after the sealing.

Anchored dye	J_{SC} \ mA cm^{-2}	V_{OC} \ mV	FF \ %	η \ %
		Day of sealing of the cells		
N719_6	**6.67**	622	44	1.82
N719_7	5.75	624	47	1.67
		1 day after sealing of the cells		
N719_6	6.08	645	50	**1.98**
N719_7	5.34	647	50	1.74
		11 days after sealing of the cells		
N719_6	5.28	650	**56**	1.92
N719_7	4.75	**658**	55	1.70

Table 8-4: Solar cell results of electrodes immersed in dye solution for 3 d.

The JV-curves shown in Figure 8-12 were measured of the solar cells with 3 d dipping time. One can again make the observation that the curve shape (and therefore the fill factor) is poor. There is also a drastic drop in J_{SC} during the measuring period of 11 days.

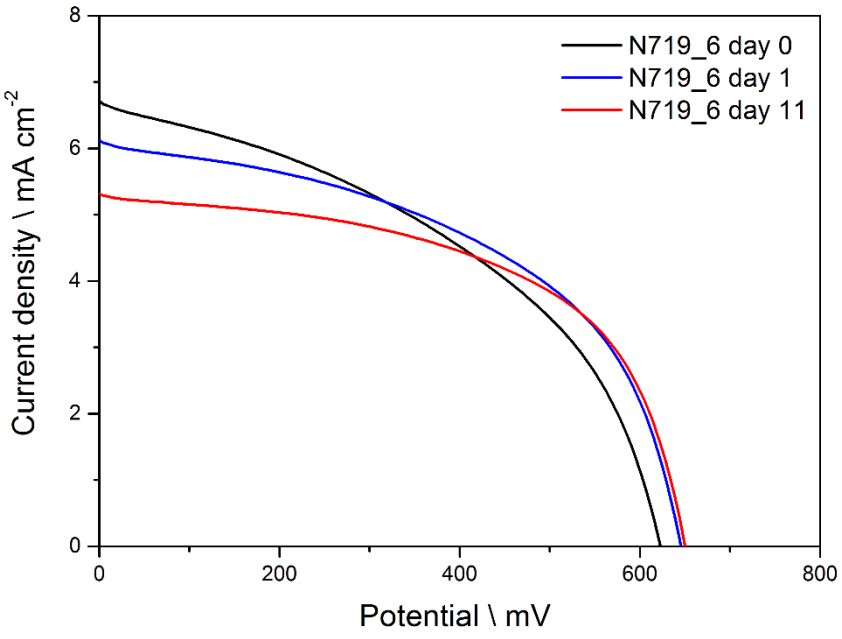

Figure 8-12: JV-curves of solar cells with 3 d dipping time in N719.

Looking at the measured efficiencies, the ones with the highest values were compared to find the optimal dipping time. Figure 8-13 shows the plotted values. From these findings it makes the most sense to use a dipping time of 1 h for future experiments.

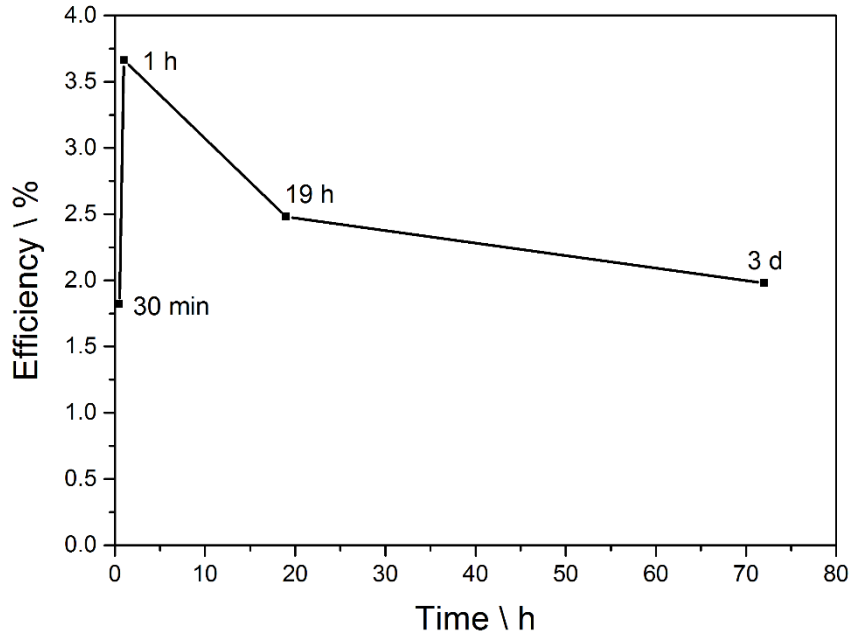

Figure 8-13: Achieved best efficiency vs. dipping time.

8.2.3. Testing of electrodes with TiO_2 scattering layer

The electrodes manufactured in section 8.1.3.1 were investigated for their properties in DSCs. For this purpose solar cells were assembled using N719 as dye and standard II as electrolyte. The dipping time in N719 was 1 h.

Solar cell measurements are shown in Table 8-5. The highest measured efficiency for this set of solar cells was 2.58% on the day of sealing. The same cell shows also the highest fill factor of 66% on the same day. The highest J_{SC} of 6.32 mA/cm^2 is also measured on the day of sealing. The best V_{OC} of 704 mV is achieved 14 days after sealing. The trends are the same as observed for the cells without a scattering layer. V_{OC} increases with time, whereas J_{SC}, fill factor and efficiency decrease over the measuring period. Compared to the most efficient cells without a scattering layer the efficiency could not be increased with the application of a TiO_2 scattering layer.

Anchored dye	J_{SC} \ mA cm^{-2}	V_{OC} \ mV	FF \ %	η \ %
Day of sealing of the cells				
N719_8	6.12	639	**66**	**2.58**
N719_9	**6.32**	605	51	1.96
2 days after sealing of the cells				
N719_8	5.93	678	63	2.52
N719_9	6.07	631	48	1.82
6 days after sealing of the cells				
N719_8	5.94	679	59	2.37
N719_9	5.94	646	44	1.70
14 days after sealing of the cells				
N719_8	5.87	**704**	51	2.09
N719_9	5.80	663	41	1.57

Table 8-5: Solar cell results of ZnO electrodes with TiO_2 scattering layer and N719 dye.

The JV-curves in Figure 8-14 show a poorer profile over time, consistent with the values of the fill factors, which decreased from initially 66% to 51% on day 14. J_{SC} on the other hand is fairly stable during the whole measuring period.

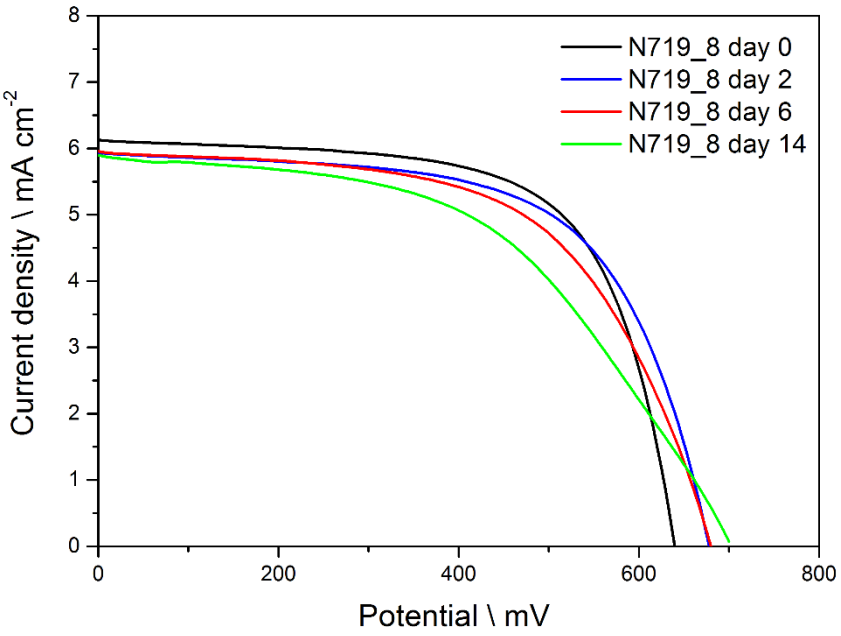

Figure 8-14: JV-curves of solar cells with TiO_2 scattering layer and dye N719.

8.2.4. Testing of electrodes with SiO_2 scattering layer

The electrodes manufactured in section 8.1.3.2 were investigated for their properties in solar cells. For this purpose DSCs were assembled using N719 as dye and standard II as electrolyte. The dipping time was 1 h.

The DSC results are shown in Table 8-6. An efficiency of 2.54% was achieved on the day of sealing, which was the highest measured. The same cell also showed the highest fill factor of 60% and J_{SC} of 6.99 mA/cm^2 on the day of sealing. The highest V_{OC} of 679 mV was measured on day 13. During the measuring period the V_{OC} increased, but all other slightly decreased. Nevertheless the cell efficiency was fairly stable over the period of 13 days.

Anchored dye	J_{SC} \ mA cm^{-2}	V_{OC} \ mV	FF \ %	η \ %
Day of sealing of the cells				
N719_10	**6.99**	611	**60**	**2.54**
N719_11	6.57	582	56	2.14
13 days after sealing of the cells				
N719_10	6.47	**679**	57	2.49
N719_11	5.85	651	54	2.04

Table 8-6: Solar cell results of ZnO electrodes with SiO_2 scattering layer and N719 dye.

The JV-curves measured show that the J_{SC} decreased and the V_{OC} increased over time. The fill factor is quite poor.

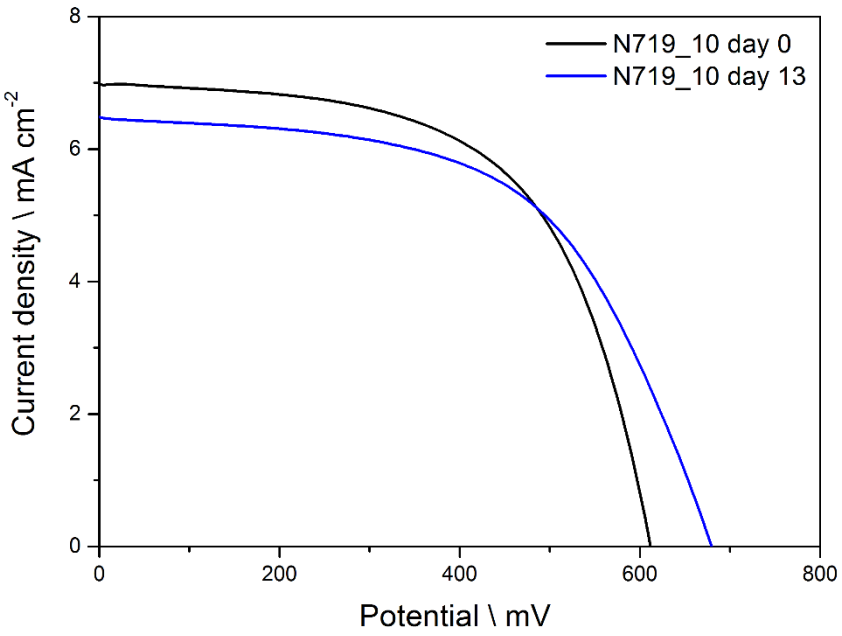

Figure 8-15: JV-curves of solar cells with SiO_2 scattering layer and dye N719.

8.2.5. Using zinc(II) bis-terpyridine based dyes

The original intention of using ZnO was to possibly improve the efficiency of zinc(II) based dyes. Therefore a set of solar cells was assembled using anchoring ligands **8** and **10** and ancillary ligand **6a** (Scheme 8-1). Two 5 layer ZnO electrodes were immersed in a 1 mM solution of **8** or **10** for 24 h. After that the electrodes were washed with DMSO and EtOH and dried. Then they were immersed into a 1 mM solution of $ZnCl_2$ in EtOH for 24 h. After that the electrodes were washed with EtOH and dried. Then they were immersed into a 1 mM solution of **6a** in CH_2Cl_2 for 24 h. After that the electrodes were washed with DCM, dried and the solar cells assembled.

The investigated dyes performed only poorly. The best obtained efficiency of 0.13% was measured on the day of assembly and is lower than the same dye supported on TiO_2 (0.71%)[60]. The best measured values were 49% for the fill factor, a J_{SC} of 0.664 mA/cm^2 and a V_{OC} of 426 mV (Table 8-7). The cells were not measured after the day of sealing, since the DSC performance was very poor.

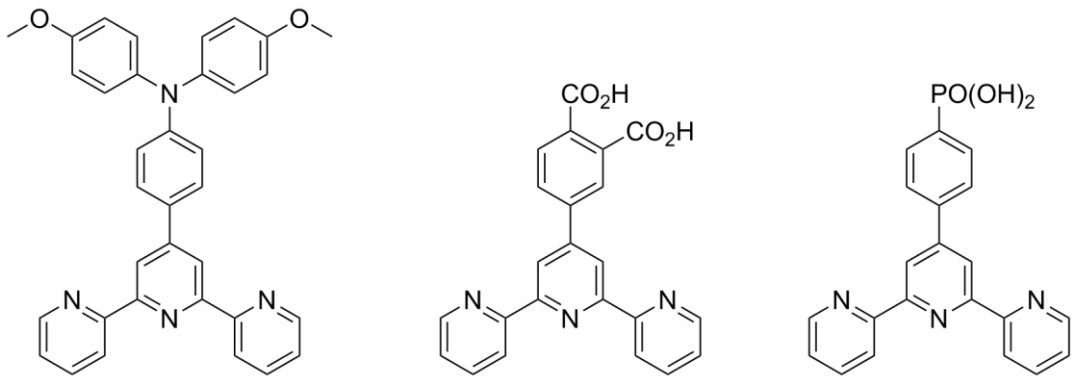

6a **8** **10**

*Scheme 8-1: Ancillary ligand **6a** and anchoring ligands **8** and **10**.*

Anchored dye and cell number	J_{SC} \ mA cm^{-2}	V_{OC} \ mV	FF \ %	η \ %	η rel. to N719 \ %
Day of sealing of the cells					
[(**8**)Zn(**6a**)]Cl_2 1	0.664	414	33	0.06	2.50
[(**8**)Zn(**6a**)]Cl_2 2	0.644	426	49	0.13	5.42
[(**10**)Zn(**6a**)]Cl_2 1	0.442	402	33	0.06	2.50
[(**10**)Zn(**6a**)]Cl_2 2	0.423	403	34	0.06	2.50
N719	7.360	607	54	2.40	100

Table 8-7: Solar cell results of ZnO electrodes with Zn(II) based dyes.

The JV-curves in Figure 8-16 show that the cell parameters are indeed very poor. Nevertheless, one can observe a separation of the J_{SC} between the dyes containing anchoring ligands **8** and **10** which was also observed in chapter 4.[60]

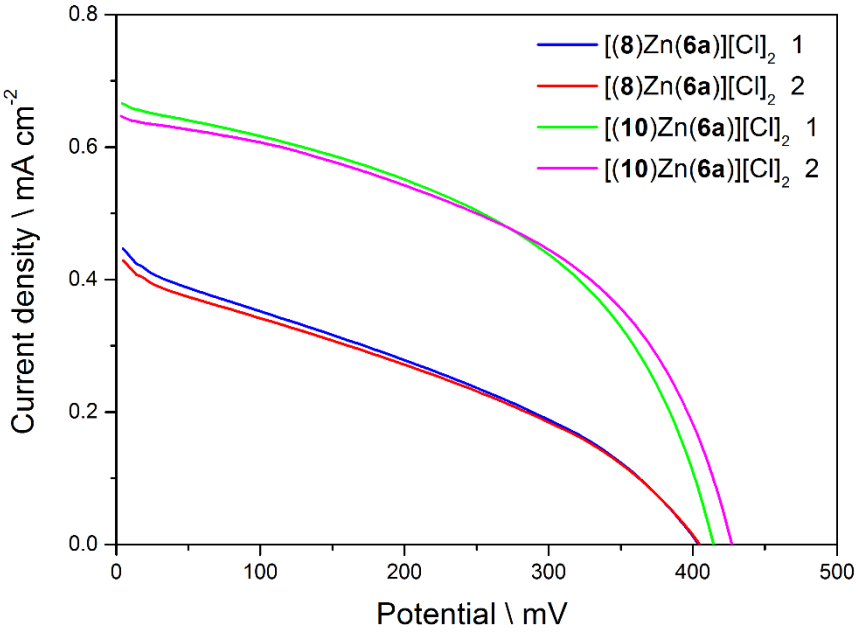

Figure 8-16: JV-curves of solar cells using Zn(II) based dyes.

Since it is known that ZnO changes its band gap upon heating,[119] the effect of heating the cells during the JV-measurements was investigated. For this purpose the cells were heated to 60 °C and 80 °C. The results are shown in Table 8-8 and it can be observed that the efficiency slightly improved. Also the J_{SC} and fill factors increased upon heating. It is interesting that the fill factor of cell [(**10**)Zn(**6a**)]Cl_2 1 still shows an improved fill factor after 17 days and at 25 °C. This means that heating the cell to 80 °C induced a change inside the cell, which is not instantly reversible when the cell was cooled back down to RT. This might be a way to post treat cells to optimize their performance after sealing.

Anchored dye and cell number	J_{SC} \ mA cm^{-2}	V_{OC} \ mV	FF \ %	η \ %	η rel. to N719 \ %	Temp.
Day of sealing of the cells						
[(**8**)Zn(**6a**)]Cl_2 1	0.664	414	33	0.06	2.50	25 °C
[(**8**)Zn(**6a**)]Cl_2 2	0.644	426	49	0.13	5.42	
[(**10**)Zn(**6a**)]Cl_2 1	0.442	402	**33**	0.06	2.50	
[(**10**)Zn(**6a**)]Cl_2 2	0.423	403	34	0.06	2.50	
N719	7.360	607	54	2.40	100	
[(**8**)Zn(**6a**)]Cl_2 1	0.696	379	50	0.13	5.80	60 °C
[(**8**)Zn(**6a**)]Cl_2 2	0.689	401	51	0.14	6.25	
[(**10**)Zn(**6a**)]Cl_2 1	0.530	370	41	0.08	3.57	
[(**10**)Zn(**6a**)]Cl_2 2	0.536	375	41	0.08	3.57	
N719	6.940	561	58	2.24	100	
[(**8**)Zn(**6a**)]Cl_2 1	0.718	380	52	0.14	6.45	80 °C
[(**8**)Zn(**6a**)]Cl_2 2	0.728	390	51	0.15	6.91	
[(**10**)Zn(**6a**)]Cl_2 1	0.590	360	**45**	0.09	4.15	
[(**10**)Zn(**6a**)]Cl_2 2	0.580	358	44	0.09	4.15	
N719	6.540	562	59	2.17	100	
17 days after sealing of the cells						
[(**10**)Zn(**6a**)]Cl_2 1	0.550	437	**45**	0.11	-	25 °C

Table 8-8: Solar cell results of ZnO electrodes with Zn(II) based dyes measured at different temperatures.

8.2.6. Using bis-bipyridine copper(I) based dyes

Since one main area of research in our group is copper(I) based dyes for DSCs, it was tested, if one of these dyes would also work with a ZnO semiconductor. Therefore an existing copper dye was used (provided by Dr. Sven Brauchli), which is shown in Scheme 8-2.

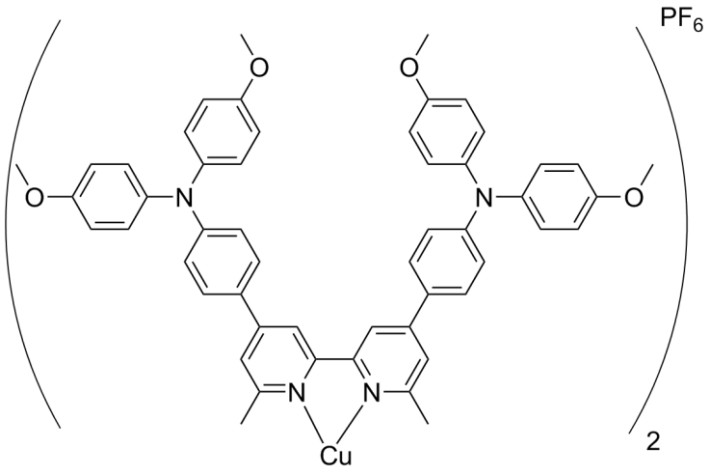

Scheme 8-2: Homoleptic copper(I) complex that was used.

The electrodes consisted of five screen printed layers of ZnO and were dyed using the classical approach discussed in section 8.2.1. For this the electrodes were first immersed into a 1 mM solution of anchoring ligand ALC1 or ALP1 (Scheme 8-3) in DMSO for 3 d. Then they were washed with DMSO and EtOH and dried. After that they were immersed into a 0.1 mM solution of the homoleptic copper(I) complex in MeCN for 2 d. After washing with MeCN and drying, the cells were assembled and filled with standard II electrolyte.

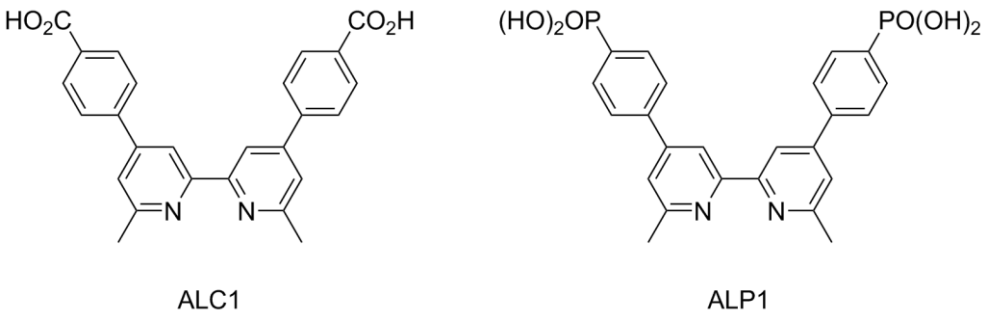

Scheme 8-3: The used anchoring ligands ALC1 and ALP1.

When the electrodes were taken out of the anchoring ligand solutions one could observe the decomposition of the semiconductor, which resulted in the partial peeling off of the ZnO. Nevertheless, measurements were done with the cells.

The JV-curves of the cells are shown in Figure 8-17. The curve shape confirms that the fill factors are not good and a discrepancy between V_{OC} values of the duplicated cells using ALC1 can be seen, whereas for the duplicated cells using ALP1, V_{OC} values are almost identical.

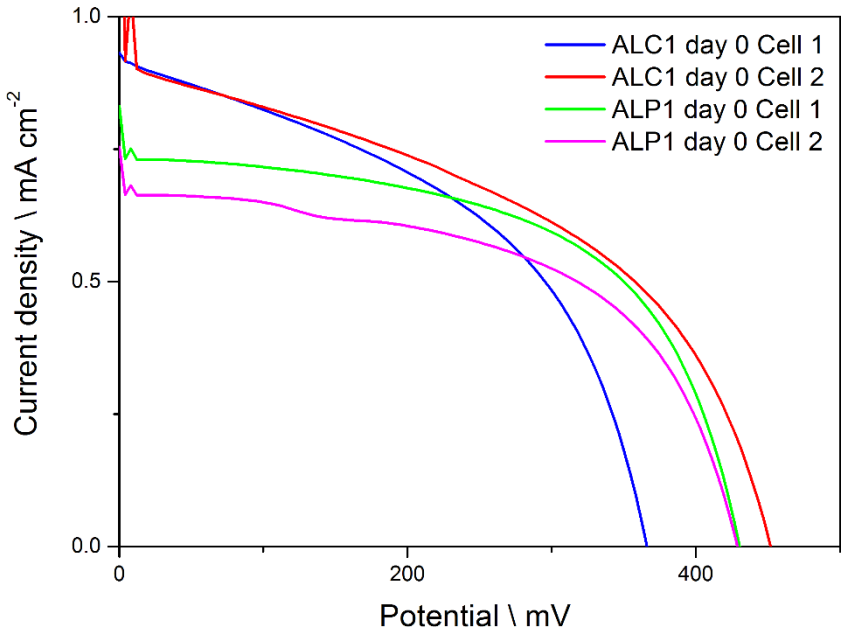

Figure 8-17: JV-curves of solar cells using Cu(I) based dyes with anchoring ligands ALC1 and ALP1.

The JV-measurements (Table 8-9) show that also the copper(I) based DSCs perform poorly. The highest achieved efficiency of 0.24% was measured nine days after the sealing by a cell using ALP1 as an anchor. The same cell also shows the highest measured V_{OC} of 501 mV in this set. The highest J_{SC} was measured on the day of sealing, achieved by a cell using ALC1. The fill factors of all measured cells are poor and lie below 56% for all cells containing the copper(I) based dye.

Cell number	Anchoring ligand	J_{SC} \ mA cm^{-2}	V_{OC} \ mV	FF \ %	η \ %	η rel. to N719 \ %
			Day of sealing of the cells			
1	ALC1	0.930	440	46	0.19	7.31
2	ALC1	**1.100**	450	38	0.19	7.31
1	ALP1	0.760	430	**55**	0.18	6.92
2	ALP1	0.690	428	54	0.16	6.15
N719	-	6.37	613	66	2.60	100
			9 days after sealing of the cells			
1	ALC1	0.810	490	45	0.18	7.29
2	ALC1	0.810	485	43	0.17	6.88
1	ALP1	0.900	**501**	53	**0.24**	9.72
2	ALP1	0.770	496	53	0.20	8.10
N719	-	6.06	676	60	2.47	100

Table 8-9: Solar cell results of ZnO electrodes with Cu(I) based dyes with anchoring ligands ALC1 and ALP1.

The performance of the copper(I) based DSCs was very poor compared to the results the same dye achieves on TiO_2 electrodes, namely efficiencies around 2%.[118] The low efficiencies of the copper(I) dye cannot be fully explained but one reason can probably be found in the first dyeing step, where the anchoring ligand solutions cause the semiconductor layer to partially peel off. To overcome this problem, shorter immersion times should be investigated. This on the other hand could have a negative influence on the later dye uptake, since less anchoring ligand molecules are present on the semiconductor.

It is not known which factor causes the ZnO layer to peel off, but if the acidity of the anchoring ligand is a problem, it could be considered in future studies to use the tetrabutylammonium salts of the anchoring ligands ALC1 and ALP1.

8.3. Conclusion and extension of the studies

In this chapter a variety of ZnO containing doctor blading and screen printing pastes were manufactured, furthermore two types of SiO_2 nanoparticles were synthesized. Using the manufactured ZnO screen printing pastes a suitable method for the printing of ZnO electrodes for DSCs was successfully developed. Additionally it was tried to apply TiO_2 and SiO_2 scattering layers, which technically worked. The screen printed electrodes were successfully investigated towards their layer composition and thickness using SEM and SEM – FIB imaging. Furthermore, it was found that 1 h immersion time in N719 dye solution provides the best results in terms of efficiency. Any attempts to improve the DSC efficiencies by the application of a TiO_2 or SiO_2 scattering layer unfortunately lead to a decrease in DSC performance. Also the use of a copper(I) based dye only showed poorly working solar cells. The same is true for the zinc(II) based dyes that were investigated ([(**8**)Zn(**6a**)]Cl_2 and [(**10**)Zn(**6a**)]Cl_2). They showed even worse performances than the Cu(I) based dyes. Nevertheless, an interesting observation was made. When the Zn(II) containing solar cells were heated up to 80 °C, an increase in the fill factor from 33% to 45% was observed, which was retained for 17 days. This finding could be used in future to post treat DSCs to gain an improvement in the fill factors.

Future work consists of further enhancement of the performance of N719 and also other dyes, in combination with ZnO electrodes. This could be achieved by the

application of ZnO scattering layers. In the case of Cu(I) dyes, one should focus on the apparent destructive effects of the anchoring ligand solutions on the ZnO surface.

8.4. Experimental

8.4.1. Experimental protocol for the synthesis of SiO_2 nanoparticles

Two types of SiO_2 nanoparticles with different sizes were synthesized, namely 240 nm (**SN240**) and 350 nm (**SN350**) in diameter. The size was defined by the variation of the different ratios of the components ammonia, water and TEOS. The ratios are given in Table 8-10.[114]

In a beaker ammonia (28%), water and EtOH were mixed (Table 8-10). This solution was stirred for 5 min at 1100 rpm at RT. In another beaker 4.5 mL of TEOS was added to 45.5 mL of EtOH. This solution was poured in one portion into the first solution and kept stirring at 1100 rpm for 1 min. After that the stirring was reduced to 400 rpm. The covered beaker was left stirring for another two hours and then separated by centrifugation at 8000 rpm and three times washed with EtOH. Then the wet particles were dried in an oven at 80 °C.

Particle	Ammonia (28 %) \ mL	Water \ mL	EtOH \ mL
SN240	4.5	18.5	27.0
SN350	6.5	18.5	25.0

*Table 8-10: Ratios of ammonia, water and EtOH used to synthesize SiO_2 particles **SN240** and **SN350**.*

8.4.2. Manufacturing of doctor blading pastes

The used ZnO nanoparticles (VP AdNano® ZnO 20) were purchased from Degussa and had a diameter of 20 nm. For the following pastes a stock solution called **A**, consisting of acetic acid (1 vol%), EtOH (66 vol%) and milliQ water (33 vol%) was prepared.

8.4.2.1. DBP1[120]

To 4.0 g of solution **A**, 1.0 g of ZnO nanoparticles was added in small portions and the resulting suspension was stirred for 5 min with a stirring bar. The still very liquid mixture was then put in a sonicator for 5 min, resulting in the thickening of the paste.

8.4.2.2. DBP2[120]

To 6.0 g of solution **A**, 1.0 g of ZnO nanoparticles was added in small portions and the resulting suspension was stirred for 5 min with a stirring bar. The still very liquid mixture was then put in a sonicator for 5 min, but it still remained a very liquid mixture. Therefore it was sonicated for another 5 min, resulting in a more viscous paste.

8.4.2.3. DBP3[120]

To 2.7 g of **A** stirring in a vial, 1.0 g of ZnO nanoparticles was added in small portions. The resulting suspension was stirred until no more particles were floating on the surface. Then 6.0 g of terpineol (mixed isomers) were added as a non-volatile dispersion medium and the mixture stirred further for 5 min. The mixture was then sonicated for 5 min and then stirred again for 5 min. The cream like paste was subjected to milling in a three-roll-mill (one cycle) and collected.

8.4.3. Manufacturing of screen printing pastes

Two stock solutions had to be prepared. Solution **B** consisting of 35.0 g ethyl cellulose powder EC (5–15 mPas, #46070, Fluka) dissolved in EtOH to give a 10 wt% solution. Solution **C** consisting of 45.0 g ethyl cellulose powder EC (30–50 mPas, #46080, Fluka) dissolved in EtOH to yield a 10 wt% solution.

8.4.3.1. SPP1[121]

A round bottomed flask was charged with 1.0 g of ZnO nanoparticles and 2.8 g of **B** and 2.2 g of **C** were added as binder. Subsequently 4.0 g of terpineol (mixed isomers) and EtOH (5 mL) were added. The mixture was then stirred for 5 min with a stirring bar and after that sonicated for 5 min. This procedure was repeated twice again. The volatile components were then removed under reduced pressure (Rotavap, 1 h, 45 °C, 120 mbar). After that the pressure was set to 30 mbar until no more EtOH condensation was visible. The paste was then subjected to milling by an Exakt 50 I three roll mill with aluminium oxide rolls, 20 µm spacing (three times) and then collected.

8.4.3.2. SPP2[114]

A round bottomed flask was charged with 1.0 g of **SN240** SiO_2 nanoparticles and 2.8 g of **B** and 2.2 g of **C** were added as binder. Subsequently 4.0 g of terpineol (mixed isomers) and EtOH (5 mL) were added. The mixture was then stirred for 5 min with a stirring bar and after that sonicated for 5 min. This procedure was repeated twice again. The volatile components were then removed under reduced pressure (Rotavap, 1 h, 45 °C, 120 mbar). After that the pressure was set to 30 mbar until no more EtOH condensation was visible. The paste was then subjected to milling by an Exakt 50 I three roll mill with aluminium oxide rolls, 20 µm spacing (three times) and collected after.

8.4.3.3. SPP3[114]

The same protocol was used as for **SPP2**, but instead of **SN240**, **SN350** SiO_2 nanoparticles were used.

Chapter 9

Chapter 9: Conclusion and outlook

In this thesis it was shown that zinc(II) bis-terpyridine complexes can be used as emitters in OLEDs and LECs, although they exhibit low life times and require high driving voltages to show reasonable luminance. Nevertheless, this was a proof of concept and further work could consist of the optimization of the LEC and OLED manufacturing process for 2+ charged species such as zinc(II).

Furthermore, it was demonstrated that zinc(II) bis-terpyridine complexes can be used as dyes for DSCs, if chromophoric ligands are used. Additionally, for this kind of dye a step-wise assembly protocol was developed that has proven to be successful and allows the assembly of the dye introducing anchoring ligand, metal and ancillary ligand one after the other, without having to synthesize the homoleptic or heteroleptic complex first. Using simple ancillary ligands such as **6a** (Scheme 9-1) leads to DSC efficiencies up to 0.71% in unmasked cells.

To further increase the cell efficiency the problem of recombination was addressed, introducing alkyl chains into the ancillary ligand to shield the dye and therefore reduce the recombination of electrons from the semiconductor to the oxidized dye. It was seen that the oktyl substituent shows the most promising results, although the cell performance in general was very poor and thus did not allow one to draw clear conclusions.

In addition a versatile building block, based on the BTZ unit, was designed and synthesized which was used to synthesize a 2,2':6',2''-terpyridine based ligand (**22**) with extended absorption range and an organic dye (**24**) (Scheme 9-1). Unfortunately, the ligand **22** in combination with zinc(II) did not show an improvement of cell efficiency. On the other hand, the organic dye (**24**) performed well in DSCs and showed an efficiency of 4.6%.

The fact that the zinc(II) containing dyes show poor performances in DSCs indicates that the communication between the ancillary and the anchoring ligand is somehow interrupted, which may be due to the fact that the zinc(II) complexes do not show any electronic ligand-metal interaction such as MLCTs or LMCTs.

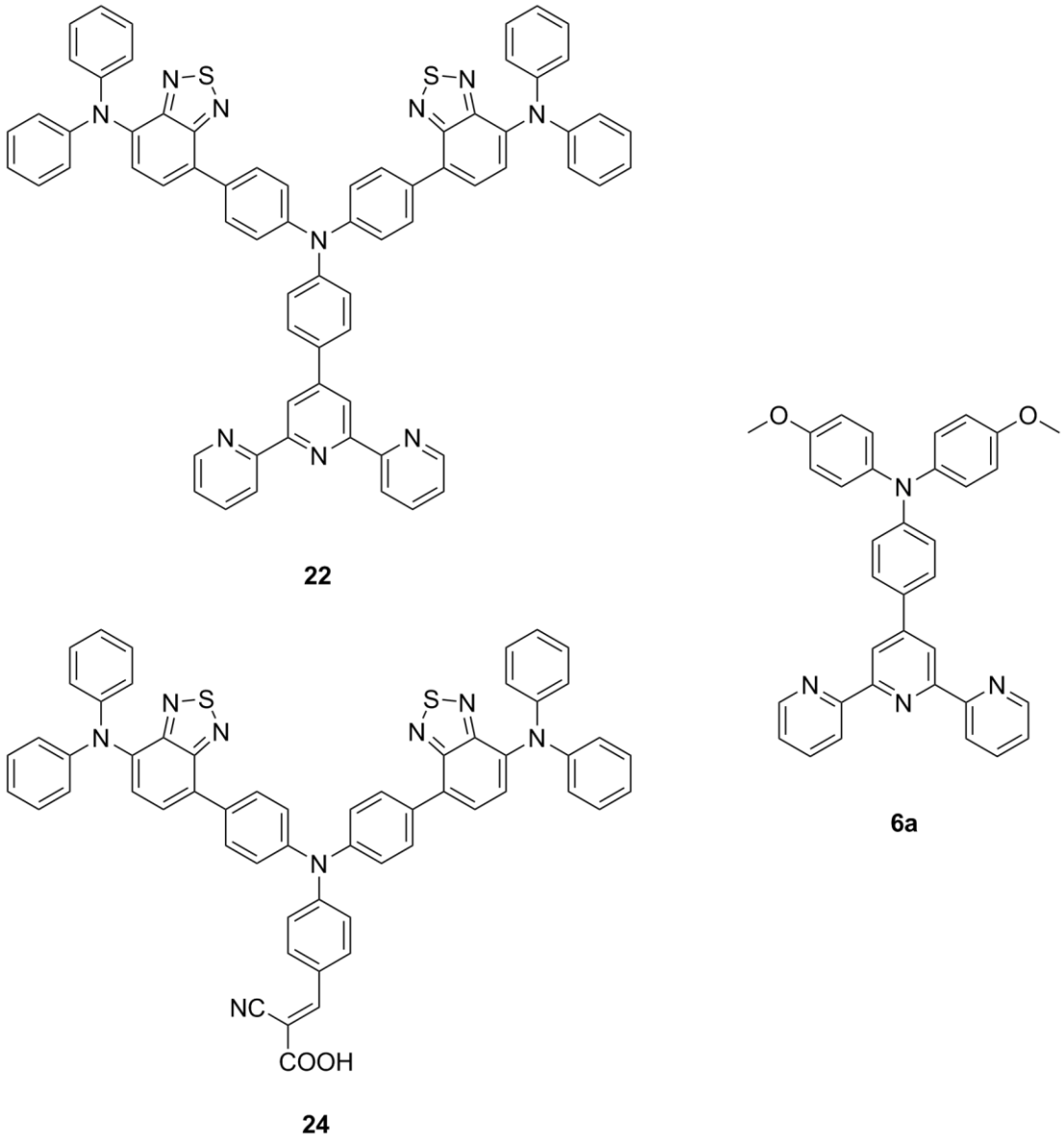

*Scheme 9-1: Ancillary ligands **6a** and **22** and organic dye **24**.*

Considering the poor cell performance one could think that the dyes do not contribute to the cell efficiency and only the semiconductor produces current. However, EQE measurements show that photon to current conversion is happening in these cells, although at very low level (below 2%) which supports the low efficiencies obtained (Figure 9-1).

Future work in this field consists of the understanding of the factors that negatively influence the communication between ancillary and anchoring ligand, and lead to low efficiencies.

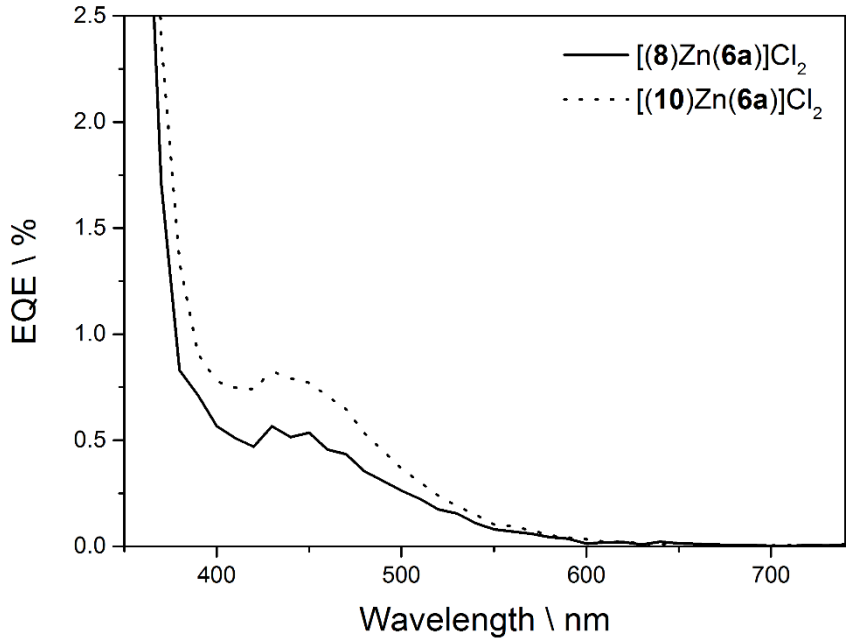

*Figure 9-1: EQE spectra of dyes [(**8**)Zn(**6a**)]Cl₂ and [(**10**)Zn(**6a**)]Cl₂.*

Furthermore, ZnO electrodes were manufactured with the intention of improving the DSC efficiencies for zinc(II) based dyes. For this purpose different methods for the manufacturing of ZnO electrodes for DSCs were evaluated and applied. Additionally, the screen printed electrodes were tested towards their efficiency using different dyes. The dye N719 was used to find the optimal dipping time which was found to be 1 h. Further, it was found that the anchoring ligands ALC1 and ALP1 degrade the ZnO layers, which resulted in poor efficiencies in copper(I) based DSCs. The solar cells that were prepared using the step-wise protocol with a zinc(II) based dye unfortunately showed lower cell performances that on TiO_2. However, it was found that, upon heating of the cells containing the zinc(II) dye, the fill factor can be improved. This improvement was retained for 17 days.

The introduction of a scattering layer by screen printing of TiO_2 or SiO_2 and by acid treatment, unfortunately did not show any improvement of the DSC efficiencies.

To further improve the performance of the solar cells using ZnO electrodes it should be tried to introduce a scattering layer made up from ZnO nanoparticles.

References

[1] Kemmler, A.; Piégsa, A.; Ley, A.; Wüthrich, P.; Keller, M.; Jakob, M.; Catenazzi, G. *Analyse des schweizerischen Energieverbrauchs 2000 - 2013 nach Verwendungszwecken*; 2014.

[2] *Schweizerische Elektrizitätsstatistik 2013*; 2013.

[3] Kaufmann, U. *Schweizerische Statistik der erneuerbaren Energien Ausgabe 2013*; 2014.

[4] Ständige Wohnbevölkerung nach Geschlecht und Alter, am Jahresende http://www.bfs.admin.ch/bfs/portal/de/index/themen/01/02/blank/key/bevoelkerungsstand/02.Document.141986.xls (accessed Nov 11, 2014).

[5] Glossary of statistical terms http://stats.oecd.org/glossary/detail.asp?ID=2112 (accessed Nov 11, 2014).

[6] *BP Statistical Review of World Energy June 2014*; 2014.

[7] Ehemalige Reaktorversuchsanlage Lucens: Tritiumwert in Entwässerungsanlage erhöht https://www.news.admin.ch/message/?lang=de&msg-id=44057 (accessed Nov 12, 2014).

[8] Tuttle, R. M.; Becker, D. V. *Semin. Nucl. Med.* **2000**, *30*, 133.

[9] Ohta, T.; Mahara, Y.; Kubota, T.; Fukutani, S.; Fujiwara, K.; Takamiya, K.; Yoshinaga, H.; Mizuochi, H.; Igarashi, T. *J. Environ. Radioact.* **2012**, *111*, 38.

[10] Bundesrat beschliesst im Rahmen der neuen Energiestrategie schrittweisen Ausstieg aus der Kernenergie http://www.admin.ch/aktuell/00089/?lang=de&msg-id=39337 (accessed Nov 11, 2014).

[11] Lampen: Effizienzanforderungen ab 2009 http://www.bfe.admin.ch/energie/00588/00589/00644/index.html?msg-id=24490 (accessed Nov 12, 2014).

[12] Häufig gestellte Fragen zu der Verordnung über die schrittweise Abschaffung herkömmlicher Glühlampen http://ec.europa.eu/energy/lumen/doc/full_faq_de.pdf (accessed Nov 12, 2014).

[13] The Nobel Prize in Physics 2014 http://www.nobelprize.org/nobel_prizes/physics/laureates/2014/ (accessed Nov 12, 2014).

[14] Elemental abundances http://upload.wikimedia.org/wikipedia/commons/0/09/Elemental_abundances.svg (accessed Nov 17, 2014).

[15] Emsley, J. *Nature's Building Blocks: An A-Z Guide to the Elements*; Oxford Pakistan Paperbacks Series; Oxford University Press, 2001.

[16] Housecroft, C. E.; Sharpe, A. G. *Anorganische Chemie*; Pearson Studium, 2006.

[17] ZINC Statistical Compendium http://minerals.usgs.gov/minerals/pubs/commodity/zinc/stat/ (accessed Nov 11, 2014).

[18] RSC periodic table http://www.rsc.org/periodic-table/element/30/zinc (accessed Nov 11, 2014).

[19] Zinc Statistics and Information http://minerals.usgs.gov/minerals/pubs/commodity/zinc/ (accessed Nov 11, 2014).

[20] Commodity profile ZINC www.bgs.ac.uk/downloads/start.cfm?id=1403 (accessed Nov 11, 2014).

[21] electrogenerated chemiluminescence http://goldbook.iupac.org/E01966.html (accessed Nov 12, 2014).

[22] Mitschke, U.; Bäuerle, P. *J. Mater. Chem.* **2000**, *10*, 1471.

[23] Schneider, G. E. Ionic Transition Metal Complexes Containing Iridium(III) for Lighting Applications, University of Basel, 2013.

[24] Hercules, D. M. *Science* **1964**, *145*, 808.

[25] Tokel, N. E.; Bard, A. J. *J. Am. Chem. Soc.* **1972**, *94*, 2862.

[26] Pope, M.; Kallmann, H. P.; Magnante, P. *J. Chem. Phys.* **1963**, *38*, 2042.

[27] Helfrich, W.; Schneider, W. *Phys. Rev. Lett.* **1965**, *14*, 229.

[28] Tang, C. W.; VanSlyke, S. A. *Appl. Phys. Lett.* **1987**, *51*, 913.

[29] Pardo, D. A.; Jabbour, G. E.; Peyghambarian, N. *Adv. Mater.* **2000**, *12*, 1249.

[30] Gustafsson, G.; Cao, Y.; Treacy, G. M.; Klavetter, F.; Colaneri, N.; Heeger, A. J. *Nature* **1992**, *357*, 477.

[31] Mizukami, M.; Hirohata, N.; Iseki, T.; Ohtawara, K.; Tada, T.; Yagyu, S.; Abe, T.; Suzuki, T.; Fujisaki, Y.; Inoue, Y.; Tokito, S.; Kurita, T. *IEEE Electron Device Lett.* **2006**, *27*, 249.

[32] Slinker, J. D.; Gorodetsky, A. a; Lowry, M. S.; Wang, J.; Parker, S.; Rohl, R.; Bernhard, S.; Malliaras, G. G. *J. Am. Chem. Soc.* **2004**, *126*, 2763.

[33] Pei, Q.; Yu, G.; Zhang, C.; Yang, Y.; Heeger, A. J. *Science* **1995**, *269*, 1086.

[34] Pei, Q.; Yu, G.; Zhang, C.; Heeger, A. J. *J. Am. Chem. Soc.* **1996**, *118*, 3922.

[35] Maness, K. M.; Terrill, R. H.; Meyer, T. J.; Murray, R. W.; Wightman, R. M. *J. Am. Chem. Soc.* **1996**, *118*, 10609.

[36] Hu, T.; He, L.; Duan, L.; Qiu, Y. *J. Mater. Chem.* **2012**, *22*, 4206.

[37] *Molecules at Work*; Pignataro, B., Ed.; Wiley-VCH Verlag GmbH & Co. KGaA: Weinheim, Germany, 2012.

[38] Peter, L. *Encyclopedia of Applied Electrochemistry*; Kreysa, G.;Ota, K.;Savinell, R. F., Eds.; Springer New York: New York, NY, 2014; pp. 357–363.

[39] Moser, J. *Monatshefte für Chemie* **1887**, *8*, 373.

[40] Anderson, S.; Constable, E. C.; Dare-Edwards, M. P.; Goodenough, J. B.; Hamnett, A.; Seddon, K. R.; Wright, R. D. *Nature* **1979**, *280*, 571.

[41] O'Regan, B.; Grätzel, M. *Nature* **1991**, *353*, 737.

[42] Grätzel, M. *Acc. Chem. Res.* **2009**, *42*, 1788.

[43] Nazeeruddin, M. K.; Baranoff, E.; Grätzel, M. *Sol. Energy* **2011**, *85*, 1172.

[44] Grätzel, M. *Inorg. Chem.* **2005**, *44*, 6841.

[45] Hagfeldt, A.; Boschloo, G.; Sun, L.; Kloo, L.; Pettersson, H. *Chem. Rev.* **2010**, *110*, 6595.

[46] Bozic-Weber, B.; Constable, E. C.; Housecroft, C. E. *Coord. Chem. Rev.* **2013**, *257*, 3089.

[47] Hagfeldt, A.; Graetzel, M. *Chem. Rev.* **1995**, *95*, 49.

[48] Valencia, S.; Marín, J. M.; Restrepo, G. *Open Mater. Sci. J.* **2010**, *4*, 9.

[49] Austin, R. H.; Lim, S. *Proc. Natl. Acad. Sci. U. S. A.* **2008**, *105*, 17217.

[50] Ogura, R. Y.; Nakane, S.; Morooka, M.; Orihashi, M.; Suzuki, Y.; Noda, K. *Appl. Phys. Lett.* **2009**, *94*, 073308.

[51] Kalyanasundaram, K.; Grätzel, M. *Coord. Chem. Rev.* **1998**, *177*, 347.

[52] Galoppini, E. *Coord. Chem. Rev.* **2004**, *248*, 1283.

[53] Sauvage, F.; Decoppet, J.; Zhang, M.; Zakeeruddin, S. M.; Comte, P.; Nazeeruddin, M.; Wang, P.; Grätzel, M. *J. Am. Chem. Soc.* **2011**, *133*, 9304.

[54] Stergiopoulos, T.; Falaras, P. *Adv. Energy Mater.* **2012**, *2*, 616.

[55] Bessho, T.; Constable, E. C.; Graetzel, M.; Hernandez Redondo, A.; Housecroft, C. E.; Kylberg, W.; Nazeeruddin, M. K.; Neuburger, M.; Schaffner, S. *Chem. Commun.* **2008**, 3717.

[56] Bozic-Weber, B.; Brauchli, S. Y.; Constable, E. C.; Fürer, S. O.; Housecroft, C. E.; Malzner, F. J.; Wright, I. a; Zampese, J. a. *Dalton Trans.* **2013**, *42*, 12293.

[57] Sandroni, M.; Favereau, L.; Planchat, A.; Akdas-Kilig, H.; Szuwarski, N.; Pellegrin, Y.; Blart, E.; Le Bozec, H.; Boujtita, M.; Odobel, F. *J. Mater. Chem. A* **2014**, *2*, 9944.

[58] Ito, S.; Miura, H.; Uchida, S.; Takata, M.; Sumioka, K.; Liska, P.; Comte, P.; Péchy, P.; Grätzel, M. *Chem. Commun.* **2008**, 5194.

[59] Mathew, S.; Yella, A.; Gao, P.; Humphry-Baker, R.; Curchod, B. F. E.; Ashari-Astani, N.; Tavernelli, I.; Rothlisberger, U.; Nazeeruddin, M. K.; Grätzel, M. *Nat. Chem.* **2014**, *6*, 242.

[60] Bozic-Weber, B.; Constable, E. C.; Hostettler, N.; Housecroft, C. E.; Schmitt, R.; Schönhofer, E. *Chem. Commun.* **2012**, *48*, 5727.

[61] Mosconi, E.; Yum, J.; Kessler, F.; Gómez García, C. J.; Zuccaccia, C.; Cinti, A.; Nazeeruddin, M. K.; Grätzel, M.; De Angelis, F. *J. Am. Chem. Soc.* **2012**, *134*, 19438.

[62] Bozic-Weber, B.; Constable, E. C.; Fürer, S. O.; Housecroft, C. E.; Troxler, L. J.; Zampese, J. A. *Chem. Commun.* **2013**, *49*, 7222.

[63] *APEX2, version 2 User Manual, M86-E01078*, Bruker Analytical X-ray Systems, Inc., Madison, WI, 2006.

[64] Altomare, A.; Cascarano, G.; Giacovazzo, C.; Guagliardi, A.; Burla, M. C.; Polidori, G.; Camalli, M. *J. Appl. Crystallogr.* **1994**, *27*, 435.

[65] Betteridge, P. W.; Carruthers, J. R.; Cooper, R. I.; Prout, K.; Watkin, D. J. *J. Appl. Crystallogr.* **2003**, *36*, 1487.

[66] Bruno, I. J.; Cole, J. C.; Edgington, P. R.; Kessler, M.; Macrae, C. F.; McCabe, P.; Pearson, J.; Taylor, R. *Acta Crystallogr. Sect. B Struct. Sci.* **2002**, *58*, 389.

[67] Macrae, C. F.; Bruno, I. J.; Chisholm, J. A.; Edgington, P. R.; McCabe, P.; Pidcock, E.; Rodriguez-Monge, L.; Taylor, R.; van de Streek, J.; Wood, P. A. *J. Appl. Crystallogr.* **2008**, *41*, 466.

[68] Ito, S.; Chen, P.; Comte, P.; Nazeeruddin, M. K.; Liska, P.; Péchy, P.; Grätzel, M. *Prog. Photovoltaics Res. Appl.* **2007**, *15*, 603.

[69] Yu, S.-C.; Kwok, C.-C.; Chan, W.-K.; Che, C.-M. *Adv. Mater.* **2003**, *15*, 1643.

[70] Slinker, J. D.; Rivnay, J.; Moskowitz, J. S.; Parker, J. B.; Bernhard, S.; Abruña, H. D.; Malliaras, G. G. *J. Mater. Chem.* **2007**, *17*, 2976.

[71] Meier, S. B.; Tordera, D.; Pertegás, A.; Roldán-Carmona, C.; Ortí, E.; Bolink, H. J. *Mater. Today* **2014**, *17*, 217.

[72] Zinkpreis http://www.finanzen.net/rohstoffe/zinkpreis (accessed Aug 29, 2014).

[73] Iridiumpreis http://www.agosi.de/ek/ek.php/frontend/verlaufssuche3waymemory/de (accessed Aug 29, 2014).

[74] Constable, E. C.; Lewis, J.; Liptrot, M. C.; Raithby, P. R. *Inorganica Chim. Acta* **1990**, *178*, 47.

[75] Wang, J.; Hanan, G. S. *Synlett* **2005**, 1251.

[76] Schneider, G. E.; Bolink, H. J.; Constable, E. C.; Ertl, C. D.; Housecroft, C. E.; Pertegàs, A.; Zampese, J. A.; Kanitz, A.; Kessler, F.; Meier, S. B. *Dalton Trans.* **2014**, *43*, 1961.

[77] Alcazar-Roman, L. M.; Hartwig, J. F.; Rheingold, A. L.; Liable-Sands, L. M.; Guzei, I. A. *J. Am. Chem. Soc.* **2000**, *122*, 4618.

[78] Walters, K. a.; Kim, Y.-J.; Hupp, J. T. *J. Electroanal. Chem.* **2003**, *554-555*, 449.

[79] Liu, Y.; Liu, M. S.; Jen, A. K.-Y. *Acta Polym.* **1999**, *50*, 105.

[80] Pommerehne, J.; Vestweber, H.; Guss, W.; Mahrt, R. F.; Bässler, H.; Porsch, M.; Daub, J. *Adv. Mater.* **1995**, *7*, 551.

[81] Constable, E. C.; Housecroft, C. E.; Schneider, G. E.; Zampese, J. A.; Bolink, H. J.; Pertegás, A.; Roldan-Carmona, C. *Dalton Trans.* **2014**, *43*, 4653.

[82] Winter, A.; van den Berg, A.; Hoogenboom, R.; Kickelbick, G.; Schubert, U. *Synthesis (Stuttg).* **2006**, *2006*, 2873.

[83] Brauchli, S. Y.; Constable, E. C.; Harris, K.; Häussinger, D.; Housecroft, C. E.; Rösel, P. J.; Zampese, J. A. *Dalton Trans.* **2010**, *39*, 10739.

[84] Goodall, W.; Wild, K.; Arm, K. J.; Williams, J. A. G. *J. Chem. Soc. Perkin Trans. 2* **2002**, 1669.

[85] Nguyen, H.; Mane, R. S.; Ganesh, T.; Han, S.; Kim, N. *J. Phys. Chem. C* **2009**, *113*, 9206.

[86] Jiang, Q.; Zhu, J.; Zhang, Y.; Xiao, N.; Guo, Z. *Biometals* **2009**, *22*, 297.

[87] Chen, X.; Zhou, Q.; Cheng, Y.; Geng, Y.; Ma, D.; Xie, Z.; Wang, L. *J. Lumin.* **2007**, *126*, 81.

[88] *Dye-sensitized solar cells*; Kalyanasundaram, K., Ed.; 1st ed.; EPFL Press, 2010.

[89] Bozic-Weber, B.; Constable, E. C.; Housecroft, C. E.; Kopecky, P.; Neuburger, M.; Zampese, J. a. *Dalton Trans.* **2011**, *40*, 12584.

[90] Rendondo, A. H.; Constable, E. C.; Housecroft, C. E. *Chim. Int. J. Chem.* **2009**, *63*, 205.

[91] Scaltrito, D. V; Thompson, D. W.; Callaghan, J. A. O.; Meyer, G. J. **2000**, *208*, 243.

[92] Snaith, H. J. *Energy Environ. Sci.* **2012**, *5*, 6513.

[93] Fang, Z.; Teo, T.-L.; Cai, L.; Lai, Y.-H.; Samoc, A.; Samoc, M. *Org. Lett.* **2009**, *11*, 1.

[94] Ardo, S.; Meyer, G. J. *Chem. Soc. Rev.* **2009**, *38*, 115.

[95] Feldt, S. M.; Gibson, E. a; Gabrielsson, E.; Sun, L.; Boschloo, G.; Hagfeldt, A. *J. Am. Chem. Soc.* **2010**, *132*, 16714.

[96] Feldt, S. M.; Wang, G.; Boschloo, G.; Hagfeldt, A. *J. Phys. Chem. C* **2011**, *115*, 21500.

[97] Brennan, B. J.; Llansola Portolés, M. J.; Liddell, P. a; Moore, T. a; Moore, A. L.; Gust, D. *Phys. Chem. Chem. Phys.* **2013**, *15*, 16605.

[98] Guerrero, G.; Mutin, P. H.; Vioux, A. *Chem. Mater.* **2001**, *13*, 4367.

[99] Shellaiah, M.; Rajan, Y. C.; Lin, H.-C. *J. Mater. Chem.* **2012**, *22*, 8976.

[100] Mishra, A.; Fischer, M. K. R.; Bäuerle, P. *Angew. Chem. Int. Ed. Engl.* **2009**, *48*, 2474.

[101] Kim, B.-G.; Chung, K.; Kim, J. *Chemistry* **2013**, *19*, 5220.

[102] Wang, X.; Sun, Y.; Chen, S.; Guo, X.; Zhang, M.; Li, X.; Li, Y.; Wang, H. *Macromolecules* **2012**, *45*, 1208.

[103] Wang, Z.; Gao, Z.; Feng, Y.; Liu, Y.; Yang, B.; Liu, D.; Lv, Y.; Lu, P.; Ma, Y. *Polymer (Guildf).* **2013**, *54*, 6191.

[104] Aspley, C. J.; Gareth Williams, J. a. *New J. Chem.* **2001**, *25*, 1136.

[105] Pelz, S.; Zhang, J.; Kanelidis, I.; Klink, D.; Hyzak, L.; Wulf, V.; Schmitz, O. J.; Gasse, J.-C.; Frahm, R.; Pütz, A.; Colsmann, A.; Lemmer, U.; Holder, E. *European J. Org. Chem.* **2013**, *2013*, 4761.

[106] Kim, J.-J.; Choi, H.; Lee, J.-W.; Kang, M.-S.; Song, K.; Kang, S. O.; Ko, J. *J. Mater. Chem.* **2008**, *18*, 5223.

[107] Lee, D. H.; Lee, M. J.; Song, H. M.; Song, B. J.; Seo, K. D.; Pastore, M.; Anselmi, C.; Fantacci, S.; De Angelis, F.; Nazeeruddin, M. K.; Gräetzel, M.; Kim, H. K. *Dye. Pigment.* **2011**, *91*, 192.

[108] Spanhel, L.; Haase, M.; Weller, H.; Henglein, A. *J. Am. Chem. Soc.* **1987**, *109*, 5649.

[109] Gopidas, K. R.; Bohorquez, M.; Kamat, P. V. *J. Phys. Chem.* **1990**, *94*, 6435.

[110] Kennedy, R.; Martini, I.; Hartland, G.; Kamat, P. V. *Proc. Indian Acad. Sci. (Chem. Sci.)* **1997**, *109*, 497.

[111] Rabani, J. *J. Phys. Chem.* **1989**, *93*, 7707.

[112] Volkert, C. A.; Minor, A. M. *MRS Bull.* **2011**, *32*, 389.

[113] Wang, Z.-S.; Kawauchi, H.; Kashima, T.; Arakawa, H. *Coord. Chem. Rev.* **2004**, *248*, 1381.

[114] Wang, Y.; Chen, E.; Lai, H.; Lu, B.; Hu, Z.; Qin, X.; Shi, W.; Du, G. *Ceram. Int.* **2013**, *39*, 5407.

[115] Watson, T.; Charbonneau, C.; Bryant, D.; Worsley, D. *Int. J. Photoenergy* **2012**, *2012*, 1.

[116] Bozic-Weber, B.; Chaurin, V.; Constable, E. C.; Housecroft, C. E.; Meuwly, M.; Neuburger, M.; Rudd, J. a; Schönhofer, E.; Siegfried, L. *Dalton Trans.* **2012**, *41*, 14157.

[117] Bozic-Weber, B.; Brauchli, S. Y.; Constable, E. C.; Fürer, S. O.; Housecroft, C. E.; Wright, I. A. *Phys. Chem. Chem. Phys.* **2013**, *15*, 4500.

[118] Brauchli, S. Y.; Bozic-Weber, B.; Constable, E. C.; Hostettler, N.; Housecroft, C. E.; Zampese, J. a. *RSC Adv.* **2014**, *4*, 34801.

[119] Sedky, A.; El-Brolossy, T. A.; Mohamed, S. B. *J. Phys. Chem. Solids* **2012**, *73*, 505.

[120] Saito, M.; Fujihara, S. *Energy Environ. Sci.* **2008**, *1*, 280.

[121] Ito, S.; Murakami, T. N.; Comte, P.; Liska, P.; Grätzel, C.; Nazeeruddin, M. K.; Grätzel, M. *Thin Solid Films* **2008**, *516*, 4613.